Influence of spin excitations on transport through a quantum-dot spin valve

Dissertation

zur Erlangung des Grades
„Doktor der Naturwissenschaften“

an der Fakultät für Physik
der Universität Duisburg-Essen

von
Dipl.-Phys. Björn Sothmann

Referent: Prof. Dr. J. König
Korreferent: Prof. Dr. M. Wegewijs
Korreferent: Prof. Dr. D. Pfannkuche
Tag der mündlichen Prüfung: 28.03.2011

Zusammenfassung

In der vorliegenden Arbeit untersuchen wir den spinabhängigen Transport durch Nanostrukturen. Der Schwerpunkt der Arbeit liegt auf dem Transport durch Quantenpunkte (QP) die durch Tunnelbarrieren an nicht kollinear magnetisierte Elektroden gekoppelt sind. Durch Anlegen einer Transportspannung an ein solches Quantenpunktspinventil (QPSV) wird eine Spinakkumulation auf dem QP erzeugt, die den Strom durch das System reduziert. Daneben führt eine spinabhängige Renormierung der Dotniveaus zu einem effektiven Austauschfeld auf dem QP, in welchem der akkumulierte Spin präzediert. Das Wechselspiel dieser beiden Effekte führt dann z. B. zu einer nichtharmonischen Abhängigkeit des Leitwerts vom Winkel zwischen den Magnetisierungen.

Das Ziel dieser Arbeit ist es, den Einfluß von Spinanregungen auf den Transport durch ein QPSV zu untersuchen. Diese können entweder in den Elektroden, in den Tunnelbarrieren oder auf dem QP auftreten. Wir betrachten hier den Einfluß von Spinwellen in den Elektroden, magnetischen Verunreinigungen in den Tunnelbarrieren und auf dem QP sowie Spinanregungen aufgrund einer komplexen internen Struktur des QPs im Falle des Transports durch einzelne magnetischer Atome.

Wir untersuchen zunächst den Einfluß von Spinwellen auf den Transport durch ein QPSV. Die Emission und Absorption von Magnonen führt zu Seitenbändern im differentiellen Leitwert, deren Stärke von der magnetischen Orientierung und Polarisation der Elektroden abhängt. Weiterhin können die Spinwellen den Fanofaktor je nach angelegter Gatespannung erhöhen bzw. erniedrigen. Wir diskutieren ferner die Nichtgleichgewichtsbesetzungen der Magnonen in den Elektroden und zeigen, wie die Magnonen einen komplett spinpolarisierten Strom ohne äußere Spannung treiben können.

Anschließend diskutieren wir den Einfluß magnetischer Verunreinigungen auf den Transport durch ein QPSV. Im Falle eines Spins in der Tunnelbarriere finden wir ein kompliziertes Wechselspiel zwischen dem strominduzierten Schalten des Spin in der Barriere, der Spinakkumulation auf dem QP und des Stroms durch den QP. Im Falle eines Spins auf dem QP (z. B. realisiert durch einen Kernspin) zeigen wir, wie der frequenzabhängige Fanofaktor Aufschluß über die nichttriviale Spindynamik gibt und eine experimentelle Bestimmung der Spin-Austausch-Kopplung ermöglicht.

Wir wenden uns dann der inelastischen Spektroskopie einzelner magnetischer Atome zu. Wir zeigen, daß ein vollständiges Verständnis des beobachteten differentiellen Leitwerts nur möglich ist, wenn man eine Nichtgleichgewichtsbesetzung der atomaren Spinzustände berücksichtigt. Ferner schlagen wir vor mit Hilfe des Stromrauschens weitere Informationen über die Nichtgleichgewichtsbesetzungen zu erhalten. Darüber hinaus zeigen wir, daß die Abwesenheit gewisser Nichtgleichgewichtseffekte im Experiment durch eine anisotrope Spinrelaxation erklärt werden kann.

Obwohl das Austauschfeld wichtig ist, um den Transport durch ein QPSV zu verstehen, hat sich sein experimenteller Nachweis bis jetzt als schwierig erwiesen, da die meisten Austauschfeldeffekte nur bei großen Polarisationen der Elektroden auftreten. Wir schlagen hier eine neue Möglichkeit vor, das Austauschfeld experimentell zu detektieren. Koppelt man zusätzlich einen Supraleiter an den QP, so zeigt der Anteil des Stroms in den Supraleiter, der symmetrisch in der an die Ferromagneten angelegten Spannung ist, charakteristische Signaturen des Austauschfeldes auch bei kleinen Polarisationen der Ferromagneten.

Summary

In this thesis, we discuss spin-dependent transport through nanostructures. The main emphasis is put on transport through quantum-dot spin valves (QDSV), i.e., quantum dots coupled via tunneling barriers to noncollinearly magnetized ferromagnets. Applying a bias voltage across the system leads to a nonequilibrium spin accumulation on the quantum dot that has the tendency to block further transport. In addition, a spin-dependent level renormalization yields an effective exchange field that gives rise to a precession of the accumulated spin. The interplay between these to effects leads to interesting transport properties as, e.g., a nonharmonic dependence of the differential conductance on the angle between the magnetizations.

The main goal of this thesis is to study the influence of spin excitations on transport through a QDSV. These can be located either in the electrodes, in the tunnel barrriers or on the quantum dot. We investigate the influence of spin waves in the electrodes, magnetic impurities in the tunnel barriers or on the dot as well as spin excitations due to a complex internal structure of the quantum dot that play a role for transport through single magnetic atoms.

First, we study the influence of spin waves in the electrodes on transport through the QDSV. We find that the emission and absorption of magnons gives rise to side bands in the differential conductance whose strength depends on the magnetic orientation and the polarization of the electrodes. Additionally, the spin waves can increase or decrease the Fano factor depending on the applied gate voltage. We furthermore discuss the nonequilibrium occupations of the magnons in the electrodes and show that the magnons can drive a fully spin-polarized current without a bias voltage.

Next, we discuss the influence of magnetic impurities on transport through a QDSV. If the impurity spin is localized in the tunnel barrier, we find a complicated interplay between current-induced switching of the barrier spin, the spin accumulation on the dot and the current through the system. In the case of a spin on the quantum dot, as, e.g., realized by a nuclear spin, we show how the frequency-dependent Fano factor provides information about the nontrivial spin dynamics and allows an experimental determination of the spin-spin exchange coupling.

We then turn to the discussion of spin inelastic tunneling spectroscopy of single magnetic atoms. We show that a full understanding of the experimentally observed differential conductance is only possible if one takes into account nonequilibrium occupation of the atom spin states. We furthermore demonstrate that the Fano factor can provide additional information about the nonequilibrium occupations. Finally, we discuss that the remarkable absence of certain nonequilibrium effects in experiment can be explained by an anisotropic spin relaxation channel.

Though the exchange field is found to be important for understanding transport through a QDSV, experimentally, it has so far been detected only through its splitting of the Kondo resonance as all other exchange field effects rely on large polarizations of the electrodes. Here, we propose a new way to detect the exchange field experimentally. To this end, we consider a QDSV with an additional superconductor coupled to the quantum dot. The part of the current into the superconductor that is symmetric with respect to the bias applied between the ferromagnets then shows characteristic signatures of the exchange field even for small polarizations.

Contents

1 Introduction **1**

2 Spin-dependent transport through quantum dots **5**
2.1 Transport through quantum dots . . . 5
2.2 Spin-dependent transport . . . 9
2.3 Spin accumulation . . . 12
2.4 Quantum-dot spin valves . . . 13
2.4.1 Model . . . 14
2.4.2 Master equation . . . 15
2.4.3 Transport properties . . . 17
2.4.4 Experimental realizations . . . 25

3 Diagrammatic real-time transport theory **29**
3.1 Density matrix and propagator . . . 31
3.2 Current and current noise . . . 35
3.3 Extension of the diagrammatic theory to systems involving spin degrees of freedom . . . 37
3.4 Summary . . . 39

4 Spin waves in quantum-dot spin valves **41**
4.1 Model . . . 41
4.2 Reduced density matrix and master equation . . . 44
4.3 Results . . . 48
4.3.1 Transport processes . . . 48
4.3.2 Magnon-assisted tunneling . . . 49
4.3.3 Nonequilibrium magnon distribution . . . 52
4.3.4 Magnon-driven electron transport . . . 52
4.3.5 Current noise . . . 55
4.4 Summary . . . 59

5 Quantum-dot spin valves with magnetic impurities **63**
5.1 Model . . . 65
5.1.1 Model A: Impurity in the barrier . . . 65
5.1.2 Model B: Impurity on the dot . . . 66
5.2 Reduced density matrix and master equation . . . 68
5.2.1 Model A: Impurity in the barrier . . . 68
5.2.2 Model B: Impurity on the dot . . . 71
5.3 Results - Impurity in the barrier . . . 77
5.3.1 Noncollinear magnetizations . . . 82
5.4 Results - Impurity on the dot . . . 88

5.4.1 Large magnetic field . . . 88
5.4.2 Small magnetic field . . . 92
5.5 Summary . . . 94

6 Nonequilibrium current and noise in inelastic tunneling through a magnetic atom 95
6.1 Introduction . . . 95
6.2 Model . . . 96
6.3 Results . . . 98
6.3.1 Differential conductance . . . 98
6.3.2 Fano factor . . . 100
6.3.3 Anisotropic relaxation . . . 102
6.4 Summary . . . 103

7 Probing the exchange field of a quantum-dot spin valve by a superconducting lead 105
7.1 Model . . . 106
7.2 Reduced density matrix and master equation . . . 108
7.3 Results . . . 111
7.3.1 Symmetric quantum-dot spin valve . . . 111
7.3.2 Asymmetry effects . . . 116
7.4 Summary . . . 120

8 Conclusions 121

A Diagrammatic rules 125
A.1 Spin waves in quantum-dot spin valves . . . 125
A.2 Magnetic impurities in quantum-dot spin valves . . . 126
A.3 Quantum-dot spin valves with a superconducting lead . . . 126

B Master equations 129
B.1 Spin waves in quantum-dot spin valves . . . 129
B.2 Impurity in tunnel barrier . . . 131
B.3 Impurity on the dot . . . 134
B.4 Proximized quantum-dot spin valve . . . 135

C Density matrix for two spin-1/2 particles 137

D Equation of motions for two spin-1/2 particles 139

Bibliography 141

Publications 155

Acknowledgments 157

1 Introduction

In 1947, Shockley, Bardeen and Brattain invented the first transistor for which they were awarded the Nobel prize in 1956. Since then, there is an ongoing miniaturization and optimization of transistor devices. This has lead to transistors on the chips of modern computers that have sizes of just a few 10 nm. This miniaturization is empirically described by Moore's law which states that the number of transistors in commercially fabricated integrated circuits doubles approximately every two years. However, it is clear that there are fundamental limitations to this miniaturization process. Transistors cannot be made smaller than the atoms and molecules out of which they are built. But even before reaching this ultimate limit of miniaturization, another limitation sets in. As the size of an electronic device shrinks, quantum mechanical effects become important. These effects are, however, not only a problem for further shrinking transistors. They also open up the possibility to build devices with completely new functionalities.

It is particularly interesting to study these quantum mechanical effects in **quantum dots**, both from an experimentally as well as from a theoretical point of view. Quantum dots are effectively 0-dimensional systems where the electrons are confined in all three spatial dimensions. They therefore show a discrete level spectrum like an atom. However, quantum dots offer the additional advantage of being highly tunable in their properties. For this reason, they are also termed **artificial atoms**. Experimentally, quantum dots can be realized in a number of different ways. They can be formed by small metallic grains, carbon nanotubes and even single molecules as, e.g., a C_{60} bucky ball. They can also be made from semiconducting materials, e.g., by defining a quantum dot in a semiconducting nanowire using metallic gates or by growing self-assembled, semiconducting nanoislands on a substrate.

Studying **electrical transport** through quantum dots provides one way to investigate their properties. To this end, one contacts a quantum dot by electronic reservoirs via tunnel barriers. Furthermore, gate electrodes are coupled capacitively to the quantum dot to allow control over the level positions of the dot. Due to its small size, the quantum dot has a small capacitance. Hence, the charging energy, i.e., the energy needed to add an additional electron on the dot, is large. Therefore, usually, the number of electrons on the dot is fixed and transport is **Coulomb blockaded**. Only when two charge states become degenerate in energy by appropriately tuning the gate voltage, **sequential tunneling** through the quantum dot sets in. An electron enters the dot from the source electrode. In a subsequent tunneling event, the electron then leaves to the drain electrode, i.e., electrons are transferred through the quantum dot one by one. As the current through the quantum dot can be controlled by the gate voltage, such a device is called a **single-electron transistor**. Inside the Coulomb blockade regions, sequential tunneling is exponentially suppressed. Here, transport takes place via higher-order processes. In a **cotunneling** process, an electron tunnels onto the dot to occupy an intermediate, energetically forbidden state before it leaves

the dot in a second tunneling event.

So far, only the charge degree of freedom of the electrons entered our discussion. However, the electron possesses a spin degree of freedom, too. This spin degree of freedom is made use of, e.g., in a **spin valve**. One possible realization of such a spin valve consists of two ferromagnets separated by a nonmagnetic metall. The current through the spin valve depends on the relative orientation of the two magnetizations. Usually, in the parallel configuration, the spin valve is "open" and a large current flows while in the antiparallel configuration, it is "closed" and a only small current flows. This **giant magnetoresistance** (GMR) effect was discovered independently by Grünberg and Fert who were awarded the Nobel prize in 2007 for their discovery. It results from spin-dependent scattering of electrons either at the interface or from impurities. Alternatively, a spin valve can be realized by coupling two ferromagnets via an insulating tunnel barrier. Again, the current is large for parallel and small for antiparallel magnetizations. This **tunnel magnetoresistance** (TMR) arises from spin-dependent tunneling through the barrier. Both effects have already found technological applications, e.g., in the read heads of modern hard drives. While a first generation made use of the GMR, nowadays these have been superseded by devices using the TMR, which demonstrates the rapid technological advancements made in this field.

Here, we consider transport through a **quantum-dot spin valve**, i.e., a quantum dot coupled to two ferromagnetic electrodes with magnetizations pointing in arbitrary directions. A quantum-dot spin valve shows the characteristic effects of transport through quantum dots, as, e.g., the Coulomb blockade discussed above. In addition, the quantum-dot spin valve also exhibits spin-related effects. First of all, there is a nonequilibrium **spin accumulation** on the quantum dot. This spin accumulation is driven by the spin-dependent tunneling processes between the dot and the two ferromagnets. The spin accumulation in turn leads to a tunnel magnetoresistance, as the quantum-dot spin valve can be viewed as two spin valves in series.

The quantum-dot spin valve is however not just the sum of a quantum dot and two spin valves. Additionally, charge fluctuations on the quantum dot lead to a spin-dependent renormalization of the dot levels. This level renormalization manifests itself as an effective **exchange field** that acts on the spin accumulated on the dot. The interplay between spin accumulation and spin precession then leads to interesting, nontrivial transport properties, such as an anharmonic dependence of the differential conductance on the angle between the magnetizations, broad regions of negative differential conductance and characteristic features in the finite-frequency current noise at the Larmor frequency associated with the exchange field.

The main aim of this thesis is to study the influence of **spin excitations** on transport through a quantum-dot spin valve. The spin excitations can occur either in the electrodes, in the tunnel barriers or on the quantum dot. We consider the influence of **spin waves** as an example of spin excitations in the ferromagnetic electrodes. We furthermore investigate the influence of **magnetic impurities** which can be located either in the tunnel barrier or on the quantum dot. Finally, we study the possibility of spin excitations on the quantum dot due to a complex internal structure of the dot.

To study the influence of spin waves, we consider a model where tunneling electrons can emit and absorb magnons in the ferromagnetic electrodes. The influence of magnetic impurities is investigated in two different models where a spin is localized

either in the tunnel barrier or on the quantum dot. The latter case may serve, e.g., to describe the influence of **nuclear spins** on transport through a quantum-dot spin valve.

Quantum dots with a complex internal structure can be realized, e.g., by **magnetic atoms** that have a large, anisotropic spin. Recently, there has been much interest in transport through single magnetic atoms absorbed on a nonmagnetic substrate and contacted by a nonmagnetic scanning tunneling microscope tip. By performing **inelastic tunneling spectroscopy** measurements on the adatoms, one can study magnetic properties and couplings on an atomic scale. The differential conductance of the adatom shows steps at bias voltages which correspond to the excitation energies of the atom spin. The height of these steps can be related to certain spin matrix elements. This picture, which implicitly assumes an equilibrium occupation of the dot states, can indeed explain the experimentally observed conductance steps. However, it does not address the recently observed nonmonotonicities in the differential conductance. Here, we show using a master equation approach that a **nonequilibrium occupation** can explain the observed overshooting at the steps. We furthermore predict nonequilibrium effects in the current noise and discuss how the remarkable absence of nonequilibrium effects at certain steps points at the presence of an anisotropic relaxation channel.

Apart from the influence of spin excitations, we also discuss a new way to detect the exchange field experimentally even for small polarizations of the ferromagnets. To this end, we show that the current into a third **superconducting** lead coupled to the quantum dot turns out to be very sensitive to spin precession on the dot due to the exchange field.

This thesis is organized as follows. In Chapter 2, we review the basics of transport through quantum dots. We furthermore address the various magnetoresistance effects. Finally, we discuss the transport properties of a quantum-dot spin valve which forms the basics for the rest of this thesis. In Chapter 3, we review the real-time diagrammatic technique that we use in this thesis to describe transport through the quantum-dot spin valve. It enables us to deal with strong Coulomb interaction on the dot, a nonequilibrium situation and to perform a systematic expansion in the tunnel coupling between the dot and the electrodes. Furthermore, we discuss the extensions of the technique needed for the systems under investigation. In Chapter 4, we then discuss the influence of spin waves on transport through a quantum dot spin valve. On the one hand, we show how the effects known from the ordinary quantum-dot spin valve are modified by the presence of magnons. On the other hand, we show that the magnons can give rise to completely new effects, e.g., a fully spin-polarized magnon-driven current at zero bias. In Chapter 5, we turn to the influence of magnetic impurities. We first discuss the case of a localized spin embedded in one of the tunnel barriers, where a nontrivial interplay between the current-induced switching of the impurity, the spin accumulation on the quantum dot and the current through the dot arises. Afterwards, we turn to the situation of a spin on the quantum dot. We show how the finite-frequency noise can be used to study the nontrivial spin dynamics on the dot due to the interplay between exchange interactions between the spin, the coupling to external magnetic fields and the exchange field effects that arise in a quantum-dot spin valve. In Chapter 6, we turn to the discussion of spin inelastic electron tunneling spectroscopy of single magnetic adatoms. We discuss the relevance of nonequilibrium spin occupations to understand all features of the differential conductance observed in

recent experiments. We furthermore predict new nonequilibrium effects in the current noise. In Chapter 7, we consider a quantum-dot spin valve in which a third superconduting lead is coupled to the quantum dot. We show that the current into the superconductor can provide information about the exchange field even in the limit of small polarizations of the ferromagnets. This is in contrast to most other exchange field effects and can therefore provide an alternative way to access the exchange field in experiment. Finally, we finish this thesis with conclusions presented in Chapter 8.

2 Spin-dependent transport through quantum dots

In this chapter we introduce the physical concepts that govern transport through quantum-dot spin valves that is a quantum dot coupled to ferromagnetic electrodes. We first discuss transport through quantum dots in general where Coloumb-blockade physics plays an important role. We then turn to spin-dependent transport phenomena which give rise to tunnel magnetoresistance and spin accumulation. Afterwards, we discuss how these concepts influence the transport through quantum-dot spin valves. We conclude this chapter by giving an overview of current experimental realizations of quantum-dot spin valves.

2.1 Transport through quantum dots

In this section, we discuss the basics of single-charge tunneling in nanostructures [1]. We consider a single-electron transistor as depicted schematically in Fig. 2.1. It consists of a single island, either semiconducting or metallic, that is tunnel coupled to electronic reservoirs at different chemical potentials. The chemical potential of the island can be tuned by changing the gate voltage applied to the island.

Typical sizes of islands range from a few nanometers for metallic systems up to 100 nm for semiconducting systems. Due to their small size, the islands have small capacitances of typically a few pF. For single molecules, which are the ultimate limit of miniaturization of such islands, the capacitances can even be as small as a few aF. The small capacitances in turn give rise to a large energy that is needed to put an excess electron on the island. If this charging energy is large compared to the temperature

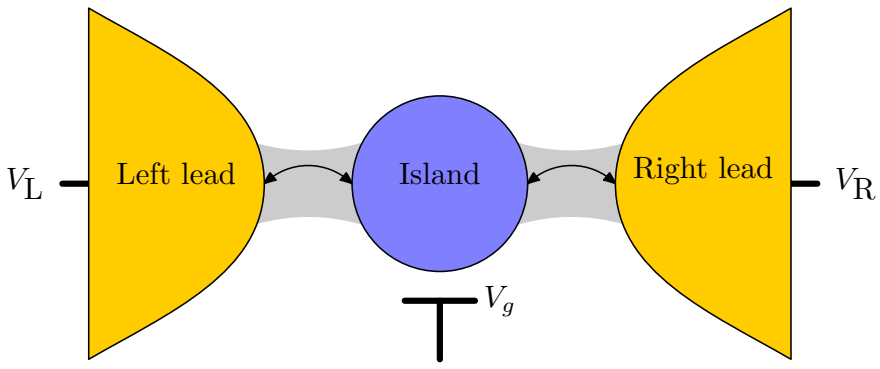

Figure 2.1: Schematic of a single-electron transistor. An island is tunnel coupled to two electronic reservoirs at chemical potentials V_L and V_R. The Fermi level of the island can be tuned via the gate voltage V_g.

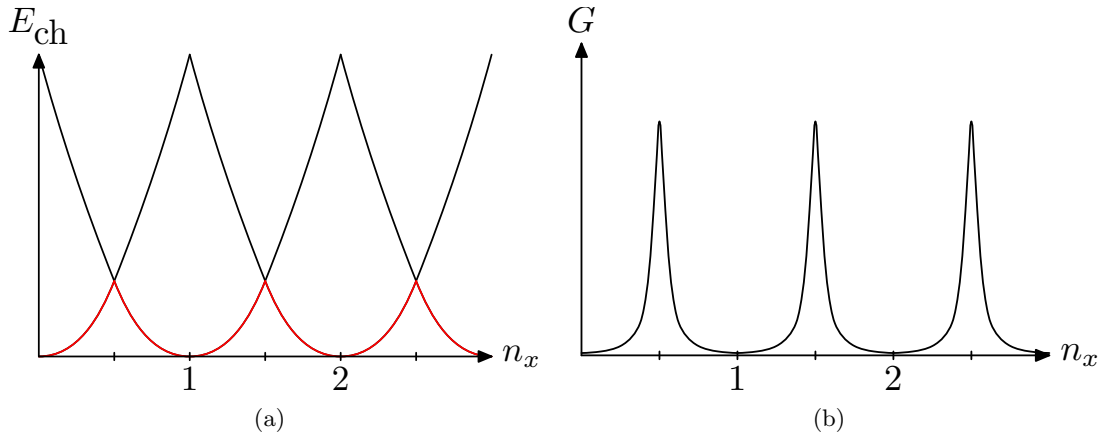

Figure 2.2: Charging energy of a quantum dot as a function of the excess charge n_x (left panel). Differential conductance as a function of n_x (right panel). Transport can take place only at the degeneracy points where states with N and $N+1$ have equal energies giving rise to a series of peaks in the conductance. These are broadened by temperature and tunnel coupling strength.

of the system, interesting new transport properties arise which we will discuss in the following.

In a simple electrostatic model of the single-electron transistor, the total capacitance of the island C is the sum of the capacitances of the tunnel barriers coupling the island to the electronic reservoirs, C_r, where r = L,R, and the capacitance of the gate electrode C_g. The energetically most favorable configuration in this case has an electron number n_x that is given by $en_x = C_{\mathrm{L}}V_{\mathrm{L}} + C_{\mathrm{R}}V_{\mathrm{R}} + C_gV_g$ which in experiment can be tuned by adjusting the gate voltage V_g. The charging energy of the system containing N electrons is then given by

$$E_{\mathrm{ch}}(N, n_x) = \frac{e^2}{2C}(N - n_x)^2, \tag{2.1}$$

i.e., it depends quadratically on n_x, cf. Fig. 2.2(a). In consequence, for different gate voltages, the ground state of the single-electron transistor contains different numbers of electrons. If the energetically most favorable configuration of the single-electron transistor contains N electrons, transport through the system is blocked as the number of electrons on the island is fixed. Only at the degeneracy points where the configurations with N and $N+1$ electrons on the island have equal energies, transfer of electrons through the island becomes possible. Hence, by tuning the gate voltage, we can change the number of electrons on the island and thereby the current flowing through the system. This behaviour, which is a typical property of a transistor, can be seen clearly in Fig. 2.2(b) where the differential conductance $G = \partial I/\partial V|_{V=0}$ is shown as a function of n_x. A series of conductance peaks which are broadened by temperature and tunnel coupling strengths is separated by regions of low conductance, the so called *Coulomb blockade* regime, giving rise to *Coulomb oscillations*.

So far, we discussed a simple electrostatic model of the single-electron transistor

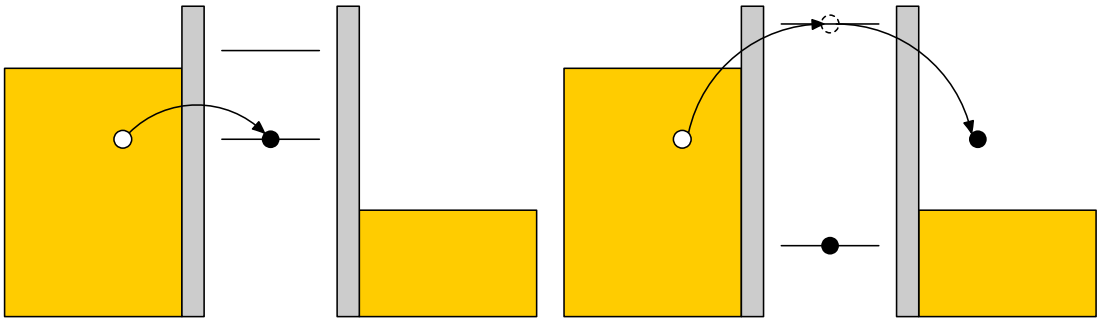

Figure 2.3: Tunneling through a quantum dot. On the left, a sequential tunneling event where a single electron is transferred onto the dot is depicted. On the right a cotunnling process which brings the dot into a virtual intermediate state with two electrons and ends up with the electron being transferred to the right electrode.

which assumed that the level spacing $\delta\varepsilon$ is small compared to the charging energy. For semiconductor quantum dots or very small metallic grains, the level spacing can become large due to the *quantum confinement*. For bias voltages small enough such that only a single level can contribute to transport, one can model the quantum dot in terms of an Anderson Hamiltonian [2],

$$H = \sum_r H_r + H_{\text{dot}} + H_{\text{tun}}. \tag{2.2}$$

Here, $H_r = \sum_{r\mathbf{k}\sigma} \varepsilon_{r\mathbf{k}} a^\dagger_{r\mathbf{k}\sigma} a_{r\mathbf{k}\sigma}$ models the electrodes as reservoirs of noninteracting electrons at chemical potential μ_r with a constant density of states ρ_r. The quantum dot is modelled as a single, spin-degenerate level with energy ε measured relative to the Fermi energy of the electrodes in equilibrium. Additionally, it is characterized by the Coulomb energy U necessary to occupy the dot with two electrons. Hence, the dot is described by $H_{\text{dot}} = \sum_\sigma \varepsilon c^\dagger_\sigma c_\sigma + U c^\dagger_\uparrow c_\uparrow c^\dagger_\downarrow c_\downarrow$. Finally, the coupling between dot and electrodes is described by the tunneling Hamiltonian $H_{\text{tun}} = \sum_{r\mathbf{k}\sigma} t_r a^\dagger_{r\mathbf{k}\sigma} c_\sigma + \text{h.c.}$ Here, the tunnel matrix element t_r characterizes the strength of the dot-lead hybridization. It is related to the tunnel coupling strength by $\Gamma_r = 2\pi |t_r|^2 \rho_r$.

In the following we are going to discuss in more detail the transport processes arising in a single-electron transistor described by the Hamiltonian (2.2).

In a *sequential tunneling* process, a single electron is transferred from one of the reservoirs onto the island or vice versa as shown in Fig. 2.3(a). Due to the charging energy, a second electron cannot enter the island until the first one has left it again. Hence, in the sequential tunneling regime, transport takes place by transferring one electron after the other through the island in independent tunneling events. As each sequential tunneling event changes the occupation of the island by ± 1, sequential tunneling is possible in the vicinity of the degeneracy points where the states with N and $N+1$ electrons have the same energy. Away from these points, sequential tunneling becomes exponentially suppressed. From a theoretical point of view, sequential tunneling is described by *orthodox theory* [3–5].

Inside the Coulomb blockade regime, *cotunneling* processes become important because they are only algebraically suppressed [6, 7]. They furthermore play an important role when the tunnel coupling strength Γ becomes comparable to temperature, $\Gamma \sim k_\mathrm{B}T$: As on the one hand they lead to a broadening of the level while on the other hand they also renormalize the level position [8, 9]. In a cotunneling process, two tunneling events take place as one coherent quantum process. An example of a cotunneling process is shown in Fig. 2.3(b). An electron enters the quantum dot from the left to occupy a virtual state which is energetically forbidden. In a subsequent tunneling event, the electron leaves the dot to the drain lead such that the total process conserves energy. For transport through a spin-degenerate, single-level quantum dot, all cotunneling processes are elastic as there is no possibility to excite particle-hole pairs or to bring the dot into an excited state. This is different for more complicated quantum-dot systems. In Chapter 6, we discuss inelastic cotunneling through a single iron atom where the tunneling electrons can excite the atom spin when the applied bias voltage passes a certain threshold.

For even stronger coupling to the leads (or smaller temperatures), tunnel processes of arbitrarily high order become important. They give rise to the *Kondo effect* in the Coulomb valleys where the dot is occupied by an odd number of electrons. The Kondo effect manifests itself as an increased zero-bias conductance approaching the unitary limit $G = 2e^2/h$ as $T \to 0$. This is in contrast to the expectation from sequential tunneling which predicts the conductance to vanish in the limit $T \to 0$, a behavior that can be observed in the Coulomb valleys with an even number of electrons on the dot where no Kondo effect occurs.

Originally, the Kondo effect [10] was observed in metals containing magnetic impurities [11]. Here it gives rise to an anomalous temperature dependence of the resistivity. Instead of approaching a constant value for $T \to 0$, the resistivity has a minimum at some temperature and then rises again for smaller temperatures to take some finite value at $T \to 0$. This behaviour is due to the formation of a Kondo cloud of conduction electrons forming a spin singlet with the impurity spin. Thereby, the impurity gets screened and gives rise to an increased scattering. In the quantum dot case, a spin singlet forms between the spin on the dot and the electrons in the lead. This gives rise to a resonance at the Fermi energy and therefore to an increased transport through the dot. The Kondo effect in quantum dots can be accessed experimentally [12, 13]. It was also oberserved in systems having ferromagnetic [14–16] or superconducting [17] electrodes as well as for transport through a single molecule [18, 19].

In the equilibrium case, the Kondo effect can be described theoretically by first mapping the Anderson model onto an *s-d* model using a Schrieffer-Wolff transformation [20] which eliminates the charge fluctuation and allows the description of the impurity/quantum dot in terms of a spin 1/2. In a next step, one integrates out the high-energy degrees of freedom using a perturbative renormalization group method, the so-called poor man's scaling [21]. Solving the lowest order renormalization group equation, one finds that the antiferromagnetic exchange coupling between the impurity/dot spin and the spin of the itinerant electrons grows as the bandwidth is reduced. Historically, this was the first example of a system showing asymptotic freedom. The other important example is quantum chromodynamics where the coupling constant vanishes as the energy scale becomes arbitrarily large [22–25]. When the bandwidth

reaches the Kondo temperature

$$T_{\mathrm{K}} = \frac{\sqrt{\Gamma U}}{2} \exp\left(\pi \frac{\varepsilon(\varepsilon + U)}{\Gamma U}\right), \tag{2.3}$$

that was computed for the first time by Haldane [26], the exchange coupling formally diverges, thereby signaling the breakdown of perturbation theory. By using numerical renormalization group methods, Wilson [27] could establish the formation of a spin singlet between the localized spin and the spin of the itinterant electrons.

In this thesis, we will not deal with the Kondo effect. Instead, we will restrict our attention most of the time to transport in the sequential tunneling regime. Inelastic cotunneling through a single magnetic atom is discussed in Chapter 6.

2.2 Spin-dependent transport

Conventional electronics only deals with the charge degree of freedom of electrons (cf. the discussion of the single-electron transistor in Section 2.1 where the spin of the electron did not enter the discussion at all) while spintronics [28, 29] additionally takes into account the electron spin. On the one hand, this gives rise to a lot of possible technical applications. On the other hand, it is also interesting as a subject of fundamental research.

Nowadays, spintronics has grown to an enormous field with many different aspects, for recent reviews see Ref. [30–35]. Here we will focus on magnetoresistive effects, i.e., on changes of the electrical resistance due to the transport of spin-polarized electrons. There are several different magnetoresistance effects, the most prominent being giant magnetoresistance (GMR), colossal magnetoresistance (CMR) and tunnel magnetoresistance (TMR).

The *giant magnetoresistance* occurs in multilayer systems consisting of ferromagnetic and normal metals [36, 37] where a current is flowing either parallel (current-in-plane, CIP) or perpendicular (current-perpendicular-to-plane, CPP) to the layers. It manifests itself as an increased resistance when changing the orientation of the magnetizations from parallel to antiparallel. Control over the relative orientation of the magnetizations can be obtained in two ways. When the thickness of the nonmagnetic spacer is chosen appropriately, the ferromagnetic layers are exchange-coupled antiferromagnetically. By applying an external magnetic field, the antiparallel configuration can be switched into a parallel one. Alternatively, when using thicker nonmagnetic spacers such that the exchange coupling becomes negligible, one can employ ferromagnetic layers with different coercitive fields which also allows to control the relative orientation of the ferromagnets by applying an external field.

The GMR can be understood using the two spin channel model by Mott [38, 39] which assumes that majority and minority spin electrons behave as independent charge carriers with different transport properties. This is a reasonable approximation as long as spin-flip scattering rates are small. Assuming the scattering time for electrons with spin antiparallel to the magnetization of a layer to be larger than the scattering time for electrons with parallel spin explains the occurrence of GMR. For a parallel geometry, majority spins have small and minority spins large scattering times in both ferromagnetic layers. As both channels behave like two resistors in parallel, the total

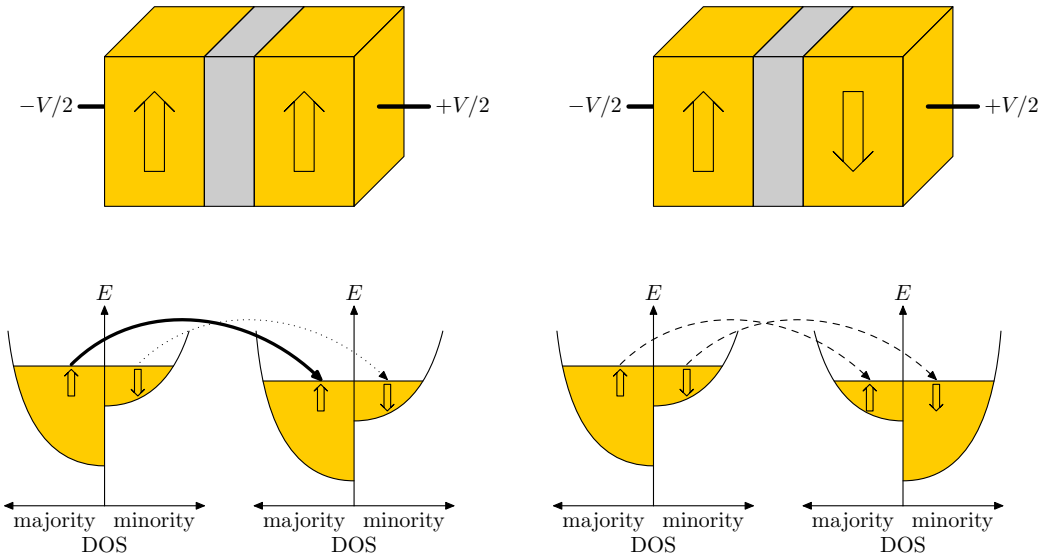

Figure 2.4: Tunnel magnetoresistance is due to the different densities of states for majority and minority spin electrons at the Fermi energy. In the parallel configuration, there is a large contribution to the current from tunneling of majority spin electrons. In the antiparallel case, majority spins of the one electrode become minority spins of the other electrode. Hence, both spin channels only carry a small current.

resistance is small. In the antiparallel geometry, electrons are majority spins in the one and minority spins in the other layer. Hence, we now have the situation of two large resistances in parallel, which gives rise to an increased total resistance compared to the parallel case.

The different scattering rates for majority/minority spins can arise for different reasons resulting in intrinsic and extrinsic GMR. The intrinsic GMR relies on the fact that majority spin electrons only see small potential steps at the ferromagnet/normal metal interface while minority spin electrons feel a much larger modulation of the potential landscape. In consequence, minority spin electrons experience a stronger scattering compared to majority spin electrons. The extrinsic GMR relies on the scattering from impurities. It depends on the details of the scattering mechanism and can therefore have either the same or opposite sign as the intrinsic GMR, therefore either enhancing, suppressing or even inverting it.

Next, we address *tunnel magnetoresistance* which occurs in systems where two ferromagnets are separated by a thin insulating barrier. This is the most important magnetoresistance effect to understand the transport properties of a quantum-dot spin valve. It was first observed by Jullière [40]. Recently, interest in TMR was renewed when Moodera et al. [41] detected TMR at room temperature in high-quality $Co/Al_2O_3/Ni_{80}Fe_{20}$ junctions.

The dependence of the junction resistance on the relative orientation of the magnetizations can be understood in a simple model due to Jullière [40] which neglects, e.g., interface effects needed for a more thorough description of the effect. Let us consider a tunnel barrier with ferromagnetic electrodes. In the sense of a Stoner model, we

describe the ferromagnetism by assuming a different density of states for majority and minority spin electrons at the Fermi energy, cf. Fig. 2.4. In the parallel configuration, majority spin electrons from the source end up as majority spin electrons of the drain electrode, as the rate for spin-flip tunneling in general will be much smaller than the rate of spin-conserving tunneling. Similarly, minority spins end up in minority spin states. As the tunnel probability of electrons with spin $\sigma = \pm$ is proportional to the density of states at the Fermi energy $\rho_{r\sigma}(E_\mathrm{F})$ in the source $r = \mathrm{L}$ and drain $r = \mathrm{R}$ electrode, the current in the parallel configuration is given by

$$I^\mathrm{P} \sim \rho_{\mathrm{L}+}(E_\mathrm{F})\rho_{\mathrm{R}+}(E_\mathrm{F}) + \rho_{\mathrm{L}-}(E_\mathrm{F})\rho_{\mathrm{R}-}(E_\mathrm{F}). \tag{2.4}$$

Since the density of states for majority spin electrons is larger than the one for minority spins, $\rho_{r+}(E_\mathrm{F}) > \rho_{r-}(E_\mathrm{F})$, we therefore find that a large current is carried by tha majority spins while the minority spins only give a small contribution. In the antiparallel configuration, the current is suppressed because now majority spins electrons from the source end up as minority spins in the drain and vice versa. The current in this case is hence given by

$$I^\mathrm{AP} \sim \rho_{\mathrm{L}+}(E_\mathrm{F})\rho_{\mathrm{R}-}(E_\mathrm{F}) + \rho_{\mathrm{L}-}(E_\mathrm{F})\rho_{\mathrm{R}+}(E_\mathrm{F}). \tag{2.5}$$

The difference between the current in the parallel and antiparallel configuration can be described quantitatively by introducing the TMR ratio

$$\mathrm{TMR} = \frac{I^\mathrm{P} - I^\mathrm{AP}}{I^\mathrm{AP}}. \tag{2.6}$$

Introducing the spin polarization in the ferromagnets as $p_r = \frac{\rho_{r+}(E_\mathrm{F}) - \rho_{r-}(E_\mathrm{F})}{\rho_{r+}(E_\mathrm{F}) + \rho_{r-}(E_\mathrm{F})}$, the TMR can be expressed as

$$\mathrm{TMR} = \frac{2p_\mathrm{L}p_\mathrm{R}}{1 - p_\mathrm{L}p_\mathrm{R}}. \tag{2.7}$$

The above expression was generalized by Slonczewski [42] to systems where the magnetizations enclose an angle ϕ. In this case, the overlap between majority from source and drain is reduced by a factor of $\cos^2 \frac{\phi}{2}$, while at the same time the overlap between majority spins form the source and minority spins from the drain behaves as $\sin^2 \frac{\phi}{2}$. The TMR is therefore modified to

$$\mathrm{TMR}(\phi) = \frac{I^\phi - I^\mathrm{AP}}{I^\mathrm{AP}} = \frac{2p_\mathrm{L}p_\mathrm{R}}{1 - p_\mathrm{L}p_\mathrm{R}} \cos^2 \frac{\phi}{2}. \tag{2.8}$$

The angular dependence of the current has been observed by Moodera et al. [43] and Jaffrès et al. [44].

The *colossal magnetoresistance* differs from the two magnetoresistance effects discussed so far in that it does not rely on transport across some interface but is rather a property of the bulk system. It arises in mixed valence manganese oxides as, e.g., $\mathrm{La}^{3+}_{1-x}\mathrm{Ca}^{2+}_{x}\mathrm{Mn}^{3+}_{1-x}\ \mathrm{Mn}^{4+}_{x}\mathrm{O}^{2-}_{3}$ where it was discovered in the 1950s by van Santen and Jonker [45]. Interest in the effect was renewed when von Helmolt [46] and Jin [47] measured relative resistance changes of up to 1300 percent at room temperature when applying a large external magnetic field of 6 T.

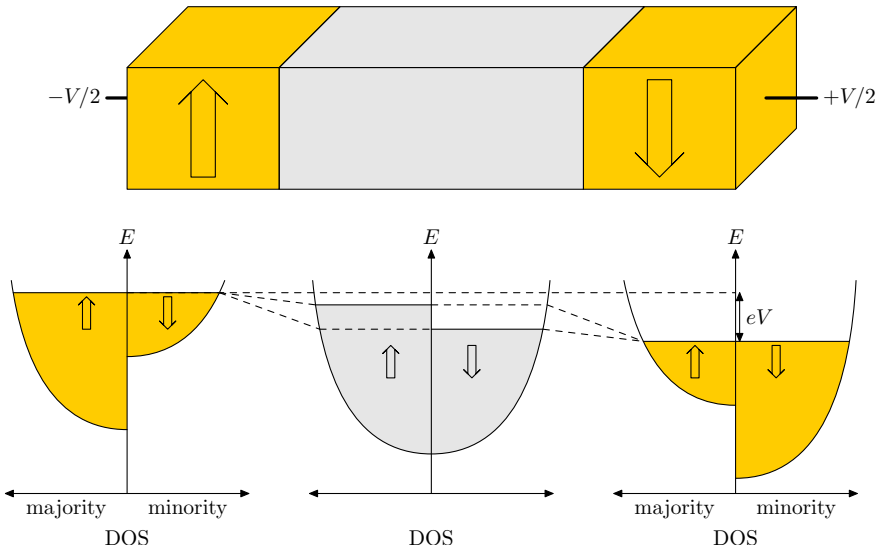

Figure 2.5: Spin accumulation in a normal metal sandwiched between two antiparallelly orientend ferromagnets. Due to the different interface resistances of the two spin channels, a different voltage drop for the spin up and down channel arises at each interface. This leads to a different chemical potential of spin up and down electrons in the normal metal, indicating the spin accumulation there.

According to Hund's rule, the three, respectively four, d electrons of the Mn^{4+} and Mn^{3+} ions have parallel spins. As the manganese ions are separated by oxygen ions, direct exchange processes can be neglected and the relative spin orientation is governed by superexchange processes which align ions of the same valency antiparallel while double exchange processes keep the spins of ions of opposite valency parallel [48–50]. Here an electron is transferred from the oxygen onto the Mn^{4+} ion followed by an electron transfer from the Mn^{3+} ion onto the oxygen. Due to the Pauli principle this process is only possible for parallel spins of the manganese ions. Close to the Curie temperature, where the spins of the manganese ions point in arbitrary directions, electron transport by hopping is therefore suppressed. When applying a large external field, the manganese spins become aligned giving rise to an increased hopping and therefore to a large magnetoresistive effect.

2.3 Spin accumulation

In this section, we discuss spin accumulation which is another important concept of spintronics needed to understand tranport through a quantum-dot spin valve. To begin with, we consider a normal metal sandwiched between to ferromagnets with antiparallel magnetizations. For large spin-flip times, we can describe the system using the two-current model [39] which assumes that spin up and spin down charge carriers behave independently such that a spin up and spin down current flow in the system in parallel.

When applying a bias voltage to the system, the spin up and down current enter the normal metal from the source ferromagnet. This gives rise to a voltage drop at the

interface. In the spin up channel, which corresponds to the majority spin of the source ferromagnet, the interface resistance is smaller than in the spin down channel due to magnetoresistive effects. Hence, for the spin up channel, there will be a smaller voltage drop than for the spin down channel. The situation is reversed at the interface to the drain ferromagnet. Now, the spin up channel corresponds to the minority spins of the ferromagnet and hence shows the larger interface resistance and larger bias drop. In consequence, we find that in the normal metal the chemical potential for the spin up electrons is larger than that for the spin down electrons indicating the accumulation of spin up. We note that the spin accumulation relies on the voltage drops at the interface and consequently is a nonequilibrium property of the system.

The spin accumulation was first observed by Johnson and Silsbee [51, 52] who contacted an aluminum bar with two permalloy strips. Since then, it has been observed in many different systems including mesoscopic islands [53, 54], mesoscopic spin valves [55–58] and most recently graphene [59–63].

Another example of a system where spin accumulation plays an important role is a single-level quantum dot coupled to ferromagnetic electrodes. For electrodes magnetized in parallel, spin up electrons enter the dot from the source and leave the dot to the drain with a rate $\Gamma(1+p)/2$ where p is the polarization of the ferromagnet and Γ the tunnel coupling strength. Similarly, spin down electrons will enter/leave with a rate given by $\Gamma(1-p)/2$. As for both spin channels the rate for entering is equal to the rate for leaving the dot, no spin accumulates on the dot. This changes when considering an antiparallel configuration. While the rates for entering stay the same, spin up (down) electrons now leave the dot with a rate $\Gamma(1\mp p)/2$. Hence, a spin up electron can enter the dot easily but can hardly leave it. Similarly, spin down electrons can hardly enter the dot but easily leave it. In consequence, to lowest order in the tunnel coupling, an average spin $S_z = \frac{2p}{3+p^2}$ accumulates on the dot if only the empty and singly-occupied dot contribute to transport. Furthermore, the accumulated spin will also influence the further transport through the dot as it prevents electrons from being transferred from the source to the drain lead. We will discuss the current experimental realizations of quantum dots coupled to ferromagnetic electrodes in Section 2.4.4.

2.4 Quantum-dot spin valves

In this section we describe the transport properties of a quantum-dot spin valve, i.e., a single-level quantum dot tunnel coupled to two ferromagnetic electrodes with magnetizations pointing in arbitrary directions [64–68]. Such systems turn out to be very interesting from a theoretical point of view as they show a nonequilibrium spin accumulation on the dot as well as a spin precession in an exchange field arising from virtual tunneling between dot and leads. The interplay between these two effects gives rise to a number of non-trivial transport properties as, e.g., negative differential conductance in a broad bias range. Quantum-dot spin valves are not only interesting from a fundamental point of view. They may also serve to store information in the spin state of the quantum dot. Furthermore, they could be useful for quantum computing as they allow the precise control and manipulation of a single spin that can serve as a qubit. We note that in the following, we restrict the discussion to sequential tunneling through a single-level quantum dot. In the literature, there are, however, also studies

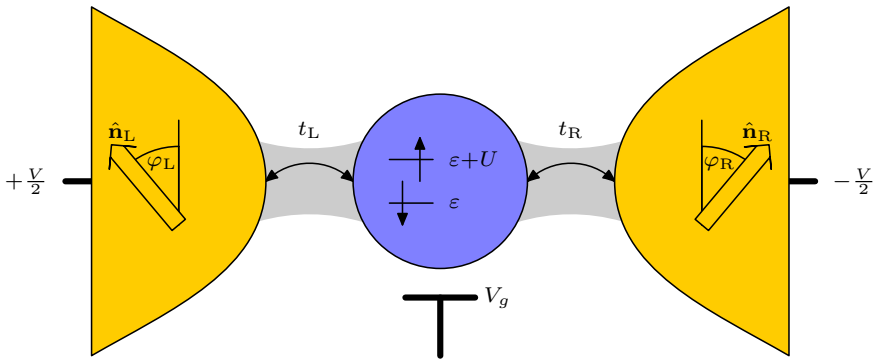

Figure 2.6: Schematic of a quantum-dot spin valve: A single-level quantum dot is coupled via tunnel barriers to two ferromagnetic leads with noncollinear magnetizations.

of cotunneling effects [69–72] as well as of the Kondo regime [73–80]. In addition, more complex quantum dots coupled to ferromagnetic electrodes have been investigated, including double quantum dots [81–83], multi-level dots [84, 85], and carbon nanotube quantum dots [86–90].

2.4.1 Model

A quantum-dot spin valve consists of a single-level quantum dot tunnel coupled to two ferromagnetic electrodes. The magnetizations of the two ferromagnets can point in arbitrary directions $\mathbf{n}_\mathrm{L}$ and $\mathbf{n}_\mathrm{R}$. A gate electrode allows tuning the level position of the quantum dot. Applying a bias voltage across the system induces a nonequilibrium situation leading to transport through the quantum-dot spin valve.

The Hamiltonian describing the quantum-dot spin valve consists of three parts,

$$H = \sum H_r + H_\mathrm{dot} + H_\mathrm{tun} \tag{2.9}$$

describing the electrodes, the dot and the tunnel coupling, respectively. We model the ferromagnetic electrodes as reservoirs of noninteracting electrons at chemical potential μ_r. The Hamiltonian then takes the form

$$H_r = \sum_{\mathbf{k}\sigma} \varepsilon_{\mathbf{k}\sigma} a^\dagger_{r\mathbf{k}\sigma} a_{r\mathbf{k}\sigma}, \tag{2.10}$$

$r = \mathrm{L,R}$, $\sigma = \pm$, where we choose the quantization axis for each electrode in the direction of its magnetization. The ferromagnetic properties of the electrodes are incorporated into the model in the sense of a Stoner model by assuming different densities of state for majority and minority spin electrons, $\rho_{r\sigma}(\omega)$. We furthermore assume the densities of states to be independent of energy, $\rho_{r\sigma}(\omega) = \rho_{r\sigma}$, as typical transport measurements only probe a small region around the Fermi energy. The asymmetry between majority and minority spin electrons is characterized by the spin polarization, $p_r = (\rho_{r+} - \rho_{r-})/(\rho_{r+} + \rho_{r-})$. Here, $p_r = 0$ corresponds to a nonmagnetic electrode, while $p_r = 1$ describes a half-metallic electrode with only majority spins only at the Fermi energy.

The quantum dot is described by

$$H_{\mathrm{dot}} = \sum_{\sigma} \varepsilon c_{\sigma}^{\dagger} c_{\sigma} + U c_{\uparrow}^{\dagger} c_{\uparrow} c_{\downarrow}^{\dagger} c_{\downarrow} \tag{2.11}$$

as a single, spin-degenerate level with energy ε measured relative to the Fermi energies of the electrodes in equilibrium. The charging energy U is the energy needed to occupy the quantum dot with two electrons. Due to the smallness of the quantum dot, the charging energy is the largest energy scale (see discussion in Section 2.1) of the problem and therefore has to be taken into account exactly.

Due to the noncollinear geometry it is most convenient to quantize the dot spin in the direction of $\mathbf{n}_{\mathrm{L}} \times \mathbf{n}_{\mathrm{R}}$. In this case, the tunnel Hamiltonian takes the form

$$H_{\mathrm{tun}} = \sum_{r\mathbf{k}} \frac{t_r}{\sqrt{2}} \left[a_{r\mathbf{k}+}^{\dagger} \left(e^{i\phi_r/2} c_{\uparrow} + e^{-i\phi_r/2} c_{\downarrow} \right) + a_{r\mathbf{k}-} \left(-e^{i\phi_r/2} c_{\uparrow} + e^{-i\phi_r/2} c_{\downarrow} \right) \right] + \mathrm{h.c.}, \tag{2.12}$$

i.e., it couples majority spins from the electrodes to spin up and spin down states of the quantum dot. Here $\phi_{\mathrm{L}} = -\phi_{\mathrm{R}}$ is half the angle enclosed between the magnetizations. The tunnel matrix elements t_r are related to the spin-dependent tunnel couplings by $\Gamma_{r\pm} = 2\pi |t_r|^2 \rho_{r\pm}$. Due to the coupling between dot and leads, the dot states therefore acquire a finite level width $\Gamma_r = (\Gamma_{r+} + \Gamma_{r-})/2$.

2.4.2 Master equation

Transport through a quantum-dot spin valve can be described theoretically by using the real-time diagrammatic transport theory [91–94] which we introduce in more detail in Chapter 3. The basic idea of the real-time diagrammatic technique is to integrate out the noninteracting fermions in the electrodes and to describe the remaining system in terms of its reduced density matrix ρ^{red}. In the case of a quantum-dot spin valve, the reduced density matrix has six nonvanishing entries. Three of them describe the probabilities to find the quantum dot empty, P_0, singly occupied, P_1, and doubly occupied, P_d. The other three matrix elements describe the quantum-statistical average of the spin on the quantum dot. In this section, we present the generalized master equation governing the time evolution of the density matrix elements as well as the expressions for the current that were obtained by Braun et al. [65]. Similar equations have were found by Urban et al. for the description of a quantum-dot spin transistor [95].

The generalized master equations for the six density matrix elements can be split into one set of equations governing the occupation probabilities and one set describing the evolution of the dot spin. The first set of equations reads

$$\begin{aligned} \frac{d}{dt} \begin{pmatrix} P_0 \\ P_1 \\ P_d \end{pmatrix} = \sum_r \Gamma_r \begin{pmatrix} -2f_r^+(\varepsilon) & f_r^-(\varepsilon) & 0 \\ 2f_r^+(\varepsilon) & -f_r^-(\varepsilon) - f_r^+(\varepsilon+U) & 2f_r^-(\varepsilon) \\ 0 & f_r^+(\varepsilon+U) & -2f_r^-(\varepsilon+U) \end{pmatrix} \begin{pmatrix} P_0 \\ P_1 \\ P_d \end{pmatrix} \\ + \sum_r 2p_r\Gamma_r \begin{pmatrix} f_r^-(\varepsilon) \\ -f_r^-(\varepsilon) + f_r^+(\varepsilon+U) \\ -f_r^+(\varepsilon+U) \end{pmatrix} \mathbf{S} \cdot \mathbf{n}_r. \end{aligned} \tag{2.13}$$

Here $f_r^+(\omega) = 1/[\exp(\beta(\omega - \mu_r)) + 1]$ denotes the Fermi function in lead r which describes the probability that a state with energy ω in lead r is occupied. Similarly

$f_r^-(\omega) = 1 - f_r^+(\omega)$ describes the probability to find the state empty. From Eq. (2.13) we see that on the one hand, the occupation probabilities are coupled among each other in the same way as for a quantum-dot coupled to nonmagnetic electrodes. Additionally, we find a coupling between the occupation probabilities and the spin accumulated on the quantum dot if the polarizations are nonvanishing, $p_r \neq 0$. This reflects the fact that a spin accumulation on the quantum dot influences the transport through the dot.

The master equations governing the time evolution of the quantum dot spin (we note that as $\mathbf{S}$ denotes a quantum-statistical expectation value, its components can take any value between $S_i = -1/2$ and $S_i = +1/2$) can be cast into the form of a Bloch equation,

$$\frac{d\mathbf{S}}{dt} = \left(\frac{d\mathbf{S}}{dt}\right)_{\text{acc}} + \left(\frac{d\mathbf{S}}{dt}\right)_{\text{rel}} + \left(\frac{d\mathbf{S}}{dt}\right)_{\text{prec}}. \tag{2.14}$$

Here, the first term,

$$\left(\frac{d\mathbf{S}}{dt}\right)_{\text{acc}} = \sum_r p_r \Gamma_r \left[f_r^+(\varepsilon) P_0 - \frac{f_r^-(\varepsilon) - f_r^+(\varepsilon + U)}{2} P_1 - f_r^-(\varepsilon + U) P_d \right] \mathbf{n}_r, \tag{2.15}$$

describes the accumulation of spin on the quantum dot due to the spin-polarized tunneling of electrons on the quantum dot as well as due to the spin-dependent tunneling of electrons from the dot into the electrodes. The second term,

$$\left(\frac{d\mathbf{S}}{dt}\right)_{\text{rel}} = -\frac{\mathbf{S}}{\tau_c}, \tag{2.16}$$

describes a relaxation of the dot spin with the rate $1/\tau_c = \sum_r \Gamma_r \left[f_r^-(\varepsilon) + f_r^+(\varepsilon + U) \right]$. There are two mechanism behind this relaxation. On the one hand, electrons can tunnel out of the singly-occupied, spin-polarized dot. On the other hand, a second electron with opposite spin can enter the singly-occupied quantum dot, thereby forming a spin singlet. The last term,

$$\left(\frac{d\mathbf{S}}{dt}\right)_{\text{prec}} = \mathbf{S} \times \sum_r \mathbf{B}_r, \tag{2.17}$$

describes a precession of the spin in an energy-dependent exchange field given by

$$\mathbf{B}_r = -\mathbf{n}_r \frac{p_r \Gamma_r}{\pi} \left[\operatorname{Re} \psi \left(\frac{1}{2} + i \frac{\beta(\varepsilon - \mu_r)}{2\pi} \right) - \operatorname{Re} \psi \left(\frac{1}{2} + i \frac{\beta(\varepsilon + U - \mu_r)}{2\pi} \right) \right], \tag{2.18}$$

where $\psi(z)$ denotes the digamma function. The exchange field, whose bias dependence is shown in Fig. 2.10, arises due to virtual tunneling processes between the quantum dot and the electrodes. The virtual processes give rise to a spin-dependent level renormalization which in turn may be interpreted as a magnetic field acting on the dot spin. It is interesting to note that the exchange field influences the transport properties even in the sequential tunneling limit. Normally, effects of level renormalization come into play only when considering cotunneling contributions as the renormalization effect is of order Γ while the transport process which probes it is also of order Γ. The situation in the quantum-dot spn valve is different as here the exchange field, which is of order Γ, acts on the dot spin during the whole time an electron resides on the dot. As this time

scale is proportional to $1/\Gamma$, the spin precession due to the exchange field becomes detectable even in sequential tunneling transport.

The current flowing from electrode r into the quantum dot can be written as the sum of two parts,

$$I_r = I_r^{\mathrm{P}} + I_r^{\mathrm{S}}. \tag{2.19}$$

The first term,

$$I_r^{\mathrm{P}} = -2e\Gamma_r \left[f_r^+(\varepsilon) P_0 - \frac{f_r^-(\varepsilon) - f_r^+(\varepsilon+U)}{2} P_1 - f_r^-(\varepsilon+U) P_d \right], \tag{2.20}$$

depends on the occupation probabilities only. For vanishing polarizations, it is the only contribution and reduces to the expression known for transport through a single-level quantum dot coupled to nonmagnetic leads. The second term,

$$I_r^{\mathrm{S}} = 2ep_r\Gamma_r \left[f_r^-(\varepsilon) + f_r^+(\varepsilon+U) \right] \mathbf{S} \cdot \mathbf{n}_r, \tag{2.21}$$

only depends on the spin accumulated on the dot. It therefore arises only if the quantum dot is coupled to ferromagnetic electrodes.

2.4.3 Transport properties

We now turn to the discussion of the transport properties of a quantum-dot spin valve [64, 65, 67]. Unless stated otherwise, we will consider a symmetric system where the ferromagnetic electrodes have the same polarization, $p_{\mathrm{L}} = p_{\mathrm{R}} \equiv p$ and couple with equal strengths to the quantum dot, $\Gamma_{\mathrm{L}} = \Gamma_{\mathrm{R}} \equiv \Gamma$. Furthermore, we assume a symmetrically applied bias voltage, $\mu_{\mathrm{L}} = -\mu_{\mathrm{R}} \equiv V/2$.

Linear response

We start our discussion of the transport properties by considering the regime of linear response, $eV \ll k_{\mathrm{B}}T$. Expanding the master equation (2.14) for the dot spin to first order in the applied bias voltage, we find that the spin accumulation takes the form

$$\left(\frac{d\mathbf{S}}{dt}\right)_{\mathrm{acc}} = p\Gamma \left[f'(\varepsilon) \left(P_0 + \frac{P_1}{2} \right) + f'(\varepsilon+U) \left(\frac{P_1}{2} + P_d \right) \right] \frac{eV}{2k_{\mathrm{B}}T} \left(\mathbf{n}_{\mathrm{R}} - \mathbf{n}_{\mathrm{L}} \right). \tag{2.22}$$

Hence, the spin on the dot accumulates in the direction of $\mathbf{n}_{\mathrm{L}} - \mathbf{n}_{\mathrm{R}}$. This behaviour can be understood in terms of conservation of angular momentum. Electrons with spin pointing in the direction of $\mathbf{n}_{\mathrm{L}}$ enter the dot from the left lead while electrons with a spin pointing in the direction of $\mathbf{n}_{\mathrm{R}}$ leave the dot to the right lead. The size of the spin accumulation is limited by the spin relaxation term, Eq. (2.16).

The third term in the master equation for the spin (2.17) gives rise to a precession of the dot spin around $\mathbf{n}_{\mathrm{L}} + \mathbf{n}_{\mathrm{R}}$ by an angle of

$$\tan\alpha = -B\tau_c, \tag{2.23}$$

where $B = |\mathbf{B}_{\mathrm{L}} + \mathbf{B}_{\mathrm{R}}|$ denotes the absolute value of the exchange field. The dependence of the angle α on the level position is shown in Fig. 2.7. The sign of α reflects the sign of the exchange field. Deep inside the Coulomb bloackade regime, we find that α is close

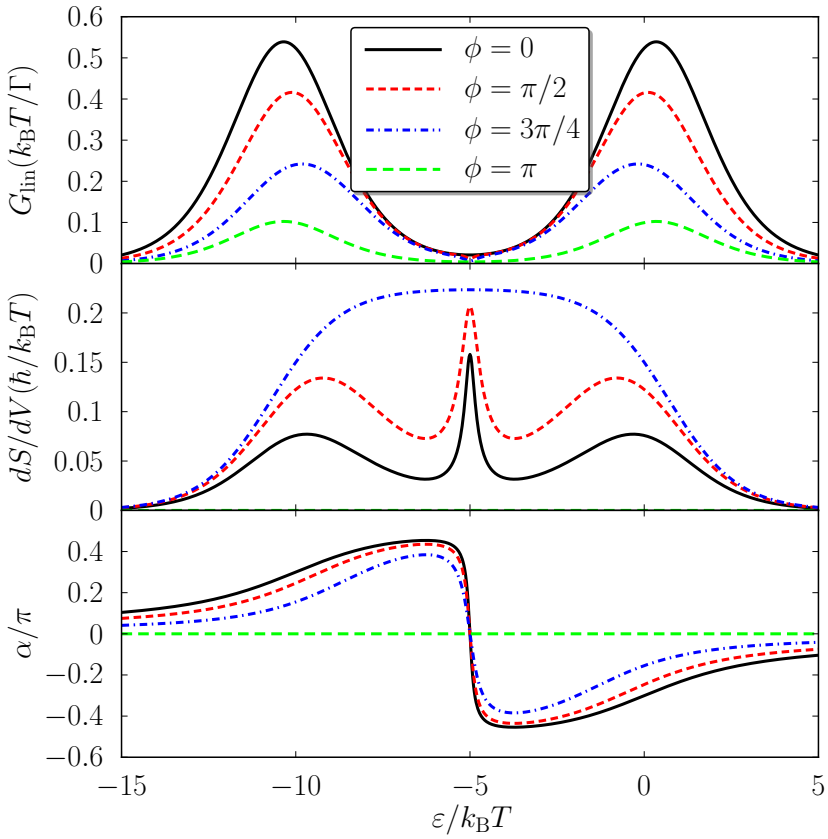

Figure 2.7: Differential conductance, spin accumulation and angle enclosed between the accumulated spin and $\mathbf{n}_{\mathrm{L}} - \mathbf{n}_{\mathrm{R}}$ as a function of level position. Parameters are $U = 10k_{\mathrm{B}}T$ and $p = 0.9$.

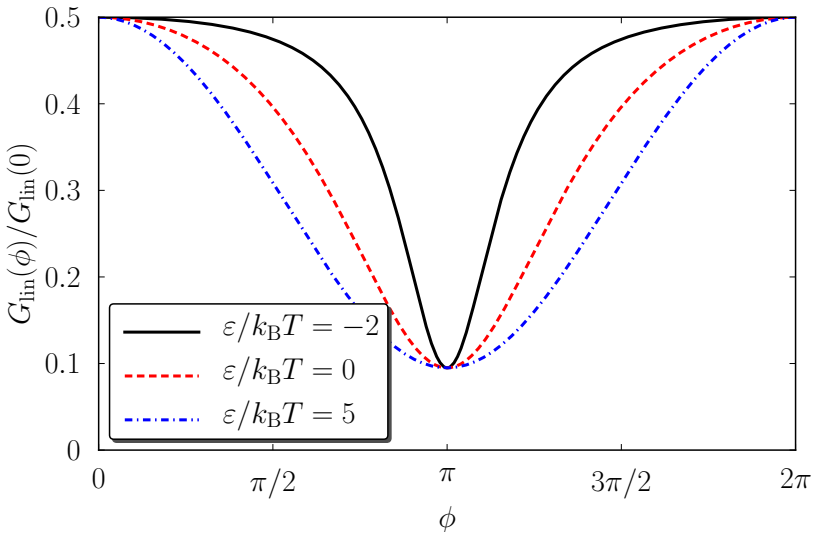

Figure 2.8: Normalized conductance as a function of the angle between the magnetizations. Parameters are the same as in Fig. 2.7.

to $\pm\pi/2$ as the electron has a long dwell time on the dot such that the exchange field can act on the dot spin significantly. At the particle-hole symmetry point $\varepsilon = -U/2$, the exchange field vanishes. In consequence, we have $\alpha = 0$ there. Furthermore, we find a fast variation of α in the vicinity of the particle-hole symmetry point as the exchange field changes sign there and therefore α goes from $+\pi/2$ to $-\pi/2$.

From the spin master equation (2.14) one can derive the following equation for the magnitude of the spin

$$\frac{d|\mathbf{S}|}{dt} = \frac{\mathbf{S}}{|\mathbf{S}|} \cdot \left(\frac{d\mathbf{S}}{dt}\right)_{\rm acc} - \frac{|\mathbf{S}|}{\tau_c}. \tag{2.24}$$

In the stationary limit, this equation yields the solution $|\mathbf{S}| = \tau_c |(d\mathbf{S}/dt)_{\rm acc}| \cos\alpha$. We therefore find that the precession not only gives rise to a change of the spin direction but additionally leads to a reduction of the spin magnitude. This can be seen in the middle panel of Fig. 2.7 where $d|\mathbf{S}|/dV$ is shown as a function of the level position. Deep inside the Coulomb blockade region where the effect of the exchange field is strong (cf. the discussion of α above) we find a significant reduction of the spin accumulation. Furthermore, at the particle-hole symmetry point where the exchange field vanishes, a sharp peak arises as here the spin magnitude is not reduced by precession.

The exchange field also affects the differential conductance as can be seen in the upper panel of Fig. 2.7. As the angle between the magnetizations is increased, the conduction is reduced due to the spin accumulation on the quantum dot. However, the conductance peaks are also moved towards each other as the exchange field counteracts the spin accumulation in the region $-U < \varepsilon < 0$ such that the conductance reduction is weakened there.

Furthermore, the exchange field also directly influences the angular dependence of the differential conductance which is given by

$$\frac{G(\phi)}{G(0)} = 1 - p^2 \frac{\sin^2\phi/2}{1 + (B\tau_c)^2 \cos^2\phi/2} \tag{2.25}$$

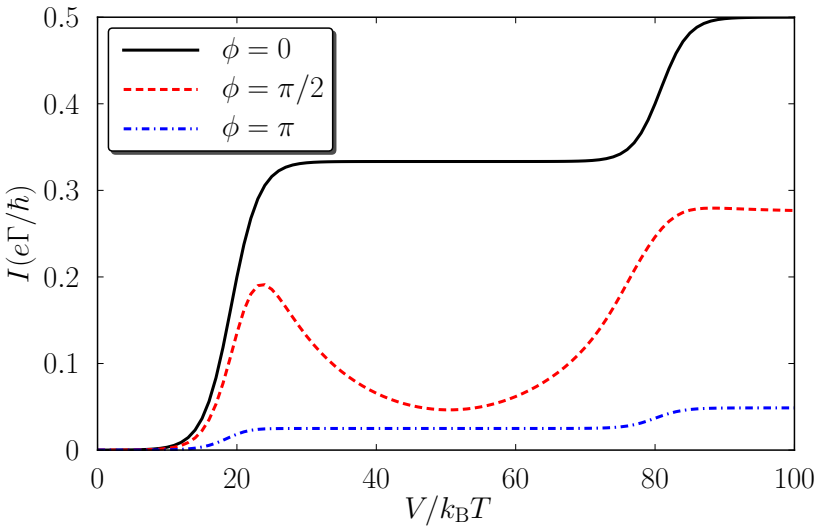

Figure 2.9: Current through the quantum-dot spin valve as a function of bias voltage for different orientations of the magnetizations. For noncollinear geometries a nontrivial bias dependence arises due to the exchange field influencing the spin accumulation on the dot. Parameters are $\varepsilon = 10k_\mathrm{B}T$, $U = 30k_\mathrm{B}T$, $p = 0.95$.

and is shown in Fig. 2.8. For $\varepsilon = 5k_\mathrm{B}T$ the influence of the exchange field is negligible as the dot is empty most of the time. We therefore find a cosine-like dependence of the conductance on ϕ similar to the angular dependence of the TMR or a tunnel junction found by Jullière [40]. On the other hand for $\varepsilon = -2k_\mathrm{B}T$, the probability to find the dot singly occupied is large such that exchange field effects become relevant. As can be seen in Fig. 2.8 the conductance becomes enhanced, thereby reducing the spin-valve effect and yielding a deviation from the harmonic angular dependence.

Nonlinear response

We now turn to the transport properties in the nonlinear regime, $eV > k_\mathrm{B}T$. In Fig. 2.9, we show the current flowing through the quantum-dot spin valve for different orientations of the magnetizations. In the parallel case, spin channels are independent and there is no spin accumulation on the quantum dot. Hence the exchange field does not have any influence on the transport properties either. We therefore simply find a steplike I-V curve as for a quantum dot coupled to nonmagnetic electrodes.

In the antiparallel configuration, the I-V curve basically has the same form as in the parallel case. However, the magnitude of the current is clearly reduced. This reduction is due to the spin accumulating on the quantum dot which blocks further transport as the electron on the dot has the wrong spin to leave to the drain electrode while a second electron cannot enter the dot for energetical reasons. We therefore find that a quantum-dot spin valve gives rise to a tunnel magnetoresistance that was analyzed in more detail in Ref. [69, 70] where also effects of cotunneling have been taken into account.

In the noncollinear case, the exchange field acts on the quantum dot spin, giving rise

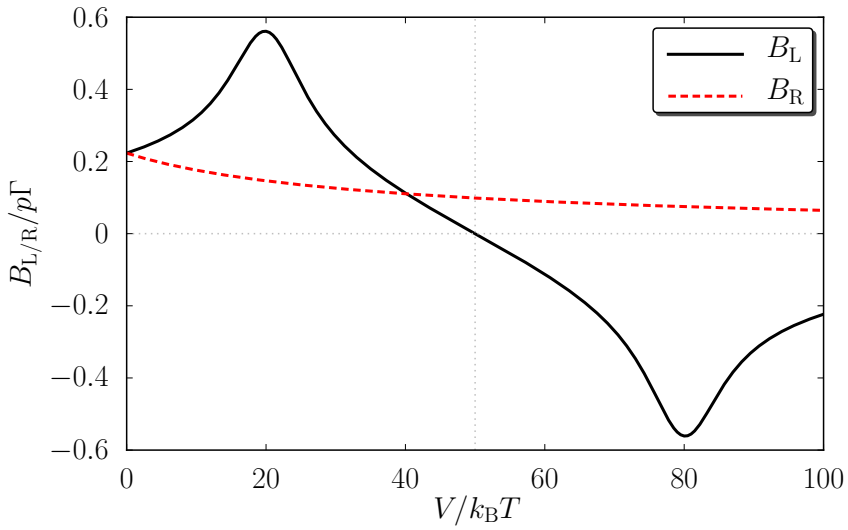

Figure 2.10: Exchange field contributions from the left and right electrode as a function of bias voltage. Parameters as in Fig. 2.9.

to a nontrivial $I-V$ characteristic. At the particle-hole symmetry point, $V = 2\varepsilon + U$, the exchange field acting on the dot spin vanishes, cf. Fig. 2.10. In consequence, only the spin bloackade arises that reduces the current through the dot compared to the parallel configuration. Away from the symmetry point, however, the exchange field gives rise to a precession of the dot spin. As the spin is moved out of the blocking position, transport through the dot is increased which gives rise to a characteristic U-shaped curve with a broad region of negative differential conductance. We note that in order to see this negative differential conductance, a rather large polarization close to $p = 1$ is needed which is difficult to achieve in experiment. This is typical of most exchange field effects as they rely on a strong spin blockade on the dot. However, in Chapter 7 we will demonstrate a way to detect the exchange field even for small polarizations by probing the quantum-dot spin valve with an additional superconducting electrode.

Current noise

Besides the average current, the spin accumulation and precession also influence the current noise [67]. We start our discussion with the zero-frequency noise of a quantum-dot spin valve.

In the parallel configuration, we find that the Fano factor, i.e., the ratio between current noise and average current is super-Poissonian. This is due to a dynamical spin blockade [96–103]. For a certain period, majority spin electrons are tunneling through the dot until a minority spin electron tunnels onto the dot. At this point, transport becomes interrupted, as the minority spin has a small probability to leave to the drain lead and blocks the tunneling of further electrons. Once it has left the dot, majority spins can again be transferred through the dot. Transport through the quantum dot therefore is chopped into bunches of majority spin electrons that are interrupted by the slow transfer of a minority spin electron giving rise to an increased Fano factor

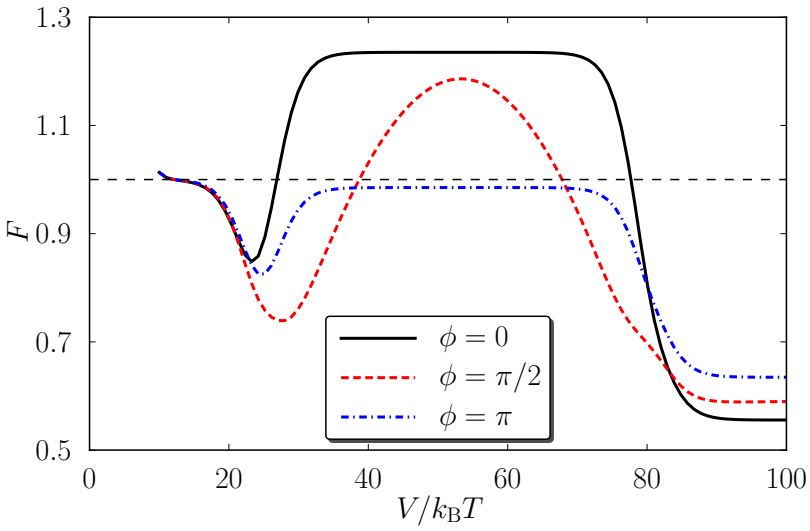

Figure 2.11: Fano factor for a quantum-dot spin valve as a function of bias voltage for different magnetic configurations. While in the parallel case the Fano factor is super-Poissonian, it is close to the Poissonian limit in the antiparallel case. For perpendicular magnetizations, the Fano factor shows a nontrivial bias-dependence due to the exchange field. Parameters are $\Gamma_L = 2\Gamma_R$, $p = 0.55$, $U = 30k_BT$, $\varepsilon = 10k_BT$.

that even diverges as $p \to 1$.

In the antiparallel situation, the Fano factor is sub-Poissonian but approaches the Poissonian limit as $p \to 1$. This behaviour occurs, because in the antiparallel configuration with large polarizations, electrons couple strongly to one lead while they are nearly pinched off completely from the other electrode. In consequence, the system rather acts like a simple tunnel junction than a quantum dot and therefore shows Poissonian current noise.

For noncollinear geometries, a nontrivial bias-dependence of the Fano factor arises. As in the parallel case, a dynamical spin blockade gives rise to a super-Poissonian behaviour. However, as the exchange field acts on the quantum dot, the spin on the dot starts to precess which counteracts the spin blockade. Lifting of the spin blockade is strongest when the exchange field is large which occurs in the vicinity of $V/2 = \varepsilon$ and $V/2 = \varepsilon + U$. It vanishes at $V/2 = \varepsilon + U/2$, giving rise to a peak in the Fano factor. While the effects of the exchange field on the current arise only for very large polarizations, the influence of the exchange field on the current noise occurs already for smaller polarizations which might be achievable in current experiments.

By using the methods of full counting statistics, one can also obtain higher current cumulants. Here, again signs of the exchange field become visible for noncollinear configurations as has been discussed in Ref. [68].

The finite-frequency Fano factor $F(\omega)$ is related to the Fourier transform of the current-current correlation function

$$S(\omega) = \int dt \, \langle I(t)I(0) + I(0)I(t)\rangle e^{i\omega t} - 4\pi\langle I^2\rangle\delta(\omega) \tag{2.26}$$

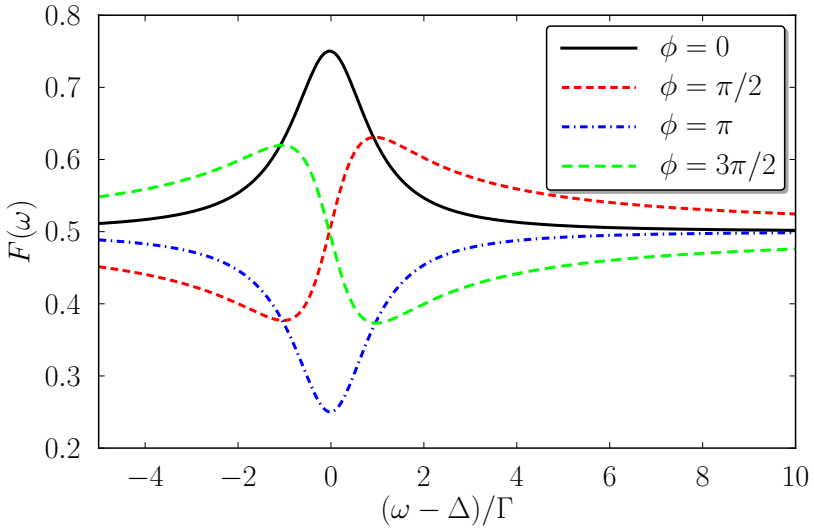

Figure 2.12: Finite-frequency noise for large frequencies in the vicinity of the Larmor frequency Δ of a magnetic field applied externally that is perpendicular to the plane spanned by the magnetization of the leads. The shape of the signal at Δ depends on the relative orientation of the magnetizations. Parameters are $p = 1$ and $\Gamma_\mathrm{L} = 2\Gamma_\mathrm{R}$, the bias voltage is chosen such that only the empty and singly occupied dot are allowed.

via $F(\omega) = S(\omega)/(2eI)$. It is therefore sensitive to the average of two current measurements made at times separated by $1/\omega$. In the limit $\omega \gg \Gamma$, the Fano factor hence is sensitive to the correlations between two subsequent tunneling events while for $\omega \ll \Gamma$ it measures the average properties of the system as, e.g., the average dwelling time of electrons on the dot.

We start our discussion of the finite-frequency noise by considering the situation where a large external magnetic field is applied perpendicularly to the magnetizations of the quantum-dot spin valve, thereby giving rise to a Zeeman splitting $\Delta \gg \Gamma$. We can therefore expect the interesting features of the finite-frequency noise to occur at frequencies $\omega \approx \Delta \gg \Gamma$. By choosing the applied bias appropriately, we can achieve a situation where bunching effects and effects of the internal exchange field can be neglected. If the dot can be approximated to be either empty or singly occupied, we find for the frequency-dependent Fano factor [67]

$$F(\omega) = \frac{1}{2} + \frac{p^2}{4} \frac{\Gamma_\mathrm{R}^2 \cos\phi + \Gamma_\mathrm{R}(\omega - \Delta)\sin\phi}{\Gamma_\mathrm{R}^2 + (\omega - \Delta)^2}. \tag{2.27}$$

As can be seen in Fig. 2.13, the Fano factor develops a characteristic feature at $\omega = \Delta$ where the precise shape depends upon the relative orientation of magnetizations of the electrodes. This behaviour is due to the following mechanism. When an electron enters the dot from the drain electrode, it is polarized along $\mathbf{n}_\mathrm{L}$ with probability p. As it starts to precess around the external magnetic field, the tunneling out rates get modulated by $1 + p\cos(\Delta t + \phi)$ where the phase ϕ is the angle between the magnetizations. Hence, in the parallel configuration, the electron has a large probability to leave the dot either

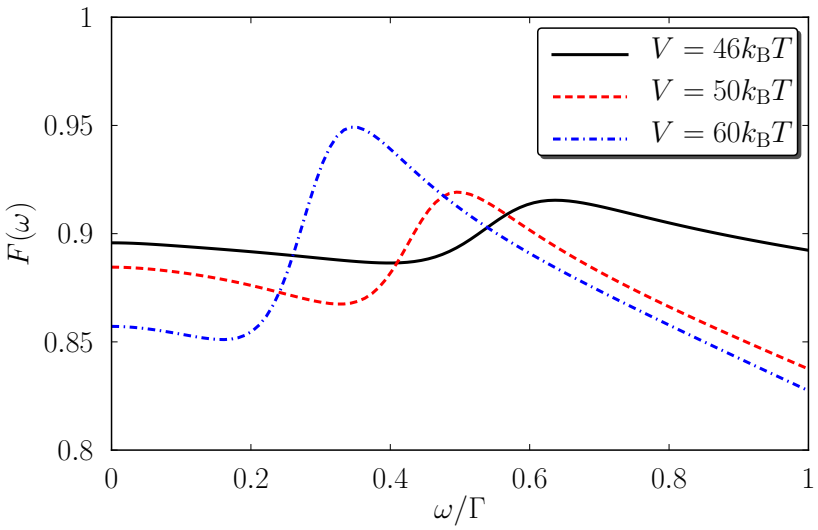

Figure 2.13: Finite-frequency noise of a quantum-dot spin valve. As the dot spin precesses in the exchange field, it gives rise to a signature in the finite-frequency noise at the Larmor frequency of the exchange field. Parameters are $\Gamma_L = 10\Gamma_R$, $p = 0.6$, $\varepsilon = 20k_BT$, $U = 60k_BT$, $\phi = \pi/2$.

immediately or after a full precession period. Therefore, the Fano factor is enhanced at $\omega = \Delta$. On the contrary, for antiparallel magnetization, the electron leaves the dot preferably after half a precession period, leading to a reduced Fano factor at $\omega = \Delta$. Finally, for perpendicular magnetizations, the electron has the greatest probability to leave the dot after performing a rotation by $\pi/2$ or $3\pi/2$ which leads to a dispersion-like feature in the Fano factor.

The frequency-dependent Fano factor does not only provide access to the precessional dynamics of the electron spin in an external magnetic field. When considering $F(\omega)$ for frequencies of the order of the tunnel coupling, $\omega \approx \Gamma$, one also gets information about the dynamics of the dot spin in the exchange field. This is shown in Fig. 2.13 where $F(\omega)$ is shown for a noncollinear geometry and different bias voltages. As the bias voltage is is increased, the exchange field acting on the dot spin is reduced (cf. Fig. 2.10). In consequence, the peak at the Larmor frequency associated with the exchange field is shifted towards smaller frequencies. When applying an additional external field of the same order of magnitude as the exchange field, one finds that the signal occurs at the Larmor frequency of the total magnetic field. In Chapter 4, we will make use of this property to discuss the contributions to the exchange field arising from the creation and annihilation of spin waves in the electrodes. Furthermore, as in the situation where $\omega = \Delta \gg \Gamma$ which we discussed above, the form of the resonance feature depends on the relative alignment of magnetizations and external field [67]. We will make use of this property in Chapter 5 to detect a change of sign of the exchange field that arises when a magnetic impurity in the tunnel barrier gets switched by the spin-polarized current flowing through the quantum-dot spin valve.

2.4.4 Experimental realizations

In the following, we are going to present the various experimental realizations of quantum-dot spin valves that exist today. As typical experimental realizations involve the combination of ferromagnetic, metallic electrodes with semiconducting quantum dot structures, a conductance mismatch arises at the interfaces which renders spin injection difficult [104–107].

Using lithographically defined metallic islands instead of semiconducting quantum dots overcomes this problem. While lithographic methods have the advantage of allowing a precise control over size, shape and properties of the quantum dot as well as the tunnel barriers, it is currently not possible to define metallic structures small enough such that the level quantization becomes detectable. Hence such systems cannot be described in terms of the Anderson model as a single-level quantum dot but rather have to be described as metallic islands.

This problem can be circumvented by studying granular systems [108–117]. Such systems consist of small metallic grains which are embedded in an oxide barrier between two ferromagnetic electrodes. While these metallic grains are much smaller than lithographically defined quantum dots, measurements in granular systems have the disadvantage of providing only ensemble averages such that certain features might get averaged out. Furthermore, the level position of the grains cannot be controlled via a gate voltage. Nevertheless, clear signs of Coulomb blockade and TMR were found at 4 K [108–110] as well as signs of spin-dependent transport in the shot noise [113]. Furthermore, measurements of the spin relaxation time showed spin life times enhanced compared to the bulk value up to several nanoseconds [111, 112, 116].

Contacting only a single metallic grain was achieved for the first time by Deshmukh et al. [118]. They created a nano pinhole in an insulating Si_3N_4 layer covering an aluminum electrode, deposited an aluminum grain with a sorrounding oxide layer on one side of the pinhole and finally covered the other side with a cobalt electrode. Hence, at the measurement temperature of 40 mK one lead became superconducting while the other one was ferromagnetic. From their measurements, they could determine the polarization of the electrons tunneling to the grain. Similarly, Bernand-Mantel et al. [119, 120] covered a cobalt electrode and an Al_2O_3 tunnel barrier with embedded gold clusters with photoresist. After digging a nanohole using an AFM tip, they removed the tip and covered the hole with another cobalt electrode. In this system, they could observe a gate-voltage effect by thermal cycling of the sample as well as by changing the direction of an externally applied magnetic field which offers the possibility of a single-electron transistor with only two electrodes. Furthermore, a spin-valve like magnetoresistance was found.

Recently, contacting self-assembled InAs quantum dots by ferromagnetic electrodes was realized [121–126]. These systems showed clear signs of Coulomb blockade and gate-dependent magnetoresistance. An inverse TMR was found and explained in terms of spin-dependent tunneling through excited states [124, 125]. For a spin-diode configuration with one normal and one ferromagnetic electrode a current suppression due to spin blockade was found [126]. For strong dot-lead couplings, the Kondo effect was observed. A negative TMR was observed for small bias due to a suppression of the Kondo effect for parallel magnetizations [123].

Instead of using metallic grains or semiconductor quantum dots, one can also study

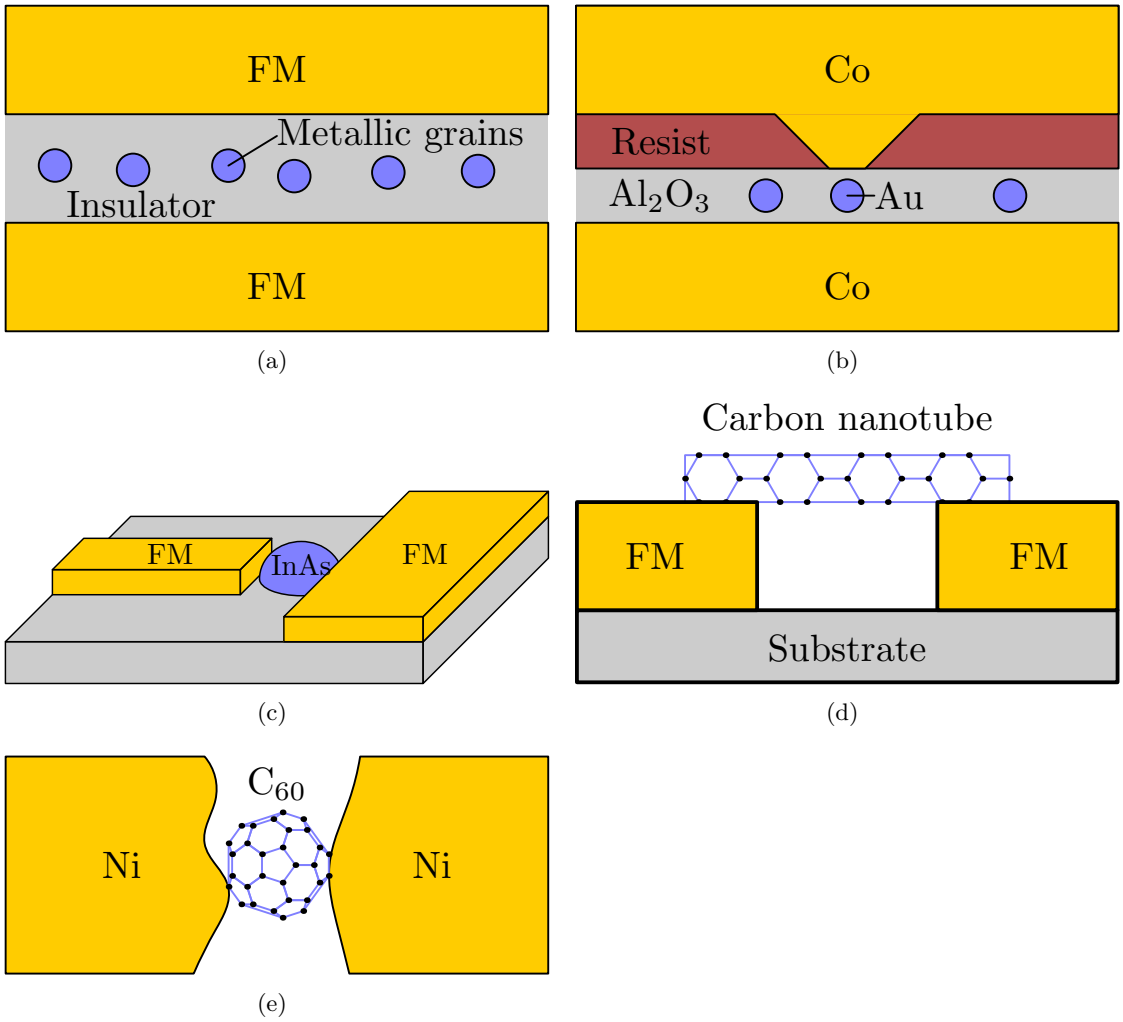

Figure 2.14: Schematic drawings of various ways to experimentally realize a quantum-dot spin valve: (a) granular system of metallic nanoparticles in a tunnel barrier between two ferromagnetic electrodes, (b) metallic grains in a nano pinhole, (c) self-assembled semiconductor quantum dots with lateral gates, (d) carbon nanotubes, (e) molecular devices

devices where a single molecule is contacted by ferromagnetic electrodes. Due to their small size, molecules show large level spacings and Coulomb energies which allows the detection of Coulomb-blockade physics at higher temperatures up to room temperature. Carbon nanotubes turned out to be particularly suited to study transport through single molecules. They have been coupled successfully to ferromagnetic metals [15, 127–130] and semiconductors [131]. Similarly to the systems discussed so far, Coulomb blockade and magnetoresistance effects could be observed. Hauptmann et al. [15] measured a splitting of the Kondo resonance due to a gate-dependent exchange field in good agreement with the predictions from numerical renormalization group studies [73–77, 80].

Apart from carbon nanotubes, single C_{60} molecules have successfully been contacted by Ni electrodes [14]. Due to the strong coupling between the molecule and the leads, the Kondo effect could be observed in these systems. Similar to the experiments on carbon nanotubes [15], for parallely magnetized electrodes, a splitting of the Kondo resonance due to the exchange field was found. The splitting could be compensated by applying an appropriately tuned external field to the system.

Another method to realize quantum-dot spin valves could be the use of ferromagnetic scanning tunneling microscope tips to contact individual atoms or molecules on a substrate [132]. By using nonmagnetic electrodes to contact single magnetic atoms, Hirjibehedin et al. [133] recently could determine magnetic properties at the atomic scale. In Chapter 6, we provide a theory that explains the observed conductance features and furthermore predicts a super-Poissonian current noise due to nonequilibrium effects.

3 Diagrammatic real-time transport theory

In this chapter we introduce the real-time diagrammatic technique that we use to describe nonequilibrium transport through strongly interacting quantum dots weakly coupled to electronic reservoirs. Apart from this method, there is now a large number of approaches available to study transport in mesoscopic system.

The *Landauer-Büttiker formalism* [134–138] allows the description of phase-coherent transport through mesoscopic systems with an arbitrarily strong coupling between the reservoirs and the mesoscopic scattering region. As it relies on noninteracting electrons, it is, however, not suited to describe transport through quantum dots where the Coulomb interaction sets the largest energy scale of the system.

Interaction effects can be taken into account by using a set of rate equations for the occupation probabilities of the quantum dot. They treat the Coulomb interaction exactly while performing a perturbative expansion in the tunnel coupling. In the regime of sequential tunneling, i.e., for first-order transport, the rates are given by Fermi's golden rule giving rise to what is called *orthodox theory* [3–5]. By using a T-matrix approach [139], one can also evaluate cotunneling corrections. However, this requires an ad-hoc regularization of the resulting divergent integrals and an identification of the cotunneling contributions [140–143]. Recently, it was shown that the regularization schemes that exist in the literature yield cotunneling rates that disagree with those obtained by the real-time diagrammatic technique (see below) [144]. Additionally, the rate equation formalism has the drawback that it is not able to deal with coherences, i.e., off-diagonal density matrix elements.

The current through an interacting nanostructure can also be expressed in terms of *nonequilibrium Green's functions* [145, 146] which then have to be determined. Usually, this is not possible exactly. One therefore uses an equation of motion approach and cuts off the resulting infinite hierarchy of equations. The disadvantage of this method is the lack of a formal expansion parameter such that the validity of the approximations made is unclear a priori.

The *numerical renormalization group* [27, 147] allows to treat the interaction on the dot exactly. Furthermore, it allows for arbitrarily strong couplings between the dot and the reservoirs. However, it is only applicable to systems that are in equilibrium such that only linear transport properties can be evaluated.

In equilibrium, an exact solution of the Kondo model was found in 1980 by using a *Bethe ansatz* [148] independently by Andrei [149] and Wiegmann [150]. One year later, an exact solution for the Anderson model was found [151, 152].

In this thesis, we will make use of the *real-time diagrammatic transport theory* [91–94] to evaluate the transport properties of different quantum dot systems coupled to electronic reservoirs. The main idea of this theory is to split the system into noninteracting regions with many degrees of freedom and a strongly interacting region that contains only a small number of degrees of freedom such that it can be diagonalized

exactly. [1] The noninteracting reservoirs are integrated out using Wick's theorem [153]. The remaining system is described in terms of its reduced density matrix. The time evolution of the reduced density matrix is governed by a generalized master equation in Liouville space. The kernels that enter the master equation can be obtained diagrammatically as irreducible self-energy blocks of the dot propagator on the Keldysh contour in a perturbation expansion in the tunnel couplings whereas the Coulomb interaction on the dot is taken into account exactly.

The real-time diagrammatic technique offers a number of advantages over the approaches discussed above. It allows for a systematic expansion in the tunnel coupling. This allows the calculation of cotunneling contributions without the need to regularize the resulting integrals by hand [94, 144, 154]. Furthermore, it captures renormalization effects correctly. On the one hand, it accounts for the renormalization of the level positions as well as for a level broadening in the cotunneling regime [9, 94, 155]. On the other hand, it also takes into account renormalization effects due to virtual tunneling that is relevant for systems involving coherent superpositions of states as, e.g., in a quantum-dot spin valve [64, 65], in double quantum dots [156] and in systems with superconducting electrodes [157]. These renormalization effects would be missing in a rate equation picture because the rate equations only allow the determination of the diagonal density matrix elements.

In certain cases, the real-time technique also allows the description of effects that are nonperturbative in the tunnel coupling Γ by summing up irreducible diagrams of arbitrarily high order in Γ. This allows, e.g., the description of the Kondo effect by considering off-diagonal matrix elements of the total density matrix that include at most one electron-hole pair in the leads [91, 92]. For a quantum dot coupled to a BCS (Bardeen-Cooper-Schrieffer [158]) superconductor with an infinite superconducting gap, one can even sum up all diagrams that describe the coupling to the superconductor exactly [159–161]. Hence, one can describe quantum dots with an arbitrarily strong coupling to the superconductor and the formation of Andreev bound states on the quantum dot. Physically, the summation is possible because the sub-gap transport between the dot and the superconductor is only sensitive to the empty and doubly occupied dot state and therefore does not feel the presence of the strong Coulomb interaction on the quantum dot. In Chapter 7 we will discuss how a superconductor strongly coupled to a quantum-dot spin valve can serve as a probe to measure the exchange field acting on the dot spin even for small polarizations.

The real-time diagrammatic technique not only allows us to evaluate the current through a quantum dot. Additionally, it provides ways to compute the current noise at zero and finite frequency. Furthermore, one can extend the technique to allow the computation of the full counting statistics [68, 103, 162–164]. The central quantity of interest here is the probability that a given number of electrons have passed the system in a given time.

This chapter is organized as follows. In Section 3.1, we derive the generalized master equation for the reduced density matrix of the quantum dot. In the following section, we derive diagrammatic representations of the current as well as the current noise at finite frequencies. In Section 3.3, we discuss the relevance of coherent superpositions

[1] We will call this region quantum dot in the following, though in general it can be a metallic island, a double quantum dot, a single molecule or even a single atom as well.

in quantum-dot spin valves that contain additional magnetic degrees of freedom and how to deal with them in the diagrammatic approach (we note that our discussion can also be applied to other systems where coherences can occur).

3.1 Density matrix and propagator

The quantum-statistical expectation value of an operator A at time t is given by

$$\langle A(t)\rangle = \mathrm{Tr}\left[A(t)_{\mathrm{H}}\rho(t_0)\right]. \tag{3.1}$$

Here, $A(t)_{\mathrm{H}}$ is the operator A in the Heisenberg picture and $\rho(t_0)$ is the density matrix of the system under investigation at some initial time t_0. We assume the density matrix of the whole system consisting of reservoirs and quantum dot to factorize at t_0 such that it can be written as

$$\rho(t_0) = \rho_{\mathrm{dot}}(t_0)\otimes\rho_{\mathrm{res}}(t_0). \tag{3.2}$$

Here, $\rho_{\mathrm{res}}(t_0) = Z_{\mathrm{res}}^{-1}\prod_{r=\mathrm{L,R}}\exp\left(-\beta_r(H_r-\mu_r\hat{N}_r)\right)$ is the equilibrium density matrix of the reservoirs where $\beta = 1/k_{\mathrm{B}}T$ is the inverse temperature of the reservoirs (which in the following we will assume to be the same for all leads), μ_r is the electrochemical potential and $\hat{N}_r = \sum_{\mathbf{k}\sigma} a^\dagger_{r\mathbf{k}\sigma}a_{r\mathbf{k}\sigma}$ is the number operator of the lead electrons. The normalization factor Z_{res} is chosen such that $\mathrm{Tr}_{\mathrm{res}}\,\rho_{\mathrm{res}}(t_0) = 1$ is fulfilled.

As the stationary state does not depend on the initial state, we may choose the initial density matrix of the dot to be of the form $\rho_{\mathrm{dot}}(t_0) = \sum_\chi P_\chi|\chi\rangle\langle\chi|$ where the probabilities P_χ to find the dot in state $|\chi\rangle$ satisfy $\sum_\chi P_\chi = 1$. We note that it is always possible to choose the initial density matrix of the dot to be diagonal although in the stationary state nonvanishing off-diagonal matrix elements can arise, e.g. in a quantum-dot spin valve [64–68, 72, 82, 95, 165] or for a quantum dot coupled to superconducting electrodes [157, 159].

In the next step, we switch to the interaction picture by introducing

$$A(t)_{\mathrm{H}} = \tilde{T}\exp\left(i\int_{t_0}^{t}dt'H_{\mathrm{tun}}(t')_{\mathrm{I}}\right)A(t)_{\mathrm{I}}T\exp\left(-i\int_{t_0}^{t}dt'H_{\mathrm{tun}}(t')_{\mathrm{I}}\right), \tag{3.3}$$

where T ($\tilde{T}$) denotes the time ordering (anti-time ordering) operator. We obtain for the expectation value (3.1)

$$\langle A(t)\rangle = \mathrm{Tr}\left[\tilde{T}\exp\left(-i\int_{t_0}^{t}dt'H_{\mathrm{tun}}(t')_{\mathrm{I}}\right)A(t)_{\mathrm{I}}T\exp\left(i\int_{t_0}^{t}dt'H_{\mathrm{tun}}(t')_{\mathrm{I}}\right)\rho_{\mathrm{res}}(t_0)\rho_{\mathrm{dot}}(t_0)\right]. \tag{3.4}$$

The time evolution of the above equation can be visualized on the Keldysh contour, a closed time path running from t_0 to t and back (cf. Fig. 3.1 and discussion below). Introducing T_K, the time ordering operator along the Keldysh contour which orders operators such that those with the later position on the Keldysh contour appear further left and combining the time integrations into one integral $\int_K dt'\cdots$ along the Keldysh contour, we can write the expectation value as

$$\langle A(t)\rangle = \mathrm{Tr}\left[T_K\exp\left(-i\int_K dt'H_{\mathrm{tun}}(t')_{\mathrm{I}}\right)A(t)_{\mathrm{I}}\rho_{\mathrm{res}}(t_0)\rho_{\mathrm{dot}}(t_0)\right]. \tag{3.5}$$

It should be noted that the Keldysh time ordering operator T_K acts on all operators standing right to it, i.e., it also acts on $A(t)$ and $\rho(t_0)$.

For the particular case of the projection operator $A = |\chi_2\rangle\langle\chi_1|$, where χ_1 and χ_2 indicate two dot states, we introduce the full propagator of the reduced system via

$$\mathbf{\Pi}(t,t_0) = \mathrm{Tr}_{\mathrm{res}}\left[T_K \exp\left(-i\int_K dt' H_{\mathrm{tun}}(t')_{\mathrm{I}}\right)\rho_{\mathrm{res}}(t_0)\right] \tag{3.6}$$

which is a rank four tensor acting on the reduced density matrix $\boldsymbol{\rho}_{\mathrm{dot}}$. The time dependence of the reduced density matrix elements $P^{\chi_1}_{\chi_2}(t) = \langle\chi_1|\boldsymbol{\rho}_{\mathrm{dot}}(t)|\chi_2\rangle$ (for later convenience, we introduce the short-hand notation $P^{\chi}_{\chi} = P_\chi$ for the diagonal density matrix elements which denote the probability to find the system in state χ) is therefore given by

$$P^{\chi_1}_{\chi_2}(t) = \sum_{\chi_1'\chi_2'} \Pi^{\chi_1\chi_1'}_{\chi_2\chi_2'}(t,t_0) P^{\chi_1'}_{\chi_2'}(t_0). \tag{3.7}$$

We now expand the exponential in Eq. (3.5) in powers of the tunnel Hamiltonian:

$$T_K \exp\left(-i\int_K dt' H_{\mathrm{tun}}(t')_{\mathrm{I}}\right) = \sum_{n=0}^{\infty}(-i)^n \int_K dt_1 \cdots \int_K dt_n \; T_K\left\{H_{\mathrm{tun}}(t_1)_{\mathrm{I}}\cdots H_{\mathrm{tun}}(t_n)_{\mathrm{I}}\right\}. \tag{3.8}$$
$$t_1 \geq \cdots \geq t_n$$

After disentangling the dot and lead operators in Eq. (3.8) which gives rise to a minus sign whenever we interchange dot and reservoir operators, we can apply Wick's theorem [153], as the reservoir Hamiltonian H_r is bilinear in the lead electron operators, to contract pairs of lead operators using

$$\langle a^\dagger_{r\mathbf{k}\sigma}(t) a_{r'\mathbf{k}'\sigma'}(t')\rangle = \delta_{rr'}\delta_{\mathbf{k}\mathbf{k}'}\delta_{\sigma\sigma'} e^{i\varepsilon_{r\mathbf{k}\sigma}(t-t')} f^+_r(\varepsilon_{r\mathbf{k}\sigma}), \tag{3.9}$$

$$\langle a_{r\mathbf{k}\sigma}(t') a^\dagger_{r'\mathbf{k}'\sigma'}(t)\rangle = \delta_{rr'}\delta_{\mathbf{k}\mathbf{k}'}\delta_{\sigma\sigma'} e^{i\varepsilon_{r\mathbf{k}\sigma}(t-t')} f^-_r(\varepsilon_{r\mathbf{k}\sigma}). \tag{3.10}$$

Here, $f^+_r(\omega) = f^+(\omega-\mu_r)$ with $f^+(\omega) = 1/(e^{\beta\omega}+1)$ is the Fermi distribution function of lead r which denotes the probability to find the state with energy ω in lead r occupied. Similarly, $f^-_r(\omega) = 1 - f^+_r(\omega)$ gives the probability to find the state with energy ω empty.

Combining Eq. (3.5) and (3.8), we can now visualize the time evolution of the reduced system as shown in Fig. 3.1. The system evolves along the upper branch of the Keldysh contour from the initial time t_0 to the final time t. Afterwards it evolves backwards in time along the lower branch of the contour back to the initial time. Every insertion of a tunnel Hamiltonian arising from the expansion of the exponential in Eq. (3.8) is denoted by a black dot (internal vertex) on the contour. The pairwise contractions of reservoir operators are visualized as dashed lines connecting a pair of tunnel vertices. These tunneling lines have an orientation indicated by an arrow such that the arrow points away from the vertex at which an electron is annihilated on the dot. As the dot Hamiltonian H_{dot} contains terms which are not bilinear in the dot operators, Wick's theorem is not applicable to the dot operators. Hence, we have to deal with the dot operators in H_{tun} by taking into account their action on the dot state explicitly. This is done by keeping track of the dot state along the Keldysh contour. Finally, the operator $A(t)$ is also represented as a black dot (external vertex) at the final time t of measuring.

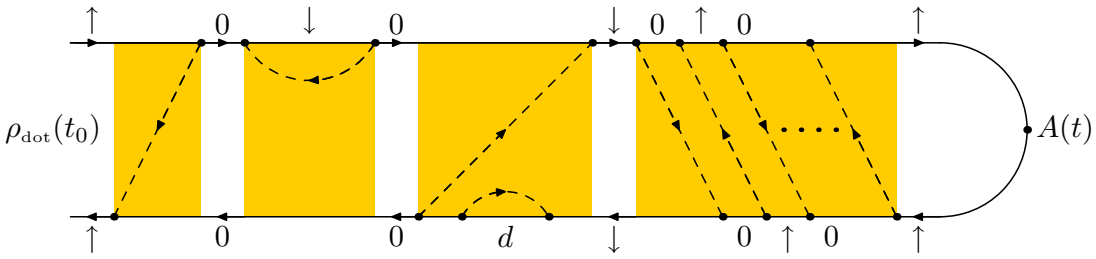

Figure 3.1: Example for the time evolution of the reduced density matrix along the Keldysh contour. The reduced quantum system evolves along the upper branch of the contour from t_0 to t where the operator A is measured. Afterwards the time path is closed along the lower branch of the contour. Every tunnel Hamiltonian from the expansion of the exponential in Eq. (3.8) gives rise to a vertex which changes the dot state and is connected to another vertex by a directed tunneling line.

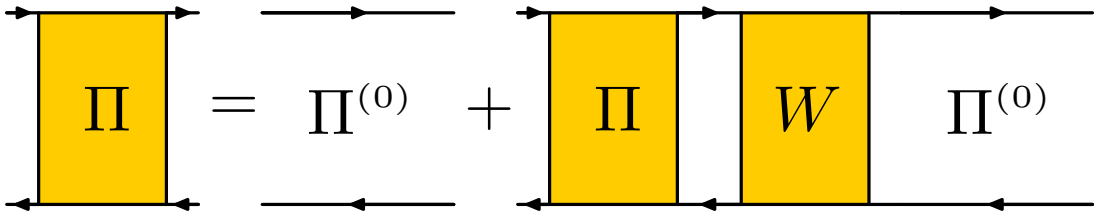

Figure 3.2: Dyson equation for the full propagator of the reduced density matrix. The full propagator of the reduced system can be represented recursively as the free propagator plus the product of full propagator, self-energy insertion and free propagator.

The general structure of the diagrammatic representation in Fig. 3.1 consists of irreducible self-energies $W^{\chi_1\chi_1'}_{\chi_2\chi_2'}(t,t')$. These describe transitions between the state $P^{\chi_1'}_{\chi_2'}$ at time t' and the state $P^{\chi_1}_{\chi_2}$ at time t. They are irreducible in the sense that any vertical cut through the self-energy will cut at least one or more tunneling lines. In between the self-energies, there are blocks where a vertical cut through the diagram does not cut any tunneling line at all. We denote these blocks as $\Pi^{(0)\chi_1\chi_1'}_{\chi_2\chi_2'}(t,t')$ because they describe the free time evolution of the reduced quantum system between times t' and t. Denoting the energies of the states on the upper and lower part of the contour as ε_{χ_1} and ε_{χ_2}, respectively, the free propagator is given by

$$\Pi^{(0)\chi_1\chi_1'}_{\chi_2\chi_2'}(t,t') = \delta_{\chi_1\chi_1'}\delta_{\chi_2\chi_2'}e^{-i(\varepsilon_{\chi_1}-\varepsilon_{\chi_2})(t-t')}. \tag{3.11}$$

Summing up the irreducible self-energies and free propagators in the sense of a Dyson equation as shown in Fig. 3.2, we obtain for the full propagator of the reduced system

$$\mathbf{\Pi}(t,t_0) = \mathbf{\Pi}^{(0)}(t,t_0) + \int_{t_0}^{t} dt_2 \int_{t_0}^{t_2} dt_1 \mathbf{\Pi}^{(0)}(t,t_2)\boldsymbol{W}(t_2,t_1)\mathbf{\Pi}(t_1,t_0). \tag{3.12}$$

Multiplying this equation with $\boldsymbol{\rho}_{\mathrm{dot}}(t_0)$ and taking the derivative with respect to t finally yields a formally exact master equation that describes the time evolution of the reduced density matrix and is valid for arbitrary initial states,

$$\dot{P}^{\chi_1}_{\chi_2}(t) = -i(\varepsilon_{\chi_1}-\varepsilon_{\chi_2})P^{\chi_1}_{\chi_2}(t) + \int_{t_0}^{t} dt' \sum_{\chi_1'\chi_2'} W^{\chi_1\chi_1'}_{\chi_2\chi_2'}(t,t')P^{\chi_1'}_{\chi_2'}(t'). \tag{3.13}$$

The first term on the right-hand side describes the coherent evolution of the reduced system. The second term characterizes the dissipative coupling to the electrodes. It includes memory effects through the kernels $W^{\chi_1\chi_1'}_{\chi_2\chi_2'}(t,t')$. A systematic perturbation expansion in the tunnel coupling is possible by expanding the kernel $W^{\chi_1\chi_1'}_{\chi_2\chi_2'}$ as well as the density matrix elements $P^{\chi_1}_{\chi_2}$ in a series in the tunnel coupling strength Γ. We will discuss the expansion in the tunnel coupling in more detail in Section 3.3.

For a system that is invariant under time translations, the propagators as well as the self-energies only depend on the time difference between the beginning and end of the corresponding block. In this case, we can introduce the Laplace transform of the full and free propagator as well as of the self-energies via $F(\omega) = \int_{t_0}^{\infty} dt\, e^{-i(\omega-i0^+)(t-t_0)}F(t-t_0)$. This will turn out to simplify the calculation of the stationary density matrix as well as of current and current noise (see next section) significantly.

Transforming the Dyson equation (3.12) yields

$$\mathbf{\Pi}(\omega) = \mathbf{\Pi}^{(0)}(\omega) + \mathbf{\Pi}^{(0)}(\omega)\boldsymbol{W}(\omega)\mathbf{\Pi}(\omega)$$

with

$$\Pi^{(0)\chi_1\chi_1'}_{\chi_2\chi_2'}(\omega) = \frac{i\delta_{\chi_1\chi_1'}\delta\chi_2\chi_2'}{\varepsilon_{\chi_2}-\varepsilon_{\chi_1}-\omega+i0^+}. \tag{3.14}$$

Solving for the full propagator gives

$$\mathbf{\Pi}(\omega) = \left(\mathbf{\Pi}^{(0)}(\omega)^{-1} - \boldsymbol{W}(\omega)\right)^{-1}, \tag{3.15}$$

i.e., the full propagator $\mathbf{\Pi}(\omega)$ depends on the free propagator $\mathbf{\Pi}^{(0)}(\omega)$ as well as on the self-energies $\boldsymbol{W}(\omega)$. Rewriting equation (3.15) in the form $\mathbf{\Pi}(\omega)(\mathbf{\Pi}^{(0)}(\omega)-\boldsymbol{W}(\omega))=\mathbf{1}$ and applying the final-value theorem $\lim_{\omega\to 0}(i\omega+0^+)\mathbf{\Pi}(\omega)=\lim_{t\to\infty}\mathbf{\Pi}(t)=\boldsymbol{\rho}^{\mathrm{stat}}$ finally yields the master equation determining the reduced density matrix in the stationary state:

$$0=\left(\mathbf{\Pi}^{(0)}(\omega=0)^{-1}-\boldsymbol{W}(\omega=0)\right)\boldsymbol{\rho}^{\mathrm{stat}}. \tag{3.16}$$

Written out in component form, it reads

$$0=-i(\varepsilon_{\chi_1}-\varepsilon_{\chi_2})P^{\chi_1}_{\chi_2}+\sum_{\chi_1'\chi_2'}W^{\chi_1\chi_1'}_{\chi_2\chi_2'}P^{\chi_1'}_{\chi_2'}. \tag{3.17}$$

The diagrammatic rules that are necessary to evaluate the kernels $W^{\chi_1\chi_1'}_{\chi_2\chi_2'}$ that enter the master equation are summarized in Appendix A for the various systems that we investigate in this thesis.

3.2 Current and current noise

The current $\hat{I}_r$ through barrier r is given by the change of particle number in reservoir r multiplied by the electronic charge $-e$. Hence, according to the equation of motion in the Heisenberg picture, we have for the current operator

$$\hat{I}_r=-e\frac{d\hat{N}_r}{dt}=-ie[H,\hat{N}_r]=-ie\sum_{\mathbf{k}\sigma}t_r a^\dagger_{r\mathbf{k}\sigma}c_\sigma+\mathrm{h.c.} \tag{3.18}$$

In the following discussion we will always choose the symmetrized current $\hat{I}=\frac{\hat{I}_\mathrm{R}-\hat{I}_\mathrm{L}}{2}$. The minus sign occurs in the symmetrization due to the direction of current flow. For the current itself this symmetrization is not really important, as due to current conservation we have $\langle\hat{I}_\mathrm{R}\rangle=-\langle\hat{I}_\mathrm{L}\rangle\equiv\langle\hat{I}\rangle$. At finite frequencies this is no longer true as displacement currents arise which make the current measured in the source-drain circuit differ from the current through the tunnel barriers. The displacement currents can be taken into account according to the Ramo-Shockley theorem [138, 166, 167] by considering the total current as the current through each barrier weighted with the capacitance C_r of the respective barrier, $\hat{I}=(C_\mathrm{L}\hat{I}_\mathrm{L}+C_\mathrm{R}\hat{I}_\mathrm{R})/(C_\mathrm{L}+C_\mathrm{R})$. For a quantum dot coupled to electronic reservoirs, the capacitances C_r of the tunnel barriers are much less sensitive to the contact geometry than the tunnel couplings Γ_r. Hence, while allowing asymmetric tunnel couplings, we restrict ourselves to symmetric capacitances $C_\mathrm{L}=C_\mathrm{R}$ giving rise to the symmetrized current defined above [67].

When calculating the average value of the current operator $I=\langle\hat{I}\rangle$, we encounter a new kind of self-energy W^I where one internal tunneling vertex is replaced by an external current vertex. As the current operator differs from the tunneling Hamiltonian only by a constant prefactor taking into account the direction of the tunneling electrons, the only difference between the self-energies W and W^I is the fact that the latter takes into account whether an electron enters or leaves the dot through the right or left tunnel barrier. Diagrammatically, this gives rise to a factor of $+1/2$ for a current vertex on the upper (lower) branch of the Keldysh contour in which an electron is annihilated in the left or created in the right (annihilated in the right or created in the left) lead

and leads to a factor of $-1/2$ in the other four cases. For a more detailed discussion of how these factors arise, we refer the reader to Ref. [93, 94].

With the help of the self-energies W^I we can now write the expression for the average current in the compact form

$$I = \langle I \rangle = \frac{e}{2} \operatorname{Tr}\left[\boldsymbol{W}^I(\omega = 0)\boldsymbol{\rho}^{\text{stat}}\right]. \tag{3.19}$$

Additional information about the transport processes through the quantum dot can be inferred from the current noise and higher cumulants of the current. In the following, we derive a diagrammatic representation of the finite-frequency noise which we define as the Fourier transform of the symmetrized current-current correlation function $S(t) = \langle I(t)I(0)\rangle + \langle I(0)I(t)\rangle - 2\langle I^2\rangle$:

$$S(\omega) = \int_{-\infty}^{\infty} dt\, e^{-i\omega t}\Big(\langle \hat{I}(t)\hat{I}(0)\rangle + \langle \hat{I}(0)\hat{I}(t)\rangle - 2\langle I^2\rangle\Big). \tag{3.20}$$

The symmetrized noise is a real quantity in contrast to the unsymmetrized noise which contains additional, complex contributions from emission and absorption processes [168–171].

Translating the finite-frequency noise (3.20) into our diagrammatic language gives rise to two tunnel vertices being replaced by current vertices. These are connected by a bosonic frequency line with energy ω which only transfers energy but no particles between the vertices. The current vertices can be arranged in two different ways. They can either appear in the same self-energy block or they can occur in different self-energies separated by the propagator $\boldsymbol{\Pi}(\omega)$. The latter equals the propagator at zero frequency apart from the frequency line traversing it from left to right.

We therefore introduce three new kinds of self-energies which are depicted in Fig. 3.3. In $\boldsymbol{W}^{II}(\omega)$ two tunnel vertices are replaced by current vertices and connected by the bosonic frequency line. In $\boldsymbol{W}^I_>(\omega)$ ($\boldsymbol{W}^I_<(\omega)$) only one tunnel vertex is replaced by a current vertex. The associated frequency line is leaving the diagram to the right (enters from the left). In the limit $\omega \to 0$ the latter two self-energies coincide and become equal to $\boldsymbol{W}^I$.

While in Fig. 3.3 we only showed insertion of the current vertex on the upper branch of the Keldysh contour, for the calculation of the symmetrized current noise (3.20) we have to take into account the diagrams with the corresponding replacements on the lower branch as well.

Having introduced the above new self-energy diagrams, we can now easily write down the diagrammatic expression for the finite-frequency current noise,

$$S(\omega) = \frac{e^2}{2} \operatorname{Tr}\left[\boldsymbol{W}^{II}(\omega)\boldsymbol{\rho}^{\text{stat}} + \boldsymbol{W}^I_<(\omega)\boldsymbol{\Pi}(\omega)\boldsymbol{W}^I_>(\omega)\boldsymbol{\rho}^{\text{stat}}\right] - 2\pi\delta(\omega)\langle \hat{I}^2\rangle + (\omega \to -\omega). \tag{3.21}$$

When dealing with sequential tunneling only, the above expression simplifies considerably for small frequencies $\omega \sim \Gamma$. In this case, the self-energies are already of first order in Γ. Therefore, including their frequency dependence as well would give rise to terms of order Γ^2. This would be inconsistent as cotunneling contributions also give rise to contributions of order Γ^2. Hence, it is obvious that we can restrict ourselves to the consideration of $\boldsymbol{W}^{II}(\omega = 0)$.

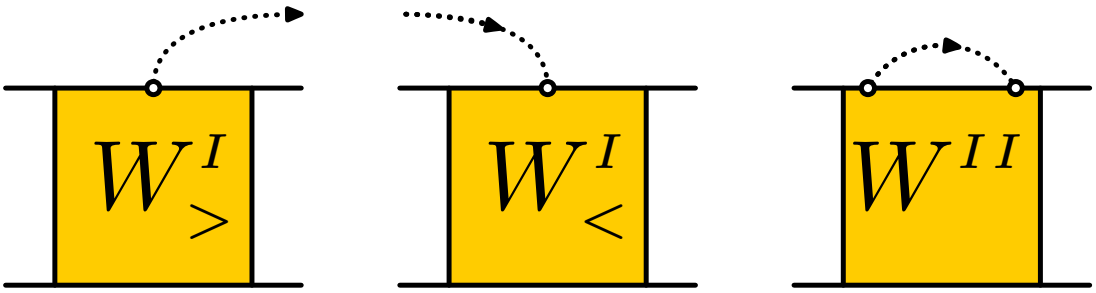

Figure 3.3: Diagrammatic representation of the self-energies $W^I_>$, $W^I_<$ and W^{II}. $W^I_>$ ($W^I_<$) has one tunnel vertex replaced by a current vertex with a bosonic frequency line attached that leaves the diagram to the right (enter from the left). W^{II} contains two current vertices conencted by a frequency line. While here we only show current vertices on the upper branch of the contour, they can also occur on the lower branch.

In the second term on the right-hand side of (3.21), the full propagator $\mathbf{\Pi}(\omega) = \left(\mathbf{\Pi}^{(0)}(\omega)^{-1} - \boldsymbol{W}(\omega)\right)^{-1}$ is treated consistently if we neglect the frequency dependence of $\boldsymbol{W}(\omega)$ as well and only keep the frequency dependence of $\mathbf{\Pi}^{(0)}(\omega)$ such that the whole expression is of order Γ^{-1}. The complete second term on the right-hand side of (3.21) therefore is of order Γ if additionally to the above approximations in the full propagator we also neglect the frequency dependence of the self-energies $\boldsymbol{W}^I_>(\omega)$ and $\boldsymbol{W}^I_<(\omega)$ which then coincide with $\boldsymbol{W}^I(\omega = 0)$.

Hence, the final result for the finite-frequency noise in the sequential tunnling regime for frequencies of order $\omega \sim \Gamma$ is given by

$$S(\omega) = \frac{e^2}{2}\,\mathrm{Tr}\left[\boldsymbol{W}^{II}\boldsymbol{\rho}^{\mathrm{stat}} + \boldsymbol{W}^{I}(\mathbf{\Pi}^{(0)}(\omega)^{-1} - \boldsymbol{W})^{-1}\boldsymbol{W}^{I}\boldsymbol{\rho}^{\mathrm{stat}}\right] - 2\pi\delta(\omega)\langle\hat{I}^2\rangle + (\omega \to -\omega), \tag{3.22}$$

i.e., the frequency dependence arises only from the free propagator. The delta function only gives a contribution to the zero-frequency noise. For finite frequencies, it can be dropped together with the $i0^+$ prescription in the numerator of the free propagator.

3.3 Extension of the diagrammatic theory to systems involving spin degrees of freedom

So far, we considered the general formalism of the real-time diagrammatic technique having in mind a single-level quantum dot coupled to electronic reservoirs. In this section, we discuss the generalizations that are necessary to allow for a description of a quantum-dot spin valve that contains additional spin degrees of freedom. In this thesis, three different types of such systems will be investigated. First, we consider the influence of spin waves that are excited in the ferromagnetic electrodes of the quantum-dot spin valve. We then consider magnetic impurities that are located in one of the tunnel barriers. Finally, we discuss systems where a magnetic impurity is located on the quantum dot itself.

To describe a quantum-dot spin valve where spin waves can be excited in the electrodes, we make use of the Holstein-Primakoff representation which allows to describe spins in terms of bosonic degrees of freedom [172]. Taking into account only leading terms of an expansion in the number of bosons, we find that spin waves are described as a non-interacting gas of bosons. In principle, we could integrate out the bosonic degrees of freedom together with the electronic ones [173]. However, as we are interested in nonequilibrium effects of the magnon distribution here, we instead treat the magnons as being part of the reduced quantum system. We therefore have to keep track of the number of bosons in each electrode explicitly. As the number of magnons is not bounded from above, our reduced system becomes infinite dimensional. As we initially assumed the number of magnons to be small, we cut off the Hilbert space at a given magnon number $N_{\max}$ and afterwards check that our results to not depend on the precise choice of the cut-off $N_{\max}$.

When dealing with quantum-dot spin valves that contain magnetic impurities, which we describe as localized spins, we similarly keep track of the spin state explicitly in the density matrix of the reduced system. On the one hand, this is necessary as there is no equivalent of Wick's theorem that can be applied to spins. On the other hand, here, we are again interested in the effects that are caused by a nonequilibrium occupation of the impurity spin states.

For the cases discussed above, a number of coherent superpositions between states with either different numbers of magnons or different impurity spin states can arise. In the following, we discuss under which circumstances these coherences have to be included and when they have to be neglected. To this end, we denote by $|\xi\rangle$ the state of the reduced quantum system which is characterized by the dot state $|\chi\rangle$ as well as the quantum numbers determining the number of magnons or the state of the impurity spin.

The starting point of our discussion is the generalized master equation in the stationary limit (3.17). We expand the density matrix elements as well as the self-energies in a series in the tunnel coupling Γ as

$$P^{\xi_1}_{\xi_2} = \sum_{n=0}^{\infty} \Gamma^n P^{(n)\xi_1}_{\xi_2}, \tag{3.23}$$

$$W^{\xi_1\xi_1'}_{\xi_2\xi_2'} = \sum_{n=1}^{\infty} \Gamma^n W^{(n)\xi_1\xi_1'}_{\xi_2\xi_2'}. \tag{3.24}$$

If the energy difference $\varepsilon_{\xi_1} - \varepsilon_{\xi_2}$ between the states ξ_1 and ξ_2 forming the coherent superposition is much larger than the tunnel coupling, $\varepsilon_{\xi_1} - \varepsilon_{\xi_2} \gg \Gamma$, the master equation for the off-diagonal matrix elements to leading order in the tunnel coupling takes the form

$$0 = -i\left(\varepsilon_{\xi_1} - \varepsilon_{\xi_2}\right) P^{(0)\xi_1}_{\xi_2} \tag{3.25}$$

as the expansion of the self-energies only starts at first order in Γ. In consequence, $P^{(0)\xi_1}_{\xi_2} = 0$ and coherent superpositions between states whose energy difference is large compared to the tunnel coupling have to be neglected in the sequential tunneling regime. A non-vanishing contribution to the coherences arises only at first order in Γ

where the master equation reads

$$0 = -i\left(\varepsilon_{\xi_1} - \varepsilon_{\xi_2}\right) P^{(1)\xi_1}_{\ \ \xi_2} + \sum_{\xi} W^{(1)\xi_1\xi}_{\ \ \xi_2\xi} P^{(0)}_{\ \ \xi}. \tag{3.26}$$

Hence, when considering transport in the cotunneling regime where the system is sensitive to the first-order corrections of the density matrix elements, coherent superpositions between any two states with different magnon numbers of spin states have to be taken into account. This is similar to the case of transport through a single molecule with a vibrational degree of freedom, where considering the coherent superpositions of states with different numbers of vibrational excitations in the cotunneling regime is also crucial [154]. However, in this thesis, we will discuss transport through quantum-dot spin valves only in the sequential tunneling regime. Hence, we have to neglect any coherent superpositions of states whose energy differs much more than the tunnel coupling.

In the opposite limit of small energy differences, $\varepsilon_{\xi_1} - \varepsilon_{\xi_2} \lesssim \Gamma$, the situation is different. Now the expansion of the generalized master equation only starts in first-order of the tunnel coupling Γ and reads

$$0 = -i\left(\varepsilon_{\xi_1} - \varepsilon_{\xi_2}\right) P^{(0)\xi_1}_{\ \ \xi_2} + \sum_{\xi_1'\xi_2'} \Gamma W^{(1)\xi_1\xi_1'}_{\ \ \xi_2\xi_2'}\Big|_{\varepsilon_{\xi_1}=\varepsilon_{\xi_2}} P^{(0)\tilde{\xi}_2'}_{\ \ \xi_1}, \tag{3.27}$$

meaning that there will be finite zeroth-order contributions to the coherences in general. It is important that the self-energies have to be evaluated at $\varepsilon_{\xi_1} = \varepsilon_{\xi_2}$ in order to consistently neglect all effects of order Γ^2. Ignoring to do so will give rise to unphysical solutions of the master equation with diagonal matrix elements satisfying $P_\xi > 1$ or $P_\xi < 0$. In Ref. [174], the same form of the master equation as in (3.27) is derived within the singular-coupling limit. However, the big advantage of our derivation is that it can be easily generalized to discuss, e.g., the first-order corrections to the coherences which become relevant when one is interested in cotunneling transport.

In summary, we found that in the sequential tunneling regime coherent superpositions have to be neglected when $\varepsilon_{\xi_1} - \varepsilon_{\xi_2} \gg \Gamma$ is fulfilled. In the opposite limit $\varepsilon_{\xi_1} - \varepsilon_{\xi_2} \lesssim \Gamma$ they have to be included. Here, one has to take care about the expansion of the self-energies, however.

3.4 Summary

In this chapter, we introduced the real-time diagrammatic technique which allows to investigate nonequilibrium transport through quantum dots taking into account the strong Coulomb interaction exactly. We derived a generalized master equation which describes the time evolution of the reduced density matrix of the quantum dot. The kernels entering this master equation can be evaluated as irreducible self-energies on the Keldysh contour which can be expanded in a perturbation series in the tunnel coupling strength. Afterwards, we derived diagrammatic representations for the current and current noise. In the end, we discussed the extension of the diagrammatic formalism to a quantum-dot spin valve with additional spin degrees of freedom. Here, the correct treatment of coherent superpositions is of crucial importance.

4 Spin waves in quantum-dot spin valves

In this chapter, we study the influence of spin waves, excited in the ferromagnetic electrodes, on transport through a quantum-dot spin valve using a suitable extension of the real-time diagrammatic technique introduced in the last chapter. While the transport properties of the idealized quantum-dot spin valve have now been investigated in quite some detail, more realistic models that include, e.g., the possibility to excite spin waves in the leads have not been addressed yet. On the one hand we want to analyze the deviations from the idealized system. To this end, we study the modifications of the conductance which we find to be particularly pronounced for large polarizations of the leads. Here, the magnonic side peaks can exhibit negative differential conductance but can also surmount the ordinary conductance peaks depending on the magnetic configuration. We, furthermore, show that the excitation of spin waves can lead to an increased as well as to a decreased Fano factor. Additionally, we demonstrate how the magnonic modifications to the exchange field can be detected in the finite-frequency noise. On the other hand, we want to address the question if the spin waves can generate completely new effects. To this end, we analyze the nonequilibrium distribution of the magnons which we find to be different for the source and drain electrode. Furthermore, we show how the magnons can drive a completely spin-polarized current through the quantum dot without any external bias voltage.

This chapter is organized as follows. In Section 4.1 we introduce our model. We then discuss the reduced density matrix of the system and the master equation that the density matrix obeys in Section 4.2. Our results are presented in Section 4.3. We summarize our findings in Section 4.4. The material presented in this chapter has previously been published in Ref. [175].

4.1 Model

We consider transport through a single-level quantum dot weakly coupled to ferromagnetic leads with non-collinear magnetizations via tunneling barriers. In order to describe spin waves which may be excited in the leads, we model the lead magnetizations as macroscopically large spins localized in the respective lead as shown in Fig. 4.1.

The Hamiltonian of our system is the sum of five parts:

$$H = H_{\mathrm{dot}} + H_{res} + H_{\mathrm{tun}} + H_{\mathrm{spin}} + H_{\mathrm{coupl}}. \tag{4.1}$$

The first term,

$$H_{\mathrm{dot}} = \sum_{\sigma} \varepsilon c_{\sigma}^{\dagger} c_{\sigma} + U c_{\uparrow}^{\dagger} c_{\uparrow} c_{\downarrow}^{\dagger} c_{\downarrow}, \tag{4.2}$$

describes the quantum dot in terms of a single, spin-degenerate level with energy ε measured relative to the Fermi energies of the leads in equilibrium and Coulomb energy U for double occupation.

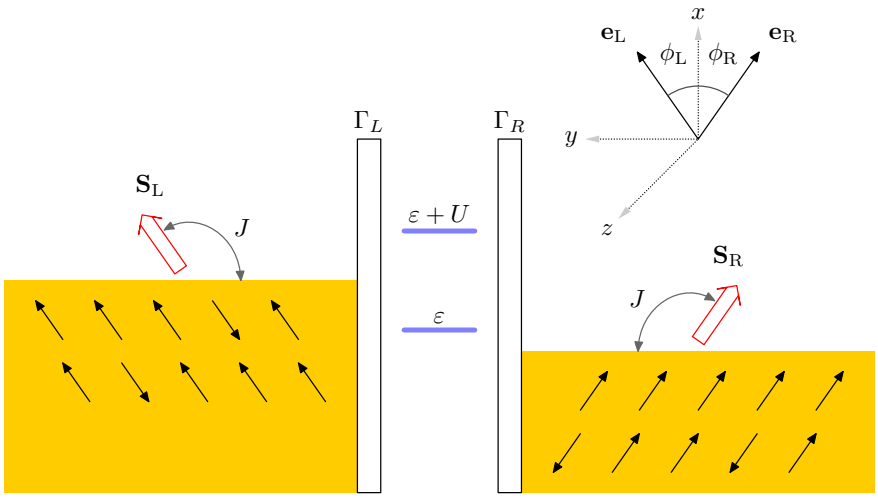

Figure 4.1: Sketch of a quantum-dot spin valve with spin wave excitations in the leads and coordinate system used.

The ferromagnetic leads are modeled as reservoirs of itinerant electrons,

$$H_{res} = \sum_{r\mathbf{k}\sigma=\pm} \varepsilon_{r\mathbf{k}} a^\dagger_{r\mathbf{k}\sigma} a_{r\mathbf{k}\sigma}. \tag{4.3}$$

Here, $a^\dagger_{r\mathbf{k}\sigma}$ denotes the creation operator for electrons in lead $r = \mathrm{L}, \mathrm{R}$ with momentum $\mathbf{k}$ and spin σ which have energy $\varepsilon_{r\mathbf{k}}$. The spin quantization axis of each lead is chosen parallel to the direction of its magnetization $\mathbf{e}_r$.

Due to the noncollinear geometry, it is convenient to quantize the spin on the dot in the direction perpendicular to the magnetizations of the leads, cf. the coordinate frame indicated in Fig. 4.1. In this case, the tunnel Hamiltonian describing the coupling between dot and leads is given by

$$H_\mathrm{tun} = \sum_{r\mathbf{k}} \frac{t_r}{\sqrt{2}} \left[a^\dagger_{r\mathbf{k}+} \left(e^{i\phi_r/2} c_\uparrow + e^{-i\phi_r/2} c_\downarrow \right) + a^\dagger_{r\mathbf{k}-} \left(-e^{i\phi_r/2} c_\uparrow + e^{-i\phi_r/2} c_\downarrow \right) \right] + \mathrm{h.c.}, \tag{4.4}$$

where ϕ_r denotes the angle enclosed between the magnetization of lead r and the x axis. It should be noted that though individual terms violate spin conservation, the total tunnel Hamiltonian is spin conserving.

Using the Holstein-Primakoff representation, the localized spins are expressed in terms of bosonic operators

$$S_{rz} = S - b^\dagger_r b_r, \tag{4.5}$$

$$S_{r+} = \left(\sqrt{2S - b^\dagger_r b_r} \right) b_r, \tag{4.6}$$

$$S_{r-} = b^\dagger_r \left(\sqrt{2S - b^\dagger_r b_r} \right). \tag{4.7}$$

Since the magnetizations are macroscopic quantities, their fluctuations will be small and hence $b^\dagger_r b_r \ll S$. We, therefore, can restrict ourselves to the leading-order terms

when expanding Eqs. (4.5)-(4.7) in $1/S$. The spins are then treated as a bosonic degree of freedom with energy ω_b, $H_{\text{spin}} = \sum_r \omega_b b_r^\dagger b_r$, corresponding to optical magnons with a single, dispersionless mode. The coupling between the localized spins and the spins of the itinerant electrons in the leads is given by

$$\begin{aligned} H_{\text{coupl}} &= -J \sum_r \mathbf{s}_r \cdot \mathbf{S}_r \\ &\approx -J \sum_{r\mathbf{k}} \Big[S \left(a_{r\mathbf{k}+}^\dagger a_{r\mathbf{k}+} - a_{r\mathbf{k}-}^\dagger a_{r\mathbf{k}-} \right) \\ &\quad + \sqrt{2S} \left(a_{r\mathbf{k}+}^\dagger a_{r\mathbf{k}-} b_r^\dagger + a_{r\mathbf{k}-}^\dagger a_{r\mathbf{k}+} b_r \right) \Big] . \end{aligned} \tag{4.8}$$

The terms in the second line are independent of the magnon number. They can be absorbed into the part of the Hamiltonian describing the lead electrons, yielding spin-dependent electron energies, $\varepsilon_{r\mathbf{k}\sigma} = \varepsilon_{r\mathbf{k}} - \sigma JS$. As a consequence, the densities of states will also acquire a spin-dependence, $\rho_{r,\sigma}(\omega)$. In the following we will refer to the electrons with greater (smaller) density of states at the Fermi energy as majority ($\sigma = +$) (minority ($\sigma = -$)) spin electrons. Since in transport only a small energy window at the Fermi energy is relevant, in the following we will take the densities of state to be independent of energy, $\rho_{r,\sigma} = \rho_{r,\sigma}(E_F)$. In this case, the tunnel matrix elements t_r can be related to the tunneling rate $\Gamma_{r\pm}$ for a majority/minority spin electron from lead r via $\Gamma_{r\pm} = 2\pi |t_r|^2 \rho_{r,\pm}$. The states of the quantum dot hence acquire a finite level width $\Gamma_r = (\Gamma_{r+} + \Gamma_{r-})/2$.

The asymmetry between majority and minority spins is then characterized by the spin polarization $p_r = (\rho_{r,+} - \rho_{r,-})/(\rho_{r,+} + \rho_{r,-})$. We note that in general for a non-constant density of states, the total number of majority spin electrons may be larger or smaller than the total number of minority spin electrons, depending on the precise form of the band structure, the size of the splitting and the position of the Fermi energy. Hence, the localized spin may point parallel or antiparallel to the majority spin direction corresponding to positive or negative values of the polarization p_r. We note that a nonconstant density of states gives rise to a modified exchange field, Eq. (4.20), see below.

The terms in the last line of Eq. (4.8) describe spin-flip interactions between the electrons and the magnons. Since our diagrammatic real-time technique requires non-interacting electrons in the reservoirs, we apply to the Hamiltonian the canonical transformation [176] $\tilde{H} = e^A H e^{-A}$ with generator

$$A = -\sum_{r\mathbf{k}} \lambda \left(a_{r\mathbf{k}+}^\dagger a_{r\mathbf{k}-} b_r^\dagger - a_{r\mathbf{k}-}^\dagger a_{r\mathbf{k}+} b_r \right) \tag{4.9}$$

where $\lambda = \sqrt{2S} J/(\omega_b + \varepsilon_{\mathbf{k}+} - \varepsilon_{\mathbf{k}-})$. Neglecting terms of order λ^2 that can be absorbed into the energies $\varepsilon_{r\mathbf{k}\sigma}$, the transformed Hamiltonian takes the form

$$\tilde{H} = H_{\text{dot}} + H_r + H_{\text{spin}} + \tilde{H}_{\text{tun}} \tag{4.10}$$

with the transformed tunneling Hamiltonian

$$\tilde{H}_{\text{tun}} = \sum_{r\mathbf{k}} \frac{t_r}{\sqrt{2}} \left[a_{r\mathbf{k}+}^\dagger \tilde{c}_{r\uparrow} + a_{r\mathbf{k}-}^\dagger \tilde{c}_{r\downarrow} \right] + \text{h.c.} \tag{4.11}$$

where

$$\tilde{c}_{r\uparrow} = \left(1 - \frac{\lambda^2}{2} b_r^\dagger b_r\right)\left(e^{i\phi_r/2} c_\uparrow + e^{-i\phi_r/2} c_\downarrow\right) - \lambda b_r^\dagger \left(-e^{i\phi_r/2} c_\uparrow + e^{-i\phi_r/2} c_\downarrow\right), \quad (4.12)$$

$$\tilde{c}_{r\downarrow} = \left(1 - \frac{\lambda^2}{2} b_r^\dagger b_r\right)\left(-e^{i\phi_r/2} c_\uparrow + e^{-i\phi_r/2} c_\downarrow\right) + \lambda b_r \left(e^{i\phi_r/2} c_\uparrow + e^{-i\phi_r/2} c_\downarrow\right) \quad (4.13)$$

In writing down the transformed tunnel Hamiltonian, Eq. (4.11), we neglected terms of order λ^2 that do not involve bosonic operators as these terms do not yield a contribution to order λ^2 in the diagrammatic expansion. The canonical transformation gives rise to new processes in the tunnel Hamiltonian. Apart from tunneling events that are already present for the ordinary quantum-dot spin valve [65], we encounter new terms in which a magnon is emitted/absorbed and the spin of the tunneling electron is flipped. Hence, the total tunnel Hamiltonian does not conserve the electron spin any longer but just the sum of electron spin and angular momentum of the magnons.

4.2 Reduced density matrix and master equation

In order to investigate the transport properties of our system, we extend the real-time diagrammatic technique introduced in Chapter 3 and adapted to systems with ferromagnetic leads in Ref. [64, 65] to include the spin-wave degrees of freedom.

After integrating out the fermionic degrees of freedom in the electrodes, we obtain an effective description of the reduced system which is characterized by the state of the quantum dot and the number of magnons in the left and right lead. The quantum dot can be either empty, occupied with a spin up or a spin down electron or doubly occupied. We denote these states as $|0\rangle$, $|\uparrow\rangle$, $|\downarrow\rangle$ and $|d\rangle$ with energies $E_0 = 0$, $E_\uparrow = E_\downarrow = \varepsilon$ and $E_d = 2\varepsilon + U$, respectively. The number of magnons is characterized by $|\mathbf{n}\rangle = |n_\mathrm{L}, n_\mathrm{R}\rangle$. The total energy of a state $|\xi\rangle = |\chi, \mathbf{n}\rangle$ is then given by $E_\xi = E_\chi + (n_\mathrm{L} + n_\mathrm{R})\omega_b$. In order to keep the Hilbert space finite-dimensional, we introduce a maximal magnon number N_max for actual computations and check that our results are independent of the cut-off value. For the parameters chosen in the analysis below, it turned out that it is sufficient to take into account at most four magnons in each lead.

As we discussed in Chapter 3, the reduced system can be described in terms of a density matrix whose elements $P_{\xi_1}^{\xi_2} = \langle\xi_2|\rho^\mathrm{red}|\xi_1\rangle$ are characterized by the states of the reduced system. The reduced density matrix obeys a generalized master equation of the form Eq. (3.17). The diagrammatic rules necessary to evaluate the kernels that enter the master equation for the system under investigation are summarized in Appendix A.1.

In the following, we will always assume the magnon energies to be much larger than the tunnel coupling, $\omega_b \gg \Gamma$. As we discussed in Section 3.3, in this case, the master equation for the matrix elements which are off-diagonal in the magnon number becomes $i(E_{\xi_2} - E_{\xi_1})P_{\xi_1}^{\xi_2} = 0$ to first order in the tunnel coupling. This implies that only matrix elements diagonal in the boson number have to be taken into account. Hence, the reduced density matrix takes a block-diagonal form $\rho^\mathrm{red} = \rho_\mathrm{dot} \otimes \rho_\mathrm{boson}$,

where each block can be written as

$$\begin{pmatrix} P_{0\mathbf{n}} & 0 & 0 & 0 \\ 0 & P_{\uparrow\mathbf{n}} & P^{\uparrow}_{\downarrow\mathbf{n}} & 0 \\ 0 & P^{\downarrow}_{\uparrow\mathbf{n}} & P_{\uparrow\mathbf{n}} & 0 \\ 0 & 0 & 0 & P_{d\mathbf{n}} \end{pmatrix}.$$

To allow for a compact notation, we write the density matrix as a vector consisting of blocks of the form $(P_{0\mathbf{n}}, P_{\uparrow\mathbf{n}}, P_{\downarrow\mathbf{n}}, P_{d\mathbf{n}}, P^{\uparrow}_{\downarrow\mathbf{n}}, P^{\downarrow}_{\uparrow\mathbf{n}})^T$. The normalization of the reduced density matrix can then be cast into the form $\mathbf{e}^T\rho^{\mathrm{red}} = 1$, where $\mathbf{e}^T$ is a vector consisting of blocks of the form $(1,1,1,1,0,0)$.

To allow an easier physical interpretation of the density matrix elements, it is convenient to express them in terms of the average dot occupations $P_{0\mathbf{n}}$, $P_{1\mathbf{n}} = P_{\uparrow\mathbf{n}} + P_{\downarrow\mathbf{n}}$ and $P_{d\mathbf{n}}$ and the average spin on the quantum dot

$$S_{x\mathbf{n}} = \frac{P^{\uparrow}_{\downarrow\mathbf{n}} + P^{\downarrow}_{\uparrow\mathbf{n}}}{2},\ S_{y\mathbf{n}} = i\frac{P^{\uparrow}_{\downarrow\mathbf{n}} - P^{\downarrow}_{\uparrow\mathbf{n}}}{2},\ S_{z\mathbf{n}} = \frac{P_{\uparrow\mathbf{n}} - P_{\downarrow\mathbf{n}}}{2} \tag{4.14}$$

in the presence of $\mathbf{n}$ magnons. The set of master equations can then be split into one describing the average charge and one describing the average spin on the dot.

The master equation for the occupation probabilities is given by

$$\frac{d}{dt}P_{\chi\mathbf{n}} = \sum_r \sum_{\mathbf{m}} \left(\sum_{\chi'} M^{(r)}_{\chi\mathbf{n},\chi'\mathbf{m}} P_{\chi'\mathbf{m}} + V^{(r)}_{\chi\mathbf{m}} \mathbf{S}_{\mathbf{m}} \cdot \mathbf{e}_r \right). \tag{4.15}$$

Here, $M^{(r)}_{\chi\mathbf{n},\chi'\mathbf{m}}$ denotes transition rates from state $\chi'\mathbf{m}$ to state $\chi\mathbf{n}$, while $V^{(r)}_{\chi\mathbf{m}}$ characterizes the dependence of the dot occupation on the accumulated spin. Their precise form is given in Appendix B.1. The sum over $\mathbf{m}$ only gives contributions if in a process involving the left (right) lead the number of magnons in the right (left) lead is kept fixed while the number of magnons in the left (right) lead changes by at most one due to the conservation of angular momentum in each tunneling event.

This restriction in the number of excited magnons is different from the case of a quantum dot coupled to a vibrational degree of freedom. In the latter case, the number of phonons that can be excited in a tunneling event is limited only by the applied bias voltage while the number of phonons that can be absorbed is only limited by the number of excited phonons [177], giving rise to a large number of conductance sidebands [143, 178, 179] as well as to a phonon distribution width that is nonperturbative in the electron-phonon coupling [177]. Furthermore, the transition rates in the vibrational case show a nontrivial dependence on the initial and final number through the Franck-Condon factors that influence the transport properties crucially, e.g., by leading to a suppression of transport for small bias voltages [143, 179].

The dot spin obeys the Bloch-type equation

$$\frac{d\mathbf{S}_{\mathbf{n}}}{dt} = \left(\frac{d\mathbf{S}_{\mathbf{n}}}{dt}\right)_{\mathrm{acc}} + \left(\frac{d\mathbf{S}_{\mathbf{n}}}{dt}\right)_{\mathrm{rel}} + \left(\frac{d\mathbf{S}_{\mathbf{n}}}{dt}\right)_{\mathrm{prec}} \tag{4.16}$$

where

$$\left(\frac{d\mathbf{S}_n}{dt}\right)_{\mathrm{acc}} = \sum_r \sum_{\mathbf{m}} \sum_{\chi} F^{(r)}_{\chi\mathbf{nm}} P_{\chi\mathbf{m}} \mathbf{e}_r, \tag{4.17}$$

$$\left(\frac{d\mathbf{S}_n}{dt}\right)_{\text{rel}} = -\sum_r G^{(r)}\mathbf{S}_n, \tag{4.18}$$

$$\left(\frac{d\mathbf{S}_\mathbf{n}}{dt}\right)_{\text{prec}} = \mathbf{S}_\mathbf{n} \times \sum_r \mathbf{B}_\mathbf{n}^{(r)}. \tag{4.19}$$

The dynamics of the dot spin is governed by three terms. The first one, Eq. (4.17), which depends only on the occupation probabilities, describes the accumulation of spin on the dot due to electrons tunneling onto the empty dot or electrons leaving the doubly occupied dot. Here, the sum over $\mathbf{m}$ is subject to the same restriction as in the master equation for the occupation probabilities. The second term, Eq. (4.18), which is proportional to the accumulated spin, describes the decay of the dot spin due to tunneling out of electrons or tunneling in with a spin opposite to the dot spin, forming a spin singlet on the dot. The precise form of the functions $F^{(r)}_{\chi\mathbf{nm}}$ and $G^{(r)}$ that enter the accumulation and relaxation term is given in Appendix B.1. Finally, the third term, Eq. (4.19), describes the precession in the exchange field generated by virtual tunneling between the dot and the leads. It is given by

$$\begin{aligned}\mathbf{B}_\mathbf{n}^{(r)} = -\mathbf{e}_r\frac{\Gamma_r}{\pi}\Bigg\{&(1-\lambda^2 n_r)p_r\left[\Phi_r(\varepsilon)-\Phi_r(\varepsilon+U)\right]\\ &+\frac{\lambda^2}{2}\Bigg[2\ln\frac{\beta W}{2\pi}-(1+p_r)(1+n_r)\Phi_r(\varepsilon-\omega_b)+(1-p_r)n_r\Phi_r(\varepsilon+\omega_b)\\ &+(1+p_r)n_r\Phi_r(\varepsilon+U-\omega_b)-(1-p_r)(1+n_r)\Phi_r(\varepsilon+U+\omega_b)\Bigg]\Bigg\},\end{aligned} \tag{4.20}$$

where $\Phi_r(x) = \operatorname{Re}\psi\left(\frac{1}{2}+i\frac{\beta(x-\mu_r)}{2\pi}\right)$, and Ψ is the digamma function. Compared to the ordinary quantum-dot spin valve [65], the exchange field contains new terms proportional to λ^2 which arise form virtual tunneling processes that emit or absorb magnons in the intermediate state. Furthermore, the terms already present in the absence of spin waves experience a magnon-number dependent renormalization $1-\lambda^2 n_r$ that has the tendency to reduce the strength of the exchange field. In Fig. 4.2 we show the exchange field as a function of the level position. The new terms give rise to side peaks and dips. As the original exchange field is rather small for small polarizations, the magnonic features tend to be more pronounced for small polarizations.

The logarithmic divergency in Eq. (4.20) that is cut off by the bandwidth of the lead electrons W (in the following, we assume $W = 100k_\mathrm{B}T$) arises as the rate for emitting and absorbing a magnon differ from each other. If the system is, e.g., in a state without magnons and the dot is singly occupied, only a spin down electron can leave the dot to the leads by a magnon-assisted process while only a spin-up electron can enter the dot in such a process. Hence, only the energy of the spin-down state is renormalized by the magnonic processes, thereby giving rise to a diverging energy shift between spin-up and spin-down electrons and hence to a diverging exchange field.

In order to take into account the finite life time of spin waves, e.g., due to scattering from phonons or electrons or due to magnon-magnon interactions, we include phenomenological relaxation terms $-\frac{1}{\tau}\left(P_{\chi\mathbf{n}} - P^{\text{eq}}_\mathbf{n}\sum_\mathbf{n} P_{\chi\mathbf{n}}\right)$ and $-\frac{1}{\tau}\left(\mathbf{S}_{\chi\mathbf{n}} - P^{\text{eq}}_\mathbf{n}\sum_\mathbf{n}\mathbf{S}_{\chi\mathbf{n}}\right)$ into the master equations (4.15) and (4.16). These terms describes a relaxation towards the equilibrium distribution of magnons $P^{\text{eq}}_n = e^{-n\omega_b/k_\mathrm{B}T_B}/(1-e^{-\omega_b/k_\mathrm{B}T_B})$ on

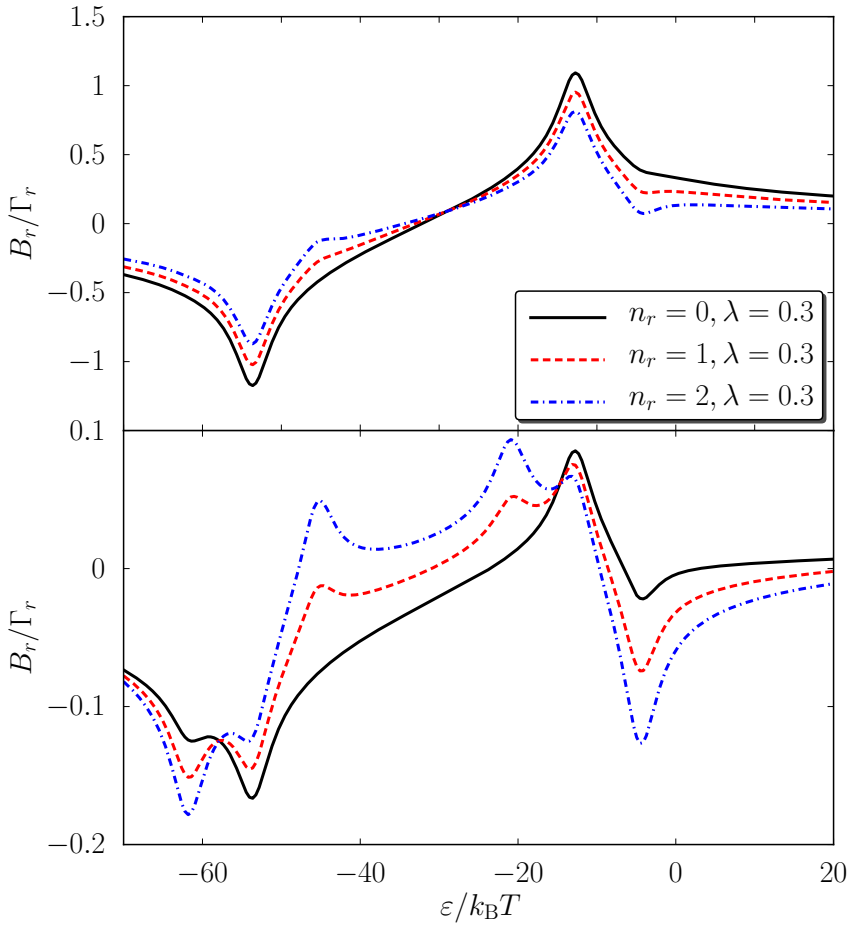

Figure 4.2: Exchange field as a function of the level position ε for $p_r = 0.9$ (upper panel) and $p_r = 0.1$ (lower panel). Other parameters are $U = 50k_\mathrm{B}T$, $\omega_B = 10k_\mathrm{B}T$.

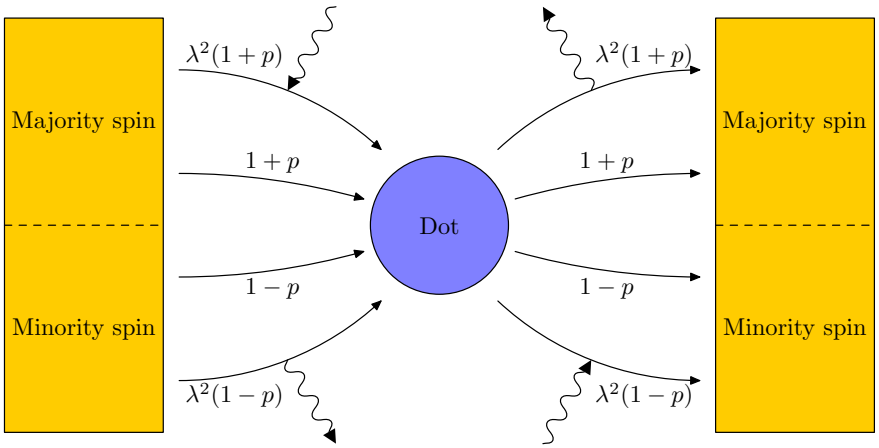

Figure 4.3: Transport processes that arise in a quantum-dot spin valve with spin wave degrees of freedom in the leads as well as their dependence on the polarization p.

a time scale τ. We allow for the most general case of a magnon temperature T_B that differs from the electron temperature T.

Besides making our model more realistic, the relaxation terms also ensure that the magnon number in the drain lead remains finite. While the emission of a magnon when tunneling out of the dot transfers the electron from minority to majority spin and thus gives rise to a rate proportional to $1+p_r$, the absorption flips the spin in the opposite direction and therefore yields a rate proportional to $1-p_r$. Hence, without any relaxation mechanism, the number of magnons would grow without bound in the drain lead.

4.3 Results

In this section, we discuss our results for the current, conductance and current noise of the quantum-dot spin valve in the presence of spin waves. Unless stated otherwise, we assume a symmetric system with equal polarizations for both leads, $p_\mathrm{L} = p_\mathrm{R} \equiv p$, and equal tunnel couplings, $\Gamma_\mathrm{L} = \Gamma_\mathrm{R} \equiv \Gamma/2$. Furthermore, we assume that the bias voltage is applied symmetrically, $V_\mathrm{L} = -V_\mathrm{R} = V/2$, too.

4.3.1 Transport processes

Before discussing the transport properties in detail, we give an overview of the different transport processes that can occur in the presence of spin waves in the leads. In Fig. 4.3, we show all transport processes that can arise. As for the ordinary quantum-dot spin valve, majority (minority) spin electrons can tunnel from the source onto the dot as well as from the dot into the drain lead. The corresponding rates are given by $(1 \pm p)\Gamma/4$.

Additionally, we now have processes that involve the emission/absorption of magnons. For example, a majority spin from the source can flip its spin by absorbing a magnon to become a minority spin that ends up on the quantum dot. Hence, the rate for this process is given by $\lambda^2 n_\mathrm{L}(1+p)\Gamma/4$. Similarly, a minority spin electron can emit a

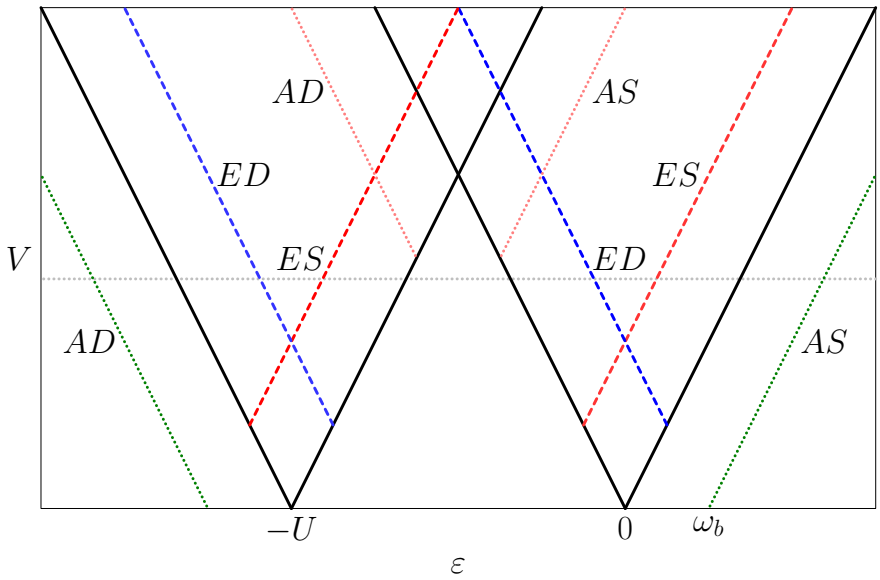

Figure 4.4: Schematic of the differential conductance in the $\varepsilon - V$ plane. The labels at the conductance lines indicate whether a magnon is emitted (E) or absorbed (A) in the source (S) or drain (D) electrode. The grey dashed horizontal line marks the position of the cuts shown in Fig. 4.5.

magnon to become a majority spin that tunnels onto the dot. Here, the corresponding rate is given by $\lambda^2(1+n_\mathrm{L})(1-p)\Gamma/4$.

Furthermore, there are two processes involving the magnons in the drain lead. Now, a minority spin of the drain can leave to the dot, emit a magnon and end up as a majority spin. The rate for this process is given by $\lambda^2(1+n_\mathrm{R})(1+p)\Gamma/4$. The opposite process which starts with a majority spin, absorbs a magnon and ends up as a minority spin finally has a rate given by $\lambda^2 n_\mathrm{R}(1-p)\Gamma/4$.

Hence, we find that for a given spin on the dot the magnonic processes have the opposite dependence on the polarization as the normal processes. We will show in the following how this unconventional polarization dependence gives rise to a number of interesting transport properties.

4.3.2 Magnon-assisted tunneling

We now turn to the discussion of the differential conductance $G = dI/dV$ for arbitrary bias and gate voltages. In Fig. 4.4, we schematically show the conductance for collinear magnetizations. [1] In addition to the resonances of the dot level with the Fermi energy of the left and right lead which are marked by the thick black lines, a number of sidebands related to the emission and absorption of magnons occur. At the red dashed lines labeled ES, the tunneling electrons bcome able to emit magnons in the source lead, while at the blue dashed lines ED the emission of magnons in the drain lead becomes energetically possible. The dashed green lines indicate where transport through the

[1] For noncollinear magnetizations, a broad region of negative differential conductance arises [65] on which the fingerprints of the magnons are superimposed. As there are no new effects compared to the collinear case, we do not discuss the noncollinear geometry here any further.

dot becomes possible by absorbing magnons to enter the empty dot with both level above the two Fermi energies (AS) or to leave the doubly occupied dot with both levels below the two Fermi energies (AD). Furthermore, there are additional peaks marked by the orange dotted lines AS and AD at which it becomes possible to absorb a magnon in order to enter the doubly occupied state which otherwise would have been out of reach energetically. Conductance sidebands inside the Coulomb blockade regime are absent because there a spin accumulates on the dot in such a way as to suppress all magnonic processes.

As discussed above, the different magnonic processes depend on the polarization of the leads as $1+p$ or $1-p$ depending on whether they involve a majority or minority spin electron in the lead. As a consequence, the different sidebands will have different strengths. In particular, while line ES is suppressed with increasing the polarization, line ED is increased. Hence, the conductance map no longer exhibits particle-hole symmetry $\varepsilon \to U-\varepsilon$ due to the presence of the magnons.

In Section 4.1 we saw that the polarization of the leads can take either sign: a positive (negative) sign indicates that the majority spins of the carriers at the Fermi energy are parallel (antiparallel) to the direction of the macroscopic magnetic moment. We now discuss how the conductance plot changes for the different combinations of positive and negative polarizations in the two leads. The case of two negative polarizations is related to the case of two positive ones by the transformation $\varepsilon \to U-\varepsilon$. This maps all lines involving the emission of magnons onto lines involving the absorption of magnons and vice versa and therefore exchanges the factors $1+p$ and $1-p$ in the magnonic rates. For polarizations of opposite signs, the conductance plot becomes particle-hole symmetric. However, now the strength of the magnonic side bands depends on the direction of current flow. While they are suppressed for one direction by $1-p$ they are enhanced by $1+p$ in the other direction. In the rest of this work, we will restrict ourselves to the case in which all polarizations are positive. All other cases can be related to this one by the above symmetry considerations.

We now turn to the discussion of the conductance at fixed bias voltage shown in Fig. 4.5, corresponding to a cut along the dotted horizontal line in Fig. 4.4. In the upper panel of Fig. 4.5, we show the differential conductance for parallel magnetizations as a function of the level position for a given bias voltage. For small polarizations, there are four large peaks at which the dot levels are in resonance with either the left or right Fermi energy, corresponding to the thick black lines in Fig. 4.4. These are accompanied by much smaller conductance peaks at distances $\pm\omega_b$. From left to right, these correspond to lines AD, ED, ES, ED, ES and AS in Fig. 4.4. The lines corresponding to the absorption of magnons (AS and AD) are only present for sufficiently high magnon temperatures, otherwise the number of magnons in the leads is too small to make these side peaks visible.

For large polarizations, there are two new effects. On the one hand, the two side peaks associated with lines labeled ES are suppressed by $1-p$ and become invisible. On the other hand, we find that the side peak corresponding to left line ED in Fig. 4.4 shows a strong negative differential conductance. This is due to the formation of a trapping state. A spin down electron can leave the doubly occupied dot by exciting a magnon in the drain lead leaving the dot in the spin up state. This blocks further transport as tunneling in of an electron is suppressed by the small density of states for spin down electrons in the source lead.

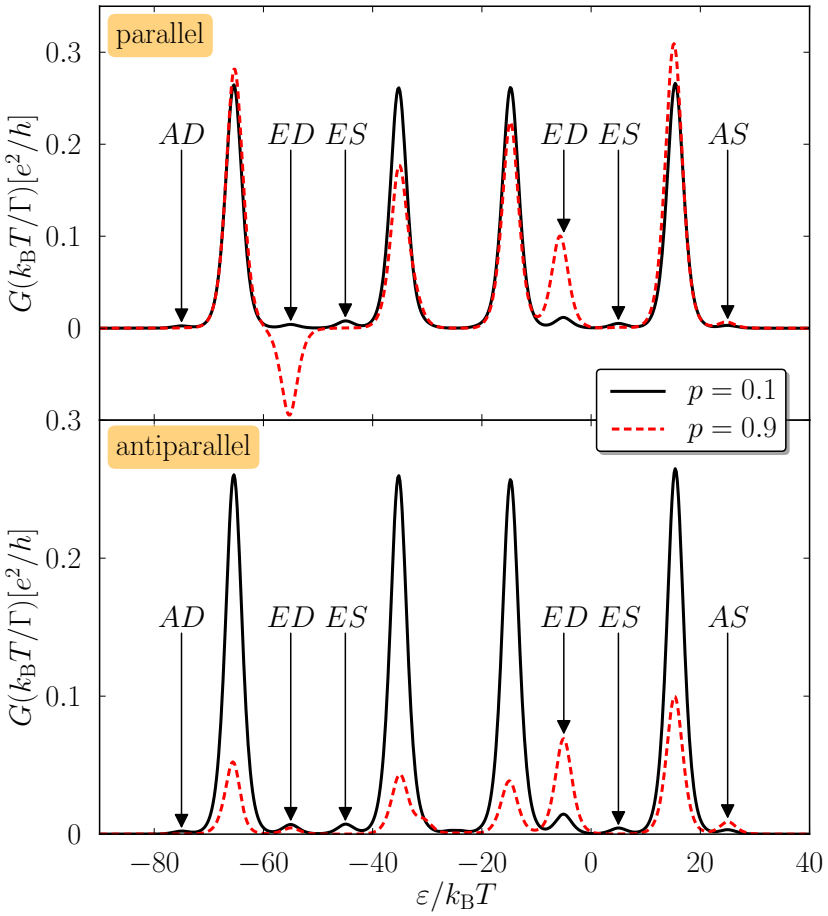

Figure 4.5: Differential conductance as a function of the level position for $V = 30k_{\mathrm{B}}T$, $U = 50k_{\mathrm{B}}T$, $\omega_B = 10k_{\mathrm{B}}T$, $\Gamma_{\mathrm{L}} = \Gamma_{\mathrm{R}}$, $\tau = 2/\Gamma$, $\lambda = 0.3$, $T_B = 5T$ for small and large polarizations. In the upper panel, we show the case of parallel magnetizations, while in the lower panel they are chosen to be antiparallel. As in Fig. 4.4, the labels of the side peaks indicate the emission (E) and absorption(E) of magnons in source (S) and drain (D) lead.

We now turn to the case of antiparallel magnetizations. For small polarizations, the conductance resembles the one for the parallel configuration because the effects of the finite polarization are only weak. For large polarizations, there is a large spin accumulation on the dot which is antiparallel to the magnetization of the drain lead. When transport takes place through the states $|0\rangle$ and $|1\rangle$ only, the rate for normal tunneling into the drain is suppressed by $1-p$ while the rate for tunneling via a spin flip is proportional to $\lambda^2(1+p)$. Hence, for large polarizations and not too small couplings to the magnons, the side peaks can dominate over the main peaks. On the other hand, for transport through the states $|1\rangle$ and $|d\rangle$, the bottleneck is given by the tunneling in of electron. This bottleneck cannot be overcome by magnonic processes. Hence, we do not find large side peaks in this case.

In summary, this means that for large polarizations the magnons tend to decrease the current for transport through singly and doubly occupied dot in the parallel configuration while they tend to increase the current for transport through the empty and singly occupied dot for antiparallel magnetizations. As a consequence, the tunnel magnetoresistance will be reduced by the magnons for all transport regimes.

4.3.3 Nonequilibrium magnon distribution

As the tunneling processes in the quantum-dot spin valve can emit and absorb magnons, they will give rise to a nonequilibrium magnon distribution in the source and drain lead. As we discussed in Section 4.3.1, the rate for absorbing a magnon in the source lead is enhanced compared to the rate for emitting a magnon. Hence, the average magnon number in the source will be reduced compared to the equilibrium distribution. For the drain lead, the situation is reversed. Here, the rate for emitting a magnon is enhanced resulting in an increased magnon number compared to equilibrium. In Fig. 4.6 we plot the difference between the average magnon number in the source and drain lead as a function of gate and bias voltage. We find that indeed the number of magnons in the drain lead is larger than the one in the source lead. For parallel magnetizations, this effect occurs for all gate voltages, while for antiparallel configurations the effect occurs only for transport through the states $|0\rangle$ and $|1\rangle$ as only in this case the magnons can help to overcome the spin blockade on the dot. As they do this very efficiently, the nonequilibrium effects are more pronounced here compared to the parallel configuration giving rise to a larger deviation between the average magnon number in source and drain.

4.3.4 Magnon-driven electron transport

In the following, we show how an asymmetric coupling to the magnons in the left and right lead together with a breaking of detailed balance, $W_{\xi\xi'} = e^{\beta(E_\xi - E_{\xi'})}W_{\xi'\xi}$, e.g., by different equilibrium temperatures for the magnons and electrons, $T_\mathrm{B} \neq T$, can give rise to a magnon-assisted current at zero bias voltage. Such an effect occurs quite generally when the system couples asymmetrically to external fields and breaks detailed balance [93, 180]. Experimentally, this mechanism has been realized by coupling microwaves to the gate electrode defining a quantum dot in a two-dimensional electron gas [181–184] and in a carbon nanotube [185] giving rise to photon-assisted tunneling.

For the quantum-dot spin valve, there are different ways to achieve an asymmetric

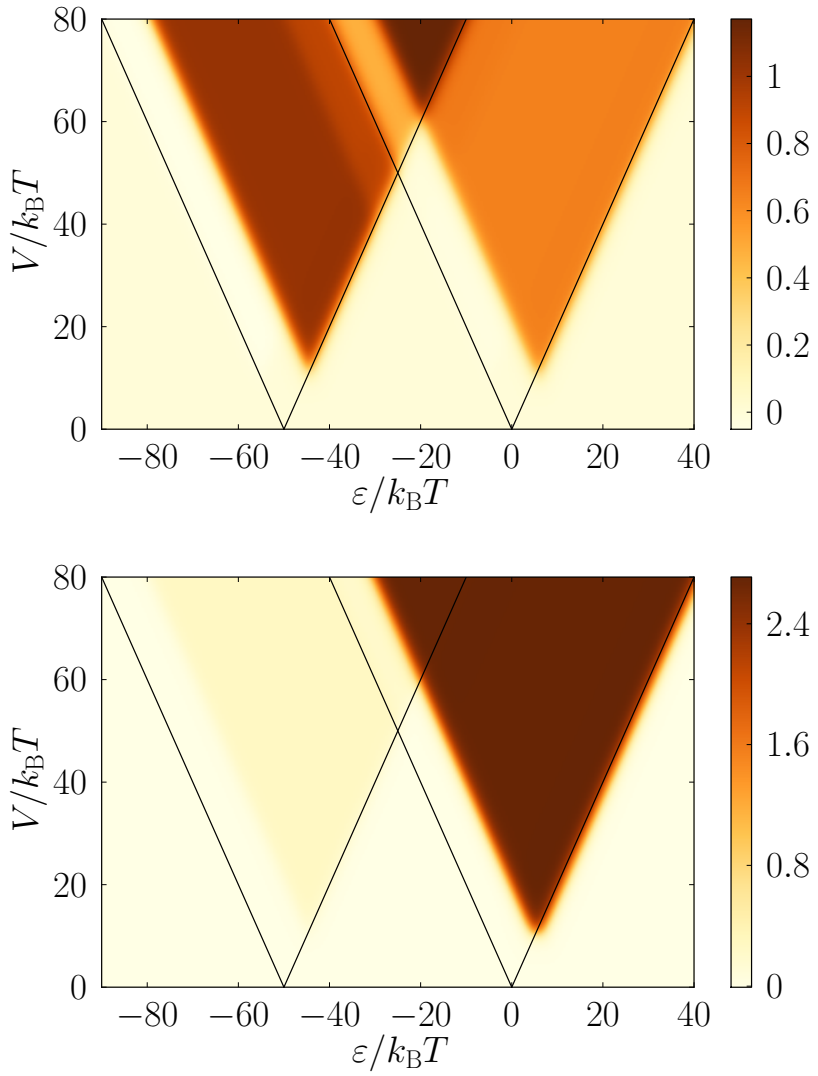

Figure 4.6: Difference between the average number of magnons in the source and drain lead in the parallel (upper panel) and antiparallel (lower panel) configuration for $\tau = 100/\Gamma$, $p = 0.9$ and $T_B = T$. Other parameters are the same as in Fig. 4.5.

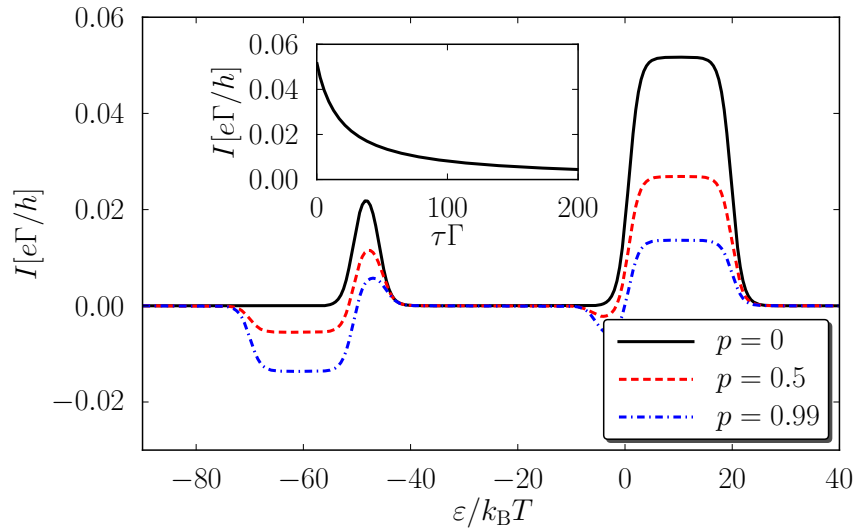

Figure 4.7: Current at zero bias voltage vs. level position for $U = 50k_\mathrm{B}T$, $\omega = 20k_\mathrm{B}T$, $\Gamma_\mathrm{L} = \Gamma_\mathrm{R}$, $\tau = 1/\Gamma$, $\lambda = 1/3$, $T_B = 10T$ at different polarizations. Inset: Increased relaxation time leads to a reduction of the magnon-driven current (shown here the peak value at $\varepsilon = 10k_\mathrm{B}T$) since it allows a stronger cooling of the magnons.

coupling to the magnonic degrees of freedom. We can either choose asymmetric tunnel couplings, $\Gamma_L \neq \Gamma_R$, different couplings to the spin waves λ_r or different polarizations p_r. In the following, we choose a system with one ferromagnetic and one normal lead, i.e., we have magnons only in the left lead and $p_\mathrm{R} = 0$. In order to violate detailed balance, we choose the equilibrium distribution of the magnons to have a larger temperature than the electrons in the leads. We note that to describe magnon-assisted tunneling, we do not have to keep track of the magnon numbers in the leads explicitly. Instead, we could also integrate out the magnons and described them as an additional bath with temperature T_B.

In Fig. 4.7, we show the magnon-assisted current for vanishing transport voltage as a function of level position for different polarizations. For $0 < \varepsilon < \omega_b$, a completely spin-polarized current flows from the ferromagnet into the normal lead. A spin down electron in the ferromagnet can absorb a magnon and tunnel onto the empty dot. Subsequently, the electron can leave the dot either into the ferromagnet or into the normal metal giving rise to a net current into the normal metal. Increasing the polarization enhances the probability of the spin-flip processes that populate the quantum dot. Furthermore, the tunneling rates for the spin-flipped electron back into the ferromagnet are decreased. Hence, with increasing the polarization of the ferromagnet we find an increased magnon-assisted current.

Similarly, for $-U - \omega_b < \varepsilon < -U$, a completely spin-polarized current flows from the normal lead into the ferromagnet. In this case, a spin up electron can leave the quantum dot into the ferromagnet by absorbing a magnon. Afterward, electrons from the left as well as the right lead can tunnel onto the dot, yielding a net current from the normal to the ferromagnetic lead. Since the rate for the absorption processes

now is proportional to $1 - p$, these processes become strongly suppressed for large polarizations.

In addition to these current plateaus whose width scales with the magnon energy, there are additional peaks at $\varepsilon = 0$ and $\varepsilon = -U$ whose width is given by the electron temperature. They occur since at resonance with the leads, the system may flip the spin on the quantum dot which tends to align as to inhibit magnon-absorption processes, thereby making the processes described above possible again and yielding a finite current.

As just illuminated, the key ingredient to the zero-bias current at $T_\mathrm{B} > T$ is the absorption of magnons (similarly, for $T_\mathrm{B} < T$ it would be the emission of magnons). This explains why the height of the current plateaus scales linearly with the average number of magnons. Furthermore, it explains why the current is reduced when the relaxation time is increased (see inset of Fig. 4.7). In this case, the system absorbs magnons in the processes discussed above. Since it takes more time to relax to the equilibrium magnon distribution now, the average number of magnons is reduced and therefore also the current is reduced.

If we compare our results for the magnon-driven current to the case of a current driven by photon-assisted tunneling, we find that although the basic mechanism of absorbing bosons to gain energy is the same in both cases, there are nevertheless some striking differences. First, in contrast to the photon case, there are no processes which involve the absorption of more than one magnon which is a result of angular momentum conservation during tunneling, cf. the discussion in Section 4.2. Second, while the photons drive an unpolarized current, the magnons yield a *fully* spin-polarized current since in absorption processes they couple only to minority spins. This also leads to a breaking of particle-hole symmetry for finite values of p_L.

4.3.5 Current noise

So far we discussed the current and conductance of a quantum-dot spin valve with spin wave degrees of freedom. We now turn to the discussion of the current noise which can provide additional information about the transport processes occurring in the system.

Zero-frequency noise

We start with the discussion of the zero-frequency noise. As shown in Fig. 4.8, where we plot the zero-frequency Fano factor $F(\omega = 0) = S(\omega = 0)/(2eI)$ as a function of the level position, for sufficiently high polarizations, a quantum dot coupled to ferromagnetic leads with parallel magnetizations will exhibit super-Poissonian Fano factors in the regime where only two charge states of the dot contribute to transport. This is due to a dynamical spin blockade [67, 96–102, 186], where minority spin electrons block transport due to their longer dwell time on the dot. Thereby, they chop the current into bunches of majority spin electrons.

If the excitation of spin waves is energetically possible, the Fano factor still remains super-Poissonian. However, it is significantly reduced when transport takes place through the states $|0\rangle$ and $|1\rangle$ (right plateau in Fig. 4.8) while it is slightly increased for transport through the states $|1\rangle$ and $|d\rangle$ (left plateau in Fig. 4.8). The reduction of the Fano factor on the right plateau can be understood qualitatively by

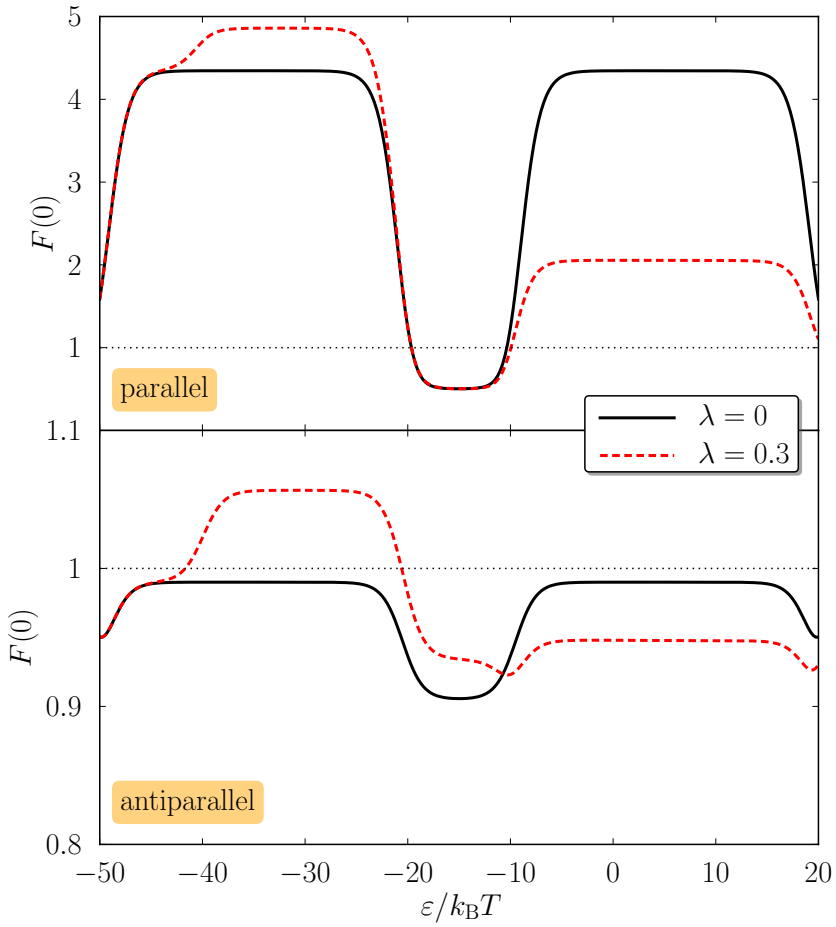

Figure 4.8: Fano factor as a function of the level position for parallel (upper panel) and antiparallel (lower panel) magnetizations. In both cases the Fano factor can be increased or decreased by the coupling to the magnons. Parameters are $V = 40k_BT$, $U = 50k_BT$, $\omega_b = 10k_BT$, $\Gamma_L = \Gamma_R$, $p = 0.9$, $\tau = 2/\Gamma$ and $T_B = T$.

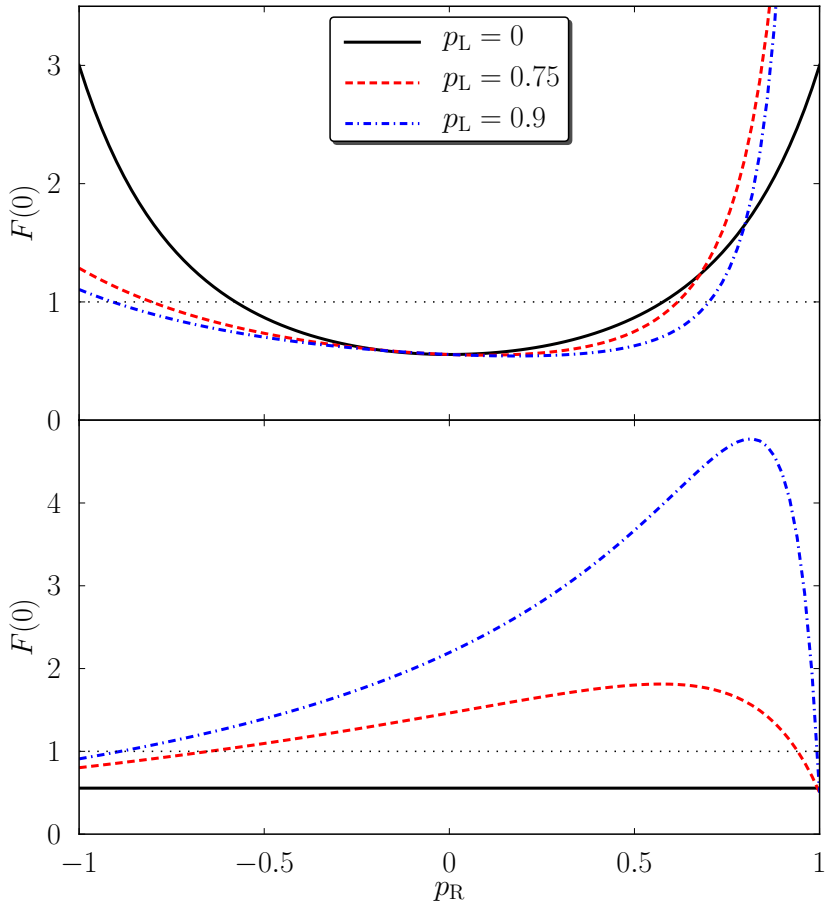

Figure 4.9: Zero-frequency Fano factor for a quantum dot symmetrically coupled to collinear magnetized leads as a function of the polarization of the right lead for different values of the polarization of the left lead. In the upper panel, transport takes place through the empty and singly occupied dot only, while in the lower panel, it takes place through the singly and doubly occupied dot only.

taking into account that the emission of a magnon in the drain lead gives the possibility for a minority spin to leave the dot. Therefore, magnonic processes reduce the waiting time between bunches of majority spin electrons and reduce the Fano factor in consequence. On the left plateau, due to the magnonic processes, there are now two ways to get into the blocking state. Either a spin down electron tunnels to the drain in a normal tunneling event or it does so in a spin-flip process by exciting a spin wave. Hence, the bunching effect becomes stronger in this region and the Fano factor is increased.

In order to gain a more quantitative understanding of the influence of magnons on the Fano factor, we define an effective polarization of the leads which takes into account the magnonic processes. As the ratio between the rates for transferring a spin-up electron from the dot into the lead and the rate for transferring any electron from the dot to the lead equals $(1+p)/2$ in the absence of magnons, we define

$$\frac{1+p_{\mathrm{L,eff}}}{2} = \frac{W_{\uparrow n_\mathrm{L} n_\mathrm{R},0 n_\mathrm{L} n_\mathrm{R}} + W_{\uparrow n_\mathrm{L}+1 n_\mathrm{R},0 n_\mathrm{L} n_\mathrm{R}}}{W_{\uparrow n_\mathrm{L} n_\mathrm{R},0 n_\mathrm{L} n_\mathrm{R}} + W_{\downarrow n_\mathrm{L} n_\mathrm{R},0 n_\mathrm{L} n_\mathrm{R}} + W_{\uparrow n_\mathrm{L}+1 n_\mathrm{R},0 n_\mathrm{L} n_\mathrm{R}} + W_{\downarrow n_\mathrm{L}-1 n_\mathrm{R},0 n_\mathrm{L} n_\mathrm{R}}}, \tag{4.21}$$

$$\frac{1+p_{\mathrm{R,eff}}}{2} = \frac{W_{0 n_\mathrm{L} n_\mathrm{R},\uparrow n_\mathrm{L} n_\mathrm{R}} + W_{0 n_\mathrm{L} n_\mathrm{R}-1,\uparrow n_\mathrm{L} n_\mathrm{R}}}{W_{0 n_\mathrm{L} n_\mathrm{R},\uparrow n_\mathrm{L} n_\mathrm{R}} + W_{0 n_\mathrm{L} n_\mathrm{R},\downarrow n_\mathrm{L} n_\mathrm{R}} + W_{0 n_\mathrm{L} n_\mathrm{R}-1,\uparrow n_\mathrm{L} n_\mathrm{R}} + W_{0 n_\mathrm{L} n_\mathrm{R}+1,\downarrow n_\mathrm{L} n_\mathrm{R}}}. \tag{4.22}$$

In the above formula, we take for the number of magnons in the leads the average magnon number found from the solution of the master equation.

Hence, the system with spin waves can be interpreted as a quantum dot coupled to ferromagnetic leads with different polarizations p_L and p_R (Note that here different signs of p_L and p_R correspond to antiparallel magnetizations and are *not* related to the negative polarizations discussed in Section 4.1). For such a system, the Fano factor can be computed analytically and is given by

$$F(0) = \frac{(1-2p_\mathrm{L}p_\mathrm{R}+p_\mathrm{R}^2)(5+2p_\mathrm{L}p_\mathrm{R}+p_\mathrm{R}^2)}{(3-2p_\mathrm{L}p_\mathrm{R}-p_\mathrm{R}^2)^2} \tag{4.23}$$

on the right plateau. On the left plateau, the same expression holds with p_L and p_R exchanged. In Fig. 4.9, we show the Fano factor as a function of p_R for various values of p_L in both transport regions. It is interesting to note that for large polarizations, the Fano factor depends quite sensitively on the precise polarization value such that the spin waves can significantly alter the Fano factor. Furthermore, the behavior on the two plateaus is completely different.

Using the picture of effective polarizations, we find that for the parameters of Fig. 4.8 where due to $\omega_b \gg T_\mathrm{B}$ and $\tau \sim 1/\Gamma$ the average number of magnons is nearly vanishing, we have $p_{\mathrm{L,eff}} = 0.90$ and $p_{\mathrm{R,eff}} = 0.83$. According to Eq. (4.23), this yields $F(0) = 2.1$ for the right plateau in good agreement with the numerically obtained value. Similarly, by exchanging p_L and p_R in Eq. (4.23), we find $F(0) = 4.8$ for the left plateau, which is also in good agreement with the full calculation.

In the antiparallel case, shown in the lower panel of Fig. 4.8, the zero-frequency Fano factor tends to unity for large polarizations without magnons. In this case, an electron leaving the dot to the drain lead will be easily replaced by another majority electron from the source lead which then blocks transport for a long time. Hence, the tunneling

out events become uncorrelated and the Fano factor Poissonian. As in the case of parallel magnetizations, the presence of magnons will result in an effective polarization of the drain smaller than the true polarization. As can be read off from Fig. 4.9, this results in a reduced, sub-Poissonian Fano factor for the right plateau, while it leads to an increased, slightly super-Poissonian Fano factor for the left plateau. For transport at the right plateau, the magnons allow the spin up electron on the quantum dot to leave to the drain lead by flipping its spin. This reduces the waiting times between tunneling events to the drain and therefore makes the Fano factor sub-Poissonian. On the other hand, at the left plateau, after a spin-up electron has left the dot by emitting a magnon in the drain, another spin up electron will enter the dot. In the next step, this scheme will either be repeated or a spin down electron will leave the dot, resulting in the spin-blockaded state. Hence, the magnons can initiate minibunches that lead to slightly super-Poissonian Fano factors.

Since for perpendicular magnetizations, where the Coulomb plateaus become modulated due to the influence of the exchange field [67], one does not find any new effects beside the already discussed reduction of the Fano factor for the right and an increase for the left plateau, we do not discuss this case here further.

Finite-frequency noise

We finally turn to the discussion of the finite-frequency Fano factor $F(\omega)$ for frequencies comparable to the tunnel couplings, $\omega \lesssim \Gamma$. As was discussed in Ref. [67], in contrast to the average current which is only sensitive to the average spin on the dot, the finite-frequency current noise provides more direct access to the spin dynamics on the quantum dot. In the following, we discuss how the frequency-dependent Fano factor can be used to detect the magnonic contributions to the exchange field. The exchange field can only give rise to a precession of an accumulated spin if the exchange field and spin are not collinear to each other. Since the exchange-field contribution of the each lead is parallel to its magnetization direction, the leads magnetization should not be collinear. To be specific, we choose perpendicularly magnetized leads in the following.

In Fig. 4.10, we show the frequency-dependent Fano factor for two different bias voltages and different coupling strengths to the spin waves. For a vanishing coupling to the magnons, the Fano factor exhibits a peak at the Larmor frequency associated with the exchange field. As the strength of the coupling to the spin waves is increased, the height of the resonance peak is reduced. Furthermore, the position of the resonance peak is shifted as the strength of the exchange field is altered. Since the magnonic contributions to the exchange field have a different bias dependence as the standard contributions [65], the magnitude and sign of the Larmor frequency shift depends on the bias voltage. Hence, measuring the frequency-dependent Fano factor as a function of bias voltage can provide experimental access to the magnonic exchange field contributions.

4.4 Summary

We investigated the influence of spin waves, excited in the electrodes, on transport through a quantum-dot spin valve. We found that the emission and absorption of spin waves gives rise to conductance sidebands whose strength depends on the polarization

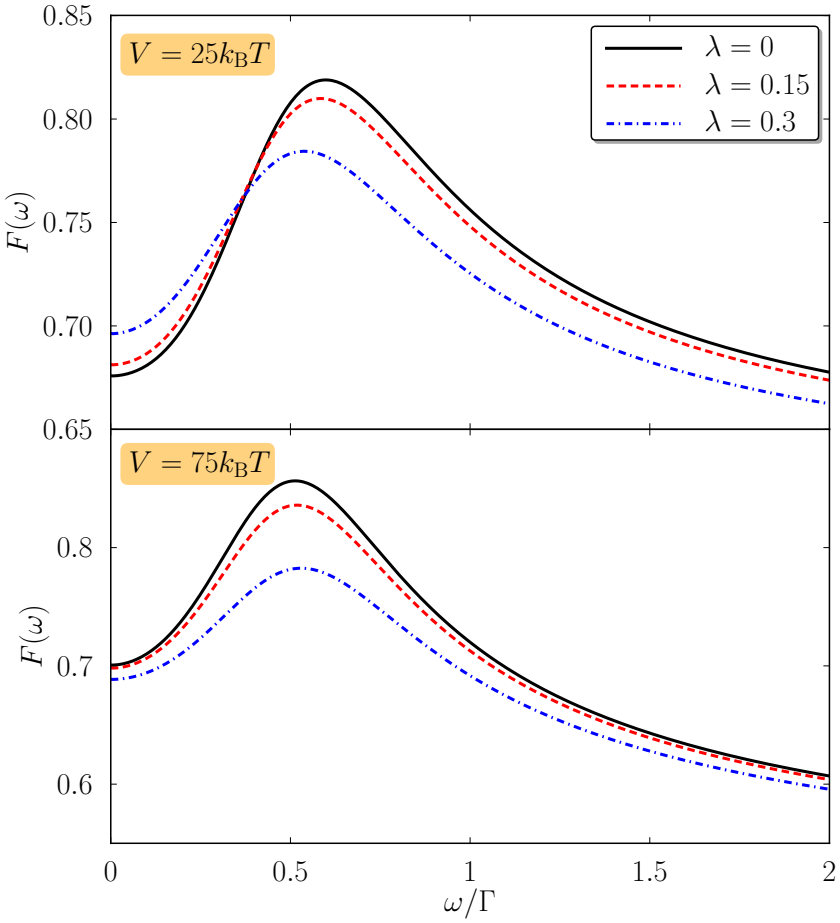

Figure 4.10: Frequency-dependent Fano factor for perpendicular magnetizations for $V = 25k_BT$ (upper panel) and $V = 75k_BT$ (lower panel). Other parameters are $U = 50k_BT$, $\varepsilon = 10k_BT$, $\omega_B = 10k_BT$, $\Gamma_L = 2\Gamma_R$, $\tau = 1/\Gamma_L$, $p = 0.8$, $T_B = T$.

and the relative orientation of the magnetizations. We furthermore found that the transport through the system gives rise to a nonequilibrium occupation of the magnons with an increased magnon number in the drain and a decreased magnon number in the source lead. For a system that couples asymmetrically to the magnons in the source and drain, we showed how magnon-assisted tunneling leads to a completely spin-polarized current without an applied bias voltage. Finally, we studied the current noise. We found that the magnons can increase as well as decrease the Fano factor depending on the dot states involved in transport. Additionally, we showed that the frequency-dependent Fano factor provides access to the magnonic contributions to the exchange field.

5 Quantum-dot spin valves with magnetic impurities

In this chapter, we discuss transport through a quantum-dot spin valve that contains magnetic impurities either embedded in one of the tunnel barriers or localized on the quantum dot.

We first consider transport through a quantum-dot spin valve with a magnetic impurity embedded in one of the tunnel barriers, as realized, e.g., by a magnetic atom. Transport through single tunnel barriers containing a magnetic atom or a single molecular magnet have been investigated extensively in the recent past, both from a theoretical [187–195] as well as from an experimental [133, 196–201] point of view. It was shown that the steps observed in the differential conductance can be used to extract magnetic properties like anisotropies of the atom spin [133, 190–193]. Furthermore, the influence of nonequilibrium spin occupations was discussed [195], explaining the overshooting observed at the conductance steps in experiment and predicting a super-Poissonian current noise. The absence of certain nonequilibrium features in turn was interpreted in terms of an anisotropic relaxation channel, cf. also the discussion in Chapter 6. For systems with magnetic electrodes, the possibility to switch the embedded spin by the spin-polarized current through the barrier was predicted theoretically [188, 189, 194] and observed in experiment [201].

Here, we investigate the influence of a magnetic impurity embedded in one of the tunnel barriers of a quantum-dot spin valve, giving rise to a number of interesting phenomena. In a single tunnel barrier, interference between direct and exchange tunneling only plays a role for ferromagnetic electrodes or higher-order transport [187, 194, 201, 202]. We find that in the quantum-dot system, interference effects already play a role for nonmagnetic electrodes and lowest order in the tunnel coupling. We furthermore demonstrate how the Coulomb energy of the quantum dot can help to perform spectroscopy on the embedded spin. If the excitation energy between the ground state and the first excited state is larger than any other excitation energy, in a single tunnel barrier, one can only measure this first excitation energy. For the quantum-dot system, we find that all other excitation energies can be studied as well when additional charge states of the dot start to contribute to transport through the system. Additionally, we point out a nontrivial interplay between the switching of the impurity spin by the spin-polarized current, the spin accumulation on the quantum dot and the current flowing through the system. Finally, we discuss the sensitivity of the exchange field to the state of the impurity spin and its influence on the current and frequency-dependent Fano factor for noncollinear magnetizations.

The second case that we consider in this chapter consists of an $S = 1/2$ impurity that is localized on the quantum dot and exchange coupled to the electron spin on the dot. Such a model can serve to describe different systems.

First, it can describe transport through a quantum dot that is doped with a magnetic

atom. Transport through a quantum dot doped with a single manganese atom has already been studied theoretically. It was shown how the frequency-dependent shot noise can reveal the spin relaxation times [203]. Furthermore, the electrical control of the manganese spin state as well as the back action of the spin state on transport have been investigated in the absence of Coulomb interaction in the quantum dot [204].

Our model can also serve as a simplistic model of transport through a single molecular magnet. Such systems have already been investigated using more realistic models with a larger, anisotropic impurity spin in the presence of nonmagnetic or collinearly magnetized electrodes. Ways to write and read out the spin state of the molecule have been explored [102, 205]. Furthermore, it was shown how spin transitions and quantum tunneling of magnetization manifest themselves in the differential conductance [206–208]. In addition, the occurrence of a Kondo effect due to quantum tunneling of magnetization has been discussed [209–211].

Finally, our model can be used to describe the coupling of the electron spin on the dot to a nuclear spin via the hyperfine interaction. In general, such a coupling is disadvantageous as it leads to decoherence of the electron spin and therefore can lift, e.g., the Pauli spin blockade in a double quantum dot [212–215]. However, it can also be used to dynamically polarize the nuclear spins in the quantum dot which in turn may be used to control and manipulate the electron spin [216–220].

Transport through a quantum dot with a side-coupled spin 1/2 was discussed in Ref. [221] for the case of nonmagnetic electrodes. It was shown how to extract the system parameters such as the exchange couplings, the g factors and spin relaxation times from measurements of the current and Fano factor.

The case of noncollinearly magnetized ferromagnetic electrodes was recently investigated by Baumgärtel et al.[222] for a large ferromagnetic exchange interaction between the electron and impurity spin. It was shown that an $S = 1$ spin triplet forms on the dot whose description not only requires a spin dipole moment but in addition also needs spin quadrupole moments.

Here, we focus on the opposite regime of small exchange interaction between the impurity and electron spin. This situation is particularly suited for the description of the weak hyperfine interaction. We discuss how the frequency-dependent Fano factor can be used to experimentally access the strength of the exchange coupling for large and small external magnetic fields. Furthermore, for the case of a weak external magnetic field, we show how the exchange field acting on the electron spin gives rise to a highly nontrivial spin dynamics that manifests itself in the frequency-dependent Fano factor.

This chapter is organized as follows. In Section 5.1, we present the models that describe a magnetic impurity localized in the tunnel barrier and on the dot, respectively. We discuss the form of the reduced density matrix of the quantum dot system and the generalized master equation it obeys for the two systems under investigation in Section 5.2. Our results for the transport properties are presented in Section 5.3 for an impurity in the barrier and in Section 5.4 for an impurity on the dot. Finally, we summarize this chapter in Section 5.5. The material presented in this chapter has previously been published in Ref. [223].

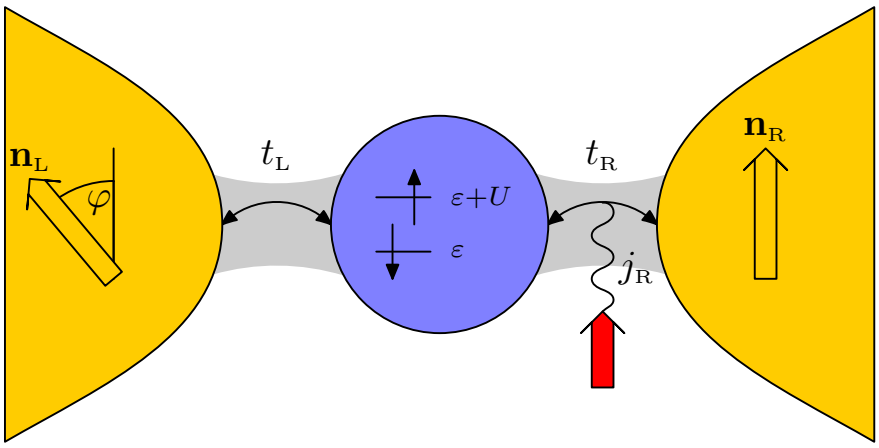

Figure 5.1: Schematic of a quantum-dot spin valve with a magnetic impurity localized in the right tunnel barrier.

5.1 Model

In this chapter, we are going to consider transport through a quantum-dot spin valve that contains additional magnetic impurities which are localized either in the tunnel barrier or on the quantum dot itself. In the following, we are going to discuss the Hamiltonians for these two cases, respectively.

5.1.1 Model A: Impurity in the barrier

Our model A, which is schematically shown in Fig. 5.1, consists of a quantum-dot spin valve with an impurity embedded in the right tunnel barrier. In this case, the Hamiltonian can be written as the sum of four terms describing the two electrodes, the quantum dot, the spin and the tunneling between dot and lead,

$$H = \sum_{r=\mathrm{L,R}} H_r + H_\mathrm{dot} + H_\mathrm{spin} + \sum_{r=\mathrm{L,R}} H_{\mathrm{tun},r}. \tag{5.1}$$

The first term,

$$H_r = \sum_{\mathbf{k}} \sum_{\sigma=\pm} \varepsilon_{r\mathbf{k}\sigma} a^\dagger_{r\mathbf{k}\sigma} a_{r\mathbf{k}\sigma}, \tag{5.2}$$

describes the ferromagnetic electrodes in terms of noninteracting electrons at chemical potential μ_r. We quantize the electron spin in the direction of the respective magnetization. We assume the density of states $\rho_{r\sigma}$ to be constant but spin dependent. The asymmetry between majority ($\sigma = +$) and minority ($\sigma = -$) spin electrons is characterized by the polarization, $p_r = (\rho_{r+} - \rho_{r-})/(\rho_{r+} + \rho_{r-})$, where $p_r = 0$ corresponds to a nonmagnetic lead while $p_r = 1$ corresponds to a halfmetallic ferromagnet with majority spins only.

The quantum dot is described by

$$H_\mathrm{dot} = \sum_{\sigma=\uparrow,\downarrow} \varepsilon c^\dagger_\sigma c_\sigma + U c^\dagger_\uparrow c_\uparrow c^\dagger_\downarrow c_\downarrow. \tag{5.3}$$

Here, the first term characterizes the single, spin-degenerate quantum dot level with energy ε measured with respect to the Fermi energy of the leads in equilibrium. The charging energy U is needed to occupy the quantum dot with two electrons. As indicated in Fig. 5.1, we choose the quantization axis of the dot parallel to the magnetization of the right electrode as this simplifies the expressions for the tunnel Hamiltonian, see below.

The third term in Eq. (5.1) describes the magnetic impurity embedded in the right tunnel barrier as a localized spin with Hamiltonian

$$H_{\text{spin}} = -DS_z^2 - BS_z. \tag{5.4}$$

We model the spin of magnitude S as having a uniaxial anisotropy D which favors the spin to be in the eigenstates pointing along the z axis. We, furthermore, assume the presence of a magnetic field B acting on the impurity spin. For concreteness, we assume this field to be pointing along the z direction. This choice is motivated by the presence of stray fields from the ferromagnetic electrode which have the tendency to align the impurity along the magnetization of the electrode. As for the quantum dot, we quantize the impurity spin along the direction of the magnetization of the right electrode.

The last part of the Hamiltonian (5.1) describes the tunneling between the dot and the electrodes. For the coupling to the left lead, it takes the form

$$H_{\text{tun,L}} = \sum_{\mathbf{k}} t_{\text{L}} \left[a^\dagger_{\text{L}\mathbf{k}+} \left(\cos\frac{\varphi}{2} c_\uparrow - \sin\frac{\varphi}{2} c_\downarrow \right) + a^\dagger_{\text{L}\mathbf{k}-} \left(\sin\frac{\varphi}{2} c_\uparrow + \cos\frac{\varphi}{2} c_\downarrow \right) \right] + \text{h.c.}, \tag{5.5}$$

i.e., majority and minority spin electrons of the leads couple to spin up and spin down states of the quantum dot due to our choice of quantization axes. The coupling to the right lead consists of two terms,

$$H_{\text{tun,R}} = \sum_{\mathbf{k}\sigma} t_{\text{R}} a^\dagger_{\text{R}\mathbf{k}\sigma} c_\sigma + \sum_{\mathbf{k}\alpha\beta} j_{\text{R}} a^\dagger_{\text{R}\mathbf{k}\alpha} \mathbf{S} \cdot \boldsymbol{\sigma}_{\alpha\beta} c_\beta + \text{h.c.}. \tag{5.6}$$

Here, $\boldsymbol{\sigma}_{\alpha\beta}$ denotes the vector of Pauli matrices. While the first part describes normal tunneling processes between the dot and the lead, the second term describes an exchange interaction between the spin of the tunneling electron and the impurity spin.

The tunnel matrix elements t_{L} and t_{R} (which can be chosen real) are related to the spin-dependent tunneling rates via $\Gamma_{r,\sigma} = 2\pi|t_r|^2\rho_\sigma$. The width of the dot level due to the dot-lead coupling is then given by $\Gamma_r = \sum_\sigma \Gamma_{r\sigma}/2$. Similarly, for the exchange tunneling, we relate the corresponding tunneling rate to its (real) matrix element by $J_{\text{R}} = 2\pi|j_{\text{R}}|^2 \frac{\rho_+ + \rho_-}{2}$. Furthermore, there will be a contribution due to the interference between direct and exchange tunneling through the right barrier. It is characterized by $\eta\sqrt{\Gamma_{\text{R}} J_{\text{R}}}$. Here, $\eta = \pm 1$ determines the sign of the interference contribution which is governed by the relative sign of t_{R} and j_{R}. The upper sign, $\eta = +1$ applies for equal signs of t_{R} and j_{R}, while the lower sign, $\eta = -1$ applies for different signs of t_{R} and j_{R}.

5.1.2 Model B: Impurity on the dot

Model B consists of a quantum-dot spin valve with an additional spin localized on the quantum dot as shown schematically in Fig. 5.2. In the following analysis, we will

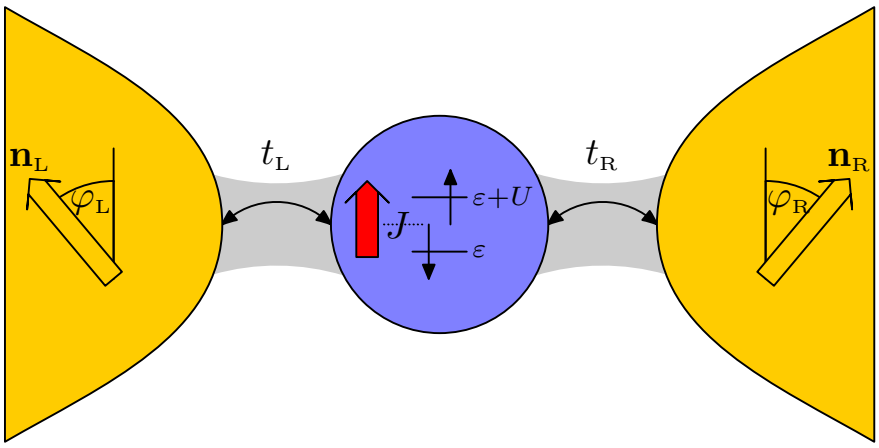

Figure 5.2: Schematic of model B which consists of a quantum-dot spin valve with a magnetic impurity on the quantum dot.

restrict ourselves to the case of a $S = 1/2$ impurity spin on the dot to keep the size of the Hilbert space small. The total Hamiltonian now takes the form

$$H = \sum_{r=\mathrm{L,R}} H_r + H_\mathrm{dot} + H_\mathrm{tun}, \tag{5.7}$$

describing the electrodes, the dot containing the impurity spin and the tunneling between dot and leads. The first part, H_r, is identical to the one given in Eq. (5.2). For the second term, we have

$$H_\mathrm{dot} = \sum_{\sigma=\uparrow,\downarrow} \varepsilon c_\sigma^\dagger c_\sigma + \frac{B}{2}\left(n_\uparrow - n_\downarrow\right) + U n_\uparrow n_\downarrow + B S_z + J \sum_{\sigma\sigma'} c_\sigma^\dagger \frac{\mathbf{S}\cdot\boldsymbol{\sigma}_{\sigma\sigma'}}{2} c_{\sigma'}, \tag{5.8}$$

The first two terms describe the single dot level with energy ε and Zeeman splitting B due to an external magnetic field. For simplicity, we assume the magnetic field to point along the quantization axis of the dot which we choose perpendicular to the magnetizations of the leads. The third term describes the Coulomb interaction U which is needed to doubly occupy the quantum dot. The fourth term describes the Zeeman energy of the additional spin on the quantum dot. Here, we assume the same g factor for the electrons on the dot and the impurity spin, for a discussion of a system where electron and impurity spin have different g factors, cf. Ref. [221]. Finally, the last term describes an exchange interaction between the spin of the electron on the dot and the impurity spin.

The eigenstates of the dot Hamiltonian (5.8) and their corresponding energies are summarized in Tab. 5.1. The eight states can be classified according to the number of electrons on the dot. For the empty and doubly-occupied dot, we have two states each that differ in energy by the Zeeman energy B with the impurity spin pointing up or down. For the singly-occupied dot, we have in total four states. These can be classified according to their total angular momentum as three triplet states ($S^\mathrm{tot} = 1$) and one singlet state ($S^\mathrm{tot} = 0$). While the triplet states are energetically split by the Zeeman energy, singlet and triplet are split by the exchange coupling J.

Eigenstate	Energy
$\|0\uparrow\rangle$	$E_{0\uparrow} = B/2$
$\|0\downarrow\rangle$	$E_{0\downarrow} = -B/2$
$\|T^+\rangle = \|\uparrow\uparrow\rangle$	$E_{T^+} = \varepsilon + J/4 + B$
$\|T^0\rangle = (\|\uparrow\downarrow\rangle + \|\downarrow\uparrow\rangle)/\sqrt{2}$	$E_{T^0} = \varepsilon + J/4$
$\|T^-\rangle = \|\downarrow\downarrow\rangle$	$E_{T^-} = \varepsilon + J/4 - B$
$\|S\rangle = (\|\uparrow\downarrow\rangle - \|\downarrow\uparrow\rangle)/\sqrt{2}$	$E_S = \varepsilon - 3/4J$
$\|d\uparrow\rangle$	$E_{d\uparrow} = 2\varepsilon + U + B/2$
$\|d\downarrow\rangle$	$E_{d\downarrow} = 2\varepsilon + U - B/2$

Table 5.1: Eigenstates of the dot Hamiltonian (5.8) and corresponding eigenenergies. The first entry in each ket denotes the state of the quantum dot while the second entry characterizes the impurity spin state.

The coupling between dot and leads is described by the tunneling Hamiltonian

$$H_{\text{tun}} = \sum_{r\mathbf{k}} t_r \left[a^\dagger_{r\mathbf{k}+} \left(e^{i\phi_r/2} c_\uparrow + e^{-i\phi_r/2} c_\downarrow \right) + a^\dagger_{r\mathbf{k}-} \left(-e^{i\phi_r/2} c_\uparrow + e^{-i\phi_r/2} c_\downarrow \right) \right] + \text{h.c.}, \tag{5.9}$$

where $\phi_{\text{L}} = -\phi_{\text{R}} = \phi/2$ denotes half the angle enclosed by the magnetizations. Due to the choice of quantization axes, majority (minority) spin electrons couple to both, spin up and down on the dot. As for the spin in the barrier, the tunnel matrix elements t_r are related to the spin-dependent tunnel coupling strengths by $\Gamma_{r\pm} = 2\pi|t_r|^2\rho_{r\pm}$ while the dot-lead coupling is given by $\Gamma_r = (\Gamma_{r+} + \Gamma_{r-})/2$. Instead of using the tunnel coupling strength to the left and right lead, we can characterize the dot-lead coupling alternatively by the total tunnel coupling $\Gamma = \Gamma_{\text{L}} + \Gamma_{\text{R}}$ and the asymmetry $a = (\Gamma_{\text{L}} - \Gamma_{\text{R}})/\Gamma$ with $-1 < a < 1$.

5.2 Reduced density matrix and master equation

In order to calculate the transport properties of the two models introduced in Section 5.1, we again make use of the real-time diagrammatic technique, i.e., we integrate out the electronic reservoirs and describe the remaining system in terms of its reduced density matrix. In the following, we discuss the form of the reduced density matrix for the two models under investigation. We furthermore write down the generalized master equations that determine the time evolution of the density matrix elements in a physical intuitive form for both systems.

5.2.1 Model A: Impurity in the barrier

For a quantum-dot spin valve with an impurity embedded in the tunnel barrier, the eigenstates of the reduced system consisting of quantum dot and impurity spin are products of dot eigenstates $|\chi\rangle \in \{|0\rangle, |\uparrow\rangle, |\downarrow\rangle, |d\rangle\}$ and impurity spin eigenstates $|S_z\rangle \in \{|+S\rangle, \ldots, |-S\rangle\}$, $|\xi\rangle = |\chi\rangle \otimes |S_z\rangle$. Assuming the energies of states with different impurity states to differ more than the tunnel coupling, $E_{S_z} - E_{S'_z} \gg \Gamma$, we have to neglect coherent superpositions between states with different impurity states, cf. Section 3.3.

The reduced density matrix therefore takes a block diagonal form given by

$$\rho^{\mathrm{red}} = \bigoplus_{m=-S}^{S} \begin{pmatrix} P_{0,m} & 0 & 0 & 0 \\ 0 & P_{\uparrow,m} & P^{\uparrow}_{\downarrow,m} & 0 \\ 0 & P^{\downarrow}_{\uparrow,m} & P_{\downarrow,m} & 0 \\ 0 & 0 & 0 & P_{d,m} \end{pmatrix}. \tag{5.10}$$

In order to give a physically intuitive interpretation of the generalized master equations, we introduce the probabilities to find the dot empty, $P_{0,m}$, singly occupied, $P_{1,m} = P_{\uparrow,m} + P_{\downarrow,m}$, and doubly occupied, $P_{d,m}$, with the impurity in state $|m\rangle$. We collect these quantities in the vector $\mathbf{P}_m = (P_{0,m}, P_{1,m}, P_{d,m})^T$. We furthermore introduce the average spin on the quantum dot $s_{x,m} = \frac{P^{\uparrow}_{\downarrow,m} + P^{\downarrow}_{\uparrow,m}}{2}$, $s_{y,m} = i\frac{P^{\uparrow}_{\downarrow,m} - P^{\downarrow}_{\uparrow,m}}{2}$, $s_{z,m} = \frac{P_{\uparrow,m} - P_{\downarrow,m}}{2}$. The set of master equations can then be split into one determining the occupation probabilities and one set governing the average dot spin. For the first set, we have

$$\begin{aligned} \dot{\mathbf{P}}_{\mathbf{m}} = {} & \mathbf{W}_{\mathrm{L}}^{(0)}\mathbf{P}_m + \mathbf{W}_{\mathrm{R}}^{(0)}\mathbf{P}_m + \mathbf{W}_{\mathrm{R}}^{(+1)}\mathbf{P}_{m+1} + \mathbf{W}_{\mathrm{R}}^{(-1)}\mathbf{P}_{m-1} \\ & + V_{\mathrm{L}}^{(0)}\mathbf{s}_m \cdot \mathbf{n}_{\mathrm{L}} + V_{\mathrm{R}}^{(0)}\mathbf{s}_m \cdot \mathbf{n}_{\mathrm{R}} + V_{\mathrm{R}}^{(+1)}\mathbf{s}_{m+1} \cdot \mathbf{n}_{\mathrm{R}} + V_{\mathrm{R}}^{(-1)}\mathbf{s}_{m-1} \cdot \mathbf{n}_{\mathrm{R}}. \end{aligned} \tag{5.11}$$

Here, $\mathbf{W}_r^{(\alpha)}$ is a matrix which describes processes that transfer an electron between the dot and lead r and change the state of the impurity spin from $|m\rangle$ to $|m+\alpha\rangle$. Since the impurity is located in the right tunnel barrier, tunneling through the left lead cannot change the impurity state and therefore $\mathbf{W}_{\mathrm{L}}^{(\pm 1)} = 0$. Changing the impurity state is possible, however, for tunneling through the right barrier which provides a coupling between $\mathbf{P}_m$ and $\mathbf{P}_{m\pm 1}$. Similarly, $V_r^{(\alpha)}$ is a vector which describes the coupling of the occupation probabilities to the spin on the dot, a feature characteristic of a quantum-dot spin valve. Again, we have $V_{\mathrm{L}}^{(\pm 1)} = 0$. The precise form of $\mathbf{W}_r^{(\alpha)}$ and $V_r^{(\alpha)}$ is given in Appendix B.2.

The time evolution of the dot spin obeys a Bloch-like equation,

$$\begin{aligned} \dot{\mathbf{s}}_{\mathbf{m}} = {} & \left(\frac{d\mathbf{s}_m}{dt}\right)^{(0)}_{\mathrm{acc,L}} + \left(\frac{d\mathbf{s}_m}{dt}\right)^{(0)}_{\mathrm{acc,R}} + \left(\frac{d\mathbf{s}_m}{dt}\right)^{(+1)}_{\mathrm{acc,R}} + \left(\frac{d\mathbf{s}_m}{dt}\right)^{(-1)}_{\mathrm{acc,R}} \\ & + \left(\frac{d\mathbf{s}_m}{dt}\right)^{(0)}_{\mathrm{rel,L}} + \left(\frac{d\mathbf{s}_m}{dt}\right)^{(0)}_{\mathrm{rel,R}} + \mathbf{s}_m \times (\mathbf{B}_{m,\mathrm{L}} + \mathbf{B}_{m,\mathrm{R}}). \end{aligned} \tag{5.12}$$

The first four terms on the right-hand side describe the nonequilibrium spin accumulation on the quantum dot due to the tunneling from and to the spin-polarized leads. Similarly to the master equation for the occupations, we get accumulation terms that change the state of the impurity when tunneling takes place through the right barrier.

The next two terms account for the relaxation of the spin on the dot due to the tunneling out of an electron or the tunneling in of an electron forming a spin singlet with the electron already present on the dot. As these terms arise from generalized transition rates which start and end in a singly-occuppied state, in the sequential tunneling approximation the state of the impurity spin cannot be changed in these processes. We give the explicit forms of the accumulation and relaxation terms in Appendix B.2.

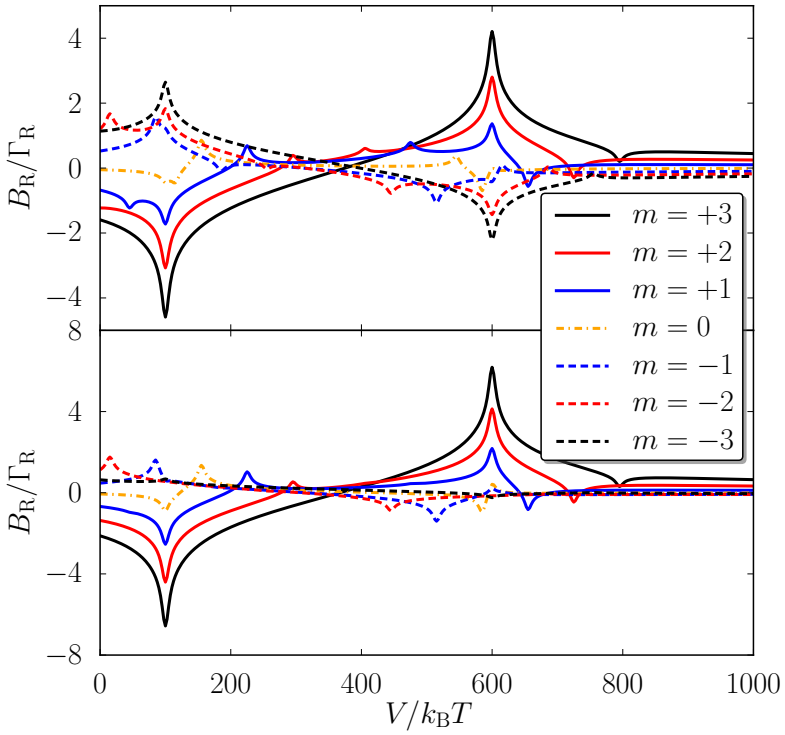

Figure 5.3: Exchange field due to virtual tunneling through the right barrier as a function of bias voltage V for $p = 0.3$ (upper panel) and $p = 0.9$ (lower panel). Other parameters are $\varepsilon = -300k_BT$, $U = 250k_BT$, $D = 17.5k_BT$, $B = 10k_BT$, $\Gamma_R = 10J_R$, $\eta = +1$, $W = 500k_BT$, $S = 3$.

The last term describes the precession of the dot spin in an exchange field due to virtual tunneling to the leads. For the coupling to the left lead, we find the usual exchange field [65] which is independent of the state of the impurity spin. It is given by

$$\mathbf{B}_{m,\mathrm{L}} = -\mathbf{n}_\mathrm{L} \frac{p_\mathrm{L}\Gamma_\mathrm{L}}{\pi} \left(\Phi_\mathrm{L}(\varepsilon) - \Phi_\mathrm{L}(\varepsilon + U)\right), \tag{5.13}$$

where $\Phi_r(x) = \mathrm{Re}\,\psi\left(\frac{1}{2} + i\frac{\beta(x-\mu_r)}{2\pi}\right)$. While the first term arises from the spin-dependent level renormalization of an electron virtually tunneling to the lead and back, the second term stems from processes where an electron first tunnels onto the dot and then back into the lead.

The exchange field due to the coupling to the right lead which points in the direction

of $\mathbf{n}_\mathrm{R}$ is given by

$$\begin{aligned}\mathbf{B}_{m,\mathrm{R}} = &-\mathbf{n}_\mathrm{R}\frac{\tilde{\gamma}}{\pi}\Big(\Phi_\mathrm{R}(\varepsilon)-\Phi_\mathrm{R}(\varepsilon+U)\Big)\\ &+\mathbf{n}_\mathrm{R}\frac{A_+(m-1)J_\mathrm{R}}{\pi}\left(\frac{1+p_\mathrm{R}}{2}\Phi_\mathrm{R}(\varepsilon-\alpha_-)+\frac{1-p_\mathrm{R}}{2}\Phi_\mathrm{R}(\varepsilon+U+\alpha_-)-\ln\frac{\beta W}{2\pi}\right)\\ &-\mathbf{n}_\mathrm{R}\frac{A_-(m+1)J_\mathrm{R}}{\pi}\left(\frac{1-p_\mathrm{R}}{2}\Phi_\mathrm{R}(\varepsilon+\alpha_+)+\frac{1+p_\mathrm{R}}{2}\Phi_\mathrm{R}(\varepsilon+U-\alpha_+)-\ln\frac{\beta W}{2\pi}\right)\end{aligned} \tag{5.14}$$

where $\tilde{\gamma} = p_\mathrm{R}\Gamma_\mathrm{R} + m^2 p_\mathrm{R} J_\mathrm{R} + 2m\eta\sqrt{\Gamma_\mathrm{R}J_\mathrm{R}}$, $\alpha_\pm = B + (2m\pm 1)D$ and $A_\pm(m) = S(S+1) - m(m\pm 1)$.

Here, the first term on the right-hand side describes exchange field contributions due to virtual tunneling between dot and lead that does not change the state of the impurity spin. The other two terms are due to virtual tunneling where the intermediate state has an increased/decreased impurity spin state. These processes give rise to a logarithmic divergency of the exchange field cut off by the bandwith W of the lead electrons. To understand this, we consider the impurity in the state $|S_z = S\rangle$. In this case, only the sequences $|\downarrow, S\rangle \to |0, S-1\rangle \to |\downarrow, S\rangle$ and $|\downarrow, S\rangle \to |d, S-1\rangle \to |\downarrow, S\rangle$ of (virtual) transitions are possible while there are no such processes starting from $|\uparrow, S\rangle$. Hence, these processes only renormalize the energy of the spin down state, giving rise to the logarithmic divergency. Similarly, when the impurity is in any other state, the logarithmic contributions to the exchange field do not cancel between processes that increase and decrease the intermediate impurity spin state. As we only consider sequential tunneling, it is clear that our results are only valid if $J_\mathrm{R}\ln\frac{\beta W}{2\pi} \ll k_\mathrm{B}T$ and $J_\mathrm{R}\ln\frac{\beta W}{2\pi} \lesssim \Gamma_r$, otherwise higher-order logarithmic corrections become important.

We, therefore, find that the presence of the impurity spin in the tunnel barrier has two basic effects on the exchange field. First of all, it alters its strength. Second, due to the presence of the spin-flip processes, it also alters its energy dependence (cf. Fig. 5.3), giving rise to additional peaks and dips whose separation is governed by the anisotropy D, the Zeeman energy B and the size of the impurity spin S. Since the transition energies between the various impurity states depend on the states itself, the position of the additional peaks and dips depends on the value of S_z.

5.2.2 Model B: Impurity on the dot

For the case of a $S = 1/2$ impurity localized on the quantum dot, the reduced density matrix in the most general case takes the form

$$\rho^\mathrm{red} = \begin{pmatrix} P_{0\uparrow} & P_{0\downarrow}^{0\uparrow} & 0 & 0 & 0 & 0 & 0 & 0\\ P_{0\uparrow}^{0\downarrow} & P_{0\downarrow} & 0 & 0 & 0 & 0 & 0 & 0\\ 0 & 0 & P_{T+} & P_{T0}^{T+} & P_{T-}^{T+} & P_S^{T+} & 0 & 0\\ 0 & 0 & P_{T+}^{T0} & P_{T0} & P_{T-}^{T0} & P_S^{T0} & 0 & 0\\ 0 & 0 & P_{T+}^{T-} & P_{T0}^{T-} & P_{T-} & P_S^{T-} & 0 & 0\\ 0 & 0 & P_{T+}^{S} & P_{T0}^{S} & P_{T-}^{S} & P_S & 0 & 0\\ 0 & 0 & 0 & 0 & 0 & 0 & P_{d\uparrow} & P_{d\downarrow}^{d\uparrow}\\ 0 & 0 & 0 & 0 & 0 & 0 & P_{d\uparrow}^{d\downarrow} & P_{d\downarrow} \end{pmatrix}, \tag{5.15}$$

Case	Parameters	Superpositions of
(i)	$B, J, \lvert B-J\rvert \gg \Gamma$	–
(ii)	$B \gg \Gamma$, $J \lesssim \Gamma$	$\lvert T^0\rangle$, $\lvert S\rangle$
(iii)	$B, J \gg \Gamma$, $\lvert B-J\rvert \lesssim \Gamma$	$\lvert T^-\rangle$, $\lvert S\rangle$
(iv)	$J \gg \Gamma$, $B \lesssim \Gamma$	$\lvert 0\uparrow\rangle$, $\lvert 0\downarrow\rangle$ $\lvert T^+\rangle$, $\lvert T^0\rangle$, $\lvert T^-\rangle$ $\lvert d\uparrow\rangle$, $\lvert d\downarrow\rangle$
(v)	$B, J \lesssim \Gamma$	$\lvert 0\uparrow\rangle$, $\lvert 0\downarrow\rangle$ $\lvert T^+\rangle$, $\lvert T^0\rangle$, $\lvert T^-\rangle$, $\lvert S\rangle$ $\lvert d\uparrow\rangle$, $\lvert d\downarrow\rangle$

Table 5.2: Coherent superpositions that have to be taken into account in the sequential tunneling regime for different values of the external magnetic field B and the exchange coupling J between the two spins.

i.e., apart from the eight diagonal matrix elements that describe the probability to find the system in one of its eigenstates there can be up to 16 coherences. Coherences between states with different electron numbers vanish due to the conservation of total particle number. As discussed in Section 3.3, depending on the energy differences of the states forming the coherent superposition, we either have to take them into account or neglect them in the sequential-tunneling regime. In Tab. 5.2, we summarize the different transport regimes that arise consequently.

In the following, we will only consider the cases (ii) and (v), i.e., we only consider the case of weak exchange couplings, $J \lesssim \Gamma$. When a large magnetic field is applied, $B \gg \Gamma$, only S-T^0 coherences have to be taken into account. When the externally applied magnetic field is weak, $B \lesssim \Gamma$, we have to take into account all coherences. There are two reasons for focussing on the two cases. On the one hand, they are particularly suited to demonstrate the information about the transport processes contained in the finite-frequency noise. On the other hand, the cases of small exchange couplings are suited to describe the influence of nuclear spins, that couple to the electron spin via hyperfine interaction, on transport through the quantum dot.

Case (ii): Large magnetic field

We first turn to the discussion of the master equation in case (ii) where $B \gg \Gamma$, $J \lesssim \Gamma$. In this case, there are only superpositions of S and T^0 present. It is therefore natural to introduce the isospin $\mathbf{I}$ via

$$I_x = \frac{P_{T^0}^S + P_S^{T^0}}{2}, \qquad I_y = i\frac{P_{T^0}^S - P_S^{T^0}}{2},$$
$$I_z = \frac{P_{T^0} - P_S}{2}, \qquad I_0 = P_{T^0} + P_S,$$

to bring the master equation into a physically intuitive form. Similar to the case of an ordinary quantum-dot spin valve [65], we can now split the master equation into one set governing the occupation probabilities that we summarize in the vector $\mathbf{P} = (P_{0\uparrow}, P_{0\downarrow}, P_{T^+}, I_0, P_{T^-}, P_{d\uparrow}, P_{d\downarrow})$ and one set governing the time evolution of the isospin $\mathbf{I} = (I_x, I_y, I_z)$. However, there is an important difference. While in the ordinary

quantum-dot spin valve, there is a real spin accumulating on the quantum dot, here we have an isospin accumulation as a real spin accumulation is suppressed by the large external magnetic field. The master equation of the occupation probabilities reads

$$\dot{\mathbf{P}} = \mathbf{W} \cdot \mathbf{P} + \mathbf{V}(\mathbf{I} \cdot \mathbf{e}_x), \tag{5.16}$$

where $\mathbf{W}$ denotes a matrix that contains the golden rule transition rates between the various dot states and $\mathbf{V}$ is a vector that characterizes the influence of the isospin on the dot occupation whose precise form is given in Appendix B.3.

The master equation that governs the time evolution of the isospin is given by

$$\dot{\mathbf{I}} = \left(\frac{d\mathbf{I}}{dt}\right)_{\text{acc}} + \left(\frac{d\mathbf{I}}{dt}\right)_{\text{relax}} + \mathbf{I} \times \sum_r \mathbf{B}_r. \tag{5.17}$$

Here, the first term,

$$\begin{aligned}\left(\frac{d\mathbf{I}}{dt}\right)_{\text{acc}} = \frac{1}{2}\sum_r \Gamma_r \Big\{ &- f_r^+(\varepsilon - B/2)P_{0\uparrow} + f_r^+(\varepsilon + B/2)P_{0\downarrow} \\ &- f_r^+(\varepsilon + U + B/2)P_{d\uparrow} + f_r^-(\varepsilon + U - B/2)P_{d\downarrow} \\ + \frac{1}{2}\Big[f_r^-(\varepsilon - B/2) - f_r^-(\varepsilon + B/2) + f_r^+(\varepsilon + U + B/2) - f_r^+(\varepsilon + U - B/2)\Big] I_0 \Big\} \mathbf{e}_x,\end{aligned} \tag{5.18}$$

describes the accumulation of the isospin along the x axis due to electrons tunneling onto and off the dot. Similarly, the second term describes a relaxation of the isospin,

$$\begin{aligned}\left(\frac{d\mathbf{I}}{dt}\right)_{\text{relax}} = -\frac{1}{2}\sum_r \Gamma_r \Big[&f_r^-(\varepsilon - B/2) + f_r^-(\varepsilon + B/2) \\ &+ f_r^+(\varepsilon + U - B/2) + f_r^+(\varepsilon + U + B/2)\Big] \mathbf{I}.\end{aligned} \tag{5.19}$$

Finally, the last term describes the precession of the isospin in an exchange field that is given by

$$\begin{aligned} B_{rx} &= \frac{\Gamma_r}{2\pi}\Big(\Phi_r(\varepsilon - B/2) - \Phi_r(\varepsilon + B/2) + \Phi_r(\varepsilon + U + B/2) - \Phi_r(\varepsilon + U - B/2)\Big) \\ B_{ry} &= 0 \\ B_{rz} &= J \end{aligned} \tag{5.20}$$

The exchange field describes the level splitting between $|T^0\rangle$ and $|S\rangle$ which is due to the finite exchange coupling J as well as due to virtual tunneling processes that renormalize the energies of the two states in a different way. As can be inferred from Eq. (5.17), it gives rise to a precession of the accumulated isospin around the exchange field.

The current through the quantum dot is given by

$$
\begin{aligned}
I = \frac{\Gamma_\mathrm{L}}{2}\Big[&\Big(f_\mathrm{L}^+(\varepsilon+B/2)+f_\mathrm{L}^+(\varepsilon-B/2)\Big)\Big(P_{0\uparrow}+P_{0\downarrow}\Big)\\
&-\Big(f_\mathrm{L}^-(\varepsilon+U+B/2)+f_\mathrm{L}^-(\varepsilon+U-B/2)\Big)\Big(P_{d\uparrow}+P_{d\downarrow}\Big)\\
-\Big(f_\mathrm{L}^-(\varepsilon+B/2)-f_\mathrm{L}^+(\varepsilon+U-B/2)\Big)P_{T^+}&-\Big(f_\mathrm{L}^-(\varepsilon-B/2)-f_\mathrm{L}^+(\varepsilon+U+B/2)\Big)P_{T^-}\\
-\frac{1}{2}\Big(f_\mathrm{L}^-(\varepsilon+B/2)+f_\mathrm{L}^-(\varepsilon-B/2)&-f_\mathrm{L}^+(\varepsilon+U+B/2)-f_\mathrm{L}^+(\varepsilon+U-B/2)\Big)I_0\\
-\Big(f_\mathrm{L}^-(\varepsilon+B/2)-f_\mathrm{L}^-(\varepsilon-B/2)&+f_\mathrm{L}^+(\varepsilon+U+B/2)-f_\mathrm{L}^+(\varepsilon+U-B/2)\Big)I_x\Big]\\
&-(\mathrm{L}\to\mathrm{R})\,. \qquad (5.21)
\end{aligned}
$$

It depends on the occupation probabilities as well as on the x component of the accumulated isospin. This resembles the normal quantum-dot spin valve where the current also depends on both, the dot occupations as well as on the dot spin [65].

Case (v): Small magnetic field

We now turn to the discussion of the master equation in the case $B, J \lesssim \Gamma$. In this case, we have to include all coherences of the reduced density matrix, Eq. (5.15).

To allow for a physical interpretation of the different matrix elements, we introduce the probabilities to find the quantum dot empty, P_0, singly occupied, P_1, and doubly occupied, P_d. Furthermore, we introduce the expectation values of the electron spin on the dot, $\mathbf{S}_1$, as well as the expectation values for the impurity spin when the dot is empty, $\mathbf{S}_0$, singly occupied, $\mathbf{S}_2$, and doubly occupied, $\mathbf{S}_d$. While for a single spin 1/2 the description of its density matrix in terms of spin expectation values is sufficient, this is in general no longer true for a system of two spin 1/2 particles [222]. For the case of small magnetic fields that we consider here, we therefore have to introduce in addition the expectation values of the scalar product between electron and impurity spin, $\mathbf{S}_1 \cdot \mathbf{S}_2$, and their vector product, $\mathbf{S}_1 \times \mathbf{S}_2$. Finally, we also need to introduce the quadrupole moment [224]

$$
Q_{ij} = \frac{1}{2}\left(S_{1i}S_{2j} + S_{1j}S_{2i}\right) - \frac{1}{3}\mathbf{S}_1 \cdot \mathbf{S}_2 \delta_{ij}. \qquad (5.22)
$$

The quadrupole moment is a symmetric tensor, $Q_{ij} = Q_{ji}$. Its diagonal elements are not independent of each other as they satisfy the sum rule $\sum_i Q_{ii} = 0$, which guarantees a vanishing trace of $\mathbf{Q}$.

In Appendix C we give the explicit expressions that relate the above quantities to the density matrix elements in Eq. (5.15). We note that in the case $B \gg \Gamma$, $J \lesssim \Gamma$ where we only have taken into account the S-T^0 superpositions, we could have expressed the reduced density matrix in terms of the quantities just introduced as well. However, by choosing a description in terms of the isospin, we obtain a much simpler master equation.

Using the physical quantities we just discussed, we can split the master equation into several sets. The first set,

$$\frac{d}{dt}\begin{pmatrix} P_0 \\ P_1 \\ P_d \end{pmatrix} = \sum_r \Gamma_r \begin{pmatrix} -2f_r^+(\varepsilon) & f_r^-(\varepsilon) & 0 \\ 2f_r^+(\varepsilon) & -f_r^-(\varepsilon) - f_r^+(\varepsilon+U) & 2f_r^-(\varepsilon+U) \\ 0 & f_r + (\varepsilon+U) & -2f_r^-(\varepsilon+U) \end{pmatrix} \begin{pmatrix} P_0 \\ P_1 \\ P_d \end{pmatrix} + \sum_r 2p_r\Gamma_r \begin{pmatrix} f_r^-(\varepsilon) \\ -f_r^-(\varepsilon) + f_r^+(\varepsilon+U) \\ -f_r^+(\varepsilon+U) \end{pmatrix} \mathbf{S}_1 \cdot \mathbf{n}_r, \quad (5.23)$$

describes the evolution of the occupation probabilities. It takes a form identical to the case of a normal quantum-dot spin valve, i.e., it exhibits a coupling of the occupations to the spin accumulated on the quantum dot. Interestingly, the occupations do not couple neither to the impurity spin, the scalar or vector product of $\mathbf{S}_1$ and $\mathbf{S}_2$ nor to the quadrupole moments directly. They are only influenced by these quantities due to their influence on the accumulated electron spin $\mathbf{S}_1$.

The equation governing the time evolution of the electron spin in the dot is given by

$$\frac{d\mathbf{S}_1}{dt} = \sum_r \Bigg[p_r\Gamma_r \left(f_r^+(\varepsilon)P_0 - \frac{f_r^-(\varepsilon) - f_r^+(\varepsilon+U)}{2} P_1 - f_r^-(\varepsilon+U)P_d \right) \mathbf{n}_r - \frac{\mathbf{S}_1}{\tau_r} - \mathbf{S}_1 \times \mathbf{B}_{r,\mathrm{ex}} \Bigg] - \mathbf{S}_1 \times \mathbf{B} + J(\mathbf{S}_1 \times \mathbf{S}_2), \quad (5.24)$$

where $1/\tau_r = \Gamma_r \left(f_r^-(\varepsilon) + f_r^+(\varepsilon+U) \right)$ and $\mathbf{B}_{r,\mathrm{ex}} = -\frac{p\Gamma_r}{\pi} \left(\Phi_r(\varepsilon) - \Phi_r(\varepsilon+U) \right) \mathbf{n}_r$ is the usual exchange field acting on the electron spin accumulated on the dot. Again, we find a strong similarity to the case of the normal quantum-dot spin valve. While the first term in brackets describes the accumulation of spin on the dot along $\mathbf{n}_r$ due to spin-dependent tunneling of electrons between dot and leads, the second term describes a relaxation of the dot spin due to tunneling. The third term in brackets describes the precession of the dot spin in the exchange field generated by virtual tunneling between dot and leads. The last two terms finally describe the influence of an external magnetic field and the exchange coupling to the impurity spin.

The master equations for the impurity spin in the presence of zero, one and two electrons on the dot can be written as

$$\frac{d}{dt}\begin{pmatrix} \mathbf{S}_0 \\ \mathbf{S}_2 \\ \mathbf{S}_d \end{pmatrix} = \sum_r \Gamma_r \begin{pmatrix} -2f_r^+(\varepsilon) & f_r^-(\varepsilon) & 0 \\ 2f_r^+(\varepsilon) & -f_r^-(\varepsilon) - f_r^+(\varepsilon+U) & 2f_r^-(\varepsilon+U) \\ 0 & f_r^+(\varepsilon+U) & -2f_r^-(\varepsilon+U) \end{pmatrix} \begin{pmatrix} \mathbf{S}_0 \\ \mathbf{S}_2 \\ \mathbf{S}_d \end{pmatrix} + \sum_r 2p_r\Gamma_r \begin{pmatrix} f_r^-(\varepsilon) \\ -f_r^-(\varepsilon) + f_r^+(\varepsilon+U) \\ -f_r^+(\varepsilon+U) \end{pmatrix} \left[\left(\mathbf{Q} + \frac{1}{3}\mathbf{S}_1 \cdot \mathbf{S}_2 \right) \cdot \mathbf{n}_r + \frac{1}{2} \left(\mathbf{S}_1 \times \mathbf{S}_2 \right) \times \mathbf{n}_r \right] - \begin{pmatrix} \mathbf{S}_0 \\ \mathbf{S}_2 \\ \mathbf{S}_d \end{pmatrix} \times \mathbf{B} + J \begin{pmatrix} 0 \\ \mathbf{S}_1 \times \mathbf{S}_2 \\ 0 \end{pmatrix}. \quad (5.25)$$

Here, the first term on the right-hand side describes transitions between the three quantities by tunneling of electrons in analogy to the first term in the equation for the

occupations, Eq. (5.23). The second term characterizes the coupling to the quadrupole moments as well as the scalar and vector product of $\mathbf{S}_1$ and $\mathbf{S}_2$. This resembles the coupling of the dot occupations to the electron spin on the dot in Eq. 5.23. Finally, the terms in the third line describe the precession of the impurity spin in an externally applied magnetic field as well as the influence of the exchange interaction between electron and impurity spin.

The master equations governing the time evolution of the scalar and vector product between the electron and impurity spin are given by

$$\frac{d}{dt}(\mathbf{S}_1\times\mathbf{S}_2)=\sum_r\Bigg[-p_r\Gamma_r\left(f_r^+(\varepsilon)\mathbf{S}_0-\frac{f_r^-(\varepsilon)-f_r^+(\varepsilon+U)}{2}\mathbf{S}_2-f_r^-(\varepsilon+U)\mathbf{S}_d\right)\times\mathbf{n}_r \\ -\frac{\mathbf{S}_1\times\mathbf{S}_2}{\tau_r}+\left(\mathbf{Q}-\frac{2}{3}(\mathbf{S}_1\cdot\mathbf{S}_2)\right)\cdot\mathbf{B}_{r,\mathrm{ex}}\Bigg]-(\mathbf{S}_1\times\mathbf{S}_2)\times\mathbf{B}+\frac{J}{2}\left(\mathbf{S}_1-\mathbf{S}_2\right), \quad (5.26)$$

$$\frac{d}{dt}(\mathbf{S}_1\cdot\mathbf{S}_2)=\sum_r\Bigg[p_r\Gamma_r\left(f_r^+(\varepsilon)\mathbf{S}_0-\frac{f_r^-(\varepsilon)+f_r^+(\varepsilon+U)}{2}\mathbf{S}_2-f_r^-(\varepsilon+U)\mathbf{S}_d\right)\cdot\mathbf{n}_r \\ -\frac{\mathbf{S}_1\cdot\mathbf{S}_2}{\tau_r}+(\mathbf{S}_1\times\mathbf{S}_2)\cdot\mathbf{B}_{r,\mathrm{ex}}\Bigg]. \quad (5.27)$$

Their structure closely resembles Eq. (5.24) in that there are terms which describe the accumulation, relaxation and the influence of the spin precession due to the exchange field. Furthermore, the vector product turns out to be sensitive to an external magnetic field as well as to the exchange coupling between the spins.

Finally, the master equation for the quadrupole moment takes the form

$$\frac{d}{dt}\mathbf{Q}_{ij}=\sum_r\Bigg[p_r\Gamma_r f_r^+(\varepsilon)\left(\frac{1}{2}\left(\mathbf{S}_{0,i}\mathbf{n}_{r,j}+\mathbf{S}_{0,j}\mathbf{n}_{r,i}\right)-\frac{1}{3}(\mathbf{S}_0\cdot\mathbf{n}_r)\delta_{ij}\right) \\ -p_r\Gamma_r\frac{f_r^-(\varepsilon)-f_r^+(\varepsilon+U)}{2}\left(\frac{1}{2}\left(\mathbf{S}_{2,i}\mathbf{n}_{r,j}+\mathbf{S}_{2,j}\mathbf{n}_{r,i}\right)-\frac{1}{3}(\mathbf{S}_2\cdot\mathbf{n}_r)\delta_{ij}\right) \\ -p_r\Gamma_r f_r^-(\varepsilon+U)\left(\frac{1}{2}\left(\mathbf{S}_{d,i}\mathbf{n}_{r,j}+\mathbf{S}_{d,j}\mathbf{n}_{r,i}\right)-\frac{1}{3}(\mathbf{S}_d\cdot\mathbf{n}_r)\delta_{ij}\right) \\ -\frac{\mathbf{Q}_{ij}}{\tau_r}-\frac{1}{2}\left(\frac{1}{2}(\mathbf{S}_1\times\mathbf{S}_2)_i(\mathbf{B}_{r,\mathrm{ex}})_j+\frac{1}{2}(\mathbf{S}_1\times\mathbf{S}_2)_j(\mathbf{B}_{r,\mathrm{ex}})_i-\frac{1}{3}(\mathbf{S}_1\times\mathbf{S}_2)\cdot\mathbf{B}_{r,\mathrm{ex}}\delta_{ij}\right) \\ -\frac{1}{2}\varepsilon_{ilm}\mathbf{Q}_{lj}(\mathbf{B}_{r,\mathrm{ex}})_m-\frac{1}{2}\varepsilon_{jlm}\mathbf{Q}_{li}(\mathbf{B}_{r,\mathrm{ex}})_m\Bigg]-\varepsilon_{ilm}\mathbf{Q}_{lj}\mathbf{B}_m-\varepsilon_{jlm}\mathbf{Q}_{li}\mathbf{B}_m. \quad (5.28)$$

The first three terms on the right-hand side describe the accumulation of quadrupole moment on the quantum dot. Similarly, the fourth term is related to the relaxation of the quadrupole moment. Finally, the other terms describe the precesional motion of the quadrupole moment in the exchange field as well as due to an external magnetic field.

The current through tunnel barrier r is given by

$$I_r=\Gamma_r f_r^+(\varepsilon)P_0-\Gamma_r\frac{f_r^-(\varepsilon)-f_r^+(\varepsilon+U)}{2}P_1-\Gamma_r f_r^-(\varepsilon+U)P_d \\ -p\Gamma_r\left[f_r^-(\varepsilon)+f_r^+(\varepsilon+U)\right]\mathbf{S}_1\cdot\mathbf{n}_r. \quad (5.29)$$

Although this is precisely the same form as for the normal quantum-dot spin valve, the current nevertheless contains information about the nontrivial spin dynamics on the dot, as the master equation for the dot spin couples to the other density matrix elements.

5.3 Results - Impurity in the barrier

From the form of the tunneling Hamiltonian (5.6) it is obvious that interference can take place between electrons tunneling directly through the barrier and electrons experiencing an exchange interaction with the impurity spin. For transport through a single tunnel barrier containing a localized spin [187, 189, 195, 225, 226], the interference contributions cancel between the spin up and spin down channel. Only for ferromagnetic leads [194, 201, 202, 227] or in the presence of spin-orbit interactions, one is sensitive to the interference terms.

This is different for the system under investigation here. We find that the interference terms influence the current even for unpolarized leads. In contrast to the single-barrier case where we just have to sum up the contributions from spin up and down electrons to the current, in the quantum dot case we have to separately compare the rates for tuneling in and out of the dot for each spin direction. While in the nonmagnetic case equal amounts of spin up and spin down electrons enter the dot from the left lead, the rates for leaving the dot are different due to the interference terms. This in turn gives rise to a spin accumulation on the quantum dot which reduces the current through the quantum dot.

Unfortunately, in our system there is no way to tune the phase of the interference terms experimentally as is possible, e.g., in an Aharonov-Bohm interferometer and thereby check the influence of the interference terms on the current. Nevertheless, it should be possible to detect the presence of the interference term experimentally and to detect its sign. Approximating the Fermi functions as step functions which is reasonable away from the threshold voltages, we can calculate the current through the system analytically in the various transport regions.

We first consider the case of unpolarized leads, $p_r = 0$. In this case, the current in region I where transport takes place through the singly- and doubly-occupied dot (cf. Fig. 5.4) is given by

$$I_{\mathrm{I}} = \frac{2\Gamma_{\mathrm{L}}(\Gamma_{\mathrm{R}} + S^2 J_{\mathrm{R}})}{\Gamma_{\mathrm{L}} + 2(\Gamma_{\mathrm{R}} + S^2 J_{\mathrm{R}})}, \tag{5.30}$$

i.e. it is sensitive to the couplings and the size of the barrier spin but not to the interference term. Similarly, in region II where spin excitations become possible, the current turns out to be insensitive to the interference term,

$$I_{\mathrm{II}} = \frac{2\Gamma_{\mathrm{L}}(\Gamma_{\mathrm{R}} + S(S+1) J_{\mathrm{R}})}{\Gamma_{\mathrm{L}} + 2(\Gamma_{\mathrm{R}} + S(S+1) J_{\mathrm{R}})}. \tag{5.31}$$

This is different in region III where transport takes place through the empty and singly-occupied dot but the spin cannot be excited. Here, the current is given by

$$I_{\mathrm{III}} = \frac{2\Gamma_{\mathrm{L}}((\Gamma_{\mathrm{R}} + S^2 J_{\mathrm{R}})^2 - 4S^2 \sqrt{\Gamma_{\mathrm{R}} J_{\mathrm{R}}}^2)}{(\Gamma_{\mathrm{R}} + S^2 J_{\mathrm{R}})((2\Gamma_{\mathrm{L}} + \Gamma_{\mathrm{R}} + S^2 J_{\mathrm{R}}) - 4S^2 \sqrt{\Gamma_{\mathrm{R}} J_{\mathrm{R}}}^2)}, \tag{5.32}$$

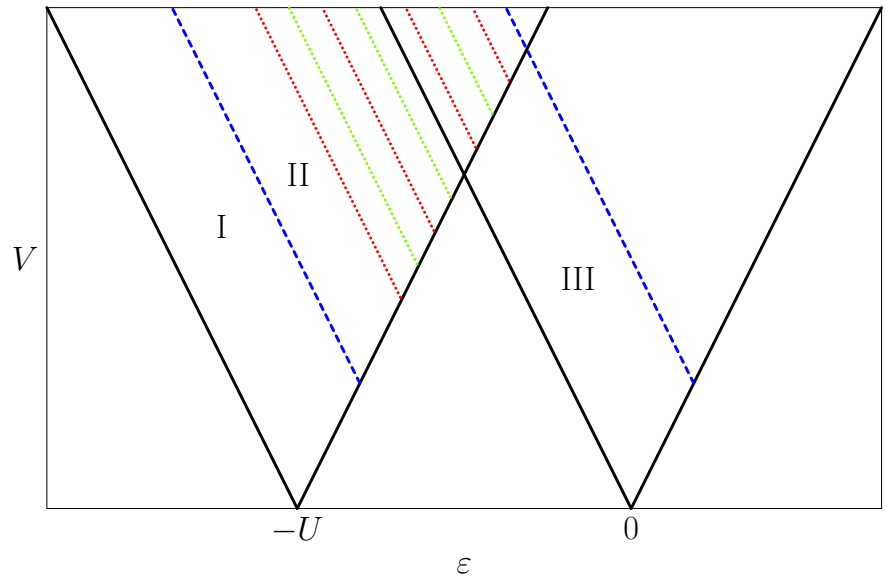

Figure 5.4: Schematic of the differential conductance as a function of level position and applied bias voltage. Thick black lines mark the onset of transport through the dot. Blue dashed lines indicate the onset of impurity excitations. Dashed lines mark the gaining of energy from the impurity to allow all three charge states of the dot.

i.e., the current now also depends on the interference term. From Eq. (5.32), we infer that for $\Gamma_\mathrm{R} = SJ_\mathrm{R}$ the current vanishes exactly in region III. Equation (5.32) also shows that the current in region III is only sensitive to the absolute value of the interference term but not to its sign η.

This is different in the regime where the empty and singly-occupied dot contribute to transport and spin excitations are possible. As the analytic result for the current in this regime is rather lengthy, we do not give it here. Instead, we now focus on transport for parallely magnetized leads. In region I, the current is now given by

$$I_\mathrm{I} = \frac{2\Gamma_\mathrm{L}\left(\Gamma_\mathrm{R} + S^2 J_\mathrm{R} + 2pS\eta\sqrt{\Gamma_\mathrm{R} J_\mathrm{R}}\right)}{\Gamma_\mathrm{L} + 2\left(\Gamma_\mathrm{R} + S^2 J_\mathrm{R}\right)}. \tag{5.33}$$

Here, the current is clearly sensitive to the sign of the interference term which provides a way to access it in experiments. Similar expressions for the current in regions II and III can be found for parallely magnetized leads. As these expressions are rather lengthy, we do not give them here.

Spin spectroscopy

Inelastic spin tunneling spectroscopy [133, 190–197, 199, 200] allows to determine the spectrum of a spin embedded in a tunnel barrier by studying the steps in the differential conductance that occur whenever an inelastic transport channel opens up. However, for a simple spin Hamiltonian of the form (5.4) this does not allow to determine the parameters D and B separately. In this case, the energy difference between the ground state and the first excited state is larger than all other excitation energies. In

consequence, as soon as the system can be brought into the first excited state, all other excited states can also be reached energetically. Hence, there would be only a signal at $\Delta = E_{S-1} - E_S = (2S-1)D + B$.

This is different for the system additionally containing a quantum dot between the electrodes, as is shown schematically in Fig. 5.4. For level positions $\varepsilon < -U$, the dot is doubly occupied when no bias is applied. Upon increasing the bias, we enter region I where transport takes place through the singly- and doubly-occupied dot. When increasing the bias voltage above the blue dashed line, exciting the spin becomes possible, similarly as in a single barrier discussed above which only provides information about a linear combination of D and B. However, upon increasing the bias further, we reach the red dotted line. At this point, the electron on the dot with an energy below the right Fermi level can gain enough energy to leave the dot to the right lead by changing the impurity state from $S_z = S-1$ to $S_z = S$. As this opens up a new transport channel, the onset of this process yields a signal in the differential conductance. Similarly, at the next green line the process $|\downarrow\rangle \otimes |-S+1\rangle \rightarrow |0\rangle \otimes |-S\rangle$ becomes possible, again giving rise to a conductance signal. This scheme continues for all transitions of the impurity spin which are characterized by transition energies $(2S_z - 1)D + B$ for $S_z > 0$ and $(-(2S_z + 1)D - B)$ for $S_z < 0$. When we finally reach the thick black line, the empty dot state can also be reached by ordinary tunneling events. For even larger bias voltages we find another series of conductance signals which are now associated with electrons in the lower level which become able to excite the impurity when leaving to the right lead. The important difference to the small bias case discussed above is that now transport through the upper level can bring the impurity spin into all excited states such that transitions between these states also are all visible.

For unpolarized leads, the conductance pattern discussed above allows to determine D and the absolute value of B. As no spatial direction is distinguished, there is no possibility to determine also the sign of B. This is different for polarized leads where the spatial symmetry is broken by the magnetizations. In this case, one finds that the differential conductance shows an alternating pattern of positive and negative differential conductance which depends on the sign of B. We discuss the mechanism leading to this behaviour in the following.

Current-induced switching and spin-dependent transport

Here, we discuss the dynamics of the dot and impurity spin that gives rise to the sequence of positive and negative differential conductance features at the red and green dotted lines in Fig. 5.4 for polarized electrodes and which is manifest in the current oscillations of the I-V characteristics shown in Fig. 5.5. (In our discussion, we focus on the case $B > 0$. For $B < 0$, the impurity ground state is $|-S\rangle$ and basically the role of the cases $\eta = +1$ and $\eta = -1$ are interchanged.)

As tunneling into a ferromagnet is spin-dependent, we find that the rates for the impurity spin transitions $|m\rangle \rightarrow |m+1\rangle$ and $|m\rangle \rightarrow |m-1\rangle$ are different in general, because one transition involves tunneling of a minority spin electron, while the other involves tunneling of a majority spin electron. We therefore have for the rates $W_{m\rightarrow m+1} \propto 1 - p$ and $W_{m\rightarrow m-1} \propto 1 + p$. In consequence, once exciting the impurity spin becomes energetically possible, the spin-polarized current through the right bar-

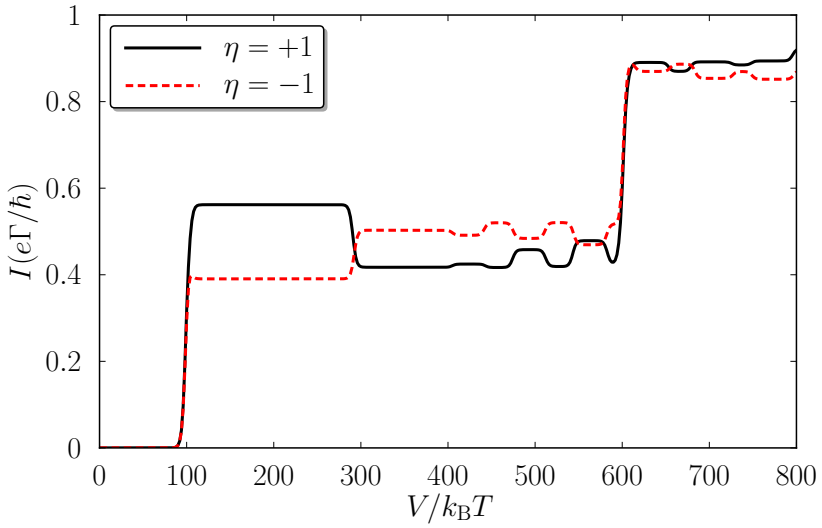

Figure 5.5: Current as a function of bias voltage for parallel magnetizations, $p = 0.3$ and $\Gamma_{\mathrm{L}} = \Gamma_{\mathrm{R}} = J_{\mathrm{R}}$. Other parameters are the same as in Fig. 5.3.

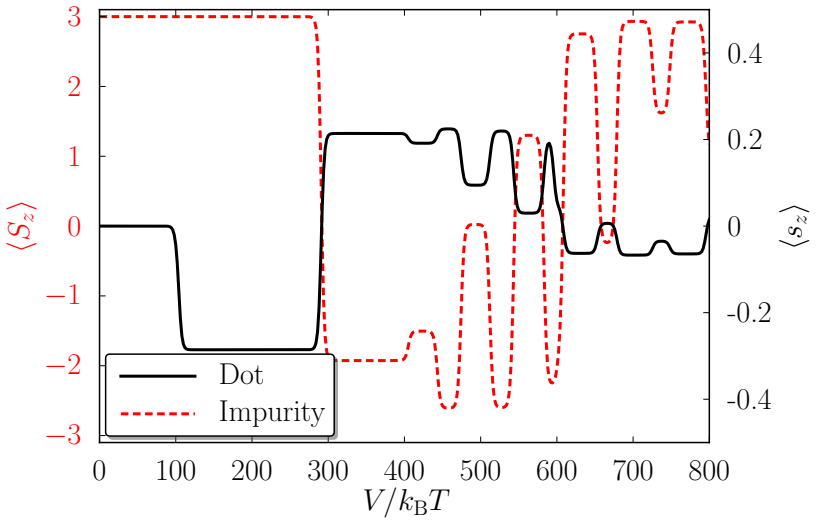

Figure 5.6: Average z component of dot and impurity spin as a function of bias voltage for $\eta = +1$. Other parameters are the same as in Fig. 5.5.

rier has the tendency to flip the impurity spin into the state $|-S\rangle$ which in Fig. 5.5 and 5.6 occurs at $V = 2(\varepsilon + U + \Delta) = 295 k_{\mathrm{B}}T$.

At larger bias, transitions where energy is gained from the impurity come into play. Alternatingly, they either lower the z component of the impurity spin, $|-S+i\rangle \rightarrow |-S+i-1\rangle$, or raise it, $|S-i\rangle \rightarrow |S-i+1\rangle$, with $i \in [0, S]$. Hence, the expectation value of S_z is found to oscillate as a function of bias voltage as is shown in Fig. 5.6.

The other key ingredient for understanding the conductance oscillations is the fact that tunneling through the right barrier is spin-dependent in two respects. On the one hand, there is the dependence on the spin of the tunneling electron due to the polarization of the lead, mentioned already above. However, the tunneling also depends on the state of the impurity spin as the tunneling rate for spin up (down) electrons is proportional to $|t_{\mathrm{R}} + S_z j_{\mathrm{R}}|^2$ ($|t_{\mathrm{R}} - S_z j_{\mathrm{R}}|^2$). This kind of spin-dependence is then responsible for relating the dot spin to the impurity spin state. If, e.g., the impurity is in the ground state $|+S\rangle$, spin up electrons can leave more easily to the right lead than spin down electrons. This results in a spin down accumulating on the quantum dot, see Fig. 5.6, $2(\varepsilon+U) < V < 2(\varepsilon+U+\Delta)$. When the z component of the impurity spin has a negative expectation value, the situation is reversed. Now, spin down leaves the dot more easily such that spin up accumulates on the dot.

The spin accumulation on the dot affects the current through the system. If the lower dot level is occupied by a spin up electron, Pauli principle prevents a second spin up electron to enter the dot while transport of spin down electrons is suppressed by their smaller density of states. Hence, the accumulation of spin up on the dot suppresses the current. On contrary, a spin down in the lower level does hardly affect the current, as it can proceed by spin up electrons tunneling through the upper level.

Hence, in symmary we find that the interplay between the current-induced switching of the impurity spin and the spin-dependent tunneling through the right barrier results in an interesting spin dynamics in the quantum-dot spin valve which manifests itself in the transport properties of the system. We emphasize that the transport signatures discussed here are present for moderate polarizations. Hence, the polarizations of Fe, Co or Ni [14, 228] should be sufficient to experimentally detect them. For very large polarizations, the current oscillations discussed above are even absent, because in this case the current-induced switching mechanism is so strong that the impurity will be kept in state $|-S\rangle$ once spin excitation becomes possible.

Giant Fano factor

In the above discussion of the current oscillations, we found the current to be sensitive to the average impurity spin only. The current noise however sheds more light on the dynamics of the impurity spin. As can be seen in Fig. 5.7, in the region where energy can be gained from the impurity to allow electrons to leave the dot to the right (corresponding to the region of dotted lines in Fig. 5.4), the Fano factor is strongly enhanced (note the logarithmic scale).

The mechanism which gives rise to these giant Fano factors is the following. As can be seen in the upper panel of Fig. 5.8, the probability to find the impurity in the states $|\pm S\rangle$ is finite for both states in the region where the Fano factor becomes large. The dot spin follows the behaviour of the impurity spin which means that it will point either up or down, depending on the sign of S_z as shown in the middle and lower panel

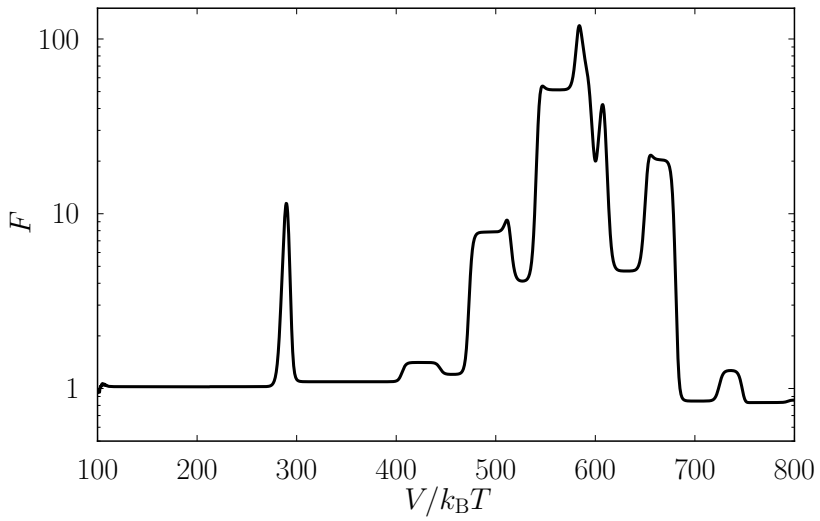

Figure 5.7: Fano factor as function of bias voltage. Parameters are the same as in Fig. 5.6.

of Fig. 5.8. The two dot spin configurations carry a different current, because only for the spin up accumulation transport through the dot becomes spin-blockaded. Hence, the system switches between two current states on a rather large time scale (as it takes several spin flip processes to reverse the impurity spin) which gives rise to random telegraph noise. Similar behaviour can be found, e.g., in arrays of moveable colloid particles [229], transport through molecules with strong electron-phonon coupling and strong vibrational relaxation [143] or double dot Aharonov-Bohm interferometers [103].

It is interesting to note that the giant Fano factor occurs for parallel as well as antiparallel magnetizations. This is due to the fact that the moderate polarizations chosen here the effects of bunching for parallel magnetizations and spin blockade for antiparallel magnetizations are rather weak such that they are unimportant compared to the random telegraph switching.

5.3.1 Noncollinear magnetizations

So far, we only discussed the transport properties for nonmagnetic or collinearly magnetized electrodes. When dealing with noncollinear magnetizations, a new physical effect comes into play: the precession of the dot spin in an exchange field generated by virtual tunneling between the dot and the leads. As discussed in Section 2.4, the interplay between spin accumulation and spin precession gives rise to a number of characteristic transport signatures. In the following, we discuss how the dependence of the exchange field on the state of the impurity spin influences the transport properties, in particular the current and the finite-frequency Fano factor.

Current

As discussed in Section 2.4.3, the current-voltage characteristics of a normal quantum-dot spin valve provides information about the exchange field acting on the dot spin.

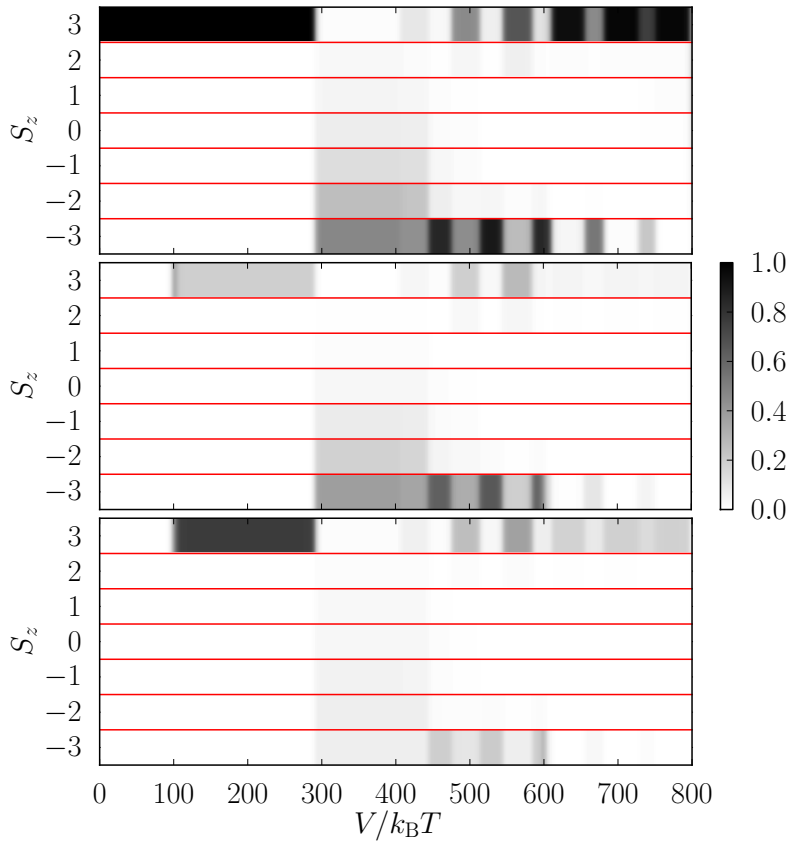

Figure 5.8: Probabilities to find the impurity in spin state $|S_z\rangle$ as a function of bias voltage (upper panel). The middle (lower) panel shows the probability to find the system in the state $|\uparrow\rangle \otimes |S_z\rangle$ ($|\downarrow\rangle \otimes |S_z\rangle$). Parameters are the same as in Fig. 5.6.

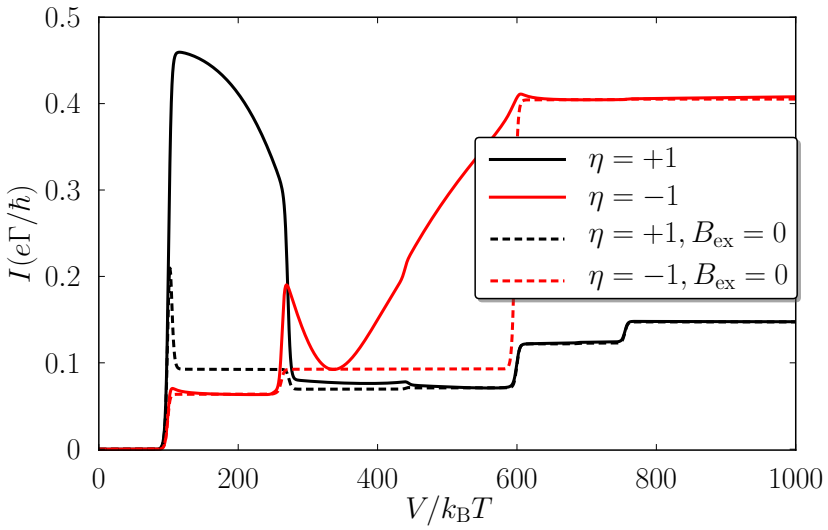

(a)

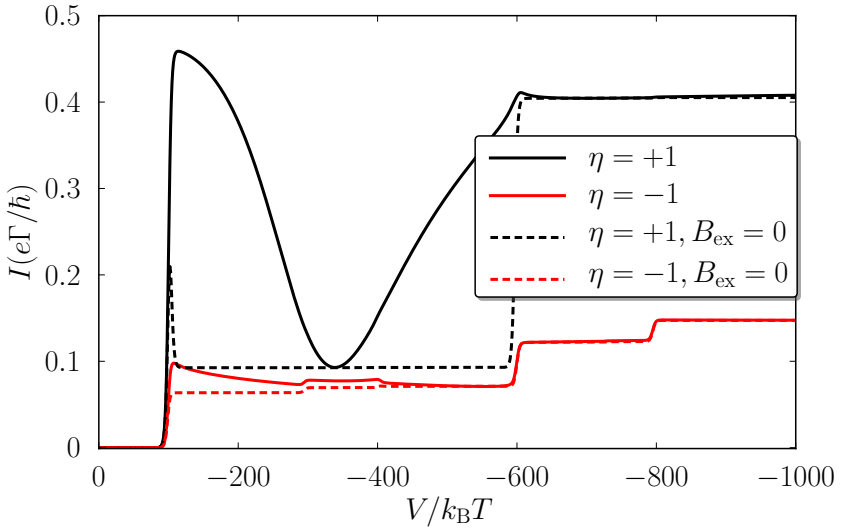

(b)

Figure 5.9: Current as a function of bias voltage for perpendicular magnetizations for $p = 0.9$ and $\Gamma_{\mathrm{L}} = \Gamma_{\mathrm{R}} = 10J_{\mathrm{R}}$. Black curves are for $\eta = +1$ while red curves are for $\eta = -1$. For the upper panel, $\varepsilon = -300k_{\mathrm{B}}T$ while for the lower panel $\varepsilon = 50k_{\mathrm{B}}T$. Other parameters as in Fig. 5.3. While the solid lines represent the full result, for the dashed curves the exchange field was set to zero by hand.

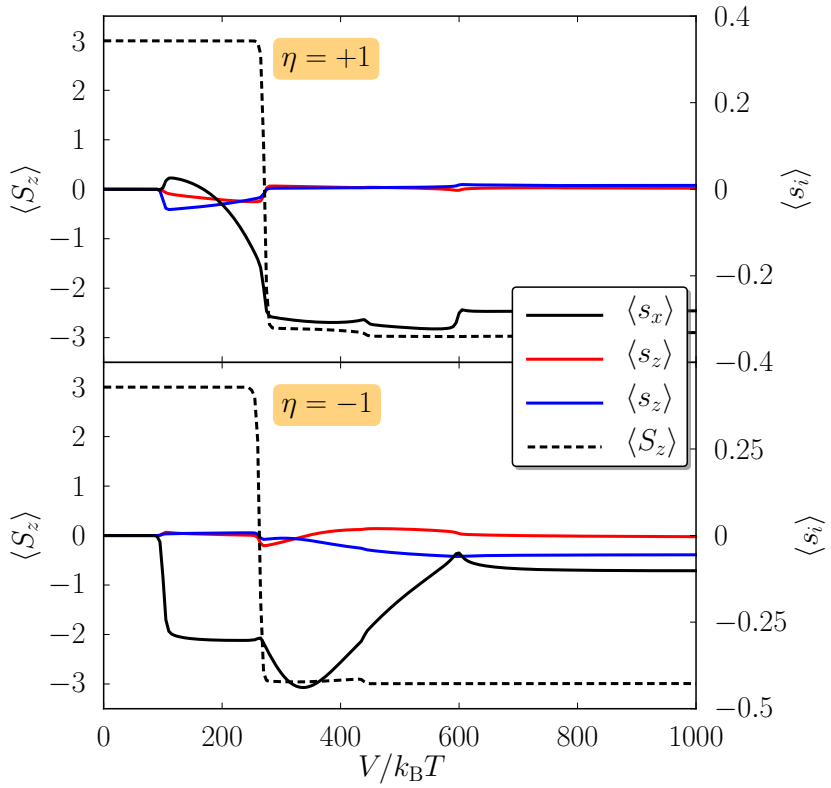

Figure 5.10: x, y and z component of the average dot spin and z component of the average impurity spin for perpendicular magnetizations as function of bias voltage for positive (upper panel) and negative (lower panel) sign of the interference term. Parameters as in Fig. 5.9(a).

For the quantum-dot spin valve with an impurity embedded in one of the tunnel barriers studying the current as a function of bias voltage allows us to investigate the dependence of the exchange field on the state of the impurity. We will first focus on the situation where the interference term has positive sign and $V > 0$. In this case, if the impurity is in state $|+S\rangle$, there is a large exchange field acting on the dot spin (cf. Fig. 5.3), giving rise to a strong precession and thereby to a clear lifting of the spin blockade. If the impurity is in state $|-S\rangle$, however, there is only a small exchange field acting on the dot. Consequently, the spin blockade persists and the current is not much enhanced by the exchange field.

As is shown in Fig. 5.9(a) (solid black curve), we therefore find a large current at the onset of transport through the quantum dot. When increasing the bias voltage, the current decreases slightly as the exchange field becomes weaker. When the bias voltage is increased above the threshold for impurity excitations, the impurity is switched from its ground state $|+S\rangle$ into the state $|-S\rangle$ by the spin polarized current (cf. upper panel of Fig. 5.10). Consequently, the exchange field changes abruptly at threshold towards smaller values. This implies that the spin blockade on the dot cannot be lifted anymore and the current is suppressed compared to its values below threshold.

When the interference term has a negative sign (red curves in Fig. 5.9(a)), the situation is reversed. Now the exchange field takes on small values when the impurity is in state $|+S\rangle$ while it takes large values when the impurity is in state $|-S\rangle$. Hence, the current is now suppressed below threshold, while above threshold we find a nontrivial bias dependence of the current due to the energy dependence of the exchange field.

When a negative bias voltage is applied, no switching occurs at the impurity excitation threshold as the spin-polarized current has the tendency to bring the impurity into the state $|+S\rangle$ which is the ground state. We therefore find that now the exchange field effects are clearly visible for a positive sign of the interference term, while they are very small for a negative interference term.

In summary, we have shown how the current-voltage characteristics for noncollinear magnetizations provide access to the dependence of the exchange field on the impurity spin state as well as to the sign of the interference term. We note however, that the observation of exchange field effects in the current relies on large polarizations.

Frequency-dependent Fano factor

The effects of the exchange field switching on the I-V characteristic occur only for large polarizations as otherwise the spin blockade on the dot is too weak. Another method to gain information about the exchange field which also works for smaller polarizations is to study the frequency-dependent Fano factor [67].

In Fig. 5.11, the frequency-dependent Fano factor is shown for different bias voltages and different parameters of the spin Hamiltonian. Parameters are chosen such that for the smaller of the two bias voltages (black curves) the impurity spin cannot be excited. For the larger bias voltage, the impurity parameters allow an excitation of the impurity spin only for the red solid curves, while for the red dashed curves the impurity still stays in the ground state.

For large polarizations and voltages below the excitation threshold, the finite-frequency noise shows a peak at the Larmor frequency of the exchange field. As the impurity is

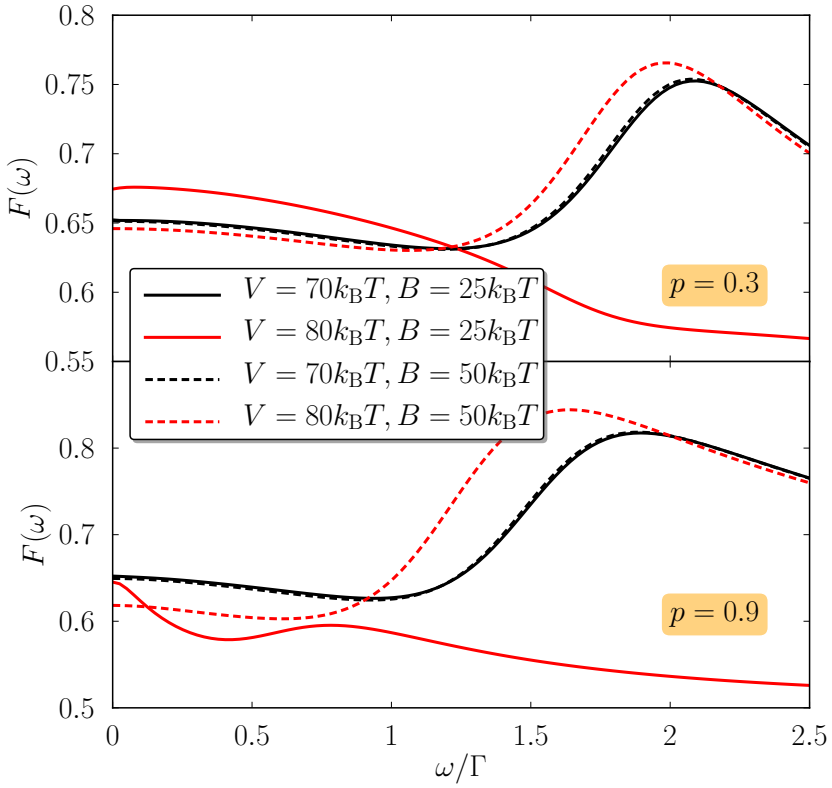

Figure 5.11: Frequency-dependent Fano factor for moderate ($p = 0.3$, upper panel) and large ($p = 0.9$, lower panel) polarizations. For $p = 0.3$, an external magnetic field perpendicular $B_{\text{ext}} = 1.5\Gamma$ is applied to the quantum dot alongs its quantization axis. Other parameters are the same as in Fig. 5.9, except that now $D = 0$ and $\eta = +1$.

in the ground state, the system is not sensitive to the impurity parameters and both curves practically coincide. If the bias is increased but the impurity stays in the ground state, the absolute value of the exchange field is slightly reduced, cf. lower panel of Fig. 5.3, resulting in a small shift of the resonance signal towards smaller frequencies. If the bias is increased and a switching of the impurity spin occurs, we instead find that the exchange field is significantly reduced, cf. Fig. 5.3, and therefore the resonance peak is also shifted to much smaller frequencies. Hence, by detecting the resonance frequency as a function of bias voltage one can gain information about the switching of the exchange field as a consequnce of the switching of the impurity spin.

For small polarizations, the effect does not work the same way as just described. Now, the exchange field just changes sign upon switching the impurity spin, cf. Fig. 5.3. Therefore, no clear shifting of the resonance position occurs. To overcome this problem, an external magnetic field of strength comparable to the exchange field can be applied perpendicularly to the plane defined by the electrode magnetizations. Now, the position is defined by the Larmor frequency of the total magnetic field while the form of the resonance signal depends on the relative angle between external field and exchange field as can be seen in the upper panel of Fig. 5.11. If the impurity spin stays in the ground state, a peak shows up in $F(\omega)$ while a shoulder occurs at the Larmor frequency if the impurity spin can be switched by the current.

Hence, we have shown that the switching of the exchange field can be monitored also for moderate polarizations by measuring the finite-frequency current noise for a series of applied bias voltages.

5.4 Results - Impurity on the dot

In this section, we discuss the transport properties of a quantum-dot spin valve containing an additional spin 1/2 on the quantum dot. We will focus on the two transport regimes (ii) and (v) introduced above, cf. Tab. 5.2. In these regimes, the exchange coupling is small, $J \lesssim \Gamma$, making them particularly suited to describe the influence of nuclear spins on transport through a quantum-dot spin valve. In regime (ii), the externally applied magnetic field B is much larger than the tunnel coupling between dot and leads. In this regime, we show that the coherent superpositions of the singlet and one of the triplet states do not show up in the current. However, they lead to a signature in the finite-frequency Fano factor. In regime (v), the external magnetic field is weak, $B \lesssim \Gamma$. In this case, we discuss how to extract the exchange coupling and external field from measurements of the finite-frequency Fano factor.

5.4.1 Large magnetic field

We start our discussion with the case $B \gg \Gamma$, $J \lesssim \Gamma$ where only superpositions of the singlet S and the triplet state T^0 are relevant. In Fig. 5.12 we show schematically the differential conductance as a function of bias voltage V and level position ε. The thick black lines indicate where a dot level is in resonance with either the left or right Fermi energy. Hence, they separate the Coulomb-blockaded regions from the regions where sequential through the dot is possible. For concreteness, we will now discuss the sequence of transport processes that come into play upon increasing the bias voltage for a fixed level position $\varepsilon = B/2$. For small bias voltages, transport is possible only

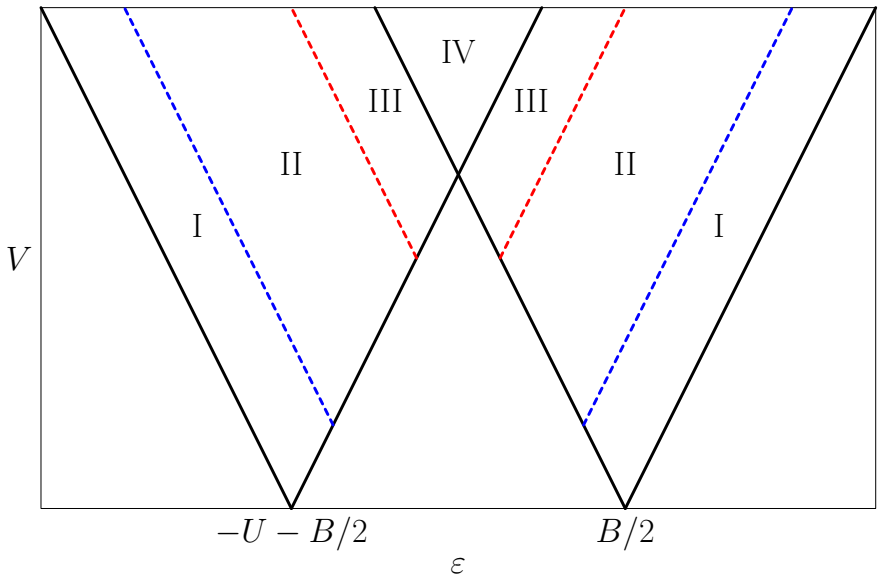

Figure 5.12: Schematic of the conductance for the situation where $B \gg \Gamma$, $J \lesssim \Gamma$. The lines indicate peaks in the differential conductance.

through the states $|0\downarrow\rangle$ and $|T^-\rangle$ as transitions from $|0\downarrow\rangle$ to any of the other singly occupied states are energetically forbidden while transitions from $|T^-\rangle$ to $|0\uparrow\rangle$ are impossible as they violate spin conservation.

When the bias voltage is increased across the blue dashed line, the bias window becomes large enough to also allow transitions from $|0\downarrow\rangle$ to $|T^0\rangle$ and $|S\rangle$. As for both of these states there is a finite probability to find the impurity spin in state $\uparrow$, both, $|T^0\rangle$ and $|S\rangle$, can serve as a starting point for a transition into the state $|0\uparrow\rangle$ which then allows transitions into state $|T^+\rangle$. Hence, we find that as soon as the bias is large enough to excite the $|0\downarrow\rangle$-$|T^0\rangle$ and $|0\downarrow\rangle$-$|S\rangle$ transition, all empty and singly occupied dot states contribute to transport.

Upon increasing the bias voltage further across the red dashed line, another set of transport processes becomes energetically possible. While transitions from singly occupied dot state with the lowest energy, $|T^-\rangle$, to the doubly occupied state $|d\downarrow\rangle$ are still not possible, it is nevertheless possible to occupy the dot with two electrons by taking as a starting point either $|T^0\rangle$ or $|S\rangle$.

Finally, when crossing another black line, the bias voltage is large enough to allow transitions between any two dot states that conserve spin.

Approximating the Fermi function as step functions, one can derive the following analytical expressions for the current through the quantum dot in the different transport

regimes:

$$I_{\mathrm{I}} = \frac{\Gamma_{\mathrm{L}}\Gamma_{\mathrm{R}}}{\Gamma_{\mathrm{L}}+\Gamma_{\mathrm{R}}} = \frac{1-a^2}{2}\Gamma, \tag{5.34}$$

$$I_{\mathrm{II}} = \frac{2\Gamma_{\mathrm{L}}\Gamma_{\mathrm{R}}}{2\Gamma_{\mathrm{L}}+\Gamma_{\mathrm{R}}} = \frac{2(1-a^2)}{3+a}\Gamma, \tag{5.35}$$

$$I_{\mathrm{III}} = \frac{\Gamma_{\mathrm{L}}\Gamma_{\mathrm{R}}(\Gamma_{\mathrm{L}}+2\Gamma_{\mathrm{R}})}{\Gamma_{\mathrm{L}}+\Gamma_{\mathrm{R}}} = \frac{(3-a)(1-a^2)}{4}\Gamma, \tag{5.36}$$

$$I_{\mathrm{IV}} = \frac{2\Gamma_{\mathrm{L}}\Gamma_{\mathrm{R}}}{\Gamma_{\mathrm{L}}+\Gamma_{\mathrm{R}}} = (1-a^2)\Gamma. \tag{5.37}$$

The Fano factor at zero frequency is given by

$$F_{\mathrm{I}} = \frac{\Gamma_{\mathrm{L}}^2+\Gamma_{\mathrm{R}}^2}{(\Gamma_{\mathrm{L}}+\Gamma_{\mathrm{R}})^2} = \frac{1}{2}(1+a^2), \tag{5.38}$$

$$F_{\mathrm{II}} = \frac{4\Gamma_{\mathrm{L}}^2+\Gamma_{\mathrm{R}}^2}{(2\Gamma_{\mathrm{L}}+\Gamma_{\mathrm{R}})^2} = \frac{5+6a+5a^2}{(3+a)^2}, \tag{5.39}$$

$$F_{\mathrm{III}} = \frac{\Gamma_{\mathrm{L}}^3+3\Gamma_{\mathrm{L}}^2\Gamma_{\mathrm{R}}+\Gamma_{\mathrm{R}}^2}{(\Gamma_{\mathrm{L}}+\Gamma_{\mathrm{R}})^3} = \frac{1}{8}(5+3a+3a^2-3a^3), \tag{5.40}$$

$$F_{\mathrm{IV}} = \frac{\Gamma_{\mathrm{L}}^2+\Gamma_{\mathrm{R}}^2}{(\Gamma_{\mathrm{L}}+\Gamma_{\mathrm{R}})^2} = \frac{1}{2}(1+a^2). \tag{5.41}$$

It is interesting to note that these expressions are precisely the same as found by Thielmann et al. [230] for transport through a single-level quantum dot subject to a large magnetic field coupled to normal leads. Hence, in the chosen parameter regime, the current through the system and the zero-frequency Fano factor are neither sensitive to the presence of the impurity spin nor to the presence of ferromagnetic leads. The absence of any magnetoresistance is due to the presence of the large external field perpendicular to the plane spanned by the magnetizations which renders the system insensitive to the relative orientation of the magnetizations in this plane.

The fact that the system is insensitive to the presence of the impurity spin and to the coherent superpositions between $|S\rangle$ and $|T^0\rangle$ deserves some further investigation. Typically in systems where coherent superpositions of different states have to be taken into account as, e.g., a normal quantum-dot spin valve [64, 65] or double quantum dots [156], the current shows a nontrivial bias dependence with broad regions of negative differential conductance due to the energy-dependent level renormalization that arises from virtual tunneling between the dot and the leads. Such effects are clearly absent here. To understand this behaviour, we analyze the term describing the isospin accumulation, Eq. (5.18), in more detail. Due to the Fermi functions in this expression, a finite isospin accumulation can arise only in the regions marked III in Fig. 5.12. When plugging in the expressions for the occupation probabilities, we find however that

$$\left(\frac{d\mathbf{I}}{dt}\right)_{\mathrm{acc}} = \left(-\Gamma_{\mathrm{L}}\frac{\Gamma_{\mathrm{L}}^2\Gamma_{\mathrm{R}}^2}{4(\Gamma_{\mathrm{L}}+\Gamma_{\mathrm{R}})^2(\Gamma_{\mathrm{L}}^2+2\Gamma_{\mathrm{L}}\Gamma_{\mathrm{R}}+2\Gamma_{\mathrm{R}}^2)} + \Gamma_{\mathrm{R}}\frac{\Gamma_{\mathrm{L}}^3\Gamma_{\mathrm{R}}}{4(\Gamma_{\mathrm{L}}+\Gamma_{\mathrm{R}})^2(\Gamma_{\mathrm{L}}^2+2\Gamma_{\mathrm{L}}\Gamma_{\mathrm{R}}+2\Gamma_{\mathrm{R}}^2)}\right)\mathbf{e}_x = 0, \tag{5.42}$$

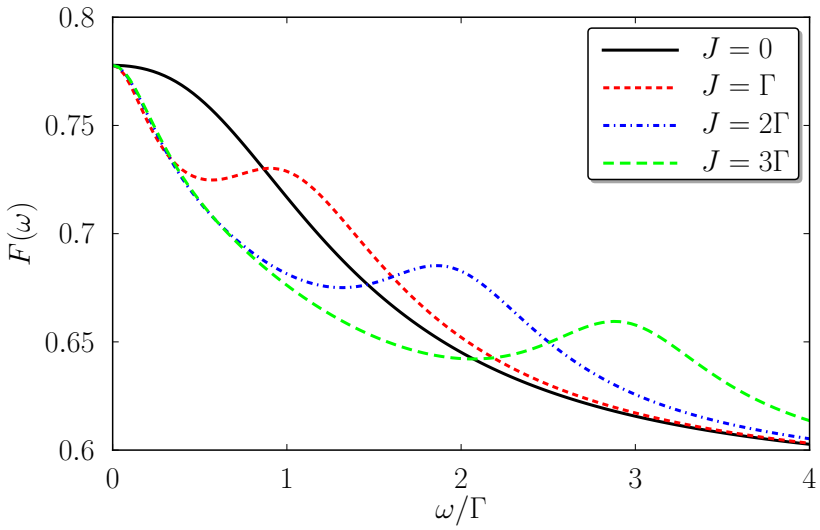

Figure 5.13: Finite-frequency Fano factor for different values of the exchange coupling J. The Fano factor shows a peak at the Larmor frequency associated with the exchange field. Parameters are $\Gamma_\mathrm{L} = 2\Gamma_\mathrm{R}$, $k_\mathrm{B}T = 10\Gamma_\mathrm{L}$, $B = 50k_\mathrm{B}T$, $U = 5B$, $\varepsilon = B/2$ and $V = 11B$.

i.e., the contributions to the isospin accumulation from the left and right lead cancel precisely. In consequence, the isospin vanishes on average in the stationary state such that the aforementioned level renormalization effects cannot influence the current and zero-frequency noise.

So far, it seems that the coherent superpositions of $|S\rangle$ and $|T^0\rangle$ do not influence the transport through the system at all, such that a description in terms of ordinary rate equations which neglects the coherences suffices. This is not true, however, as can be seen from the finite-frequency Fano factor, which is shown in Fig. 5.13. Here, apart from the usual peak which arises at zero frequency, the Fano factor additionally shows a peak associated with the Larmor frequency of the exchange field (5.20). The coherent superpositions play a role here as the finite-frequency noise is sensitive to the dynamics of the dot spins while the current only captures stationary properties of the quantum dot. While the contributions form the left and right lead to the isospin accumulation cancel on average, indivdual processes can nevertheless give a finite isospin accumulation.

In contrast to the normal quantum-dot spin valve, where the Larmor frequency associated with the exchange field depends on the level position and applied bias voltage [67], we find that in the system under investigation here, the Larmor frequency is simply given by the exchange coupling strength J. This is due to the fact that the energy-dependent contributions to the exchange field arise only in the x component which is parallel to the isospin accumulating on the dot and hence cannot influence its precessional motion. The frequency-dependent Fano factor may therefore be used to experimentally determine the exchange coupling.

5.4.2 Small magnetic field

In the last section, we saw that coherent superpositions can give rise to a signal in the frequency-dependent Fano factor $F(\omega)$ which could be interpreted as the precession of the isospin with the Larmor frequency of the exchange field. In the case where $B, J \lesssim \Gamma$, the situation is more complicated as now superpositions between any two states with the same number of electrons on the dot have to be taken into account.

In Fig. 5.14, we show the finite-frequency Fano factor $F(\omega)$ as a function of the frequency ω and the externally applied magnetic field B for fixed exchange coupling J and vice versa. In both cases, the Fano factor shows a number of features at frequencies which all show a nontrivial dependence on the external field B and the exchange coupling J. To gain a better understanding of these features, we consider a simpel spin model for the quantum dot. This is reasonable as the dot is singly occupied most of the time for the chosen parameters due to the asymmetric coupling to the leads. We model the dot as consisting of two spin 1/2 particles that are exchange coupled and subject to external magnetic fields. While the impurity spin only couples to the externally applied field, the electron spin additionally experiences the exchange field generated by quantum charge fluctuations on the dot. Hence, the Hamiltonian of our model is given by

$$H = J\mathbf{S}_1 \cdot \mathbf{S}_2 + \mathbf{B}_1 \cdot \mathbf{S}_1 + \mathbf{B}_2 \cdot \mathbf{S}_2, \tag{5.43}$$

where $\mathbf{B}_1 = B_{\mathrm{ex,L}}\mathbf{n}_\mathrm{L} + B_{\mathrm{ex,R}}\mathbf{n}_\mathrm{R} + B\mathbf{e}_z$ is the sum of the external magnetic field and the exchange field while $\mathbf{B}_2 = B\mathbf{e}_z$ is simply given by the external field. To show that this is indeed the correct way to describe the quantum dot system, in Appendix D we give the equation of motion for the density matrix elements of the two spins. Comparing them to the master equation for the quantum dot system, Eq. (5.23)-(5.28), shows the correspondence between the two systems. The only difference is the absence of dissipative terms in the equations for the spin model.

The differences between the energies of the various eigenstates of Eq. (5.43) as a function of exchange coupling and external field are indicated as black dotted lines in Fig. 5.14. We find a nice agreement between these energy differences and the features observed in the Fano factor. On the one hand, this indicates that the finite-frequency Fano factor is indeed sensitive to level splittings comparable to the tunnel couplings which cannot be resolved in the differential conductance as the conductance peaks are broadened by temperature which satisfies $\Gamma \ll k_\mathrm{B}T$. This can provide experimental access, e.g., to the coupling between the dot and impurity spin.

On the other hand, our results nicely demonstrate that the exchange field which arises due to virtual tunneling processes and *not* due to stray fields from the ferromagnetic leads, acts only on the electron spin but not on the impurity spin. If one could measure the Fano factor at finite frequency as computed above, one could therefore clearly distinguish exchange field effects from stray field effects as the latter ones would act in the same way on both spins and thereby give rise to a trivial dependence of the energy differences on the exchange coupling and the external field.

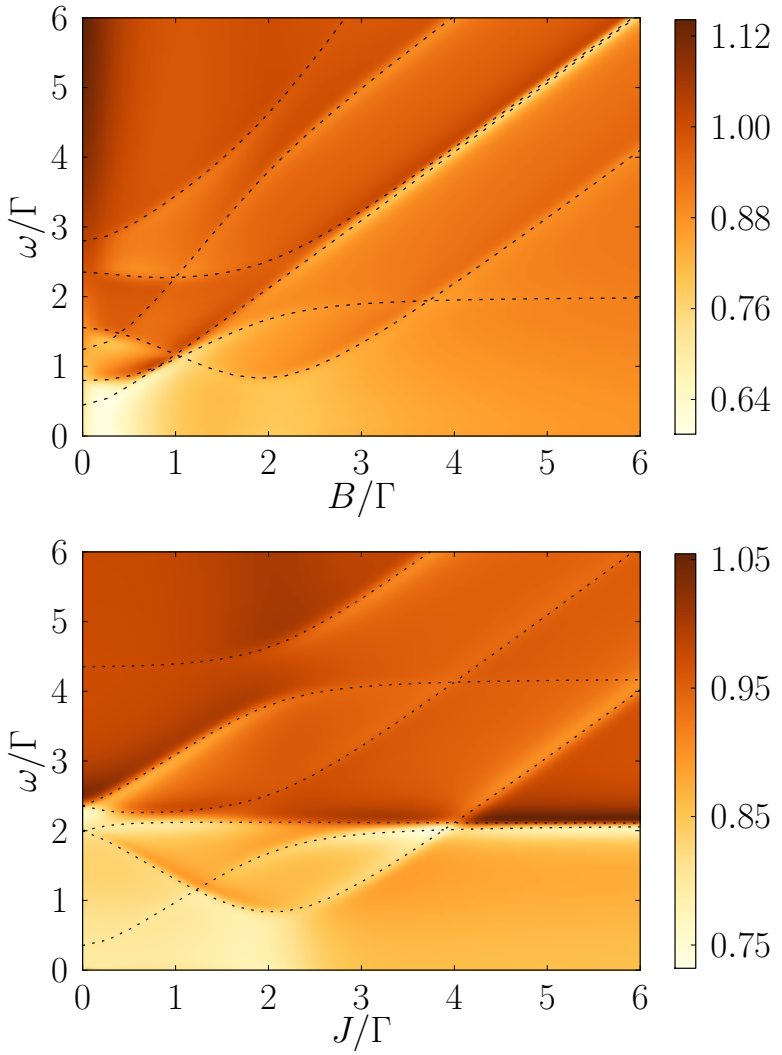

Figure 5.14: Frequency-dependent Fano factor as a function of frequency and external magnetic field (upper panel) or exchange coupling (lower panel). The level splittings calculated for a system of two exchange coupled spins in a magnetic field which is the sum of the exchange fields and the external fields are indicated by lines. $J = 2\Gamma$, $\Gamma_{\mathrm{L}} = 10\Gamma_{\mathrm{R}} = 0.05 k_{\mathrm{B}}T$, $\varepsilon = 50 k_{\mathrm{B}}T$, $V = 105 k_{\mathrm{B}}T$, $U = 150 k_{\mathrm{B}}T$, $p = 0.9$, $\phi = \pi/2$.

5.5 Summary

In this chapter, we investigated transport through quantum-dot spin valves containing magnetic impurities. First, we considered the case where the impurity is localized in one of the tunnel barriers. We found that for tunneling through the barrier containing the impurity, interference between direct and exchange tunneling takes place even for nonmagnetic systems. This is in contrast to tunnel barriers where such interference effects arise only for magnetic electrodes or for higher-order transport. We furthermore pointed out how the Coulomb interaction on the dot allows a more detailed spectroscopy of the impurity spin. For magnetic electrodes, the spin-polarized current through the system can switch the spin of the impurity. As the state of the impurity spin influences the current, an interplay between the current and the impurity arises which gives rise to a series of positive and negative differential conductance as a function of bias voltage. We furthermore found that the dynamics of the impurity spin gives rise to a random telegraph signal associated with a huge Fano factor. Finally, we found that the exchange field acting on the dot spin becomes dependent on the impurity spin state. This dependence can be observed in the current as well as in the finite-frequency noise for noncollinear magnetizations.

Furthermore, we considered a magnetic impurity localized on the dot in the regime of small exchange coupling to the electron spin. For a large external magnetic field, only coherent superpositions between $|S\rangle$ and $|T^0\rangle$ are relevant. However, they influence neither the current nor the zero-frequency noise as they vanish in the stationary state. Nevertheless, as they can be excited in an individual tunneling process, they give rise to a signal in the finite-frequency noise at $\omega = J$. For small external magnetic fields, all coherences have to be taken into account. They give rise to a large number of features in the finite-frequency noise. These provide informations about the level splittings that are influenced by renormalization effects due to virtual tunneling to the leads. Hence, in this case the finite-frequency noise opens up the possibility to study experimentally the spin-spin coupling as well as the exchange field and their respective interplay.

6 Nonequilibrium current and noise in inelastic tunneling through a magnetic atom

In recent experiments [133, 196–201] the current flowing through a single magnetic atom adsorbed on a nonmagnetic substrate was measured by contacting the adatom with a scanning tunneling microscope tip. The resulting steps in the differential conductance could be explained in terms of inelastic tunneling events through the atom exciting it out of its ground state. However, so far, certain nonmonotonic features in the conductance have not been discussed. In this chapter, we explain these features in terms of a nonequilibrium occupation of the atom spin states. We furthermore predict that a nonequilibrium situation gives rise to a super-Poissonian Fano factor. Finally, we discuss that the remarkable absence of certain nonmonotonicities in the experiment hints at the presence of an anisotropic relaxation channel. The results presented in this chapter have previously been published in Ref. [195].

6.1 Introduction

Inelastic scattering processes provide a convenient tool to study the excitation spectra of various systems. By using inelastic electron tunneling spectroscopy, one can access vibrational excitations of ensembles of molecules in metallic tunnel junctions [231, 232] or single molecules in scanning tunneling microscope (STM) geometries [233]. The excitation energies reveal themselves as steps in the differential conductance whenever a new inelastic transport channel opens up. For the explanation of the measured signals, an equilibrium distribution of the molecule states was implicitly assumed. Further studies of molecular vibrations were performed using H_2 molecules [234], C_{60} molecules [235] in mechanical break junctions and suspended carbon nanotubes [236–238].

Recently, the investigation of magnetic properties and interactions on an atomic level became possible due to the advent of spin inelastic electron spectroscopy [133, 196–201]. Here, single magnetic atoms absorbed on a nonmagnetic substrate were contacted using an STM tip. Describing the atom in terms of a localized spin, Hirjibehedin *et al.* [133] related the positions of the conductance steps to the energy associated with transitions between different eigenstates, while the relative step heights depend on the matrix elements of the spin operator. A more complete theoretical description based on perturbation theory in the tunnel coupling [190–194] still relies on the assumption of equilibrium occupations.

While the above studies could explain the conductance steps assuming the atom spin to be in thermal equilibrium with the substrate, nonmonotonic features clearly present in the experimental results of Ref. [133] were not addressed. Conductance overshoots

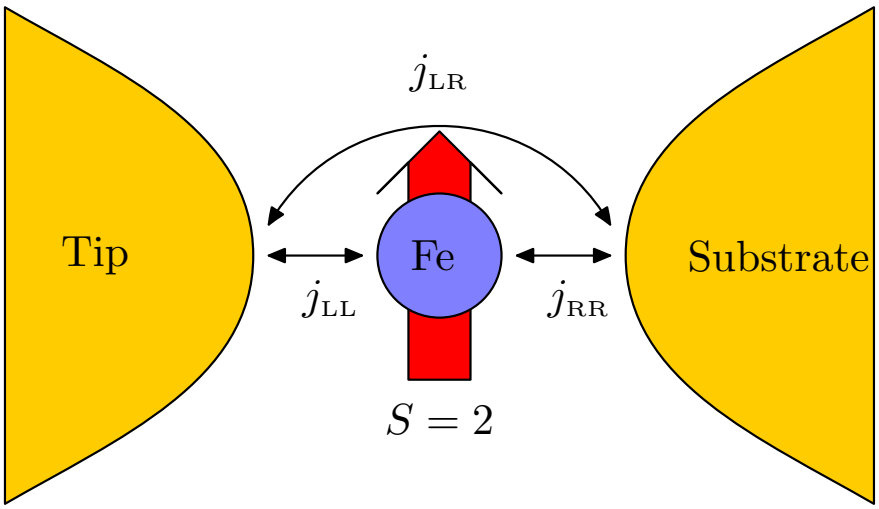

Figure 6.1: Schematic of the model under investigation. The iron atom is modelled as a single $S = 2$ spin embedded in a tunnel barrier between STM tip and substrate. It is coupled to the spin of the tunneling electrons via an exchange interaction with strength $j_{rr'}$.

due to nonequilibrium occupations together with their relaxation by spin-phonon interactions have been discussed in Ref. [239] for cotunneling through a quantum dot. A similar behaviour was found in Refs. [240–242] where additionally the low-temperature nonequilibrium logarithmic Kondo enhancement of this overshoot was studied. While the Kondo effect is relevant for transport through a single cobalt atom studied in Ref. [199, 200], it is not important here. Nonequilibrium effects have been considered in Ref. [194] for spin-transfer torque on a single atom coupled to ferromagnetic substrates and tips. In Ref. [207], the nonequilibrium current and current noise through a single molecular magnet were analyzed in the charge fluctuation regime. In the following, we explain the experimental results by calculating the nonequilibrium occupations together with a spin-dependent relaxation channel using a master-equation approach. We, furthermore, predict an enhanced Fano factor indicating super-Poissonian current noise as a clear sign of a nonequilibrium situation.

6.2 Model

We model the experimental setup of Ref. [133] as two reservoirs of noninteracting electrons coupled by a tunnel barrier with an embedded spin as shown schematically in Fig. 6.1. Hence, the Hamiltonian describing the system is given by

$$H = \sum_r H_r + H_{\mathrm{spin}} + H_{\mathrm{tun}}. \tag{6.1}$$

Here $H_r = \sum_{\mathbf{k}\sigma} \varepsilon_{r\mathbf{k}} a^\dagger_{r\mathbf{k}\sigma} a_{r\mathbf{k}\sigma}$ models the two electrodes as reservoirs of noninteracting electrons with constant density of states ρ_r and electrochemical potential μ_r. The operator $a^\dagger_{r\mathbf{k}\sigma}$ creates an electron in lead $r = \mathrm{L,R}$ with momentum $\mathbf{k}$ and spin σ. The

$B_z = 7\,\mathrm{T}$	E_m(meV)	$\|2\rangle_z$	$\|1\rangle_z$	$\|0\rangle_z$	$\|-1\rangle_z$	$\|-2\rangle_z$
$\|0\rangle$	7.982	0.021	0	0.097	0	0.995
$\|1\rangle$	4.612	0.987	0	0.157	0	0.036
$\|2\rangle$	2.813	0	0.402	0	0.916	0
$\|3\rangle$	0.287	0	0.916	0	0.402	0
$\|4\rangle$	0.194	0.159	0	0.983	0	0.092

$B_x = 3\,\mathrm{T}$	E_m(meV)	$\|2\rangle_z$	$\|1\rangle_z$	$\|0\rangle_z$	$\|-1\rangle_z$	$\|-2\rangle_z$
$\|0\rangle$	6.392	0.697	0.032	0.161	0.032	0.697
$\|1\rangle$	6.236	0.704	0.069	0	0.069	0.704
$\|2\rangle$	2.444	0.069	0.704	0	0.704	0.069
$\|3\rangle$	1.005	0.030	0.612	0.500	0.612	0.030
$\|4\rangle$	0.577	0.114	0.354	0.851	0.354	0.114

Table 6.1: Eigenenergies E_m and eigenstates $|m\rangle$ of the spin Hamiltonian (6.2) in the basis $|S_z\rangle_z$ of the S_z eigenstates for a magnetic field applied in the z and the x direction, respectively.

local spin is described by

$$H_{\mathrm{spin}} = -DS_z^2 + E(S_x^2 - S_y^2) + g\mu_{\mathrm{B}}\mathbf{B}\cdot\mathbf{S}, \tag{6.2}$$

where the z axis is the magnetic easy axis of the atom in its coordination environment. For an $S = 2$ iron atom on Cu_2N, the best fit to the experimental results in Ref. [133] gives an uniaxial anisotropy $D = 1.55\,\mathrm{meV}$, a transverse anisotropy $E = 0.31\,\mathrm{meV}$ and a g-factor of $g = 2.11$. Finally, the tunneling Hamiltonian is given by the Appelbaum Hamiltonian [225]

$$H_{\mathrm{tun}} = \sum_{rr'\mathbf{k}\mathbf{k}'\sigma\sigma'} j_{rr'} a^\dagger_{r\mathbf{k}\sigma} \frac{\boldsymbol{\sigma}_{\sigma\sigma'}\cdot\mathbf{S}}{2} a_{r'\mathbf{k}'\sigma'}, \tag{6.3}$$

with $\boldsymbol{\sigma}$ denoting the Pauli matrices, which describes an exchange interaction between the spin of the tunneling electron and the local spin. We neglect direct tunneling through the barrier not involving the localized spin as it only gives rise to a bias-independent elastic background to the differential conductance. Interference terms between direct and exchange tunneling do not appear in the total current and shot noise since the contributions from spin-up and -down electrons cancel out each other for nonmagnetic electrodes. The above model has been studied extensively to describe molecular magnets. The Kondo effect induced by the transverse anisotropy [209–211] as well as Berry phase effects [243, 244] and the current-induced switching of the molecule spin [188] has been discussed.

We parametrize the couplings $j_{rr'}$ through the sum $J = j_{\mathrm{LL}} + j_{\mathrm{RR}}$ and the asymmetry $a = (j_{\mathrm{LL}} - j_{\mathrm{RR}})/(j_{\mathrm{LL}} + j_{\mathrm{RR}})$, i.e., $j^2_{\mathrm{LL}} = (1+a)^2J^2/4$, $j^2_{\mathrm{RR}} = (1-a)^2J^2/4$ and $j^2_{\mathrm{LR}} = j^2_{\mathrm{RL}} = (1-a^2)J^2/4$. While the couplings j_{LR} and j_{RL} are responsible for the current through the atom, which may be accompanied with a spin excitation or disexcitation, the couplings j_{LL} and j_{RR} do not contribute to the current but give rise to a transport-induced relaxation mechanism for the local spin only.

The probabilities P_m to find the spin in one of its eigenstates $|m\rangle$ with energy E_m obey the master equation

$$\frac{dP_m}{dt} = \sum_{m'} L_{mm'} P_{m'}, \tag{6.4}$$

where $L_{mm'} = W_{mm'} - \delta_{mm'} W_m$. The Fermi's golden rule transition rates $W_{mm'}$ are obtained as

$$W_{mm'} = \sum_{rr'\alpha=x,y,z} 2\pi |j_{rr'}|^2 \rho_r \rho_{r'} |\langle m|S_\alpha|m'\rangle|^2 \zeta(\mu_r - \mu_{r'} - \Delta_{mm'}), \tag{6.5}$$

where $\zeta(x) = x/(1-e^{-x/(k_\mathrm{B}T)})$ and $\Delta_{mm'} = E_m - E_{m'}$. The elements W_m follow from $\sum_m L_{mm'} = 0$, which guarantees the conservation of probability.

To compute the current and current noise, we employ the formalism of full-counting statistics adopted to system that can be described by rate equations [162, 245]. To this end, we introduce the matrix $W^\chi_{mm'}$ which is obtained from $W_{mm'}$ by multiplying each term in the sum (6.5) with a factor $e^{i\chi}$ if $r = \mathrm{L}, r' = \mathrm{R}$, $e^{-i\chi}$ if $r = \mathrm{R}, r' = \mathrm{L}$, and 0 otherwise, where χ is called a counting field. Furthermore, we define $L^\chi_{mm'} = W^\chi_{mm'} - \delta_{mm'} W_m$ (note that W_m does not contain the counting field χ). The smallest eigenvalue of $L^\chi_{mm'}$ defines the cumulant generating function $S(\chi)$, from which we can obtain the average current I and the current noise S by performing derivatives with respect to the counting field, $I = -ie\,(dS(\chi)/d\chi)|_{\chi=0}$ and $S = (-ie)^2\,(d^2S(\chi)/d\chi^2)\big|_{\chi=0}$.

Although the full-counting statistics formalism to compute the current and noise is very compact and elegant for the calculation, we introduce, in addition, an equivalent formulation for the average current, that offers a more transparent basis for distinguishing equilibrium from nonequilibrium effect. It is easy to show that the average current can also be written as

$$I = -ie \sum_{m,m'} \frac{d}{d\chi} W^\chi_{mm'}\Big|_{\chi=0} P_{m'}\,. \tag{6.6}$$

The derivatives $i(dW^\chi_{mm'}/d\chi)|_{\chi=0}$ are the current rates. Nonequilibrium effects of the current-voltage characteristics enter via the nonequilibrium probability distribution P_m, that is obtained by solving the master equation, Eq. (6.4). These nonequilibrium effects would be neglected if one replaced the P_m by an equilibrium probability distribution, $P^\mathrm{eq}_m = \exp(-E_m/k_\mathrm{B}T)/\sum_{m'}\exp(-E_{m'}/k_\mathrm{B}T)$, i.e., for low temperature $P_0 = 1$ for the ground state and $P_m = 0$ for the excited states $m \neq 0$.

6.3 Results

6.3.1 Differential conductance

In the following we discuss the influence of a nonequilibrium spin occupation on the transport properties for the system parameters of the experiment [133]. In Fig. 6.2, we show the differential conductance in the presence of a strong magnetic field $B_z = 7\,\mathrm{T}$ along the easy axis for different values of the asymmetry parameter a in the absence of the phenomenological relaxation (6.12), see discussion below. For very large asymmetries, $a \to 1$, there are flat plateaus between the conductance steps. In this limit,

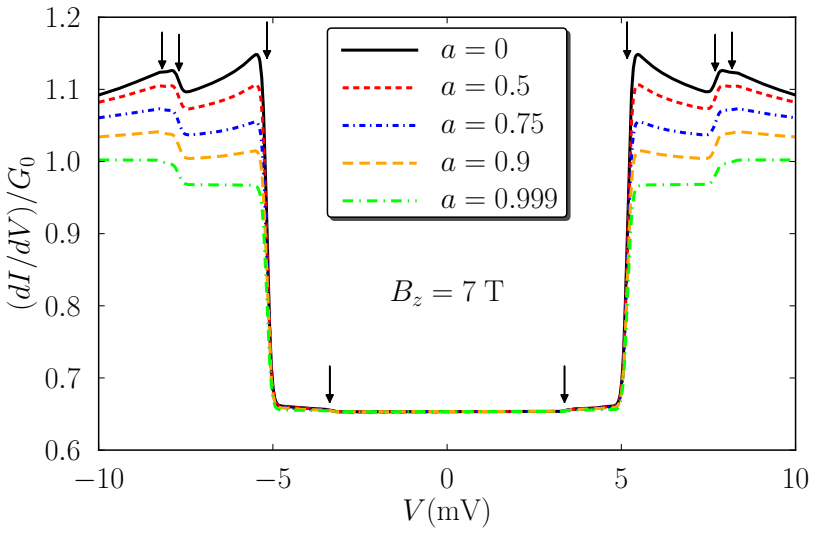

Figure 6.2: Differential conductance in units of G_0 as a function of bias voltage for different values of the asymmetry parameters a. Arrows indicate the position of the excitation energies. Parameters are $B_z = 7\,\mathrm{T}$ and $T = 0.5\,\mathrm{K}$ corresponding to the experimental values of Ref. [133]. The corresponding eigenenergies and eigenstates are summarized in Tab. 6.1.

the coupling constant j_{LR} for processes that drive the atom state population out of equilibrium is much smaller than j_{LL} for processes that let the system relax to thermal equilibrium with the left electrode. Therefore, as in [231], nonequilibrium effects are absent, and the resulting conductance curve is identical to the one obtained in [190]. For smaller asymmetries, the situation is different. The height of the conductance steps at the excitation thresholds is increased. Beyond the threshold voltages, the differential conductance shows a slow powerlaw decay towards its value for the equilibrated system again. This overshooting behavior is observed for most of the steps in the experiments of [133]. While the coupling of the adatom to the substrate is fixed in experiment, the coupling to the STM tip can be controlled by changing the tip-atom distance. This corresponds to changing the total coupling J and thereby the total tunnel current as well as the asymmetry a and thereby the nonequilibrium effects. In a recent experiment using a magnetic STM tip [201], it was confirmed that by decreasing the tip-atom distance and therefore increasing the current through the system, the nonequilibrium effects became more pronounced.

Before we discuss this for the system at hand, we illustrate the mechanism that leads to this conductance behaviour explicitly for the simpler model of a local spin-1/2 with Zeeman energy B, symmetrically coupled to the electrodes, at zero temperature. Transport takes place by either spin-flip or spin-conserving transitions. The latter contribute to the current as

$$I_{\mathrm{sc}} = \pi e |j_{\mathrm{LR}}|^2 \rho_{\mathrm{L}} \rho_{\mathrm{R}} eV, \tag{6.7}$$

independent of the probabilities $P_\uparrow$ and $P_\downarrow$ to find the spin in state up and down, respectively. The differential conductance, measured in units of $G_0 = 4\pi e^2 S(S +$

1)$|j_{\mathrm{LR}}|^2\rho_{\mathrm{L}}\rho_{\mathrm{R}}$ is $G_{\mathrm{sc}} = G_0/3$. Therefore, nonequilibrium population of the spin states is only probed by the spin-flip processes. They contribute for $eV \geq B$ as

$$I_{\mathrm{sf}} = 2\pi e|j_{\mathrm{LR}}|^2\rho_{\mathrm{L}}\rho_{\mathrm{R}}\left[(eV-B)P_\uparrow + (eV+B)P_\downarrow\right]. \tag{6.8}$$

In equilibrium, only the ground state is occupied, $P_\uparrow = 1$ and $P_\downarrow = 0$, such that only the first term in Eq. (6.8) contributes. Hence, the differential conductance $G_{\mathrm{sf}}^{\mathrm{eq}} = 2G_0/3$ remains constant above threshold. In the nonequilibrium situation, the occupation probabilities are obtained from the master equation (6.4) in the stationary state,

$$0 = \frac{d}{dt}\begin{pmatrix} P_\uparrow \\ P_\downarrow \end{pmatrix} = 2\pi e|j_{\mathrm{LR}}|^2\rho_{\mathrm{L}}\rho_{\mathrm{R}}\begin{pmatrix} -(eV-B) & eV+B \\ eV-B & -(eV+B) \end{pmatrix}\begin{pmatrix} P_\uparrow \\ P_\downarrow \end{pmatrix}. \tag{6.9}$$

The solution is $P_\uparrow = 1 - P_\downarrow = 1 - \frac{eV-B}{2(eV+B)}$. As a consequence, now both terms in Eq. (6.8) contribute, leading to the total conductance (above threshold)

$$G = \frac{2}{3}G_0\left(1 + \frac{2B^2}{(eV+B)^2}\right). \tag{6.10}$$

In the limit $V \to \infty$, both $P_\uparrow, P_\downarrow \to 1/2$ and the conductance approaches the equilibrium value G_0 with a powerlaw on voltage scale B (although the probability distribution remains highly nonequilibrium).

For the $S = 2$ spin of the iron atom with its more complicated spin Hamiltonian, the same mechanism as in the simpler spin-1/2 model gives rise to the enhanced conductance in the nonequilibrium situation. While in equilibrium only the ground state is occupied, $P_0 = 1$, leading to steps in the differential conductance, in the nonequilibrium case we obtain bias dependent occupations by solving the master equation (6.4), that lead to an overshooting. Again, the conductance decreases above threshold to approach its equilibrium value G_0 in the limit of infinite bias voltage. From our analysis it is clear that the nonmonotonic differential conductance is due an *increase* of transport enabled by the population of excited states above threshold but close to the step. It is not a signature of the excited spin states carrying less current than the ground state, i.e., a *decrease* of the conductance, as has been speculated in [194]. This conclusion can be experimentally checked by measuring the Fano factor, i.e., the ratio between current noise and average current, $F = S/(eI)$, as we explain in the following.

6.3.2 Fano factor

The Fano factor F is shown in Fig. 6.3 for different values of the asymmetry parameter a not taking into account the relaxation term (6.12), see below. For $a \to 1$, we find $F = 1$, i.e., Poissonian behavior as expected for transport through a normal tunnel barrier. When a nonequilibrium population of the atom spin states becomes important ($a < 1$ and bias voltage exceeding the inelastic threshold), the Fano factor becomes super-Poissonian, reaches a maximum and then slowly drops towards the Poissonian limit for large bias (The transition $|0\rangle \to |1\rangle$ hardly gives rise to super-Poissonian current noise as it is a very weak excitation, cf. Fig. 6.2). The latter behavior is an indicator that the nonmonotonic conductance is not due to a smaller current contribution from the excited states. If this was the case, we would expect a random telegraph signal with super-Poissonian Fano factor for $V \to \infty$.

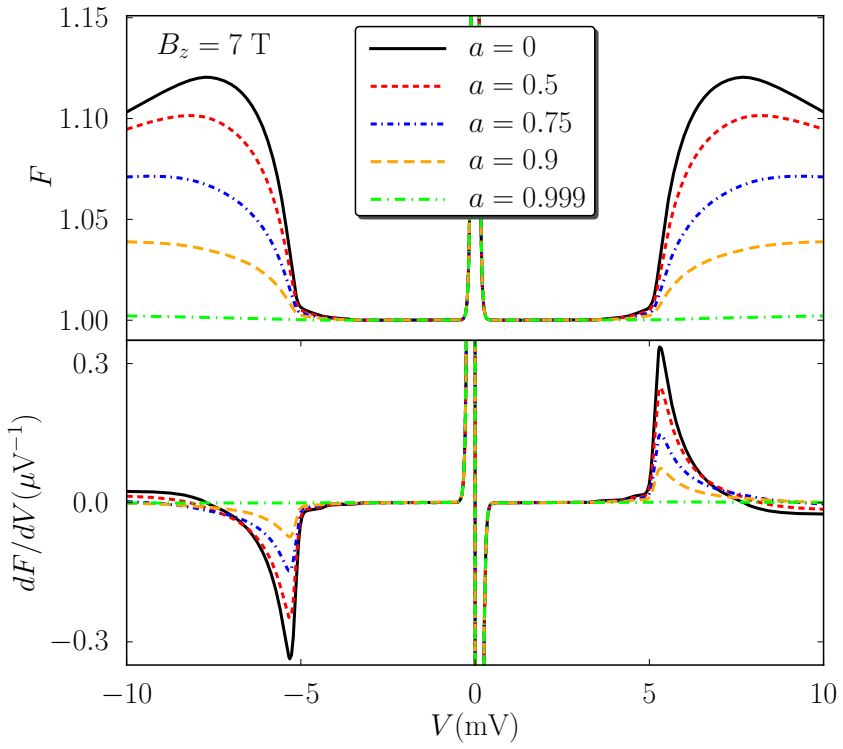

Figure 6.3: Fano factor F and dF/dV as a function of bias voltage for different values of the asymmetry parameter a. For $eV/k_\mathrm{B}T \to 0$ the Fano factor diverges due to thermal noise. Parameters as in figure 6.2.

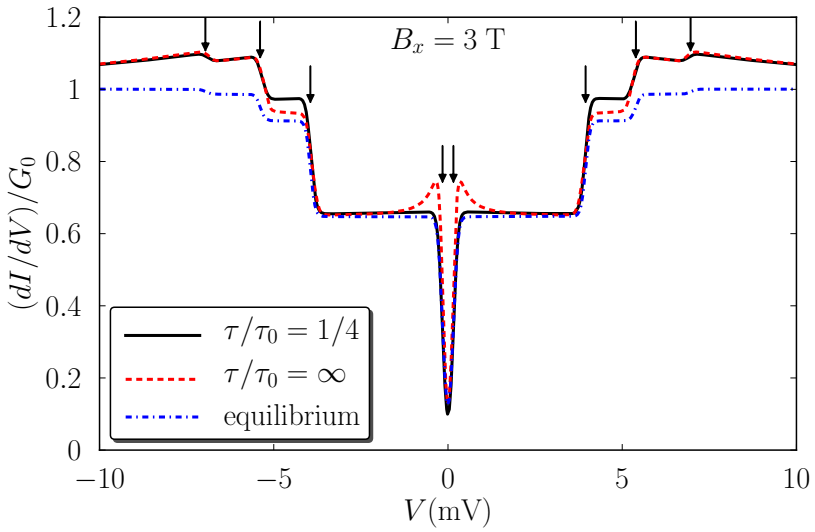

Figure 6.4: Differential conductance taking into account a spin-dependent relaxation mechanism of the form (6.12). The relaxation time is given in units of τ_0 with $\tau_0^{-1} = 2\pi DS^2|j_{\mathrm{LR}}|^2\rho_{\mathrm{L}}\rho_{\mathrm{R}}$. Parameters are $B_x = 3\,\mathrm{T}$, $T = 0.5\,\mathrm{K}$, $a = 0$. The corresponding eigenenergies and eigenstates are summarized in Tab. 6.1.

The mechanism leading to the super-Poissonian noise for bias voltages above the inelastic thresholds can most easily understood by considering the spin-1/2 model again. In this case, the Fano factor above threshold is

$$F = 1 + \frac{2B^2}{(eV+B)^2} \cdot \frac{3(eV-B)^2 + 8(eV-B)B}{3(eV-B)^2 + 9(eV-B)B + 2B^2}. \tag{6.11}$$

Spin-conserving tunnelling processes are stochastically independent of each other and of the spin-flip transitions. They obey Poissonian statistics and can be ignored for the following discussion. Once the inelastic transport channel is open, spin-flip transitions set in. They lead to an alternating sequence of the spin being in the ground and the excited state. In the limit of large bias voltage, the rates for the spin-flip transitions $\uparrow\rightarrow\downarrow$ and $\downarrow\rightarrow\uparrow$ become equal, and the transport statistics becomes Poissonian. For voltages just above threshold, $eV \geq B$, however, the two spin-flip rates differ from each other. As a consequence, we obtain an alternating sequence of a longer and a shorter waiting time, i.e., effectively there is a tendency of two electrons to bunch together, which yields super-Poissonian current noise.

6.3.3 Anisotropic relaxation

While our theory predicts an overshooting of the differential conductance at *all* conductance steps, in the experiment of [133] this feature is absent for the steps associated with the transition between the ground state $|0\rangle$ and the first excited state $|1\rangle$ whenever these steps are pronounced as is the case for a magnetic field along the x axis. This indicates that some relaxation mechanism reduces the occupation of $|1\rangle$. We note that the transition matrix element of S_z between the ground state and the first excited

state is large compared to matrix elements of S_x and S_y as well as compared to matrix elements of S_z between the ground state and any other excited state. This observation is not very sensitive to the direction and the strength of the applied magnetic field. Therefore, we make the ad-hoc assumption that there is an additional spin relaxation channel that couples to the z-component of the local spin only.

We add to our master equation (6.4) the following phenomenological, spin-dependent relaxation rates

$$W_{mm'}^{\text{relax}} = -\frac{|\langle m|S_z|m'\rangle|^2}{\tau}\Theta(\Delta_{m'm}) \tag{6.12}$$

for $m \neq m'$, where $\Theta(x)$ is the step function and τ is the time scale for relaxation. The energy dependence in Eq. (6.12) is not crucial for our conclusions. We therefore choose the simplest possible ansatz that allows relaxation only into states with lower energy. In contrast, the spin matrix elements are crucial as they suppress the nonequilibrium effects for the transition between ground and first excited state while leaving them unaffected for almost all other transitions.

In Fig. 6.4 we plot the differential conductance in the presence of a magnetic field $B_x = 3\,\text{T}$ along the x-direction. The first transition is more pronounced than in Fig. 6.2 where $B_z = 7\,\text{T}$ along the z-direction. In the limit $\tau \to \infty$ we recover the situation discussed above where an overshooting effect can be observed for each conductance step. By choosing a finite value for the relaxation time comparable to the cotunneling rates exciting the system we can, however, eliminate the overshooting at the first transition while leaving the remaining part of the conductance curve practically unaffected. In the limit $\tau = 0$, we recover the equilibrium value for the conductance at each step. These results are not sensitive to the choice of the size and direction of the magnetic field.

The anisotropic relaxation can also explain the absence of conductance steps due to transitions between excited states in the experiment. Such features should be present for a small magnetic field applied in the z direction as in this case the first excited state gets populated significantly at the first conductance step, the excitation energies satisfy $\Delta_{21} < \Delta_{20}$ such that the transition $|1\rangle \to |2\rangle$ occurs before the onset of the transition $|0\rangle \to |2\rangle$ and furthermore the transition matrix elements $\langle 2|S_\alpha|1\rangle$ do not all vanish. However, as the relaxation prevents the system from populating the first excited state, these additional conductance features vanish together with the overshooting at the first step.

6.4 Summary

We investigated the nonequilibrium effects in transport through a single iron atom. With our model, we were able to explain the nonmonotonic features of the differential conductance observed experimentally in Ref. [133]. Furthermore, we noted a striking absence of this nonmonotonicity at certain conductance steps which can be explained by the presence of an anisotropic spin relaxation channel. The anisotropy [246] points at the importance of spin-orbit coupling in this process, in addition to the splitting of the multiplet. In addition, we predicted the occurrence of super-Poissonian current noise as a consequence of the nonequilibrium spin occupation probabilities. In conclusion, for a full understanding of inelastic tunneling spectroscopy, it is crucial to account

for nonequilibrium populations of the atom states established by the competition of transport and anisotropic relaxation.

7 Probing the exchange field of a quantum-dot spin valve by a superconducting lead

In the course of this thesis we discussed the influence of spin excitations on transport through a quantum-dot spin valve. We found that transport through a quantum-dot spin valve is governed by the interplay between a nonequilibrium spin accumulation on the quantum dot and an exchange field that is caused by virtual tunneling between the quantum dot and the leads. The interplay between these effects gives rise to a number of characteristic transport properties. In Chapter 2, we discussed, e.g., a deviation from the harmonic dependence of the linear conductance on the angle enclosed by the magnetizations [64], a u-shaped conductance curve with a broad region of negative differential conductance [65], a nontrivial bias dependence of the Fano factor and characteristic features in the finite-frequency noise at the Larmor frequency associated with the exchange field [67]. In Chapter 4 and 5, we discussed further examples of exchange field effects in the finite-frequency noise [175]. Furthermore, the exchange field induces a splitting of the Kondo resonance [73–77, 80].

Unfortunately, detecting the exchange field in experiments is quite challenging as most of the effects listed above rely on a strong spin blockade of the quantum dot that exists only for large polarizations of the leads. For this reason, the exchange field has so far been detected only by the induced splitting of the Kondo resonance in C_{60} molecules [14], InAs quantum dots [16, 123], and carbon nanotubes [15] coupled to ferromagnetic leads, respectively.

In this chapter, we propose a new way to experimentally access the influence of the exchange fields on the transport properties in the regime of weak tunnel coupling by adding a superconducting electrode to the quantum dot as shown schematically in Fig. 7.1. Quantum dots coupled to superconducting electrodes are interesting on their own as they show an interplay between strong Coulomb interaction, that has the tendency to destroy superconducting correlations on the dot and nonequilibrium effects that can help to induce a superconducting proximity effect on the dot. In the subgap regime, transport between the quantum dot and superconductor takes place via Andreev reflections which have been investigated theoretically extensively [157, 159, 160, 247–252]. Further studies involved multiple Andreev reflections [253, 254] and transport in the Kondo regime [255–261]. Experimentally, quantum dots coupled to superconductors have been realized using carbon nanotubes [262–268], graphene [269], semiconductor nanowires [16, 270, 271], self-assembled semiconductor quantum dots [272], and single molecules [17].

For the system under investigation, we compute the current into the superconductor using a real-time diagrammatic approach introduced in Chapter 3 in the limit of an infinite superconducting gap[157, 159, 160]. This is a reasonable approximation as

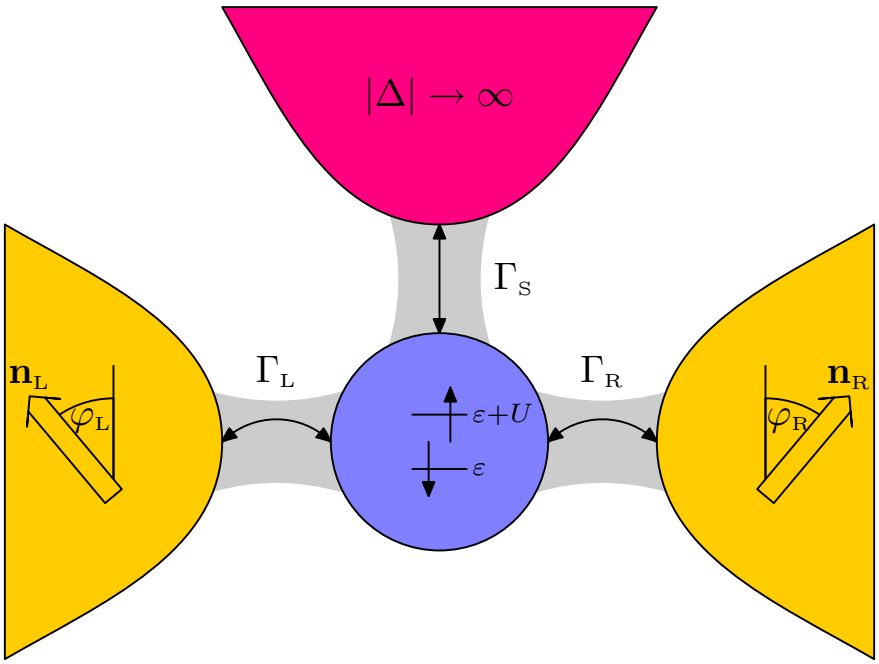

Figure 7.1: Schematic model of a quantum-dot spin valve with an additional superconducting electrode attached. A single-level quantum dot with excitation energies ε and $\varepsilon + U$ is coupled to to noncollinearly magnetized ferromagnets and a superconductor via tunnel barriers.

long as the excitation energies of the quantum dot are smaller than the gap such that subgap transport takes place. The current has, in general, even and odd components with respect to the voltage applied between the ferromagnets. We find that the even component exhibits clear evidences of the exchange field even for small polarizations of the ferromagnets.

The chapter is organized as follows. We introduce the model for the quantum dot coupled to the three electrodes in Section 7.1. In Section 7.2, we discuss the reduced density matrix and master equation for the system under investigation. We present our results in Section 7.3 and give a summary in Section 7.4. The material presented here has been published previously in Ref. [273].

7.1 Model

We consider a quantum-dot spin valve, i.e. a single-level quantum dot coupled to two ferromagnetic electrodes with magnetizations pointing in arbitrary directions $\mathbf{n}_L$, $\mathbf{n}_R$. In addition to the two ferromagnetic electrodes we consider a third superconducting lead at zero chemical potential coupled to the quantum dot. The Hamiltonian of the system hence consists of different terms describing the ferromagnetic electrodes, the superconducting electrode, the quantum dot and the tunnel coupling between the dot and the leads,

$$H = \sum_r H_r + H_S + H_{dot} + H_{tun}. \tag{7.1}$$

We model each of the two ferromagnetic electrodes with chemical potentials μ_r, $r = \mathrm{L}, \mathrm{R}$, as noninteracting electrons,

$$H_r = \sum_{\mathbf{k}\sigma} (\varepsilon_{r\mathbf{k}\sigma} - \mu_r) a^\dagger_{r\mathbf{k}\sigma} a_{r\mathbf{k}\sigma}, \tag{7.2}$$

where the quantization axis is chosen to be parallel to the magnetization of the respective leads. We assume the densities of states $\rho_{r\sigma}(\omega) = \sum_{\mathbf{k}} \delta(\omega - \varepsilon_{r\mathbf{k}\sigma})$ to be constant, $\rho_{r\sigma}(\omega) = \rho_{r\sigma}$, and spin-dependent. The asymmetry between majority ($\sigma = +$) and minority ($\sigma = -$) spins can be characterized by the polarization $p_r = (\rho_{r+} - \rho_{r-})/(\rho_{r+} + \rho_{r-})$ which varies between $p = 0$ for a nonmagnetic electrode and $p = 1$ for a halfmetallic electrode with majority spins only.

We model the superconductor by means of a mean-field BCS Hamiltonian with a superconducting gap Δ, which can be chosen to be real and positive without loss of generality. We choose the chemical potential of the superconductor as reference for energies and set it to zero. In the limit of an infinite superconducting gap, $\Delta \to \infty$, the single-level quantum dot tunnel coupled to the superconductor is described by the effective dot Hamiltonian [274–276]

$$H_{\mathrm{dot,eff}} = \sum_\sigma \varepsilon c^\dagger_\sigma c_\sigma + U c^\dagger_\uparrow c_\uparrow c^\dagger_\downarrow c_\downarrow - \frac{\Gamma_\mathrm{S}}{2} c^\dagger_\uparrow c^\dagger_\downarrow - \frac{\Gamma_\mathrm{S}}{2} c_\downarrow c_\uparrow, \tag{7.3}$$

where ε is the energy of the spin-degenerate level in the dot and U denotes the Coulomb energy for double occupancy of the dot. The effective pair potential Γ_S in Eq. (7.3) is the tunnel-coupling strength between the dot and the superconductor and it is related to microscopic parameters by $\Gamma_\mathrm{S} = 2\pi |t_\mathrm{S}|^2 \rho_\mathrm{S}$, where t_S is the tunnel matrix element between dot and superconductor and ρ_S is the normal-state density of states of the superconducting lead.

The effective dot Hamiltonian accounts for the coupling to the superconductor exactly. This allows us to deal with an arbitrarily strong superconductor-dot coupling Γ_S.

The eigenstates of the effective dot Hamiltonian (7.3) are given by the singly occupied states $|\uparrow\rangle$ and $|\downarrow\rangle$ as well as by the two states $|+\rangle$ and $|-\rangle$. The latter ones are linear combinations of the empty and doubly occupied dot states $|0\rangle$ and $|d\rangle = c^\dagger_\uparrow c^\dagger_\downarrow |0\rangle$

$$|+\rangle = \frac{1}{\sqrt{2}} \left(\sqrt{1 - \frac{\delta}{2\varepsilon_\mathrm{A}}} |0\rangle - \sqrt{1 + \frac{\delta}{2\varepsilon_\mathrm{A}}} |d\rangle \right), \tag{7.4}$$

$$|-\rangle = \frac{1}{\sqrt{2}} \left(\sqrt{1 + \frac{\delta}{2\varepsilon_\mathrm{A}}} |0\rangle + \sqrt{1 - \frac{\delta}{2\varepsilon_\mathrm{A}}} |d\rangle \right). \tag{7.5}$$

The energies of the eigenstates are given by $E_\uparrow = E_\downarrow = \varepsilon$ and $E_\pm = \delta/2 \pm \varepsilon_\mathrm{A}$. Here, $\delta = 2\varepsilon + U$ denotes the detuning from the particle-hole symmetry point while $2\varepsilon_\mathrm{A} = \sqrt{\delta^2 + \Gamma_\mathrm{S}^2}$ measures the energy difference between the states $|+\rangle$ and $|-\rangle$.

We define the Andreev bound-state energies as the excitation energies of the dot in the absence of tunnel coupling to the ferromagnets:

$$E_{\mathrm{A},\gamma'\gamma} = \gamma' \frac{U}{2} + \frac{\gamma}{2} \sqrt{\delta^2 + \Gamma_\mathrm{S}^2}, \quad \gamma, \gamma' = \pm. \tag{7.6}$$

As we allow arbitrarily oriented magnetizations of the ferromagnetic leads $\mathbf{n}_\mathrm{L}$, $\mathbf{n}_\mathrm{R}$, it turns out to be most convenient to quantize the spin on the quantum dot in the direction of $\mathbf{n}_\mathrm{L} \times \mathbf{n}_\mathrm{R}$. In this case, the tunnel coupling between the dot and the ferromagnets is characterized by

$$H_\mathrm{tun,F} = \sum_{r\mathbf{k}} \frac{t_r}{\sqrt{2}} \left[a^\dagger_{r\mathbf{k}+} \left(e^{i\phi_r/2} c_\uparrow + e^{-i\phi_r/2} c_\downarrow \right) + a^\dagger_{r\mathbf{k}-} \left(-e^{i\phi_r/2} c_\uparrow + e^{-i\phi_r/2} c_\downarrow \right) \right] + \mathrm{h.c.}, \tag{7.7}$$

i.e., the majority/minority spin electrons of the leads couple to both spin up and spin down states of the quantum dot. In the tunnel Hamiltonian, $\phi_\mathrm{L} = -\phi_\mathrm{R} = \phi/2$ is half the angle between the magnetizations. The tunnel matrix elements t_r can be related to the spin-dependent tunnel couplings $2\pi|t_r|^2\rho_{r\sigma}$. The total tunnel coupling to lead r is given by $\Gamma_r = \sum_\sigma 2\pi|t_r|^2\rho_{r\sigma}/2$.

7.2 Reduced density matrix and master equation

In order to compute the transport properties of the quantum-dot spin valve with an additional superconducting lead, we make again use of the real-time diagrammatic technique presented in Chapter 3. We therefore integrate out the lead electrons and describe the remaining system in terms of a reduced density matrix ρ^red with matrix elements $P^{\chi_2}_{\chi_1} = \langle\chi_2|\rho^\mathrm{red}|\chi_1\rangle$.

For a quantum dot coupled to both ferromagnetic and superconducting leads the reduced density matrix in the stationary limit takes the form

$$\rho^\mathrm{red} = \begin{pmatrix} P_+ & 0 & 0 & 0 \\ 0 & P_- & 0 & 0 \\ 0 & 0 & P_\uparrow & P^\uparrow_\downarrow \\ 0 & 0 & P^\downarrow_\uparrow & P_\downarrow \end{pmatrix} \tag{7.8}$$

in the basis $|+\rangle$, $|-\rangle$, $|\uparrow\rangle$ and $|\downarrow\rangle$. We note that while coherent superpositions of states $|\uparrow\rangle$ and $|\downarrow\rangle$ have to be taken into account as we are dealing with a noncollinear geometry, coherent superpositions of $|+\rangle$ and $|-\rangle$ can be neglected if $\Gamma_\mathrm{S} \gg \Gamma_r$ (which we assume from now on) as they are at least of order $O(\Gamma_r)$ and therefore do not contribute to transport in the limit of weak tunnel coupling between dot and ferromagnets.

In the stationary limit, the reduced density matrix obeys a generalized master equation of the form Eq. (3.17). The diagrammatic rules that are necessary to evaluate the kernels that appear in the master equation are summarized in Appendix A.3.

Using the effective dot description and introducing the average spin on the dot as

$$S_x = \frac{P^\downarrow_\uparrow + P^\uparrow_\downarrow}{2}, \quad S_y = \frac{P^\downarrow_\uparrow - P^\uparrow_\downarrow}{2i}, \quad S_z = \frac{P_\uparrow - P_\downarrow}{2}, \tag{7.9}$$

as well as the probability $P_1 = P_\uparrow + P_\downarrow$ to find the dot singly occupied, we can split the master equation into one set for the occupation probabilities and one set for the average spin. Introducing the abbreviations $\Gamma_{r\pm} = \Gamma_r \left(1 \pm \frac{\delta}{2\varepsilon_\mathrm{A}}\right)$ and $f^\pm_{r\gamma\gamma'} = f^\pm_r(E_{\mathrm{A},\gamma\gamma'})$, where $f^+_r = 1 - f^-_r$ denotes the Fermi function of lead r, the equations governing the

occupation probabilities are given by

$$\mathbf{0} = \frac{d}{dt}\begin{pmatrix} P_+ \\ P_- \\ P_1 \end{pmatrix} = \sum_r \mathbf{A}_r \begin{pmatrix} P_+ \\ P_- \\ P_1 \end{pmatrix} + \sum_r p_r \mathbf{b}_r (\mathbf{S}_r \cdot \mathbf{n}_r), \tag{7.10}$$

where the expressions for the matrices $\mathbf{A}_r$ and the vectors $\mathbf{b}_r$ are given in Appendix B.4. We see that similar to the case of an ordinary quantum-dot spin valve [65], the dynamics of the occupation probabilities couples to the average spin accumulated on the quantum dot.

As in the case of the normal quantum-dot spin valve, the master equation for the average dot spin can be cast into the form of a Bloch equation,

$$\frac{d\mathbf{S}}{dt} = \left(\frac{d\mathbf{S}}{dt}\right)_{\text{acc}} + \left(\frac{d\mathbf{S}}{dt}\right)_{\text{rel}} + \left(\frac{d\mathbf{S}}{dt}\right)_{\text{prec}}, \tag{7.11}$$

where the first term

$$\begin{aligned}\left(\frac{d\mathbf{S}}{dt}\right)_{\text{acc}} = \frac{p}{2}\sum_r \Big[&\left(-\Gamma_{r+} f^-_{r++} + \Gamma_{r-} f^+_{r--}\right) P_+ + \left(-\Gamma_{r-} f^-_{r+-} + \Gamma_{r+} f^+_{r-+}\right) P_- \\ &+ \frac{1}{2}\left(-\Gamma_{r-} f^-_{r--} - \Gamma_{r+} f^-_{r-+} + \Gamma_{r+} f^+_{r++} + \Gamma_{r-} f^+_{r+-}\right) P_1 \Big] \mathbf{n}_r,\end{aligned} \tag{7.12}$$

describes the nonequilibrium spin accumulation on the dot due to spin-dependent tunneling of electrons onto the dot. The relaxation of the dot spin is described by the second term,

$$\left(\frac{d\mathbf{S}}{dt}\right)_{\text{rel}} = -\frac{1}{2}\sum_r \left(\Gamma_{r-} f^-_{r--} + \Gamma_{r+} f^-_{r-+} + \Gamma_{r+} f^+_{r++} + \Gamma_{r-} f^+_{r+-}\right) \mathbf{S}, \tag{7.13}$$

which is proportional to the spin accumulated on the dot. The dot spin relaxes either by electrons with a given spin leaving the dot to the ferromagnetic leads or by electrons with a spin opposite to that on the dot entering the dot from the ferromagnets, thus forming a spin singlet. Finally, the last term

$$\left(\frac{d\mathbf{S}}{dt}\right)_{\text{prec}} = \sum_r \mathbf{S} \times \mathbf{B}_r, \tag{7.14}$$

describes a precession of the dot spin due to an exchange field which is given by

$$\mathbf{B}_r = \frac{p_r \mathbf{n}_r}{2\pi} \sum_{\gamma\gamma'} \gamma' \Gamma_{r\gamma} \operatorname{Re} \Psi \left(\frac{1}{2} + i\frac{\beta(E_{\text{A},\gamma'\gamma} - \mu_r)}{2\pi}\right). \tag{7.15}$$

where Ψ is the digamma function. The exchange field is the manifestation of a spin-dependent level renormalization due to virtual tunneling between the dot and the ferromagnetic electrodes. We emphasize that the coupling to the superconductor influences the exchange field only through the position of the Andreev bound states. As can be seen in Fig. 7.2, the exchange field takes on large values whenever one of the Andreev bound states is in resonance with the Fermi level of the ferromagnet. This

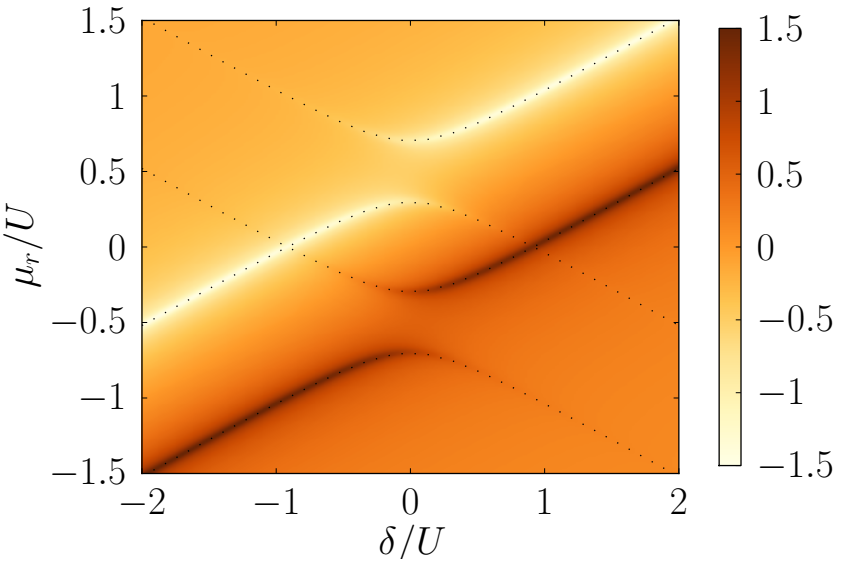

Figure 7.2: Projection of the exchange field $\mathbf{B}_r$ onto $\mathbf{n}_r$, measured in units of $p_r\Gamma_r$ for $k_\mathrm{B}T = 0.01U$, $\Gamma_\mathrm{S} = 0.4U$ as a function of the chemical potential μ_r and detuning δ. The peaks and dips map out the Andreev bound states whose energies are indicated by dotted lines.

behavior is similar to the ordinary quantum-dot spin valve where the exchange field becomes maximal at resonance as well.

The particle current flowing from the ferromagnetic leads into the quantum dot is given by

$$I_r = \sum_{\chi\chi_1\chi_2} W^{I_r\chi\chi_2}_{\chi\chi_1} P^{\chi_2}_{\chi_1}. \tag{7.16}$$

Making use of the explicit expressions for the current rates, we obtain

$$\begin{aligned} I_r = {} & \left(\Gamma_{r-} f^+_{r--} - \Gamma_{r+} f^-_{r++}\right) P_+ + \left(\Gamma_{r+} f^+_{r-+} - \Gamma_{r-} f^-_{r+-}\right) P_- \\ & + \frac{1}{2}\left(\Gamma_{r+} f^+_{r++} + \Gamma_{r-} f^+_{r+-} - \Gamma_{r-} f^-_{r--} - \Gamma_{r+} f^-_{r-+}\right) P_1 \\ & - p_r \left(\Gamma_{r-} f^-_{r--} + \Gamma_{r+} f^-_{r-+} + \Gamma_{r+} f^+_{r++} + \Gamma_{r-} f^+_{r+-}\right) \mathbf{S}\cdot\mathbf{n}_r. \end{aligned} \tag{7.17}$$

In the stationary state, the current into the superconductor is related to the currents between the dot and the ferromagnets by current conservation, which is automatically satisifed in the real-time diagrammatic theory [91–94],

$$I_\mathrm{S} = I_\mathrm{L} + I_\mathrm{R}. \tag{7.18}$$

Experimentally, one can therefore measure either the current flowing into the superconductor or the difference between the currents that enter from the left and leave to the right ferromagnet. In the following discussion we will however always refer to the current into the superconductor for simplicity.

7.3 Results

In this section, we discuss how the current into the superconductor can be used to probe the exchange field. We consider symmetrically biased ferromagnets, $\mu_\mathrm{L} = -\mu_\mathrm{R} \equiv \mu$, while the superconductor is kept at $\mu_\mathrm{S} = 0$. We split the current into a component that is a symmetric function of bias, $I_\mathrm{S}^\mathrm{sym}(\mu) = [I_\mathrm{S}(\mu) + I_\mathrm{S}(-\mu)]/2$, and a component that is an antisymmetric function of bias, $I_\mathrm{S}^\mathrm{antisym}(\mu) = [I_\mathrm{S}(\mu) - I_\mathrm{S}(-\mu)]/2$. The symmetric component of the current turns out to be very sensitive to the exchange field.

7.3.1 Symmetric quantum-dot spin valve

We start our discussion by considering a symmetric system, i.e., we assume the tunnel couplings to the left and right ferromagnet to be equal, $\Gamma_\mathrm{L} = \Gamma_\mathrm{R} \equiv \Gamma/2$. Furthermore, we assume both ferromagnets to have the same polarization p. In this particular case, due to symmetry, the current possesses only a symmetric component with respect to μ, i.e., $I_\mathrm{S}(\mu) = I_\mathrm{S}^\mathrm{sym}(\mu)$.

We first explain why the supercurrent vanishes for collinear geometries. We then show that the spin accumulation in the noncollinear configuration gives rise to a finite current into the superconductor that is sensitive to the exchange field. Finally, we show that a spin relaxation on the dot reduces the supercurrent but nevertheless still allows a detection of the exchange field.

In general, the current into the superconductor vanishes in the small-bias regime $E_{\mathrm{A}-+} < \mu < E_{\mathrm{A}+-}$, where the quantum dot is Coulomb-blockaded. For a symmetric system, the current also vanishes in the large-bias regime, $\mu > E_{\mathrm{A}++}$ or $\mu < E_{\mathrm{A}--}$, where all dot states contribute to transport, due to particle-hole symmetry. Hence, we can expect a finite current into the superconductor only in the intermediate bias regime, $E_{\mathrm{A}--} < \mu < E_{\mathrm{A}-+}$ or $E_{\mathrm{A}+-} < \mu < E_{\mathrm{A}++}$. According to Eq. (7.17) and (7.18), the supercurrent in this regime is given by

$$I_\mathrm{S} = \frac{\Gamma}{2}\left(-2\frac{\delta}{\varepsilon_\mathrm{A}}P_+ + \frac{\delta}{\varepsilon_\mathrm{A}}P_- - \frac{\delta}{2\varepsilon_\mathrm{A}}P_1 - p\mathbf{S}\cdot(\mathbf{n}_\mathrm{L}+\mathbf{n}_\mathrm{R}) + \frac{p\delta}{2\varepsilon_\mathrm{A}}\mathbf{S}\cdot(\mathbf{n}_\mathrm{L}-\mathbf{n}_\mathrm{R})\right). \quad (7.19)$$

For parallel magnetizations, where the spin accumulation on the dot vanishes and the dot occupation probabilities satisfy $P_1 = 2P_- = 1/3$, we find that the supercurrent vanishes also in the intermediate bias regime. To understand the mechanism behind this behaviour, let us consider the transport processes that contribute to the superconductor. Notice that in the intermediate regime the state $|+\rangle$ is inaccessible. We find that the contributions from the first two processes shown in Fig. 7.3 cancel each other. They both transfer equal amounts of charge between the dot and the superconductor when projecting the state $|-\rangle$ onto the state $|0\rangle$. Furthermore, both processes have identical rates (a factor of 2 due to spin is compensated by $P_1 = 2P_-$). In consequence, they give rise to a vanishing supercurrent for any value of the detuning δ. Similarly, one can show that the other two processes that probe the doubly occupied component of $|-\rangle$ cancel each other.

The situation is more complex in the antiparallel configuration due to the finite spin accumulation on the quantum dot. Processes 1 and 4 in Fig. 7.4 which build up the spin accumulation have rates proportional to $1+\delta/(2\varepsilon_\mathrm{A})$ and $1-\delta/(2\varepsilon_\mathrm{A})$, respectively.

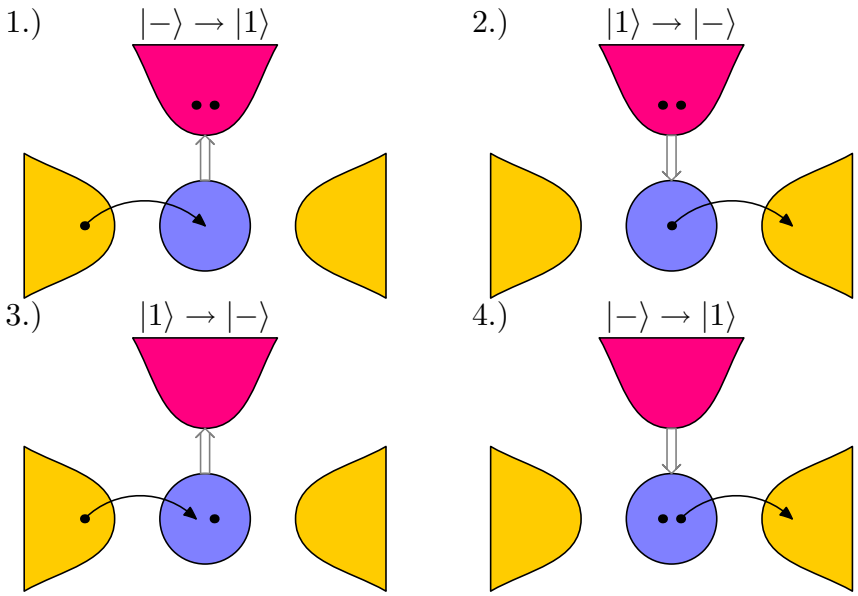

Figure 7.3: Transport processes in the proximized quantum-dot spin valve. In the first process, the $|-\rangle$ state is projected onto the $|0\rangle$ state, pushing a Cooper pair into the superconductor as indicated by the double arrow. Then an electron tunnels in from the left lead, leaving the dot in the singly occupied state. Similarly, in the second process, an electron leaves the singly occupied dot to the right lead. Then, a Cooper pair enters from the superconductor to bring the dot in the state $|-\rangle$. As both processes probe the empty contribution to $|-\rangle$, their rates are proportional to $1 + \delta/(2\varepsilon_\mathrm{A})$. Similarly, the other two processes probe the doubly occupied component of $|-\rangle$ such that their rates are proportional to $1 - \delta/(2\varepsilon_\mathrm{A})$.

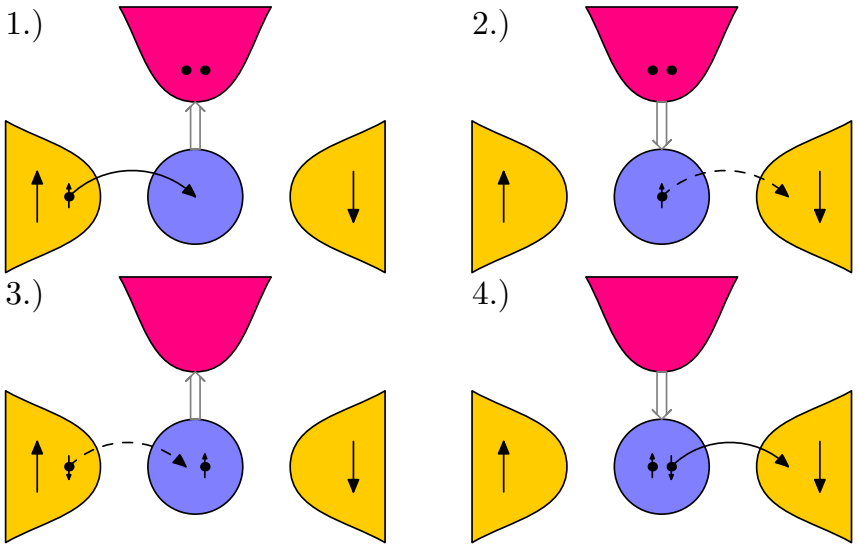

Figure 7.4: Transport processes in the proximized quantum-dot spin valve in the antiparallel configuration. Processes 1 and 4 are responsible for building up a spin accumulation. As their rates are proportional to $1+\frac{\delta}{2\varepsilon_\mathrm{A}}$ and $1-\frac{\delta}{2\varepsilon_\mathrm{A}}$, respectively, the spin accumulation is independent of δ. Similarly, processes 2 and 3 are responsible for a δ independent spin relaxation.

Hence, in sum the spin accumulation is insensitive to the detuning δ. A similar reaonsing holds for processes 2 and 3 that relax the dot spin. As the supercurrent vanishes at $\delta = 0$ due to particle-hole symmetry, it therefore has to vanish for all values of δ.

For noncollinear geometries, we find a finite current into the superconductor, cf. Fig. 7.6. To understand the mechanism leading to the finite current, we first neglect the exchange field in our discussion and turn to its effect afterwards.

In contrast to the antiparallel configuration, in the noncollinear geometries the spin accumulation on the quantum dot (and therefore also the probability to find the dot singly occupied) is sensitive to δ. This can be understood by considering again the processes 1 and 4 of Fig. 7.5 which are responsible for the spin accumulation. While process 1 builds up a dot spin in in the direction of $+\mathbf{n}_\mathrm{L}$, process 4 build up a spin in the direction of $-\mathbf{n}_\mathrm{R}$. For $\delta = 0$ both processes contribute equally to the spin accumulation. We therefore find that a spin builds up in the direction of $\mathbf{n}_\mathrm{L} - \mathbf{n}_\mathrm{R}$. For positive δ, process 1 dominates and hence the spin points towards $\mathbf{n}_\mathrm{L}$, while for negative δ, process 4 dominates and the spin points towards $-\mathbf{n}_\mathrm{R}$. As for finite δ the left-right symmetry is broken, the cancellation between the supercurrent contributions from processes 1 and 2 (3 and 4, respectively) does not hold any longer and a finite supercurrent can flow.

Neglecting the exchange field, the following analytic expression for the current into the superconductor can be found:

$$I_\mathrm{S} = \frac{\Gamma\Gamma_\mathrm{S}^2 p^4 \delta \sin^2\phi}{\varepsilon_\mathrm{A}\left[48\varepsilon_\mathrm{A}^2 - 2p^2(2\delta^2(1+2\cos\phi) - \Gamma_\mathrm{S}^2(1-\cos\phi))\right]}. \tag{7.20}$$

The above formula shows that the current into the supercurrent in the noncollinear geometry flows for any value of the polarization $p \neq 0$. It is only the magnitude of the

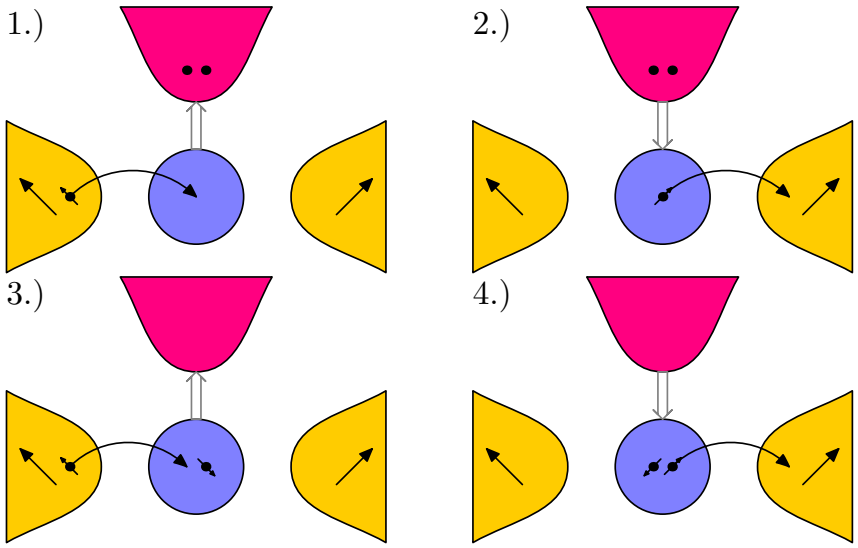

Figure 7.5: Transport processes in the proximized quantum-dot spin valve for noncollineraly magnetized electrodes. While process 1 has the tendency to build up a spin in the direction of $\mathbf{n}_\mathrm{L}$, process 4 tends to build up a spin in the direction of $\mathbf{n}_\mathrm{R}$.

current that is affected by the strength of the polarization. Using realistic parameters, $p = 0.3$, $U \sim 1\,\mathrm{meV}$, $\Gamma_\mathrm{S} \sim 0.5\,\mathrm{meV}$, $\Gamma \sim 100\,\mu\mathrm{eV}$ and $\phi = \pi/2$, we obtain as an order of magnitude of the current $I_\mathrm{S} \sim 1\,\mathrm{pA}$ which is challenging but not impossible to be measure with current techniques.

If the exchange field is taken into account, there is still a finite current flowing in the intermediate bias regime. As the dot spin now precesses in the energy-dependent exchange field, it acquires a finite z component while simultaneously the x and y components which influence the supercurrent, cf. Eq. (7.19), get reduced and show a nontrivial bias dependence. In consequence, the supercurrent also deviates from its steplike behaviour in the absence of the exchange field and even changes sign. Furthermore, there is a finite supercurrent flowing in the large bias regime, because the symmetry-breaking spin accumulation on the dot persists in this regime.

The nontrivial bias dependence of the supercurrent opens up the possibility to detect the exchange field experimentally, even for small polarizations. This is in strong contrast to the other exchange field effects that arise in the sequential tunneling regime, as, e.g., negative differential conductance [65, 82] or the nontrivial dependence of current, Fano factor and higher current cumulants on the angle between the magnetizations. [65, 67, 68] While for quantum dots that couple only to ferromagnetic leads all exchange field effects rely on a strong spin blockade, in the system under investigation here, it is the cancellation between different transport processes involving the superconductor that provides the necessary sensitivity to the spin accumulation and the exchange field. To illustrate this, let us consider a system where the superconductor is replaced by a normal metal that is coupled to the quantum dot with coupling strength Γ_N. In Fig. 7.7 we show the current into the normal metal evaluated to first order in Γ_N, an approximation valid if $\Gamma_\mathrm{N} \ll k_\mathrm{B}T$. We find that now there is indeed a

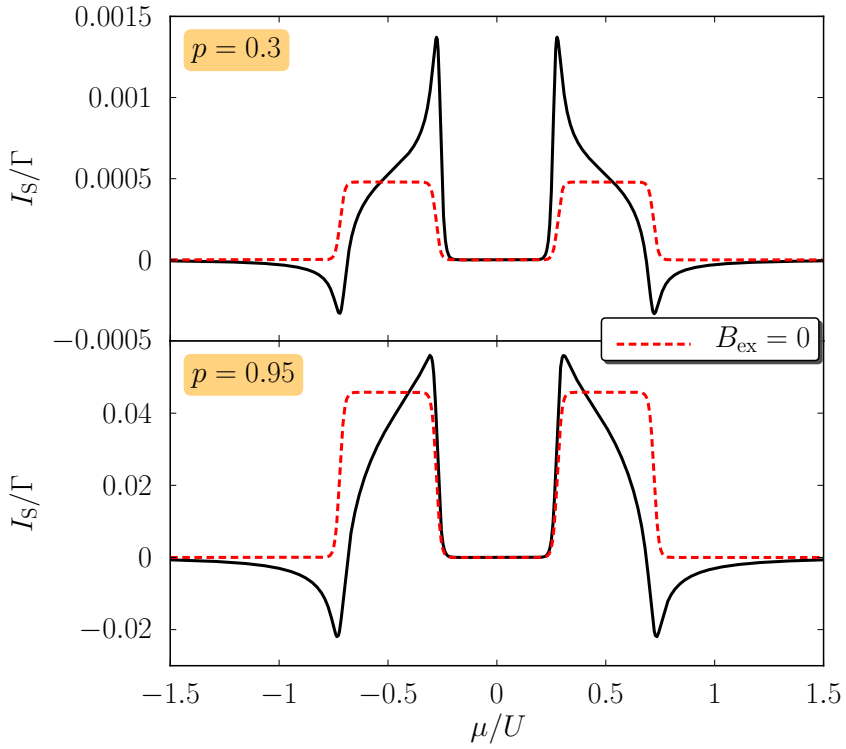

Figure 7.6: Current into the superconductor for a symmetric coupling, $\Gamma_L = \Gamma_R$, $\mu_L = -\mu_R \equiv \mu$ and perpendicularly magnetized ferromagnets. In the upper panel, we have $p = 0.3$, while in the lower panel $p = 0.95$. The black (solid) curves take into account the exchange field, it is neglected in the red (dashed) curves. Other parameters are $\delta = 0.2$, $\chi = 0.2U$, $k_B T = 0.01U$.

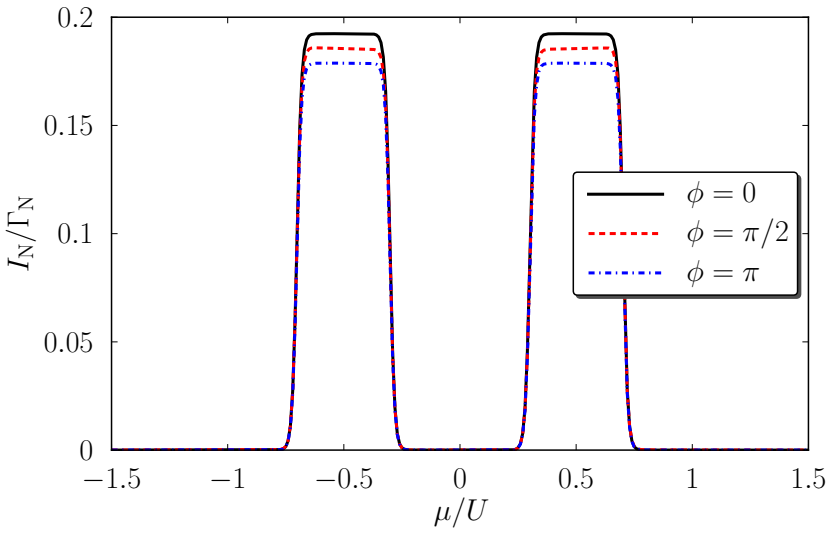

Figure 7.7: When the third lead is a normal metal instead of a superconductor, a finite current flows for any magnetic configuration, thereby completely obscuring the exchange field effects for small polarizations. Parameters are $\delta = 0.4U$, $\Gamma_r = \Gamma_N$, $p = 0.3$, $k_B T = 0.01U$.

finite current for all magnetic configurations because for a positive (negative) detuning only processes where electrons leave (enter) the dot to (from) the third lead are possible. In consequence, the exchange field effects become practically invisible for small polarizations as they are obfuscated by the large background current.

Finally, we discuss the effect of an intrinsic spin relaxation on the dot which we model by adding a term $-\mathbf{S}/\tau$ to the right-hand side of the spin master equation, Eq. 7.11. Possible mechanisms for such a spin relaxation are the coupling to nuclear spins in the quantum dot [277–279] or spin-orbit interaction on the dot [280, 281]. In Fig. 7.8, we show the current into the superconductor for different values of the relaxation time τ. As the relaxation time is decreased, the current is reduced in agreement with our discussion above which showed that the spin accumulation on the dot is crucial to get a finite current. However, we also notice that the exchange field effects still remain visible when considering a finite relaxation. This shows that an experimental detection of these effects should be feasible.

7.3.2 Asymmetry effects

We now turn to the discussion of the situation where $\Gamma_L \neq \Gamma_R$. We parametrize the tunnel couplings as $\Gamma_L = (1+a)\Gamma/2$ and $\Gamma_L = (1-a)\Gamma/2$ such that the parameter a with $-1 \leq a \leq +1$ characterizes the degree of asymmetry. In this case, the antisymmetric component of the supercurrent with respect to the applied bias, $I_S^{\text{antisym}}(\mu)$, is in general non-vanishing.

We find that for $a \neq 0$ a finite supercurrent arises in the intermediate and large bias regime for all magnetic configurations. For parallel and antiparallel magnetizations

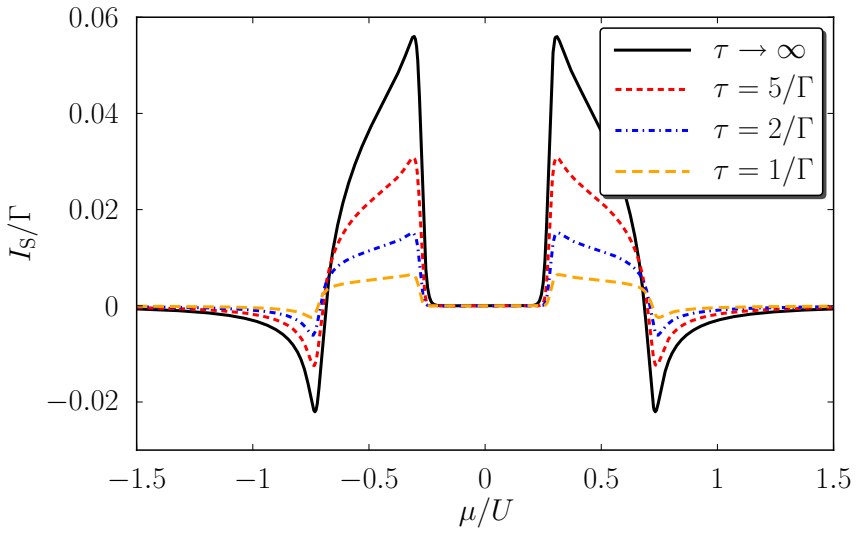

Figure 7.8: Influence of spin relaxation on the supercurrent in the noncollinear configuration. As the spin accumulation is reduced, the supercurrent is decreased. However, the exchange field effects still prevail. Polarization is $p = 0.95$, other parameters as in Fig. 7.3.

magnetizations, respectively, the supercurrent is given by

$$I_S^P = \Gamma \frac{2a\Gamma_S^2(1-p^2)(2\varepsilon_A - a\delta)}{\varepsilon_A\left[(3+a^2p^2)\Gamma_S^2 - (1-p^2)\delta(a\varepsilon_A - (3-a^2)\delta)\right]} \tag{7.21}$$

$$I_S^{AP} = \Gamma \frac{a\Gamma_S^2(1-p^2)}{\varepsilon_A\left[(1+3p^2)a\delta + 2(3+p^2)\varepsilon_A\right]} \tag{7.22}$$

in the intermediate bias regime, while it is given by

$$I_S^P = \Gamma \frac{a(1-p^2)\Gamma_S^2}{(1-p^2)\delta^2 + \Gamma_S^2}, \tag{7.23}$$

$$I_S^{AP} = \Gamma \frac{a(1-p^2)\Gamma_S^2}{(1-a^2p^2)\delta^2 + \Gamma_S^2} \tag{7.24}$$

in the large bias regime. In these formulas we assumed the current to flow from the left to the right. For a current in the opposite direction, one has to substitute $a \to -a$. Since the corresponding formulas for the noncollinear case are rather lengthy, we do not give them here.

From the above formulas we read off that the total supercurrent increases as the asymmetry is increased. Furthermore, we find that the current is decreased when the polarization is increased. This means that for experimentally realistic polarizations an asymmetry can give rise to a background current that dominates over the exchange-field signal. This problem can be overcome by looking at the symmetric and antisymmetric components of the current with respect to the voltage.

In Fig. 7.9 and 7.10, we show these two quantities as a function of applied bias for small and large polarizations, respectively. For small polarizations, we find that

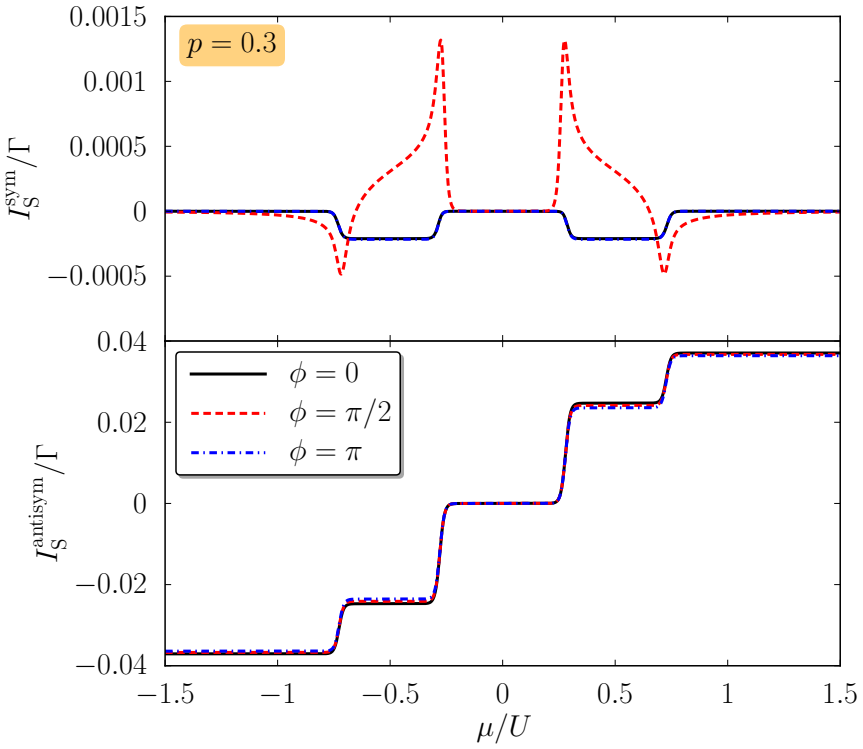

Figure 7.9: Symmetrized and antisymmetrized current into the superconductor as a function of bias voltage for different magnetic configurations and small polarizations, $p = 0.3$. The asymmetry is $a = 0.05$, other parameters as in Fig. 7.6.

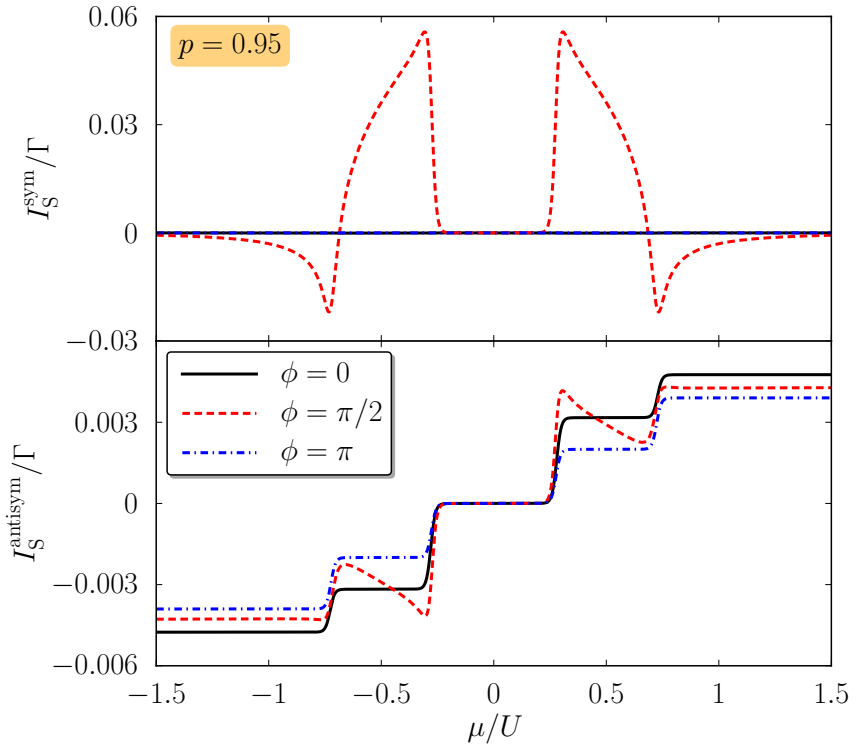

Figure 7.10: Symmetrized and antisymmetrized current into the superconductor as a function of bias voltage for different magnetic configurations and large polarizations, $p = 0.95$. The asymmetry is $a = 0.05$, other parameters as in Fig. 7.6.

the antisymmetric contribution shows a steplike behaviour that does not reveal any exchange field effects and is nearly insensitive to the magnetic configuration. In contrast, the symmetric contribution again reveals the characteristic peaks and dips that we encountered already in the symmetric system and that are a clear indication of the exchange field. For large polarizations, the system behaves rather similarly. The symmetric current contribution shows clear signs of the exchange field while the antisymmetric part is dominated by current steps. However, we now find that also the antisymmetric contribution is sensitive to the exchange field.

Hence, we have seen that an asymmetric coupling to the ferromagnets gives rise to a finite supercurrent for all magnetic configurations that could make the experimental detection of the exchange field effects difficult for small polarizations. To overcome this obstacle, we propose to measure the current symmetrized with respect to the bias voltage as this allows to recover the exchange field effects.

7.4 Summary

In this chapter, we analyzed transport through a quantum-dot spin valve with an additional superconducting electrode. We found that in the case of noncollinear magnetization even for small polarizations, the symmetric component of the supercurrent with respect to the applied bias voltage exhibits strong exchange-field effects. In particular, for a system that couples symmetrically to the ferromagnets which are at opposite bias, the supercurrent has only a symmetric component in bias voltage. In this case, a finite supercurrent can only flow for noncollinear magnetizations, as this configuration breaks the left-right symmetry for finite detuning δ. Due to the presence of an exchange field acting on the dot spin in noncollinear geometries, the supercurrent exhibits a nontrivial bias dependence and even changes sign. Interestingly, these effects occur for any polarization of the ferromagnets $p > 0$. Furthermore, they are robust towards a relaxation of the dot spin. For systems with different couplings to the ferromagnets, the supercurrent becomes finite for any magnetic configuration. We found that for small polarizations, the contribution due to the asymmetry of the system dominates over the one due to noncollinearity. We showed, however, that by considering the supercurrent symmetrized with respect to the applied bias voltage, one can extract the exchange field effects also in this case. We therefore proposed to experimentally access the exchange field by measuring the bias dependence of the supercurrent.

8 Conclusions

In this thesis, we investigated spin-dependent transport through nanostructures. We focussed on transport through quantum-dot spin valves, i.e., a quantum dot coupled to noncollinearly magnetized ferromagnetic electrodes. Such systems turn out to be particularly interesting from a theoretical point of view. They show an interplay between nonequilibrium spin accumulation on the dot and spin-dependent level renormalization effects which act as an effective exchange field on the dot spin [64, 65]. It arises from the strong Coulomb interaction on the quantum dot.

The main goal of this thesis was to investigate the influence of spin excitations on transport through a quantum-dot spin valve. We considered different kinds of spin excitations located either in the electrodes, in the tunnel barriers or on the quantum dot. In particular, we investigated the influence of spin waves excited in the electrodes, magnetic impurities located in either the tunnel barrier or on the quantum dot and spin excitations due to a complex internal dot structure as occurs for transport through single magnetic atoms.

In Chapter 4, we studied the influence of spin waves on transport through a quantum-dot spin valve. We showed that the emission and absorption of magnons gives rise to side bands in the differential conductance, similarly to a quantum dot coupled to a vibrational degree of freedom. The relative and absolute strength of these sidebands depends on the polarization as well as on the magnetic configuration. For parallel magnetizations and large polarization a side band of negative differential conductance due to the formation of a trapping state occurs. We furthermore found that the magnons can enhance or reduce the Fano factor depending on the charge states through which transport takes place. Additionally, the magnons give rise to new contributions to the exchange field which show up in the frequency-dependent Fano factor. The emission and absorption of magnons also leads to a nonequilibrium magnon distribution which we found to be different for source and drain. While in the latter the average number of magnons is increased, it is decreased in the former. Finally, we showed how the magnons can drive a fully spin-polarized current at zero bias in a system that couples asymmetrically to the magnons in source and drain.

In Chapter 5, we investigated the influence of magnetic impurities on transport through a quantum-dot spin valve. Here, we considered two different situations. In the first one, the impurity spin is localized in one of the tunnel barriers. Therefore, it is exchange coupled to the spins of the tunneling electrons. We found that interference between direct and exchange tunneling takes place even for nonmagnetic electrodes. This is in contrast to the behaviour of a simple tunnel barrier with an embedded spin where interference plays a role only for ferromagnetic electrodes or in higher-order transport. Furthermore, we showed that a spin-polarized current through the system leads to a current-induced switching of the impurity spin. This switching influences the spin accumulation on the quantum dot and therefore also the current and current noise through the system. Similarly to the quantum-dot spin valve with spin waves

in the leads, we found the exchange field to be sensitive to the state of the impurity spin. This in turn influences the I-V characteristics for noncollinear magnetizations. Furthermore, the switching of the exchange field that accompanies the switching of the impurity spin leads to a bias- and gate-voltage dependent switching of the resonance position in the finite-frequency current noise.

In the second situation, we considered an impurity spin localized on the quantum dot and exchange coupled to the electron spin on the dot. We dealt with the case of a weak exchange coupling that is of the order of the tunnel coupling strength. This limit is particularly suited to model the effect of nuclear spins on transport through a quantum dot. In the limit of a strong external magnetic field, we found the current and zero-frequency Fano factor to be insensitive to the presence of the impurity. However, we showed that the finite-frequency noise exhibits a resonance peak at the frequency corresponding to the exchange coupling, thereby allowing an experimental determination of the coupling strength. Furthermore, we discussed the case of a weak external field. In this case, the two spins experience different magnetic fields. While the impurity only feels the external field, the electron spin is also sensitive to the exchange field. In consequence, the two spins exhibit nontrivial eigenstates and spin dynamics which manifest themselves in the finite-frequency Fano factor that shows a large number of resonance features.

In Chapter 6, we dealt with spin inelastic tunneling spectroscopy of single magnetic adatoms absorbed on a nonmagnetic substrate which has attracted a lot of interest recently as it allows to study magnetic properties and interactions on an atomic scale. Recent experiments revealed steps in the differential conductance of a single iron atom [133]. Assuming an equilibrium occupation of the atom spin states, these steps could be explained in terms of inelastic tunneling processes that excite the atom spin. The position of the steps is determined by the excitation energies of the atom spin while the step heights are related to certain spin matrix elements [190]. However, nonmonotonicities in the experimentally measured conductance could not be explained within the equilibrium model. Here, we showed that a nonequilibrium occupation of the spin states leads to an overshooting at the conductance steps in agreement with the experimental results. We furthermore pointed out that the nonequilibrium occupations lead to a super-Poissonian current noise which can be used to further study the nonequilibrium conditions experimentally. Finally, we showed that the remarkable absence of certain overshootings in the experimental data can be explained by introducing an anisotropic relaxation channel into our model. We thus pointed out the importance of nonequilibrium effects to a full understanding of inelastic tunneling spectroscopy.

So far, we had dealt with spin excitations in a quantum-dot spin valve. In Chapter 7, we finally proposed a new way to probe the exchange field in a quantum-dot spin valve. Most of the exchange field effects that occur in a quantum-dot spin valve rely on a strong spin blockade on the dot which is possible only for large polarizations of the electrodes. For this reason, the exchange field has been detected experimentally only by the splitting of the Kondo resonance in a carbon nanotube coupled to ferromagnetic electrodes [15]. Here, we considered a quantum-dot spin valve with an additional superconducting electrode at zero bias coupled to the quantum dot. We investigated the current into the superconductor in the limit of an infinite superconducting gap, i.e., we focussed on subgap transport between the dot and the superconductor. In

general, the current has contributions even and odd in the bias applied between the ferromagnets. We showed that the even part of the current is particularly sensitive to the exchange field even for small polarizations. For realistic parameters, we found the resulting currents to be of the order of 1 pA which can be measured with current techniques. We therefore propose our setup as an alternative way to access the exchange field in experiment.

A Diagrammatic rules

In the following, we summarize the diagrammatic rules that are necessary to evaluate the generalized transitions rates $\mathbf{W}$ that enter the master equations as well as the kernels $\mathbf{W}^I$ and $\mathbf{W}^{II}$ that are needed for the calculation of the current and current noise for the different systems investigated in this thesis.

A.1 Spin waves in quantum-dot spin valves

For a quantum-dot spin valve with spin wave excitations in the electrodes, the diagrammatic rules are given by:

1. Draw all topological different diagrams with tunneling lines connecting vertices on either the same or opposite propagators. Assign to the four corners and all propagators states $|\chi, n_\mathrm{L}, n_\mathrm{R}\rangle$ and corresponding energies $E_\chi + \omega_b(n_\mathrm{L} + n_\mathrm{R})$ as well as an energy ω for every tunneling line.

2. For each time interval on the real axis confined by two adjacent vertices, assign a resolvent $1/(\Delta E + i\eta)$ where ΔE is the difference between left and right-going tunneling lines and propagators.

3. For each tunneling line involving lead r, the diagram acquires a factor $\frac{\Gamma_r}{2\pi} f_r^{\pm}(\omega)$ where the sign on the Fermi function depends on whether the line runs forward $(-)$ or backwards $(+)$ with respect to the Keldysh contour.

4. For each pair of vertices connected by a tunneling line the diagram is multiplied by
$$\frac{1+p}{2}\langle\xi_a'|\tilde{c}_{r\uparrow}|\xi_a\rangle\langle\xi_b'|\tilde{c}_{r\uparrow}^\dagger|\xi_b\rangle + \frac{1-p}{2}\langle\xi_a'|\tilde{c}_{r\downarrow}|\xi_a\rangle\langle\xi_b'|\tilde{c}_{r\downarrow}^\dagger|\xi_b\rangle$$
where $|\xi_a\rangle$ and $|\xi_a'\rangle$ ($|\xi_b\rangle$ and $|\xi_b'\rangle$) are the states that enter and leave the vertex the tunneling line begins (ends) at, respectively. The operators $\tilde{c}_{r\sigma}^{(\dagger)}$ are defined in Eq. (4.12) and (4.13). In evaluating the above matrix elements, take into account only terms up to order λ^2.

5. Assign a factor of $(-i)(-1)^{a+b}$ where a is the number of vertices on the lower propagator and b is the number of crossings of tunneling lines.

6. Sum over all leads r.

7. Integrate over all energies of tunneling lines. In the sequential-tunneling regime only one tunneling line is involved. In this case, the frequency integration reduces to a simple application of Cauchy's formula.

8. For the computation of $\mathbf{W}^I$ and $\mathbf{W}^{II}$, one, respectively two tunnel vertices are replaced by current vertices. These give rise to a factor $+1/2$ if they are on the upper (lower) branch of the Keldysh contour and describe the tunneling of an electron into the right (left) or out off the left (right) lead. Otherwise they result in a factor $-1/2$.

A.2 Magnetic impurities in quantum-dot spin valves

The diagrammatic rules for a quantum-dot spin valve that contains magnetic impurities either on the quantum dot or in the tunnel barriers read:

1. Draw all topological different diagrams with tunneling lines connecting vertices on either the same or opposite propagators. Assign to the four corners and all propagators states χ and corresponding energies E_χ as well as an energy ω for every tunneling line.

2. For each part of the diagram between adjacent vertices, assign a resolvent $1/(\Delta E + i0^+)$ where ΔE is the difference between the energies of left- and right-going tunneling lines and propagators.

3. For each tunneling line, the diagram acquires a factor of $\frac{1}{2\pi} f_r^{\pm}(\omega)$ where the sign is determined by whether the line runs forward (-) or backward (+) with respect to the Keldysh contour.

4. For each pair of vertices connected by a tunneling line the diagram is multiplied by
$$\frac{1+p}{2}\rho_r \langle \chi_\mathrm{i}'|C_{r\uparrow}|\chi_\mathrm{i}\rangle\langle\chi_\mathrm{f}'|C_{r\uparrow}^\dagger|\chi_\mathrm{f}\rangle + \frac{1-p}{2}\rho_r \langle \chi_\mathrm{i}'|C_{r\downarrow}|\chi_\mathrm{i}\rangle\langle\chi_\mathrm{f}'|C_{r\downarrow}^\dagger|\chi_\mathrm{f}\rangle$$
where χ_i and χ_i' (χ_f and χ_f') are the states that enter and leave the vertex the tunneling line begins (ends) at, respectively. The operators $C_{r\uparrow}$ and $C_{r\downarrow}$ are the coefficients (including the dot operators!) of $a_{r\mathbf{k}+}^\dagger$ and $a_{r\mathbf{k}-}^\dagger$ in the tunnel Hamiltonians (5.5), (5.6) and (5.9), respectively.

5. The diagram obtains a factor $(-i)(-1)^{a+b}$ where a is the number of vertices on the lower propagator and b is the number of crossings of tunneling lines.

6. Sum over all leads r and integrate over all energies ω.

7. The diagrams for $\mathbf{W}^I$ and $\mathbf{W}^{II}$ are obtained by replacing one, respectively two tunneling vertices by current vertices. These give rise to a factor of $+1/2$ (-1/2) if the vertex is on the upper (lower) branch and corresponds to an electron tunneling into the right (left) lead or out off the left (right) lead.

A.3 Quantum-dot spin valves with a superconducting lead

For a quantum-dot spin valve with an additional superconducting lead with an infinite superconducting gap, $\Delta \to \infty$, the diagrammatic rules take the following form:

1. Draw all topological different diagrams with vertices on the propagators. Assign states χ and corresponding energies E_χ to the corners and all propagators. The vertices are contracted pairwise by tunneling lines that either conserve or flip the spin.

2. Assign to all diagrams a resolvent $1/(\Delta E + i0^+)$ for each section on the contour between two adjacent vertices. Here ΔE is the energy difference between the left- and right-going propagators and tunneling lines.

3. The tunneling lines involving the ferromagnetic electrode r give rise to a factor of $\frac{\Gamma_r}{2\pi} f_r^{\pm}(\omega_i)$ if they do not flip the spin of the tunneling electron. If they flip it from up to down, they give rise to a factor of $\frac{p\Gamma}{2\pi} e^{i\phi_r} f_r^{\pm}(\omega_i)$. Flipping the spin in the opposite direction gives rise to the complex conjugate of the aforementioned factor. Here, the upper (lower) sign refers to lines running backward (forward) with respect to the Keldysh contour.

4. Associate with each vertex that annihilates (creates) a dot electron with spin σ a factor $\langle\chi_2|c_\sigma|\chi_1\rangle$ ($\langle\chi_2|c_\sigma^\dagger|\chi_1\rangle$). Here χ_1 and χ_2 are the states that enter and leave the vertex, respectively.

5. Assign an overall prefactor $(-i)(-1)^{a+b}$ where a is the number of vertices on the lower propagator and b is the number of crossings of tunneling lines.

6. Integrate over the energies of the tunneling lines ω_i and sum over all diagrams.

7. To obtain the generalized current rates $W^{I_r\chi_2\chi_2'}_{\chi_1\chi_1'}$ multiply each rate $W^{\chi_2\chi_2'}_{\chi_1\chi_1'}$ with a factor for all tunneling lines that are associated with lead r that is the sum of the following numbers:
   a) $+1$ if the line is going from the lower to the upper propagator,
   b) -1 if the line is going from the upper to the lower propagator,
   c) 0 else.

B Master equations

In the following, we give explicit expressions for the different abbreviations that we introduced to write compact expressions for the various master equations that occurred in this thesis.

B.1 Spin waves in quantum-dot spin valves

In this section, we give expressions for the various functions that enter the master equations (4.15) and (4.16) that describe transport through a quantum-dot spin valve with magnons in the electrodes.

Introducing the abbreviations

$$\begin{aligned}
r_r &= (1+p_r)n_r f_r^+(\varepsilon-\omega_b) + (1-p_r)(1+n_r)f_r^+(\varepsilon+\omega_b),\\
s_r &= (1+p_r)(1+n_r)f_r^-(\varepsilon+U-\omega_b) - (1-p_r)n_r f_r^-(\varepsilon+\omega_b),\\
x_r &= f_r^-(\varepsilon) + f_r^+(\varepsilon+U),\\
y_r &= f_r^-(\varepsilon) - f_r^+(\varepsilon+U),\\
z_{r\pm} &= (1+p_r)(1+n_r)f_r^-(\varepsilon-\omega_b) \pm (1-p_r)n_r f_r^-(\varepsilon+\omega_b)\\
&\quad \pm(1+p_r)n_r f_r^+(\varepsilon+U-\omega_b) + (1-p_r)(1+n_r)f_r^+(\varepsilon+U+\omega_b),
\end{aligned}$$

we can write the quantities $M^{(r)}_{\chi\mathbf{n},\chi'\mathbf{m}}$ as matrices in the basis $|0\rangle$, $|1\rangle$, $|d\rangle$:

$$M^{(r)}_{\mathbf{n},\mathbf{n}} = \Gamma_r \begin{pmatrix} -2(1-\lambda^2 n_r) f_r^+(\varepsilon) - \lambda^2 r_r & (1-\lambda^2 n_r) f_r^-(\varepsilon) & 0 \\ 2(1-\lambda^2 n_r) f_r^+(\varepsilon) & -(1-\lambda^2 n_r) y_r + \frac{\lambda^2}{2} z_{r+} & 2(1-\lambda^2 n_r) f_r^-(\varepsilon+U) \\ 0 & (1-\lambda^2 n_r) f_r^+(\varepsilon+U) & -2(1-\lambda^2 n_r) f_r^-(\varepsilon+U) - \lambda^2 s_r \end{pmatrix}, \tag{B.1}$$

$$M^{(r)}_{\mathbf{n},\mathbf{n}-1} = \frac{\lambda^2}{2} n_r \begin{pmatrix} 0 & \Gamma_{r+} f_r^-(\varepsilon-\omega_b) & 0 \\ 2\Gamma_{r-} f_r^+(\varepsilon+\omega_b) & 0 & 2\Gamma_{r+} f_r^-(\varepsilon+U-\omega_b) \\ 0 & \Gamma_{r-} f_r^+(\varepsilon+U+\omega_b) & 0 \end{pmatrix}, \tag{B.2}$$

$$M^{(r)}_{\mathbf{n},\mathbf{n}+1} = \frac{\lambda^2}{2}(1+n_r) \begin{pmatrix} 0 & \Gamma_{r-} f_r^-(\varepsilon+\omega_b) & 0 \\ 2\Gamma_{r+} f_r^+(\varepsilon-\omega_b) & 0 & 2\Gamma_{r-} f_r^-(\varepsilon+U+\omega_b) \\ 0 & \Gamma_{r+} f_r^+(\varepsilon+U-\omega_b) & 0 \end{pmatrix}. \tag{B.3}$$

The vectors $V^{(r)}_{\chi\mathbf{n}}$ and $F^{(r)}_{\chi\mathbf{nm}}$ that enter the master equation for the occupations, Eq. (4.15), and spin, Eq. (5.12), respectively, can be written as vectors in the basis $|0\rangle$, $|1\rangle$ and $|d\rangle$ as

$$V^{(r)}_{\mathbf{n}} = 2p_r\Gamma_r(1-\lambda^2 n_r) \begin{pmatrix} f_r^-(\varepsilon) \\ -y_r + \lambda^2 z_{r-} \\ f_r^-(\varepsilon+U) \end{pmatrix}, \tag{B.4}$$

$$V^{(r)}_{\mathbf{n}+1} = \lambda^2(1+n_r) \begin{pmatrix} \Gamma_{r-} f_r^-(\varepsilon+\omega_b) \\ 0 \\ \Gamma_{r+} f_r^-(\varepsilon+U-\omega_b) \end{pmatrix}, \tag{B.5}$$

$$V^{(r)}_{\mathbf{n}-1} = -\lambda^2 n_r \begin{pmatrix} \Gamma_{r+} f_r^-(\varepsilon-\omega_b) \\ 0 \\ \Gamma_{r-} f_r^-(\varepsilon+U+\omega_b) \end{pmatrix}. \tag{B.6}$$

and

$$F^{(r)}_{\mathbf{nn}} = p_r\Gamma_r(1-\lambda^2 n_r)\begin{pmatrix} f_r^+(\varepsilon) \\ -\frac{2y_r+z_{r-}}{2} \\ -f_r^-(\varepsilon+U) \end{pmatrix}, \tag{B.7}$$

$$F^{(r)}_{\mathbf{nn+1}} = \frac{\lambda^2}{2}(1+n_r)\begin{pmatrix} \Gamma_{r+}f_r^+(\varepsilon-\omega_b) \\ 0 \\ \Gamma_{r-}f_r^-(\varepsilon+U+\omega_b) \end{pmatrix}, \tag{B.8}$$

$$F^{(r)}_{\mathbf{nn-1}} = \frac{\lambda^2}{2}n_r\begin{pmatrix} \Gamma_{r-}f_r^+(\varepsilon+\omega_b) \\ 0 \\ \Gamma_{r+}f_r^-(\varepsilon+U-\omega_b) \end{pmatrix}. \tag{B.9}$$

Finally, we have

$$G^{(r)} = (1-\lambda^2 n_r)\Gamma_r x_r + \frac{\lambda^2}{2}\Gamma_r z_{r+}. \tag{B.10}$$

B.2 Impurity in tunnel barrier

In the following, we summarize the explicit expressions for the various quantities that occured in the master equations for the occupation probabilities and the spin, (5.11) and (5.12) which describe transport through a quantum-dot spin valve with an impurity spin embedded in the right tunnel barrier.

Introducing

$$\gamma = \Gamma_\mathrm{R} + m^2 J_\mathrm{R} + 2mp\eta\sqrt{\Gamma_\mathrm{R}J_\mathrm{R}}, \tag{B.11}$$

$$\tilde{\gamma} = p\Gamma_\mathrm{R} + m^2 p J_\mathrm{R} + 2m\eta\sqrt{\Gamma_\mathrm{R}J_\mathrm{R}}, \tag{B.12}$$

$$\alpha_\pm = B + (2m\pm 1)D, \tag{B.13}$$

$$A_\pm(m) = S(S+1) - m(m\pm 1), \tag{B.14}$$

we find for the coupling to the left lead the same expressions as for the ordinary quantum-dot spin valve [65],

$$\mathbf{W}_{\mathrm{L}}^{(0)} = \Gamma_{\mathrm{L}} \begin{pmatrix} -2f_{\mathrm{L}}^{+}(\varepsilon) & f_{\mathrm{L}}^{-}(\varepsilon) & 0 \\ 2f_{\mathrm{L}}^{+}(\varepsilon) & -f_{\mathrm{L}}^{-}(\varepsilon) - f_{\mathrm{L}}^{+}(\varepsilon+U) & 2f_{\mathrm{L}}^{-}(\varepsilon+U) \\ 0 & f_{\mathrm{L}}^{+}(\varepsilon+U) & -f_{\mathrm{L}}^{-}(\varepsilon+U) \end{pmatrix}, \tag{B.15}$$

$$V_{\mathrm{L}}^{(0)} = 2p\Gamma_{\mathrm{L}} \begin{pmatrix} f_{\mathrm{L}}^{-}(\varepsilon) \\ -f_{\mathrm{L}}^{-}(\varepsilon) + f_{\mathrm{L}}^{+}(\varepsilon+U) \\ -f_{\mathrm{L}}^{+}(\varepsilon+U) \end{pmatrix}, \tag{B.16}$$

$$\left(\frac{d\mathbf{s}_m}{dt}\right)_{\mathrm{acc,L}}^{(0)} = p\Gamma_{\mathrm{L}} \left(f_{\mathrm{L}}^{+}(\varepsilon) P_{0,m} - \frac{f_{\mathrm{L}}^{-}(\epsilon) - f_{\mathrm{L}}^{+}(\varepsilon+U)}{2} P_{1,m} - f_{\mathrm{L}}^{-}(\varepsilon+U) P_{d,m} \right) \mathbf{n}_{\mathrm{L}}, \tag{B.17}$$

$$\left(\frac{d\mathbf{s}_m}{dt}\right)_{\mathrm{rel,L}}^{(0)} = -\Gamma_{\mathrm{L}} \left(f_{\mathrm{L}}^{-}(\varepsilon) + f_{\mathrm{L}}^{+}(\varepsilon+U) \right) \mathbf{s}_m, \tag{B.18}$$

while for the coupling to the right lead, we have, written as matrices and vectors in the basis $|0m\rangle$, $|1m\rangle$, $|dm\rangle$,

$$\mathbf{W}_{\mathrm{R}}^{(0)} = \begin{pmatrix} W_{\mathrm{R},00}^{(0)} & \gamma f_{\mathrm{R}}^{-}(\varepsilon) & 0 \\ 2\gamma f_{\mathrm{R}}^{+}(\varepsilon) & W_{\mathrm{R},11}^{(0)} & 2\gamma f_{\mathrm{R}}^{-}(\varepsilon+U) \\ 0 & \gamma f_{\mathrm{R}}^{+}(\varepsilon+U) & W_{\mathrm{R},dd}^{(0)} \end{pmatrix}, \tag{B.19}$$

$$V_{\mathrm{R}}^{(0)} = 2 \begin{pmatrix} \gamma f_{\mathrm{R}}^{-}(\varepsilon) \\ \tilde{\gamma} \left[-f_{\mathrm{R}}^{-}(\varepsilon) + f_{\mathrm{R}}^{+}(\varepsilon+U) \right] + A_{+}(m-1) J_{\mathrm{R}} \left[\frac{1+p}{2} f_{\mathrm{R}}^{-}(\varepsilon-\alpha_{-}) + \frac{1-p}{2} f_{\mathrm{R}}^{+}(\varepsilon+U+\alpha_{-}) \right] \\ -A_{-}(m+1) J_{\mathrm{R}} \left[\frac{1-p}{2} f_{\mathrm{R}}^{-}(\varepsilon+\alpha_{+}) + \frac{1+p}{2} f_{\mathrm{R}}^{+}(\varepsilon+U-\alpha_{+}] \right) \\ \gamma f_{\mathrm{R}}^{+}(\varepsilon+U) \end{pmatrix}, \tag{B.20}$$

$$\mathbf{W}_{\mathrm{R}}^{(+1)} = A_{-}(m+1) J_{\mathrm{R}} \begin{pmatrix} 0 & \frac{1+p}{2} f_{\mathrm{R}}^{-}(\varepsilon-\alpha_{+}) & 0 \\ (1-p) f_{\mathrm{R}}^{+}(\varepsilon+\alpha_{+}) & 0 & (1+p) f_{\mathrm{R}}^{-}(\varepsilon+U-\alpha_{+}) \\ 0 & \frac{1-p}{2} f_{\mathrm{R}}^{+}(\varepsilon+U+\alpha_{+}) & 0 \end{pmatrix}, \tag{B.21}$$

$$V_{\mathrm{R}}^{(+1)} = A_{-}(m+1)J_{\mathrm{R}} \begin{pmatrix} -(1+p)f_{\mathrm{R}}^{-}(\varepsilon-\alpha_{+}) \\ 0 \\ -(1-p)f_{\mathrm{R}}^{+}(\varepsilon+U+\alpha_{+}) \end{pmatrix}, \tag{B.22}$$

$$\mathbf{W}_{\mathrm{R}}^{(-1)} = A_{+}(m-1)J_{\mathrm{R}} \begin{pmatrix} 0 & \frac{1-p}{2}f_{\mathrm{R}}^{-}(\varepsilon+\alpha_{-}) & 0 \\ (1+p)f_{\mathrm{R}}^{+}(\varepsilon-\alpha_{-}) & 0 & (1-p)f_{\mathrm{R}}^{-}(\varepsilon+U+\alpha_{-}) \\ 0 & \frac{1+p}{2}f_{\mathrm{R}}^{+}(\varepsilon+U-\alpha_{-}) & 0 \end{pmatrix}, \tag{B.23}$$

$$V_{\mathrm{R}}^{(-1)} = A_{+}(m-1)J_{\mathrm{R}} \begin{pmatrix} (1-p)f_{\mathrm{R}}^{-}(\varepsilon+\alpha_{-}) \\ 0 \\ (1+p)f_{\mathrm{R}}^{+}(\varepsilon+U-\alpha_{-}) \end{pmatrix}, \tag{B.24}$$

$$\begin{aligned} \left(\frac{d\mathbf{s}_m}{dt}\right)_{\mathrm{acc,R}}^{(0)} = \tilde{\gamma}f_{\mathrm{R}}^{+}(\varepsilon)P_{0,m} - \tilde{\gamma}f_{\mathrm{R}}^{-}(\varepsilon+U)P_{d,m} + \Bigg[\tilde{\gamma}\frac{-f_{\mathrm{R}}^{-}(\varepsilon)+f_{\mathrm{R}}^{+}(\varepsilon+U)}{2} \\ +A_{+}(m-1)\frac{J_{\mathrm{R}}}{2}\left(\frac{1+p}{2}f_{\mathrm{R}}^{-}(\varepsilon-\alpha_{-})+\frac{1-p}{2}f_{\mathrm{R}}^{+}(\varepsilon+U+\alpha_{-})\right) \\ -A_{-}(m+1)\frac{J_{\mathrm{R}}}{2}\left(\frac{1-p}{2}f_{\mathrm{R}}^{-}(\varepsilon+\alpha_{+})+\frac{1+p}{2}f_{\mathrm{R}}^{+}(\varepsilon+U-\alpha_{+})\right)\Bigg] P_{1,m}, \end{aligned} \tag{B.25}$$

$$\left(\frac{d\mathbf{s}_m}{dt}\right)_{\mathrm{acc,R}}^{(+1)} = A_{-}(m+1)J_{\mathrm{R}}\left[(1-p)f_{\mathrm{R}}^{+}(\varepsilon+\alpha_{+})P_{0,m+1} + (1+p)f_{\mathrm{R}}^{-}(\varepsilon+U-\alpha_{+})P_{d,m+1}\right]\mathbf{n}_{\mathrm{R}}, \tag{B.26}$$

$$\left(\frac{d\mathbf{s}_m}{dt}\right)_{\mathrm{acc,R}}^{(-1)} = -A_{+}(m-1)J_{\mathrm{R}}\left[(1+p)f_{\mathrm{R}}^{+}(\varepsilon-\alpha_{-})P_{0,m-1} + (1-p)f_{\mathrm{R}}^{-}(\varepsilon+U+\alpha_{-})P_{d,m-1}\right]\mathbf{n}_{\mathrm{R}}, \tag{B.27}$$

$$\left(\frac{d\mathbf{s}_m}{dt}\right)^{(0)}_{\mathrm{rel,R}} = -\Big[\gamma(f_{\mathrm{R}}^-(\varepsilon)+f_{\mathrm{R}}^+(\varepsilon+U)) + A_+(m-1)J_{\mathrm{R}}\left(\frac{1+p}{2}f_{\mathrm{R}}^-(\varepsilon-\alpha_-)+\frac{1-p}{2}f_{\mathrm{R}}^+(\varepsilon+U+\alpha_-)\right) + A_-(m+1)J_{\mathrm{R}}\left(\frac{1-p}{2}f_{\mathrm{R}}^-(\varepsilon+\alpha_+)+\frac{1+p}{2}f_{\mathrm{R}}^+(\varepsilon+U-\alpha_+)\right)\Big]\mathbf{s}_m. \quad \text{(B.28)}$$

B.3 Impurity on the dot

For the description of a quantum-dot spin valve with an impurity spin on the quantum dot, we introduced the matrix $\mathbf{W}$ in the master equation (5.16). This matrix can be decomposed as $\mathbf{W} = \sum_r \Gamma_r \mathbf{W}_r$ where

$$\mathbf{W}_r = \begin{pmatrix} W_{0\uparrow 0\uparrow} & 0 & f_r^-(\varepsilon+B/2) & 1/2f_r^-(\varepsilon-B/2) & 0 & 0 & 0 \\ 0 & W_{0\downarrow 0\downarrow} & 0 & 1/2f_r^-(\varepsilon+B/2) & f_r^-(\varepsilon-B/2) & 0 & 0 \\ f_r^+(\varepsilon+B/2) & 0 & W_{T_+T_+} & 0 & 0 & f_r^-(\varepsilon+U-B/2) & 0 \\ f_r^+(\varepsilon-B/2) & f_r^+(\varepsilon+B/2) & 0 & W_{I_0I_0} & 0 & f_r^-(\varepsilon+U+B/2) & f_r^-(\varepsilon+U-B/2) \\ 0 & f_r^+(\varepsilon-B/2) & 0 & 0 & W_{T_-T_-} & 0 & f_r^-(\varepsilon+U+B/2) \\ 0 & 0 & f_r^+(\varepsilon+U-B/2) & 1/2f_r^+(\varepsilon+U+B/2) & 0 & W_{d\uparrow d\uparrow} & 0 \\ 0 & 0 & 0 & 1/2f_r^+(\varepsilon+U-B/2) & f_r^+(\varepsilon+U+B/2) & 0 & W_{d\downarrow d\downarrow} \end{pmatrix}. \quad \text{(B.29)}$$

The diagonal entries $W_{\chi\chi}$ are determined by the sum rule $\sum_{\chi'} W_{\chi'\chi} = 0$ which guarantees the conservation of probability. The vector $\mathbf{V}$ in (5.16) is given by

$$\mathbf{V} = \sum_r \Gamma_r \begin{pmatrix} -f_r^-(\varepsilon-B/2) \\ f_r^-(\varepsilon+B/2) \\ 0 \\ f_r^-(\varepsilon-B/2) - f_r^-(\varepsilon+B/2) + f_r^+(\varepsilon+U+B/2) - f_r^+(\varepsilon+U-B/2) \\ 0 \\ -f_r^+(\varepsilon+U+B/2) \\ f_r^+(\varepsilon+U-B/2) \end{pmatrix}. \quad \text{(B.30)}$$

B.4 Proximized quantum-dot spin valve

In the following, we give the expressions for the quantities appearing in Eq. (7.10) that describes the occupation probabilities of a quantum-dot spin valve with an additional superconducting electrode. We employ the abbreviations $\Gamma_{r\pm} = \Gamma_r \left(1 \pm \frac{\delta}{2\varepsilon_\mathrm{A}}\right)$ and $f^{\pm}_{r\gamma\gamma'} = f^{\pm}_r(E_{\mathrm{A},\gamma\gamma'})$, where $f^{+}_r(\omega) = 1 - f^{-}_r(\omega)$ denotes the Fermi function of lead r.

The matrix $\mathbf{A}_r$ depends on the position of the Andreev excitation energies and it reads

$$\mathbf{A}_r = \begin{pmatrix} -\Gamma_{r+} f^{-}_{r++} - \Gamma_{r-} f^{+}_{r--} & 0 & \frac{\Gamma_{r-}}{2} f^{-}_{r--} + \frac{\Gamma_{r+}}{2} f^{+}_{r++} \\ 0 & -\Gamma_{r-} f^{-}_{r+-} - \Gamma_{r+} f^{+}_{r-+} & \frac{\Gamma_{r+}}{2} f^{-}_{r-+} + \frac{\Gamma_{r-}}{2} f^{+}_{r+-} \\ \Gamma_{r+} f^{-}_{r++} + \Gamma_{r-} f^{+}_{r--} & \Gamma_{r-} f^{-}_{r+-} + \Gamma_{r+} f^{+}_{r-+} & -\frac{\Gamma_{r-}}{2} f^{-}_{r--} - \frac{\Gamma_{r+}}{2} f^{-}_{r-+} - \frac{\Gamma_{r+}}{2} f^{+}_{r++} - \frac{\Gamma_{r-}}{2} f^{+}_{r+-} \end{pmatrix}. \tag{B.31}$$

The vectors $\mathbf{b}_r$ describing the influence of the average spin on the dot on the diagonal probabilities are given by

$$\mathbf{b}_r = \begin{pmatrix} \Gamma_{r-} f^{-}_{r--} - \Gamma_{r+} f^{+}_{r++} \\ \Gamma_{r+} f^{-}_{r-+} - \Gamma_{r-} f^{+}_{r+-} \\ -\Gamma_{r-} f^{-}_{r--} - \Gamma_{r+} f^{-}_{r-+} + \Gamma_{r+} f^{+}_{r++} + \Gamma_{r-} f^{+}_{r+-} \end{pmatrix}. \tag{B.32}$$

C Density matrix for two spin-$1/2$ particles

In the following, we give the relation between the physical quantities introduced in Section 5.2.2 and the density matrix elements in Eq. (5.15). For the occupation probabilities of the dot we have

$$P_0 = P_{0\uparrow} + P_{0\downarrow}, \tag{C.1}$$
$$P_1 = P_{T^+} + P_{T^0} + P_{T^-} + P_S, \tag{C.2}$$
$$P_d = P_{d\uparrow} + P_{d\downarrow}. \tag{C.3}$$

For the expectation values of the impurity spin when the dot is empty, we get

$$S_{0x} = \mathrm{Re}\, P^{0\downarrow}_{0\uparrow}, \tag{C.4}$$
$$S_{0y} = \mathrm{Im}\, P^{0\downarrow}_{0\uparrow}, \tag{C.5}$$
$$S_{0z} = \frac{P_{0\uparrow} - P_{0\downarrow}}{2}. \tag{C.6}$$

When the dot is singly occupied, we have

$$S_{2x} = \frac{-\mathrm{Re}\, P^S_{T^-} + \mathrm{Re}\, P^S_{T^+} + \mathrm{Re}\, P^{T^0}_{T^-} + \mathrm{Re}\, P^{T^0}_{T^+}}{\sqrt{2}}, \tag{C.7}$$
$$S_{2y} = \frac{\mathrm{Im}\, P^S_{T^-} + \mathrm{Im}\, P^S_{T^+} + \mathrm{Im}\, P^{T^0}_{T^+} - \mathrm{Im}\, P^{T^0}_{T^-}}{\sqrt{2}}, \tag{C.8}$$
$$S_{2z} = \frac{P_{T^+} - P_{T^-} - 2\,\mathrm{Re}\, P^S_{T^0}}{2}, \tag{C.9}$$

and for the doubly occupied dot, we find

$$S_{dx} = \mathrm{Re}\, P^{d\downarrow}_{d\uparrow}, \tag{C.10}$$
$$S_{dy} = \mathrm{Im}\, P^{d\downarrow}_{d\uparrow}, \tag{C.11}$$
$$S_{dz} = \frac{P_{d\uparrow} - P_{d\downarrow}}{2}. \tag{C.12}$$

The expectation value of the electron spin on the dot can be expressed as

$$S_{1x} = \frac{\mathrm{Re}\, P^S_{T^-} - \mathrm{Re}\, P^S_{T^+} + \mathrm{Re}\, P^{T^0}_{T^-} + \mathrm{Re}\, P^{T^0}_{T^+}}{\sqrt{2}}, \tag{C.13}$$
$$S_{1y} = \frac{-\mathrm{Im}\, P^S_{T^-} - \mathrm{Im}\, P^S_{T^+} + \mathrm{Im}\, P^{T^0}_{T^+} - \mathrm{Im}\, P^{T^0}_{T^-}}{\sqrt{2}}, \tag{C.14}$$
$$S_{1z} = \frac{P_{T^+} - P_{T^-} + 2\,\mathrm{Re}\, P^S_{T^0}}{2}. \tag{C.15}$$

For the scalar product of the electron and impurity spin, we find

$$\mathbf{S}_1 \cdot \mathbf{S}_2 = \frac{P_{T^+} + P_{T^0} + P_{T^-} - 3P_S}{4}, \tag{C.16}$$

while for their vector product, we get

$$(\mathbf{S}_1 \times \mathbf{S}_2)_x = \frac{\operatorname{Im} P^S_{T^-} - \operatorname{Im} P^S_{T^+}}{\sqrt{2}}, \tag{C.17}$$

$$(\mathbf{S}_1 \times \mathbf{S}_2)_y = \frac{\operatorname{Re} P^S_{T^+} + \operatorname{Re} P^S_{T^-}}{\sqrt{2}}, \tag{C.18}$$

$$(\mathbf{S}_1 \times \mathbf{S}_2)_z = \operatorname{Im} P^S_{T^0}. \tag{C.19}$$

Finally, the quadrupole moments are given by

$$Q_{xx} = \frac{2P_{T^0} - P_{T^-} - P_{T^+} + 6\operatorname{Re} P^{T^-}_{T^+}}{12}, \tag{C.20}$$

$$Q_{yy} = \frac{2P_{T^0} - P_{T^-} - P_{T^+} - 6\operatorname{Re} P^{T^-}_{T^+}}{12}, \tag{C.21}$$

$$Q_{zz} = \frac{P_{T^+} - 2P_{T^0} + P_{T^-}}{6}, \tag{C.22}$$

$$Q_{xy} = \frac{\operatorname{Im} P^{T^-}_{T^+}}{2}, \tag{C.23}$$

$$Q_{xz} = \frac{-\operatorname{Re} P^{T^0}_{T^-} + \operatorname{Re} P^{T^0}_{T^+}}{2\sqrt{2}}, \tag{C.24}$$

$$Q_{yz} = \frac{\operatorname{Im} P^{T^0}_{T^-} + \operatorname{Im} P^{T^0}_{T^+}}{2\sqrt{2}}. \tag{C.25}$$

D Equation of motions for two spin-1/2 particles

The equations of motion of two exchange-coupled spins $\mathbf{S}_1$ and $\mathbf{S}_2$ subject to magnetic fields $\mathbf{B}_1$ and $\mathbf{B}_2$, respectively, as described by the Hamiltonian (5.43) are given by

$$\frac{d\mathbf{S}_1}{dt} = -\mathbf{S}_1 \times \mathbf{B}_1 - J(\mathbf{S}_1 \times \mathbf{S}_2), \tag{D.1}$$

$$\frac{d\mathbf{S}_2}{dt} = -\mathbf{S}_2 \times \mathbf{B}_2 + J(\mathbf{S}_1 \times \mathbf{S}_2), \tag{D.2}$$

$$\begin{aligned}\frac{d}{dt}(\mathbf{S}_1 \times \mathbf{S}_2) = \frac{J}{2}(\mathbf{S}_1 - \mathbf{S}_2) - \frac{1}{2}(\mathbf{S}_1 \times \mathbf{S}_2) \times (\mathbf{B}_1 + \mathbf{B}_2) \\ + \left(\mathbf{Q} - \frac{2}{3}(\mathbf{S}_1 \cdot \mathbf{S}_2)\right) \cdot (\mathbf{B}_1 - \mathbf{B}_2),\end{aligned} \tag{D.3}$$

$$\frac{d}{dt}(\mathbf{S}_1 \cdot \mathbf{S}_2) = (\mathbf{S}_1 \times \mathbf{S}_2) \cdot (\mathbf{B}_1 - \mathbf{B}_2), \tag{D.4}$$

$$\begin{aligned}\frac{d}{dt}\mathbf{Q}_{ij} = -\frac{1}{2}\left(\frac{1}{2}(\mathbf{S}_1 \times \mathbf{S}_2)_i(\mathbf{B}_1 - \mathbf{B}_2)_j + \frac{1}{2}(\mathbf{S}_1 \times \mathbf{S}_2)_j(\mathbf{B}_1 - \mathbf{B}_2)_i\right. \\ \left. - \frac{1}{3}(\mathbf{S}_1 \times \mathbf{S}_2) \cdot (\mathbf{B}_1 - \mathbf{B}_2)\delta_{ij}\right) - \frac{1}{2}\varepsilon_{ilm}\mathbf{Q}_{lj}(\mathbf{B}_1 + \mathbf{B}_2)_m \\ - \frac{1}{2}\varepsilon_{jlm}\mathbf{Q}_{li}(\mathbf{B}_1 + \mathbf{B}_2)_m.\end{aligned} \tag{D.5}$$

It is interesting to note that some terms contain the sum of the two magnetic fields while other couple to the difference. For the quantum-dot system under investigation in Chapter 5, the electron spin $\mathbf{S}_1$ experiences an externally applied magnetic field as well as the exchange field due to virtual tunneling while the impurity spin $\mathbf{S}_2$ only feels the external field. In consequence, some terms in the master equations turn out to be sensitive only to the exchange field, as the external fields acts on both spins in the same way, while others are sensitive to all field contributions.

Bibliography

[1] H. Grabert and M. H. Devoret, *Single Charge Tunneling: Coulomb Blockade Phenomena in Nanostructures* (Springer, 1992).

[2] P. W. Anderson, Phys. Rev. **124**, 41 (1961).

[3] L. I. Glazman and K. A. Matveev, JETP Lett. **48**, 445 (1988).

[4] C. W. J. Beenakker, Phys. Rev. B **44**, 1646 (1991).

[5] D. V. Averin, A. N. Korotkov, and K. K. Likharev, Phys. Rev. B **44**, 6199 (1991).

[6] D. V. Averin and A. A. Odintsov, Phys. Lett. A **140**, 251 (1989).

[7] D. V. Averin and Y. V. Nazarov, Phys. Rev. Lett. **65**, 2446 (1990).

[8] J. König, H. Schoeller, and G. Schön, Phys. Rev. Lett. **78**, 4482 (1997).

[9] J. König, H. Schoeller, and G. Schön, Phys. Rev. B **58**, 7882 (1998).

[10] J. Kondo, Prog. Theor. Phys. **32**, 37 (1964).

[11] W. de Haas, J. de Boer, and G. van dën Berg, Physica **1**, 1115 (1934).

[12] D. Goldhaber-Gordon, H. Shtrikman, D. Mahalu, D. Abusch-Magder, U. Meirav, and M. A. Kastner, Nature **391**, 156 (1998).

[13] W. G. van der Wiel, S. D. Franceschi, T. Fujisawa, J. M. Elzerman, S. Tarucha, and L. P. Kouwenhoven, Science **289**, 2105 (2000).

[14] A. N. Pasupathy, R. C. Bialczak, J. Martinek, J. E. Grose, L. A. K. Donev, P. L. McEuen, and D. C. Ralph, Science **306**, 86 (2004).

[15] J. R. Hauptmann, J. Paaske, and P. E. Lindelof, Nat. Phys. **4**, 373 (2008).

[16] L. Hofstetter, A. Geresdi, M. Aagesen, J. Nygård, C. Schönenberger, and S. Csonka, Phys. Rev. Lett. **104**, 246804 (2010).

[17] C. B. Winkelmann, N. Roch, W. Wernsdorfer, V. Bouchiat, and F. Balestro, Nat. Phys. **5**, 876 (2009).

[18] L. H. Yu and D. Natelson, Nano Lett. **4**, 79 (2003).

[19] N. Roch, S. Florens, V. Bouchiat, W. Wernsdorfer, and F. Balestro, Nature **453**, 633 (2008).

[20] J. R. Schrieffer and P. A. Wolff, Phys. Rev. **149**, 491 (1966).

[21] P. W. Anderson, J. Phys. C: Solid State Phys. **3**, 2436 (1970).

[22] D. J. Gross and F. Wilczek, Phys. Rev. Lett. **30**, 1343 (1973).

[23] H. D. Politzer, Phys. Rev. Lett. **30**, 1346 (1973).

[24] D. J. Gross and F. Wilczek, Phys. Rev. D **8**, 3633 (1973).

[25] D. J. Gross and F. Wilczek, Phys. Rev. D **9**, 980 (1974).

[26] F. D. M. Haldane, Phys. Rev. Lett. **40**, 416 (1978).

[27] K. G. Wilson, Rev. Mod. Phys. **47**, 773 (1975).

[28] S. Maekawa and T. Shinjo, *Spin Dependent Transport in Magnetic Nanostructures* (Taylor & Francis, New York, 2002).

[29] S. Maekawa, *Concepts in Spin Electronics* (Oxford University Press, New York, 2006).

[30] G. A. Prinz, Science **282**, 1660 (1998).

[31] S. A. Wolf, D. D. Awschalom, R. A. Buhrman, J. M. Daughton, S. von Molnar, M. L. Roukes, A. Y. Chtchelkanova, and D. M. Treger, Science **294**, 1488 (2001).

[32] I. Žutić, J. Fabian, and S. D. Sarma, Rev. Mod. Phys. **76**, 323 (2004).

[33] P. Seneor, A. Bernand-Mantel, and F. Petroff, J. Phys.: Condens. Matter **19**, 165222 (2007).

[34] J. Fabian, A. Matos-Abiague, C. Ertler, P. Stano, and I. Zutic, Acta Phys. Slov. **57**, 565 (2007).

[35] A. Fert, Rev. Mod. Phys. **80**, 1517 (2008).

[36] M. N. Baibich, J. M. Broto, A. Fert, F. N. V. Dau, F. Petroff, P. Etienne, G. Creuzet, A. Friederich, and J. Chazelas, Phys. Rev. Lett. **61**, 2472 (1988).

[37] G. Binasch, P. Grünberg, F. Saurenbach, and W. Zinn, Phys. Rev. B **39**, 4828 (1989).

[38] N. F. Mott, Proc. R. Soc. Lond. A **153**, 699 (1936).

[39] A. Fert and I. A. Campbell, Phys. Rev. Lett. **21**, 1190 (1968).

[40] M. Julliere, Phys. Lett. A **54**, 225 (1975).

[41] J. S. Moodera, J. Nowak, and R. J. M. van de Veerdonk, Phys. Rev. Lett. **80**, 2941 (1998).

[42] J. C. Slonczewski, Phys. Rev. B **39**, 6995 (1989).

[43] J. S. Moodera and L. R. Kinder, in *The 40th annual conference on magnetism and magnetic materials*, Vol. 79 (AIP, Philadelphia, Pennsylvania (USA), 1996) pp. 4724–4729.

[44] H. Jaffrès, D. Lacour, F. N. V. Dau, J. Briatico, F. Petroff, and A. Vaurès, Phys. Rev. B **64**, 064427 (2001).

[45] J. H. Van Santen and G. H. Jonker, Physica **16**, 599 (1950).

[46] R. von Helmolt, J. Wecker, B. Holzapfel, L. Schultz, and K. Samwer, Phys. Rev. Lett. **71**, 2331 (1993).

[47] S. Jin, T. H. Tiefel, M. McCormack, R. A. Fastnacht, R. Ramesh, and L. H. Chen, Science **264**, 413 (1994).

[48] C. Zener, Phys. Rev. **82**, 403 (1951).

[49] P. W. Anderson and H. Hasegawa, Phys. Rev. **100**, 675 (1955).

[50] P. G. de Gennes, Phys. Rev. **118**, 141 (1960).

[51] M. Johnson and R. H. Silsbee, Phys. Rev. Lett. **55**, 1790 (1985).

[52] M. Johnson and R. H. Silsbee, Phys. Rev. B **37**, 5326 (1988).

[53] M. Zaffalon and B. J. van Wees, Phys. Rev. Lett. **91**, 186601 (2003).

[54] M. Zaffalon and B. J. van Wees, Phys. Rev. B **71**, 125401 (2005).

[55] F. J. Jedema, A. T. Filip, and B. J. van Wees, Nature **410**, 345 (2001).

[56] F. J. Jedema, H. B. Heersche, A. T. Filip, J. J. A. Baselmans, and B. J. van Wees, Nature **416**, 713 (2002).

[57] F. J. Jedema, M. S. Nijboer, A. T. Filip, and B. J. van Wees, Phys. Rev. B **67**, 085319 (2003).

[58] T. Kimura and Y. Otani, Phys. Rev. Lett. **99**, 196604 (2007).

[59] N. Tombros, C. Jozsa, M. Popinciuc, H. T. Jonkman, and B. J. van Wees, Nature **448**, 571 (2007).

[60] N. Tombros, S. Tanabe, A. Veligura, C. Jozsa, M. Popinciuc, H. T. Jonkman, and B. J. van Wees, Phys. Rev. Lett. **101**, 046601 (2008).

[61] C. Józsa, M. Popinciuc, N. Tombros, H. T. Jonkman, and B. J. van Wees, Phys. Rev. Lett. **100**, 236603 (2008).

[62] W. Han, W. H. Wang, K. Pi, K. M. McCreary, W. Bao, Y. Li, F. Miao, C. N. Lau, and R. K. Kawakami, Phys. Rev. Lett. **102**, 137205 (2009).

[63] M. Popinciuc, C. Józsa, P. J. Zomer, N. Tombros, A. Veligura, H. T. Jonkman, and B. J. van Wees, Phys. Rev. B **80**, 214427 (2009).

[64] J. König and J. Martinek, Phys. Rev. Lett. **90**, 166602 (2003).

[65] M. Braun, J. König, and J. Martinek, Phys. Rev. B **70**, 195345 (2004).

[66] M. Braun, J. König, and J. Martinek, Europhys. Lett. **72**, 294 (2005).

[67] M. Braun, J. König, and J. Martinek, Phys. Rev. B **74**, 075328 (2006).

[68] S. Lindebaum, D. Urban, and J. König, Phys. Rev. B **79**, 245303 (2009).

[69] I. Weymann, J. Barnaś, J. König, J. Martinek, and G. Schön, Phys. Rev. B **72**, 113301 (2005).

[70] I. Weymann, J. König, J. Martinek, J. Barnaś, and G. Schön, Phys. Rev. B **72**, 115334 (2005).

[71] I. Weymann and J. Barnaś, Eur. Phys. J. B **46**, 289 (2005).

[72] I. Weymann and J. Barnaś, Phys. Rev. B **75**, 155308 (2007).

[73] J. Martinek, Y. Utsumi, H. Imamura, J. Barnaś, S. Maekawa, J. König, and G. Schön, Phys. Rev. Lett. **91**, 127203 (2003).

[74] J. Martinek, M. Sindel, L. Borda, J. Barnaś, J. König, G. Schön, and J. von Delft, Phys. Rev. Lett. **91**, 247202 (2003).

[75] M. Choi, D. Sánchez, and R. López, Phys. Rev. Lett. **92**, 056601 (2004).

[76] Y. Utsumi, J. Martinek, G. Schön, H. Imamura, and S. Maekawa, Phys. Rev. B **71**, 245116 (2005).

[77] J. Martinek, M. Sindel, L. Borda, J. Barnaś, R. Bulla, J. König, G. Schön, S. Maekawa, and J. von Delft, Phys. Rev. B **72**, 121302 (2005).

[78] P. Simon, P. S. Cornaglia, D. Feinberg, and C. A. Balseiro, Phys. Rev. B **75**, 045310 (2007).

[79] D. Matsubayashi and M. Eto, Phys. Rev. B **75**, 165319 (2007).

[80] M. Sindel, L. Borda, J. Martinek, R. Bulla, J. König, G. Schön, S. Maekawa, and J. von Delft, Phys. Rev. B **76**, 045321 (2007).

[81] I. Weymann, Phys. Rev. B **75**, 195339 (2007).

[82] R. Hornberger, S. Koller, G. Begemann, A. Donarini, and M. Grifoni, Phys. Rev. B **77**, 245313 (2008).

[83] P. Trocha, I. Weymann, and J. Barnaś, Phys. Rev. B **80**, 165333 (2009).

[84] I. Weymann, Europhys. Lett. **76**, 1200 (2006).

[85] I. Weymann and J. Barnaś, Phys. Rev. B **77**, 075305 (2008).

[86] S. Koller, L. Mayrhofer, and M. Grifoni, New J. Phys. **9**, 348 (2007).

[87] I. Weymann, J. Barnaś, and S. Krompiewski, Phys. Rev. B **76**, 155408 (2007).

[88] I. Weymann, J. Barnaś, and S. Krompiewski, Phys. Rev. B **78**, 035422 (2008).

[89] I. Weymann and J. Barnaś, Appl. Phys. Lett. **92**, 103127 (2008).

[90] C. Schenke, S. Koller, L. Mayrhofer, and M. Grifoni, Phys. Rev. B **80**, 035412 (2009).

[91] J. König, H. Schoeller, and G. Schön, Phys. Rev. Lett. **76**, 1715 (1996).

[92] J. König, J. Schmid, H. Schoeller, and G. Schön, Phys. Rev. B **54**, 16820 (1996).

[93] H. Schoeller, *Transport theory of interacting quantum dots*, Habilitation thesis (Universität Karlsruhe, 1997) habilitation thesis.

[94] J. König, *Quantum Fluctuations in the Single-Electron Transistor* (Shaker, Aachen, 1999).

[95] D. Urban, M. Braun, and J. König, Phys. Rev. B **76**, 125306 (2007).

[96] B. R. Bułka, J. Martinek, G. Michałek, and J. Barnaś, Phys. Rev. B **60**, 12246 (1999).

[97] B. R. Bułka, Phys. Rev. B **62**, 1186 (2000).

[98] A. Cottet and W. Belzig, Europhys. Lett. **66**, 405 (2004).

[99] A. Cottet, W. Belzig, and C. Bruder, Phys. Rev. Lett. **92**, 206801 (2004).

[100] A. Cottet, W. Belzig, and C. Bruder, Phys. Rev. B **70**, 115315 (2004).

[101] W. Belzig, Phys. Rev. B **71**, 161301 (2005).

[102] F. Elste and C. Timm, Phys. Rev. B **73**, 235305 (2006).

[103] D. Urban and J. König, Phys. Rev. B **79**, 165319 (2009).

[104] G. Schmidt, D. Ferrand, L. W. Molenkamp, A. T. Filip, and B. J. van Wees, Phys. Rev. B **62**, R4790 (2000).

[105] E. I. Rashba, Phys. Rev. B **62**, R16267 (2000).

[106] A. Fert and H. Jaffrès, Phys. Rev. B **64**, 184420 (2001).

[107] G. Schmidt, J. Phys. D: Appl. Phys. **38**, R107 (2005).

[108] L. F. Schelp, A. Fert, F. Fettar, P. Holody, S. F. Lee, J. L. Maurice, F. Petroff, and A. Vaurès, Phys. Rev. B **56**, R5747 (1997).

[109] K. Yakushiji, S. Mitani, K. Takanashi, S. Takahashi, S. Maekawa, H. Imamura, and H. Fujimori, Appl. Phys. Lett. **78**, 515 (2001).

[110] F. Ernult, K. Yamane, S. Mitani, K. Yakushiji, K. Takanashi, Y. K. Takahashi, and K. Hono, Appl. Phys. Lett. **84**, 3106 (2004).

[111] K. Yakushiji, F. Ernult, H. Imamura, K. Yamane, S. Mitani, K. Takanashi, S. Takahashi, S. Maekawa, and H. Fujimori, Nat. Mater. **4**, 57 (2005).

[112] L. Y. Zhang, C. Y. Wang, Y. G. Wei, X. Y. Liu, and D. Davidović, Phys. Rev. B **72**, 155445 (2005).

[113] R. Guerrero, F. G. Aliev, Y. Tserkovnyak, T. S. Santos, and J. S. Moodera, Phys. Rev. Lett. **97**, 266602 (2006).

[114] Y. G. Wei, C. E. Malec, and D. Davidović, Phys. Rev. B **76**, 195327 (2007).

[115] H. Yang, S. Yang, and S. S. P. Parkin, Nano Lett. **8**, 340 (2007).

[116] S. Mitani, Y. Nogi, H. Wang, K. Yakushiji, F. Ernult, and K. Takanashi, Appl. Phys. Lett. **92**, 152509 (2008).

[117] F. T. Birk, C. E. Malec, and D. Davidović, Phys. Rev. B **79**, 245425 (2009).

[118] M. M. Deshmukh and D. C. Ralph, Phys. Rev. Lett. **89**, 266803 (2002).

[119] A. Bernand-Mantel, P. Seneor, N. Lidgi, M. Munoz, V. Cros, S. Fusil, K. Bouzehouane, C. Deranlot, A. Vaures, F. Petroff, and A. Fert, Appl. Phys. Lett. **89**, 062502 (2006).

[120] A. Bernand-Mantel, P. Seneor, K. Bouzehouane, S. Fusil, C. Deranlot, F. Petroff, and A. Fert, Nat. Phys. **5**, 920 (2009).

[121] K. Hamaya, S. Masubuchi, M. Kawamura, T. Machida, M. Jung, K. Shibata, K. Hirakawa, T. Taniyama, S. Ishida, and Y. Arakawa, Appl. Phys. Lett. **90**, 053108 (2007).

[122] K. Hamaya, M. Kitabatake, K. Shibata, M. Jung, M. Kawamura, K. Hirakawa, T. Machida, T. Taniyama, S. Ishida, and Y. Arakawa, Appl. Phys. Lett. **91**, 022107 (2007).

[123] K. Hamaya, M. Kitabatake, K. Shibata, M. Jung, M. Kawamura, K. Hirakawa, T. Machida, T. Taniyama, S. Ishida, and Y. Arakawa, Appl. Phys. Lett. **91**, 232105 (2007).

[124] K. Hamaya, M. Kitabatake, K. Shibata, M. Jung, M. Kawamura, S. Ishida, T. Taniyama, K. Hirakawa, Y. Arakawa, and T. Machida, Phys. Rev. B **77**, 081302 (2008).

[125] K. Hamaya, M. Kitabatake, K. Shibata, M. Jung, M. Kawamura, S. Ishida, T. Taniyama, K. Hirakawa, Y. Arakawa, and T. Machida, Appl. Phys. Lett. **93**, 222107 (2008).

[126] K. Hamaya, M. Kitabatake, K. Shibata, M. Jung, S. Ishida, T. Taniyama, K. Hirakawa, Y. Arakawa, and T. Machida, Phys. Rev. Lett. **102**, 236806 (2009).

[127] A. Jensen, J. Nygård, and J. Borggreen, in *Proceedings of the International Symposium on Mesoscopic Superconductivity and Spintronics*, edited by H. Takayanagi and J. Nitta (World Scientific, Singapore, 2003) pp. 33–37.

[128] S. Sahoo, T. Kontos, J. Furer, C. Hoffmann, M. Graber, A. Cottet, and C. Schönenberger, Nat. Phys. **1**, 99 (2005).

[129] L. W. Liu, J. H. Fang, L. Lu, H. F. Yang, A. Z. Jin, and C. Z. Gu, Phys. Rev. B **74**, 245429 (2006).

[130] C. A. Merchant and N. Markovic, in *Proceedings of the 53rd annual conference on magnetism and magnetic materials*, Vol. 105 (AIP, Austin, Texas (USA), 2009) p. 07C711.

[131] A. Jensen, J. R. Hauptmann, J. Nygård, J. Sadowski, and P. E. Lindelof, Nano Lett. **4**, 349 (2004).

[132] R. Wiesendanger, Rev. Mod. Phys. **81**, 1495 (2009).

[133] C. F. Hirjibehedin, C. Lin, A. F. Otte, M. Ternes, C. P. Lutz, B. A. Jones, and A. J. Heinrich, Science **317**, 1199 (2007).

[134] R. Landauer, Philos. Mag. **21**, 863 (1970).

[135] R. Landauer, IBM J. Res. Dev. **32**, 306 (1988).

[136] M. Büttiker, Phys. Rev. Lett. **57**, 1761 (1986).

[137] M. Büttiker, Phys. Rev. B **46**, 12485 (1992).

[138] Y. M. Blanter and M. Büttiker, Phys. Rep. **336**, 1 (2000).

[139] H. Bruus and K. Flensberg, *Many-Body Quantum Theory in Condensed Matter Physics: An Introduction* (Oxford University Press, 2004).

[140] D. Averin, Physica B **194-196**, 979 (1994).

[141] M. Turek and K. A. Matveev, Phys. Rev. B **65**, 115332 (2002).

[142] J. Koch, F. von Oppen, Y. Oreg, and E. Sela, Phys. Rev. B **70**, 195107 (2004).

[143] J. Koch, F. von Oppen, and A. V. Andreev, Phys. Rev. B **74**, 205438 (2006).

[144] S. Koller, M. Grifoni, M. Leijnse, and M. R. Wegewijs, Phys. Rev. B **82**, 235307 (2010).

[145] Y. Meir and N. S. Wingreen, Phys. Rev. Lett. **68**, 2512 (1992).

[146] A. Jauho, N. S. Wingreen, and Y. Meir, Phys. Rev. B **50**, 5528 (1994).

[147] R. Bulla, T. A. Costi, and T. Pruschke, Rev. Mod. Phys. **80**, 395 (2008).

[148] H. Bethe, Zeitschrift für Physik A Hadrons and Nuclei **71**, 205 (1931).

[149] N. Andrei, Phys. Rev. Lett. **45**, 379 (1980).

[150] P. B. Vigman, JETP Lett. **31**, 364 (1980).

[151] P. Wiegmann, Phys. Lett. A **80**, 163 (1980).

[152] N. Kawakami and A. Okiji, Phys. Lett. A **86**, 483 (1981).

[153] G. C. Wick, Phys. Rev. **80**, 268 (1950).

[154] M. Leijnse and M. R. Wegewijs, Phys. Rev. B **78**, 235424 (2008).

[155] B. Kubala, G. Johansson, and J. König, Phys. Rev. B **73**, 165316 (2006).

[156] B. Wunsch, M. Braun, J. König, and D. Pfannkuche, Phys. Rev. B **72**, 205319 (2005).

[157] M. G. Pala, M. Governale, and J. König, New J. Phys. **9**, 278 (2007).

[158] J. Bardeen, L. N. Cooper, and J. R. Schrieffer, Phys. Rev. **108**, 1175 (1957).

[159] M. Governale, M. G. Pala, and J. König, Phys. Rev. B **77**, 134513 (2008).

[160] D. Futterer, M. Governale, M. G. Pala, and J. König, Phys. Rev. B **79**, 054505 (2009).

[161] D. Futterer, M. Governale, and J. König, Europhys. Lett. **91**, 47004 (2010).

[162] A. Braggio, J. König, and R. Fazio, Phys. Rev. Lett. **96**, 026805 (2006).

[163] D. Urban, J. König, and R. Fazio, Phys. Rev. B **78**, 075318 (2008).

[164] C. Emary, Phys. Rev. B **80**, 235306 (2009).

[165] J. Splettstoesser, M. Governale, and J. König, Phys. Rev. B **77**, 195320 (2008).

[166] W. Shockley, J. Appl. Phys. **9**, 635 (1938).

[167] S. Ramo, Proceedings of the IRE **27**, 584 (1939).

[168] R. Aguado and L. P. Kouwenhoven, Phys. Rev. Lett. **84**, 1986 (2000).

[169] U. Gavish, Y. Levinson, and Y. Imry, Phys. Rev. B **62**, R10637 (2000).

[170] E. V. Sukhorukov, G. Burkard, and D. Loss, Phys. Rev. B **63**, 125315 (2001).

[171] H. Engel and D. Loss, Phys. Rev. Lett. **93**, 136602 (2004).

[172] T. Holstein and H. Primakoff, Phys. Rev. **58**, 1098 (1940).

[173] O. Strelcyk, T. Korb, and H. Schoeller, Phys. Rev. B **72**, 165343 (2005).

[174] M. G. Schultz and F. von Oppen, Phys. Rev. B **80**, 033302 (2009).

[175] B. Sothmann, J. König, and A. Kadigrobov, Phys. Rev. B **82**, 205314 (2010).

[176] E. L. Nagaev, Phys. Rev. B **58**, 827 (1998).

[177] J. Koch, M. Semmelhack, F. von Oppen, and A. Nitzan, Phys. Rev. B **73**, 155306 (2006).

[178] A. Mitra, I. Aleiner, and A. J. Millis, Phys. Rev. B **69**, 245302 (2004).

[179] J. Koch and F. von Oppen, Phys. Rev. Lett. **94**, 206804 (2005).

[180] C. Bruder and H. Schoeller, Phys. Rev. Lett. **72**, 1076 (1994).

[181] L. P. Kouwenhoven, A. T. Johnson, N. C. van der Vaart, C. J. P. M. Harmans, and C. T. Foxon, Phys. Rev. Lett. **67**, 1626 (1991).

[182] L. P. Kouwenhoven, S. Jauhar, J. Orenstein, P. L. McEuen, Y. Nagamune, J. Motohisa, and H. Sakaki, Phys. Rev. Lett. **73**, 3443 (1994).

[183] L. P. Kouwenhoven, S. Jauhar, K. McCormick, D. Dixon, P. L. McEuen, Y. V. Nazarov, N. C. van der Vaart, and C. T. Foxon, Phys. Rev. B **50**, 2019 (1994).

[184] T. H. Oosterkamp, L. P. Kouwenhoven, A. E. A. Koolen, N. C. van der Vaart, and C. J. P. M. Harmans, Semicond. Sci. Technol. **11**, 1512 (1996).

[185] C. Meyer, J. M. Elzerman, and L. P. Kouwenhoven, Nano Lett. **7**, 295 (2007).

[186] I. Weymann and J. Barnaś, J. Phys.: Condens. Matter **19**, 096208 (2007).

[187] G. Kim and T. Kim, Phys. Rev. Lett. **92**, 137203 (2004).

[188] M. Misiorny and J. Barnaś, Europhys. Lett. **78**, 27003 (2007).

[189] M. Misiorny and J. Barnaś, Phys. Rev. B **75**, 134425 (2007).

[190] J. Fernández-Rossier, Phys. Rev. Lett. **102**, 256802 (2009).

[191] J. Fransson, Nano Lett. **9**, 2414 (2009).

[192] M. Persson, Phys. Rev. Lett. **103**, 050801 (2009).

[193] N. Lorente and J. Gauyacq, Phys. Rev. Lett. **103**, 176601 (2009).

[194] F. Delgado, J. J. Palacios, and J. Fernández-Rossier, Phys. Rev. Lett. **104**, 026601 (2010).

[195] B. Sothmann and J. König, New J. Phys. **12**, 083028 (2010).

[196] A. J. Heinrich, J. A. Gupta, C. P. Lutz, and D. M. Eigler, Science **306**, 466 (2004).

[197] C. F. Hirjibehedin, C. P. Lutz, and A. J. Heinrich, Science **312**, 1021 (2006).

[198] F. Meier, L. Zhou, J. Wiebe, and R. Wiesendanger, Science **320**, 82 (2008).

[199] A. F. Otte, M. Ternes, K. von Bergmann, S. Loth, H. Brune, C. P. Lutz, C. F. Hirjibehedin, and A. J. Heinrich, Nat. Phys. **4**, 847 (2008).

[200] A. F. Otte, M. Ternes, S. Loth, C. P. Lutz, C. F. Hirjibehedin, and A. J. Heinrich, Phys. Rev. Lett. **103**, 107203 (2009).

[201] S. Loth, K. von Bergmann, M. Ternes, A. F. Otte, C. P. Lutz, and A. J. Heinrich, Nat. Phys. **6**, 340 (2010).

[202] Y. M. Galperin, V. I. Kozub, and V. M. Vinokur, Phys. Rev. B **70**, 033405 (2004).

[203] L. D. Contreras-Pulido and R. Aguado, Phys. Rev. B **81**, 161309 (2010).

[204] J. Fernández-Rossier and R. Aguado, Phys. Rev. Lett. **98**, 106805 (2007).

[205] C. Timm and F. Elste, Phys. Rev. B **73**, 235304 (2006).

[206] F. Elste and C. Timm, Phys. Rev. B **71**, 155403 (2005).

[207] C. Romeike, M. R. Wegewijs, and H. Schoeller, Phys. Rev. Lett. **96**, 196805 (2006).

[208] C. Timm, Phys. Rev. B **76**, 014421 (2007).

[209] C. Romeike, M. R. Wegewijs, W. Hofstetter, and H. Schoeller, Phys. Rev. Lett. **96**, 196601 (2006).

[210] C. Romeike, M. R. Wegewijs, W. Hofstetter, and H. Schoeller, Phys. Rev. Lett. **97**, 206601 (2006).

[211] M. R. Wegewijs, C. Romeike, H. Schoeller, and W. Hofstetter, New J. Phys. **9**, 344 (2007).

[212] K. Ono and S. Tarucha, Phys. Rev. Lett. **92**, 256803 (2004).

[213] F. H. L. Koppens, C. Buizert, K. J. Tielrooij, I. T. Vink, K. C. Nowack, T. Meunier, L. P. Kouwenhoven, and L. M. K. Vandersypen, Nature **442**, 766 (2006).

[214] J. Iñarrea, G. Platero, and A. H. MacDonald, Phys. Rev. B **76**, 085329 (2007).

[215] S. Nadj-Perge, S. M. Frolov, J. W. W. van Tilburg, J. Danon, Y. V. Nazarov, R. Algra, E. P. A. M. Bakkers, and L. P. Kouwenhoven, Phys. Rev. B **81**, 201305 (2010).

[216] W. A. Coish and D. Loss, Phys. Rev. B **75**, 161302 (2007).

[217] M. S. Rudner and L. S. Levitov, Phys. Rev. Lett. **99**, 036602 (2007).

[218] M. S. Rudner and L. S. Levitov, Phys. Rev. Lett. **99**, 246602 (2007).

[219] J. R. Petta, J. M. Taylor, A. C. Johnson, A. Yacoby, M. D. Lukin, C. M. Marcus, M. P. Hanson, and A. C. Gossard, Phys. Rev. Lett. **100**, 067601 (2008).

[220] J. Iñarrea, C. Lopez-Monis, and G. Platero, Appl. Phys. Lett. **94**, 252106 (2009).

[221] G. Kiesslich, G. Schaller, C. Emary, and T. Brandes, Appl. Phys. Lett. **95**, 152104 (2009).

[222] M. Baumgärtel, M. Hell, S. Das, and M. R. Wegewijs, arXiv:1009.5874v2 (2010).

[223] B. Sothmann and J. König, Phys. Rev. B **82**, 245319 (2010).

[224] A. R. Edmunds, *Angular Momentum in Quantum Mechanics*, reissue ed. (Princeton University Press, 1996).

[225] J. Appelbaum, Phys. Rev. Lett. **17**, 91 (1966).

[226] J. A. Appelbaum, Phys. Rev. **154**, 633 (1967).

[227] J. Fransson, O. Eriksson, and A. V. Balatsky, Phys. Rev. B **81**, 115454 (2010).

[228] D. J. Monsma and S. S. P. Parkin, Appl. Phys. Lett. **77**, 720 (2000).

[229] N. Nishiguchi, Phys. Rev. Lett. **89**, 066802 (2002).

[230] A. Thielmann, M. H. Hettler, J. König, and G. Schön, Phys. Rev. B **68**, 115105 (2003).

[231] R. C. Jaklevic and J. Lambe, Phys. Rev. Lett. **17**, 1139 (1966).

[232] D. J. Scalapino and S. M. Marcus, Phys. Rev. Lett. **18**, 459 (1967).

[233] B. C. Stipe, M. A. Rezaei, and W. Ho, Science **280**, 1732 (1998).

[234] R. H. M. Smit, Y. Noat, C. Untiedt, N. D. Lang, M. C. van Hemert, and J. M. van Ruitenbeek, Nature **419**, 906 (2002).

[235] H. Park, J. Park, A. K. L. Lim, E. H. Anderson, A. P. Alivisatos, and P. L. McEuen, Nature **407**, 57 (2000).

[236] B. J. LeRoy, S. G. Lemay, J. Kong, and C. Dekker, Nature **432**, 371 (2004).

[237] R. Leturcq, C. Stampfer, K. Inderbitzin, L. Durrer, C. Hierold, E. Mariani, M. G. Schultz, F. von Oppen, and K. Ensslin, Nat. Phys. **5**, 327 (2009).

[238] A. K. Hüttel, B. Witkamp, M. Leijnse, M. R. Wegewijs, and H. S. J. van der Zant, Phys. Rev. Lett. **102**, 225501 (2009).

[239] J. Lehmann and D. Loss, Phys. Rev. B **73**, 045328 (2006).

[240] A. Rosch, J. Paaske, J. Kroha, and P. Wölfle, Phys. Rev. Lett. **90**, 076804 (2003).

[241] J. Paaske, A. Rosch, J. Kroha, and P. Wölfle, Phys. Rev. B **70**, 155301 (2004).

[242] H. Schoeller and F. Reininghaus, Phys. Rev. B **80**, 045117 (2009).

[243] M. N. Leuenberger and E. R. Mucciolo, Phys. Rev. Lett. **97**, 126601 (2006).

[244] G. González and M. N. Leuenberger, Phys. Rev. Lett. **98**, 256804 (2007).

[245] D. A. Bagrets and Y. V. Nazarov, Phys. Rev. B **67**, 085316 (2003).

[246] M. N. Leuenberger and D. Loss, Phys. Rev. B **61**, 1286 (2000).

[247] R. Fazio and R. Raimondi, Phys. Rev. Lett. **80**, 2913 (1998).

[248] R. Fazio and R. Raimondi, Phys. Rev. Lett. **82**, 4950 (1999).

[249] K. Kang, Phys. Rev. B **58**, 9641 (1998).

[250] P. Schwab and R. Raimondi, Phys. Rev. B **59**, 1637 (1999).

[251] A. A. Clerk, V. Ambegaokar, and S. Hershfield, Phys. Rev. B **61**, 3555 (2000).

[252] J. C. Cuevas, A. Levy Yeyati, and A. Martín-Rodero, Phys. Rev. B **63**, 094515 (2001).

[253] A. Levy Yeyati, J. C. Cuevas, A. López-Dávalos, and A. Martín-Rodero, Phys. Rev. B **55**, R6137 (1997).

[254] G. Johansson, E. N. Bratus, V. S. Shumeiko, and G. Wendin, Phys. Rev. B **60**, 1382 (1999).

[255] A. A. Clerk and V. Ambegaokar, Phys. Rev. B **61**, 9109 (2000).

[256] Y. Avishai, A. Golub, and A. D. Zaikin, Phys. Rev. B **67**, 041301 (2003).

[257] G. Sellier, T. Kopp, J. Kroha, and Y. S. Barash, Phys. Rev. B **72**, 174502 (2005).

[258] Z. Nussinov, A. Shnirman, D. P. Arovas, A. V. Balatsky, and J. X. Zhu, Phys. Rev. B **71**, 214520 (2005).

[259] F. S. Bergeret, A. Levy Yeyati, and A. Martín-Rodero, Phys. Rev. B **74**, 132505 (2006).

[260] R. López, M. Choi, and R. Aguado, Phys. Rev. B **75**, 045132 (2007).

[261] C. Karrasch, A. Oguri, and V. Meden, Phys. Rev. B **77**, 024517 (2008).

[262] M. R. Buitelaar, T. Nussbaumer, and C. Schönenberger, Phys. Rev. Lett. **89**, 256801 (2002).

[263] J. Cleuziou, W. Wernsdorfer, V. Bouchiat, T. Ondarcuhu, and M. Monthioux, Nat. Nano. **1**, 53 (2006).

[264] P. Jarillo-Herrero, J. A. van Dam, and L. P. Kouwenhoven, Nature **439**, 953 (2006).

[265] H. I. Jørgensen, K. Grove-Rasmussen, T. Novotný, K. Flensberg, and P. E. Lindelof, Phys. Rev. Lett. **96**, 207003 (2006).

[266] H. I. Jørgensen, T. Novotny, K. Grove-Rasmussen, K. Flensberg, and P. E. Lindelof, Nano Lett. **7**, 2441 (2007).

[267] T. Dirks, Y. Chen, N. O. Birge, and N. Mason, Appl. Phys. Lett. **95**, 192103 (2009).

[268] L. G. Herrmann, F. Portier, P. Roche, A. Levy Yeyati, T. Kontos, and C. Strunk, Phys. Rev. Lett. **104**, 026801 (2010).

[269] T. Dirks, T. L. Hughes, S. Lal, B. Uchoa, Y. Chen, C. Chialvo, P. M. Goldbart, and N. Mason, arXiv:1005.2749v3 (2010).

[270] J. A. van Dam, Y. V. Nazarov, E. P. A. M. Bakkers, S. D. Franceschi, and L. P. Kouwenhoven, Nature **442**, 667 (2006).

[271] T. Sand-Jespersen, J. Paaske, B. M. Andersen, K. Grove-Rasmussen, H. I. Jørgensen, M. Aagesen, C. B. Sørensen, P. E. Lindelof, K. Flensberg, and J. Nygård, Phys. Rev. Lett. **99**, 126603 (2007).

[272] C. Buizert, A. Oiwa, K. Shibata, K. Hirakawa, and S. Tarucha, Phys. Rev. Lett. **99**, 136806 (2007).

[273] B. Sothmann, D. Futterer, M. Governale, and J. König, Phys. Rev. B **82**, 094514 (2010).

[274] A. V. Rozhkov and D. P. Arovas, Phys. Rev. B **62**, 6687 (2000).

[275] C. Karrasch and V. Meden, Phys. Rev. B **79**, 045110 (2009).

[276] T. Meng, S. Florens, and P. Simon, Phys. Rev. B **79**, 224521 (2009).

[277] S. I. Erlingsson and Y. V. Nazarov, Phys. Rev. B **66**, 155327 (2002).

[278] I. A. Merkulov, A. L. Efros, and M. Rosen, Phys. Rev. B **65**, 205309 (2002).

[279] A. Khaetskii, D. Loss, and L. Glazman, Phys. Rev. B **67**, 195329 (2003).

[280] A. V. Khaetskii and Y. V. Nazarov, Phys. Rev. B **64**, 125316 (2001).

[281] V. N. Golovach, A. Khaetskii, and D. Loss, Phys. Rev. Lett. **93**, 016601 (2004).

Publications

[A] B. Sothmann and J. König,
"Nonequilibrium effects in single-spin inelastic tunneling spectroscopy",
New J. Phys. **12**, 083028 (2010).

[B] A. Schumann, B. Sothmann, P. Szary, and H. Zabel,
"Charge ordering of magnetic dipoles in artificial honeycomb patterns",
Appl. Phys. Lett. **97**, 022509 (2010).

[C] B. Sothmann, D. Futterer, M. Governale, and J. König,
"Probing the exchange field of a quantum-dot spin valve by a superconducting lead",
Phys. Rev. B. **82**, 094514 (2010).

[D] B. Sothmann, J. König, and A. Kadigrobov,
"Influence of spin waves on transport through a quantum-dot spin valve",
Phys. Rev. B. **82**, 205314 (2010).

[E] B. Sothmann and J. König,
"Influence of magnetic impurities on transport through a quantum-dot spin valve",
Phys. Rev. B. **82**, 245319 (2010).

Parts of this thesis have already been published. The results presented in Chapter 4 have been published in Ref. [D]. The results of Chapter 5 are going to be published in Ref. [E]. The results presented in Chapter 7 have been published in Ref. [C]. The results of Chapter 6 have been published in Ref. [A].

Acknowledgments

At this point, I would like to thank all the people who contributed to this thesis.

First of all, I want to thank my supervisor Prof. Dr. Jürgen König for the possibility to work in his group. He was always open for discussions which helped bringing forward my understanding of physics. Furthermore, he provided me with the opportunity to attend various scientific schools, conferences and workshops. I also want to thank Prof. Dr. Maarten Wegewijs and Prof. Dr. Daniela Pfannkuche refereeing this thesis and for useful discussions.

I want to thank Michele Governale, David Futterer, Anatoli Kadigrobov, Alexandra Schumann, Philipp Szary and Prof. Dr. Hartmut Zabel for fruitful collaborations.

Additionally, I want to thank the numerous people with whom I discussed about physics during the last years, at various summer schools, and conferences. In particular, there have been fruitful discussions with Sourin Das, Michael Baumgärtel and Michael Hell.

I furthermore want to thank my office mates Daniel Urban, Nina Winkler and Björn Kubala for many interesting discussions about physics but even more for discussions not about physics, especially starting out from our "Kalender des unnützen Wissens" and Wikipedia investigations. I also want to thank Daniel and Nina for proof-reading parts and all of this thesis, respectively.

I also want to thank Stephan Lindebaum, David Futterer, Bastian Hiltscher and Stephan Rojek for playing football in Bochum and Duisburg (as well as all others who participated) which provided a nice distraction from work.

I want to thank all the members of the institutes in Bochum as well as in Duisburg, in particular Fred Hucht for keeping all computers working without problems.

Furthermore, I want to thank Jens Ruppel and Hanna Döring for keeping company on the way from Gelsenkirchen to Bochum and back in public transport.

Finally, I want to thank my family for their constant support. Especially, I want to thank my grandmother for baking all these delicious biscuits and cakes.

This work was financially supported by the DFG through SFB 491.